FLOW MEASUREMENT

Edited by **Gustavo Urquiza Beltrán**
and **Laura L. Castro Gómez**

INTECHOPEN.COM

Flow Measurement
Edited by Gustavo Urquiza Beltrán and Laura L. Castro Gómez

Published by InTech
Janeza Trdine 9, 51000 Rijeka, Croatia

Copyright © 2012 InTech
All chapters are Open Access distributed under the Creative Commons Attribution 3.0 license, which allows users to download, copy and build upon published articles even for commercial purposes, as long as the author and publisher are properly credited, which ensures maximum dissemination and a wider impact of our publications. After this work has been published by InTech, authors have the right to republish it, in whole or part, in any publication of which they are the author, and to make other personal use of the work. Any republication, referencing or personal use of the work must explicitly identify the original source.

As for readers, this license allows users to download, copy and build upon published chapters even for commercial purposes, as long as the author and publisher are properly credited, which ensures maximum dissemination and a wider impact of our publications.

Notice
Statements and opinions expressed in the chapters are these of the individual contributors and not necessarily those of the editors or publisher. No responsibility is accepted for the accuracy of information contained in the published chapters. The publisher assumes no responsibility for any damage or injury to persons or property arising out of the use of any materials, instructions, methods or ideas contained in the book.

Publishing Process Manager Vana Persen
Technical Editor Teodora Smiljanic
Cover Designer InTech Design Team

First published March, 2012
Printed in Croatia

A free online edition of this book is available at www.intechopen.com
Additional hard copies can be obtained from orders@intechopen.com

Flow Measurement, Edited by Gustavo Urquiza Beltrán and Laura L. Castro Gómez
p. cm.
ISBN 978-953-51-0390-5

Contents

Preface

Flow measurement is a basic tool in industry, engineering and research. The existing applications reveal the evolution and development of new methods and devices through the years. Some of the latest emerging technologies, such as microelectronics and nanotechnology, have put forward new challenges in the flow measurement and are treated at the beginning of this book.

This book comprises 8 chapters divided into 4 sections, starting with *"microflows"*, followed by the *"biphasic"* and *"gas flow"*. Fourth and the final section deals with the *"indirect methods of flow measurement"* involving two different applications.

In particular, the first section revolves around the challenges in microflow measurements and the importance of studying their governing laws. Second section deals with the measurement of fluids composed of two phases through different methods, initially with the separation of the two phases accompanied by the measurement of the liquid film thickness and void fraction in the narrow gap by liquid film sensors and others methods.

In third section, the flow of gases has been studied with the help of the proposed experimental setup for measuring the passage of air through a rotating disk. In another chapter, the same phenomenon has been studied using different other setups and devices.

Fourth and final section includes two chapters describing the pressure measurement as an indirect method to calculate the flow. First chapter deals with the large volumes such as hydropower plants, and the second chapter presents the measurement of low flows by pressure microsensors.

I would like to thank all the contributing authors in this book, besides the valuable cooperation of the co-editors Dr. Miguel A. Basurto Pensado and Dr. Laura L. Castro Gómez, for their meaningful help in the scientific review of some chapters published here. Special thanks to the kind attention of the publishing head Ms. Vana Persen.

Dr. Gustavo Urquiza Beltrán and **Dr. Laura L. Castro Gómez**
Research Center on Engineerging and Applied Science (CIICAp)
from the Autonomous University of Morelos State (UAEM),
Mexico

Part 1

Microflows Measurement

1

Challenges in Microflow Measurements

Boguslaw Kruczek and Siamak Lashkari
University of Ottawa
Department of Chemical & Biological Engineering
Canada

1. Introduction

The term “microflows” is often associated with microfluidics, which is a multidisciplinary field intersecting engineering, physics, chemistry, microtechnology, and biotechnology that has emerged in the beginning of the 1980s. Improvements in fabrication of microflow devices such as micropumps, microvalves, microheat exchangers, and other microcomponents and sensors have led to the rapid development of microfluidics in the last decade (Morini, 2011). For this reason, many studies have been conducted to verify if the laws governing transport phenomena within channels of macroscopic dimensions are applicable at the microscale. These studies clearly show the necessity of correcting the classical theory when applying it to flow in microchannels, but appropriate corrections of the classical theory require reliable measurement of microflows. On the other hand, microflows also originate from a diffusive transport of fluids, typically gases, through seemingly non-porous media, such as perm-selective membranes, packaging materials, and walls of nuclear and chemical vessels. Characterization of materials for gas separation membranes, packages in food industry, walls of chemical and nuclear reactors, which involve determination of diffusivity, permeability and solubility coefficients of different gases in these materials, relies on accurate measurement of microflows.

Microflows, similarly to regular flows, result from a pressure gradient across a medium (e.g. a barrier material or microchannel), and are normally measured downstream from the medium. While the term microflow may refer to both a liquid and a gas, in this Chapter it will exclusively refer to “very low” flow rates of gases. There is no specific upper limit for microflows, and often flows much greater than 1 cm^3(STP)/min are still considered as microflows in microfluidics literature (Morini et al., 2011). However, in this Chapter we will focus on the flows that are less than 0.1 cm^3(STP)/min, which coincides with the minimum gas flow rate that can be measured directly using commercial volumetric or mass flow meters. Flows in this range are measured indirectly by checking the value taken by other measurable quantities, typically pressure or volume.

Defining gas flow as the number of moles (*n*) of a particular gas species passing through a system at a given time, the primary measurement is based on an equation of state. For the level of accuracy of flow measurements the ideal gas law suffice:

$$pV = nRT \tag{1}$$

where, p is the absolute pressure, V is the volume of the system, R is the universal gas constant, and T is the temperature. A primary measurement can then be made and the flow rate is given by:

$$Q = \frac{dn}{dt} = \frac{p}{RT}\frac{dV}{dt} + \frac{V}{RT}\frac{dp}{dt} - \frac{pV}{RT^2}\frac{dT}{dt} \tag{2}$$

If two of the three variables (V, p, T) are kept constant while the third one is monitored during the experiment, the flow rate of the gas can be determined. Eq. (2) provides the basis of two techniques for the determination of microflows, namely constant pressure (CP) and constant volume (CV) techniques. In the CP technique the flow is measured by monitoring the change in volume, resulting from the flow, at the conditions of constant temperature and pressure. In the CV technique, on the other hand the flowing gas is accumulated in a tank of known volume and the flow rate is determined from the isothermal rate of pressure increase.

Due to different conditions at which microchannels and semipermeable membranes are operated, the way the CP and CV techniques are used in these applications is different. The challenges in accurate measurements of microflows in microchannels, which mainly arise from the difficulty of keeping two of the three variables strictly unchanged, have been discussed recently by Morini et al. (2011). In case of characterization of semipermeable membranes by the CP and CV techniques, it is easier to keep two of the three variables unchanged. Yet, significant differences in the properties of membranes from the same material are often reported. The objective of this Chapter is to systematically review the challenges in the measurement of microflows; in particular those related to characterization of gas separation membranes.

To accomplish this objective, we will first discuss the importance of accurate measurements of microflows in applications involving characterization of microchannels and membranes, along with the specific information being sought in these characterizations. After these introductory remarks, the discussion will be directed into two parallel streams. The first one is dedicated to the CP technique, with special emphasis on recently developed fully automated soap flowmeter and the phenomenon of back permeation of air in CP systems open to atmosphere. The second one is dedicated to the CV method with special emphasis on the phenomenon of resistance to gas accumulation in high vacuum systems and a step by step procedure for the design of new CV systems.

2. Importance of microflows

Accurate measurement of microflows is indispensable for the characterization of gas separation membranes, packages in food industry, walls of chemical and nuclear reactors, (all of which fall into a category of nonporous materials), as well as, in studies of transport phenomena in microchannels.

2.1 Characterization of nonporous materials

Gas transport in nonporous membranes is commonly described by a solution-diffusion model. In this model, the permeability coefficient (P_m) is a fundamental property of materials, which is expressed as a product of a thermodynamic factor (S_m) called the solubility coefficient, and a kinetic parameter (D_m) called the diffusion coefficient (Zolondz and Fleming, 1992):

$$P_m = D_m S_m \tag{5}$$

In the solution-diffusion model, the transport of gas *i* consists of three independent steps. First, a gas is dissolved in a film at a high pressure (feed) side, then the gas diffuses across the film according to Fick's law of diffusion, and finally the gas evaporates from the film at a low pressure (permeate) side. Assuming the applicability of Henry's law, which is a reasonable approximation in the case of dilute solutions, the three steps of the solution-diffusion model are described by the following equations:

Step 1:
$$C_{i,f} = S_{m,i}\, p_{i,f} \tag{6}$$

Step 2:
$$J_i = -D_{m,i} \frac{dC_i}{dx} \tag{7}$$

Step 3:
$$C_{i,p} = S_{m,i}\, p_{i,p} \tag{8}$$

where: C_i is the concentration of component *i* inside the membrane, p_i is the partial pressure of *i* in the gas phase, J_i is the diffusive flux, and *x* is the distance from the feed surface of the membrane. The subscripts *f* and *p* refer to the feed and permeate side, respectively.

Assuming that Step 2 is a rate controlling step, and $D_{m,i}$ and $S_{m,i}$ are pressure independent, the solution-diffusion model simplifies to:

$$N_i = \frac{Q_i}{A_m} = \frac{P_{m,i}}{L_m}\left(p_{i,f} - p_{i,p}\right) \tag{9}$$

where: L_m and A_m are the respective film thickness and area, and N_i and Q_i are the respective steady state permeate flux and permeation rate, of gas *i* in the membrane. It is important to note that because the film is a stationary medium, $J_i = N_i$. Eq. (8) may also be rearranged to:

$$P_{m,i} = \frac{Q_i L_m}{A_m\left(p_{i,f} - p_{i,p}\right)} \tag{10}$$

The selective properties of a film (membrane) for the separation of gases *i* and *j* are assessed based on the ratio of permeability coefficients, which is often referred to as permselectivity:

$$\alpha_{ij} = \frac{P_i}{P_j} \tag{11}$$

Gas permeation tests can be carried out with pure gases or gas mixtures. In the former case the partial pressure gradient in Eqs. (9) and (10) becomes the total pressure gradient, and the ratio of permeability coefficients determined with the respective pure gases is referred to as the ideal selectivity. In the latter case, apart from the measurement of the permeation rate, the composition of the permeating gas must also be determined.

The permeability and ideal selectivity of films are determined in steady state permeation experiments using both the CP and CV techniques. On the other hand, the diffusivity is determined in transient gas permeation experiments (time lag method), which are normally carried out using the CV systems.

2.2 Transport phenomena in microchannels

Similarly to the flow in regular conduits, the major objective of transport phenomena in microchannels is to predict the pressure drop at a known average velocity of a fluid, normally a gas, in a microchannel of a specific geometry at known temperature and pressure conditions. However, unlike the regular conduits, rather than setting the flow rate and measuring the resulting pressure drop, the flow rate is measured at a specific pressure gradient across the microchannel. This is due to the current state of technology being unable to produce mass flow controllers capable of controlling flows that are of interest to microfluidics.

While the transport phenomena in regular conduits are adequately described with Navier-Stokes equations, these equations often fail in the case of flows in microchannels, because of rarefactions effects. The range of applicability of Navier-Stokes equations is provided in terms of Knudsen number (*Kn*):

$$\mathrm{Kn} = \frac{\lambda}{\mathrm{D_h}} = \frac{\mu}{\mathrm{D_h p}}\sqrt{\frac{\pi \mathrm{RT}}{2}} \tag{12}$$

where, λ is the gas mean free path, D_h is the characteristic dimension of the channel, μ is the dynamic viscosity of the gas, p and T are the gas pressure and temperature, and R is the gas constant. The departure from Navier-Stokes equations starts at $Kn > 0.001$. The flows with $0.001 < Kn < 0.3$ are often referred to as slip flows, while those with $0.3 < Kn < 10$ as transition flows. When Kn is greater than 10, i.e., when the collisions between gas molecules and microchannel walls are much more frequent than those between gas molecules, the transport occurs in a free molecular regime sometimes referred to as a Knudsen regime. Over the years a number of transport models have been developed to take into considerations the rarefaction effects in the slip and transition flow regimes. Some of these models include: the first order model (Maxwell, 1879), the second-order model (Deissler, 1964), the second-order model with Deissler boundary conditions modified with Hadjiconstantinou's coefficients (Hadjiconstantinou, 2003) that was recently proposed by Pitakarnnop et al. (2010).

The key aspect in verification and development of existing and new theoretical models, as well as semi-empirical ones is the capability of accurate measurement of microflows. The microflows in microfluidics are measured using both the CP and CV techniques.

3. Microflow measurement

Indirect measurements of microflows may involve monitoring of such measurable quantities as pressure, forces, weight, volume, temperature or any combination thereof (Morini et al., 2011). However, in this Chapter we will focus only on two of these quantities, namely volume and pressure, which provide a basis for the constant pressure and constant volume techniques.

3.1 Constant pressure technique

In the constant pressure (CP) technique, the flow measurements are carried out at constant pressure and temperature conditions, while changes in volume are monitored simultaneously. Consequently, Eq. (2) simplifies to:

$$Q = \frac{dn}{dt} = \frac{p}{RT}\frac{dV}{dt} \tag{13}$$

The simplest and oldest example of a CP instrument is a soap flowmeter, which is commonly used for quick determination of gas permeability in membranes. Soap flowmeters are also used for measurements of microflows emerging from microchannels (Celata et al., 2007). However, the latter application more frequently utilizes a liquid droplet tracking (DT) method, which similarly to a soap flowmeter utilizes a calibrated tube for the actual measurements. While a soap flowmeter is operated in a vertical position, the tube in the DT method is normally operated horizontally. The velocity of the gas is determined in both cases by recording the position of a soap bubble/liquid droplet versus time. Furthermore the flow rate of the gas can be calculated, knowing the diameter of the calibrated tube (d_t). In this case Eq. (13) can be re-written as:

$$Q = \frac{p}{RT}\frac{\pi d_t^2}{4}\frac{\Delta l}{\Delta t} \tag{14}$$

It is important to note that the term "constant pressure" is also used in reference to complex instruments, which utilize a piston or a bellow controlled by an automation system to allow volume variation while maintaining a constant pressure. Examples of these instruments, which are technologically difficult to implement, are provided by McCulloh et al. (1987) and Jousten et al. (2002). These instruments are not however, discussed in this Chapter.

The main advantage of the CP technique is that it operates based on measurements of primary units, the time and volume (length). As a result, there is no correlation which could change over time and thus, there is no need to recalibrate instrument over time.

3.1.1 Soap flowmeter

The scientific description of soap flow meters was first revealed by Exner (1875), and since then these instruments have been widely used in different applications involving manual gas flow measurements. A schematic diagram of a typical soap flowmeter, outlining four key sections of the instrument, is shown in Fig. 1. The bottom part accommodates a rubber bulb containing soap, a side aperture for the gas influx, and a smooth intersection to hold a small residual of soap from which the bubble is formed. The purpose of this part is to create a bubble and to transfer it to the main tube. The second part is a part of the tube above the side aperture for the gas influx where the created bubble accelerates and reaches a constant velocity. The length of this part depends on the gas flow rate as well as on the diameter of the tube. In most flowmeters this part is very short compared to the length of the main tube. The third part is a graduated tube where the actual measurement takes place. The bubble moving in the calibrated tube should have a constant velocity, which requires a constant pressure difference across the bubble. A smooth glass wall, which is well lubricated with a soap falling down, provides a frictionless path for the soap bubble to rise. The last part is the end section of the tube, in which the bubbles break up thus creating the falling liquid soap which lubricates the tube walls. The end section should not be used for the measurement purposes because back diffusion of air may significantly affect the velocity of the bubble in this part (Czubryt and Gesser, 1968; Guo and Heslop, 2004).

In order to produce a bubble in a typical soap flowmeter shown in Fig. 1, the rubber bulb must be squeezed to push the liquid soap into the tube. When the liquid level is above the inlet gas tube, the liquid is held for a short time to wet the glass, after which the rubber bulb is released leaving, some residual liquid at the intersection with the gas inlet; this residual liquid is pushed inside the main tube, forming a bubble. The produced bubble must be thin, yet strong enough to pass through the calibrated part of the tube without breaking up. There are several parameters affecting the properties of the bubble. One of the parameters is the properties of the soap solution. The common solution is a mixture of glycerol, distilled water, and a surfactant. The influence of soap properties on the flow measurement are discussed in the literature (Barigou and Davidson, 1994).

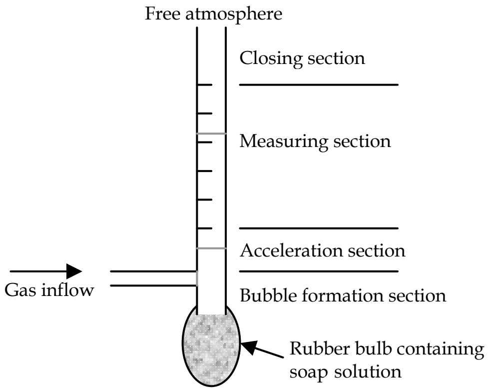

Fig. 1. Schematic diagram of typical soap flowmeter (Lashkari and Kruczek, 2008A).

It is generally believed that in order to make a thin bubble the time interval for holding the liquid in the tube should be very short, and by increasing the holding time, the curvature of the produced bubble will increase. In turn, the greater the curvature of the bubble the more liquid will be carried out by the bubble. Experimental data and equations relating the amount of liquid with the diameter of the bubble in vertical tubes are presented and discussed in the literature (Barigou and Davidson, 1994). On the other hand, Heslop et al. (1995) showed that there is a range of the liquid amount from which meta-stable bubbles can be formed.

The resolution of a soap flowmeter and hence the minimum gas flow rate that can be measured using this instrument depends on the size of the calibrated tube. To our best knowledge, the smallest commercial soap flowmeter (available from SEG) has the nominal size of 50 μL and allows the measurements of gas flow rates as low 0.005 mL/min. In principle, one could increase the resolution of a soap flowmeter by decreasing the diameter of the tube, which was actually suggested by Levy (1964) and Arenas et al. (1995). However, there is a critical radius of the tube (r_{cr}), below which a bubble cannot be formed, and instead of a bubble a liquid column (droplet) is formed. For fully wetting liquids in a vertical capillary Concus (1968) calculated the critical Bond number (B_{cr}) below which a bubble cannot be formed:

$$B_{cr} = \frac{\rho g r_{cr}^2}{\sigma} = 0.842 \qquad (15)$$

where: ρ and σ are the density and the surface tension of the soap liquid solution, and g is the gravity constant. The concept of B_{cr} also explains why the liquid solution used in bubble flow meter should contain a surfactant. If instead of a bubble a liquid droplet is formed, one can still carry out flow measurements. However, these measurements would fall into the category of DT methods, which will be discussed in the next section.

Flow measurements using soap flowmeters are normally performed manually, i.e. by squeezing a rubber bulb to push the soap liquid above a side aperture, visually observing the movement of a bubble in the calibrated tube and recording the time using a stopwatch. However, since more than a decade ago, there are commercially available soap flowmeters employing optical sensors for automatic detection of the soap bubble passing through the flowmeter, similar to those described by Arenas et al. (1995). The commercially available SF-1/2 and Optiflow supplied by STEC and Supelco tubes, respectively, utilize a timer-trigger mechanism for bubble detection. The flow rates that can be measured with Optiflow Flowmeter start from 0.1 cm^3/min, which is more than one order greater than what can be measured manually. The corresponding accuracy of this instrument is 3% of the reading. In addition to automatic flow measurements, the SF-1/2 soap flowmeter, available from STEC, is a fully automated instrument, with the bubble making mechanism based on the principle discussed by Bailey et al. (1968). Essentially, the bubble is made by pushing the liquid to touch the bottom of the flowmeter tube. This mechanism, however, is suitable for the flow rates (0.2-1000 mL/min) that are greater than those which are of interest in this Chapter.

3.1.2 Novel fully automated soap flowmeter

Recently, the current authors reported the development of novel, fully automated soap flowmeters for microflow measurements. The new instruments are based on existing soap flowmeters, in which the bubble maker and the calibrated tube are modified (Lashkari and Kruczek, 2008A).

Fig. 2 presents a schematic diagram of an automated bubble-making device developed by Lashkari and Kruczek (2008A). In order to make the process fully automated, a computer-controlled three way solenoid valve, a needle valve, a low pressure regulator and a sealed soap container are used. When the three way valve is opened by a computer signal, a low external pressure, less than 1 psig, is applied on the surface of the soap liquid in the sealed container. To avoid a sudden pressurization of the liquid soap, which would cause a jump and splash of the liquid on the tube walls, a needle valve is installed between the low pressure regulator and the three way solenoid valve. This allows pushing slowly the soap liquid inside the flowmeter tube and forming a soap bubble in front of the gas inlet to the main tube. The final height of the liquid in the tube depends on the applied pressure and the ratio of the area of the liquid soap container to the cross sectional area of the tube. Then, the solenoid valve is closed and the pressure on the liquid soap is released through the vent. This allows removing excess liquid from the tube back to the soap container.

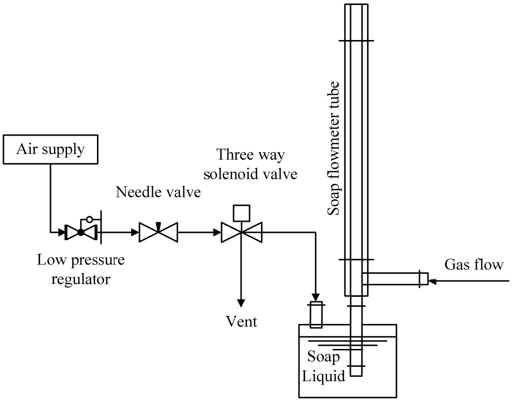

Fig. 2. Schematic diagram of a traditional soap flowmeter with an automated soap bubble maker apparatus. Adapted from Lashkari and Kruczek (2008A)

Usage of a computer controlled instrument makes it possible to adjust the time interval for holding liquid inside the tube. Consequently, the bubbles can be produced in the same way in all the experiments. This is one human error, which can be easily eliminated using the automated bubble maker shown in Fig. 2. The actual holding time of the liquid inside tube depends on its size. For example, for a 500 µL flowmeter, 0.3 second was determined to be a sufficient residence time for the soap liquid in the tube to make a thin, yet strong layer of soap at the gas entrance (Lashkari and Kruczek, 2008A). It is important to note that such a short residence time would not be attainable if the bubble were made manually by squeezing a rubber bulb. Moreover, since opening and closing of the solenoid valve is controlled by a computer program, the measurements of the flow rate can be executed automatically in a pre-scheduled routine.

The other part that was modified in the developed instrument was the calibrated tube. Fig. 3 presents a schematic of light emitting diodes (LEDs) and their corresponding photo diode sensors installed on a 500 µL Supelco soap flowmeter. The distance between any two adjacent sensors is restricted by the size of the photodiodes, and in Fig. 3 this distance is approximately 1/2 inch. The space for the light to pass into the photodiode measures about 1/16 inch. When a bubble passes through the light, the photodiode voltage is reduced due to the curvature of the bubble meniscus' light dispersion. As a result, the photodiode receives less light. This luminance allows for the best response according to this setup configuration and tube dimensions employed in this study. A gray PVC support in Fig. 3 is designed to hold the LEDs and photodiodes in a fixed position. In addition, the gray PVC body acts as an opaque barrier for the light to eliminate interference any between the light produced by the adjacent LEDs.

Instead of using a time-trigger circuit, the output of photodiodes in the new soap flowmeters are digitalized subsequently and sent to a computer for further analysis. Employing computerized data acquisition system allows for greater accuracy. A 20 Hz analog to digital converter is used in this study; however, a higher speed real time data acquisition system could be utilized for more precise measurements.

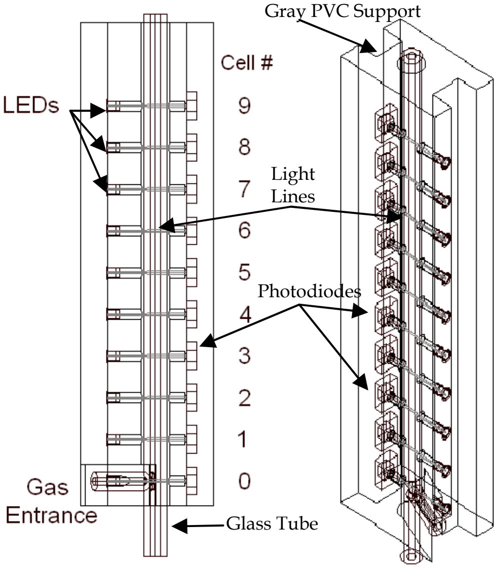

Fig. 3. Position of sensors installed on a 500 µL Supelco flowmeter. Left is the frontal exposure of the isometric view displayed on right. Adapted from Lashkari and Kruczek (2008A)

Accuracy of time measurement without actually increasing the time to be measured or decreasing tube radius is achieved in the new instrument by employing a signal analysis to find the minimum voltage of every pulse. These minima are determined by an interpolation using a 4th order Spline equation fitted to the experimental points. The time interval can then be extracted by comparing the minimum values for two subsequent photodiodes. By increasing the number of experimental points, the accuracy will increase as long as the resolution of an analog to digital converter is high enough. Based on current technology, the time that can be measured by a computer directly is in order of milliseconds; however, real time instruments can provide a much higher accuracy. As a result, having a more advanced real time data acquisition apparatus would provide a more precise measurement of measurement of time intervals, allowing for an increased accuracy of flow measurement.

The developed soap flowmeters were used for the measurement of gas permeation rates of N_2 through a poly(phenylene oxide), PPO, membrane. The permeations were controlled by adjusting the feed pressure of the membrane. The modified soap flowmeter, based on the 500 µL Supelco flowmeter, was capable of automatic measurements of microflows as low as 0.005 cm^3/min. These microflows correspond to the minimum value that can be measured using the smallest commercially available soap flowmeter. The latter, however, utilizes the capillary tube, which has the nominal size of just 50 µL. In comparison to the commercial fully automated SF-1/2 soap flowmeter available from STEC, the minimum flow rate of the new instrument is decreased by nearly two orders of magnitude.

3.1.3 Droplet tracking technique

The principle of the DT technique is the same as that of the soap flowmeter, except that the flow rates are determined by monitoring the movement of a liquid droplet rather than a soap bubble. The orientation of the calibrated tube in the DT method must be horizontal rather than vertical because that of a liquid droplet is much greater than the weight of a liquid bubble. Consequently, gravitational forces that would act on the liquid droplet in the vertical tube would not be negligible, and the pressure gradient across the liquid droplet would not be constant. As a result, the velocity of the liquid droplet in a vertical tube at a steady state would not be constant.

The DT technique is commonly used for measurement of microflows emerging from microchannels (Harley et al., 1995; Zohar et al., 2002; Maurer et al 2003; Colin et al., 2004; Ewart et al., 2006; Pitakarnnop et al, 2010). When the downstream of a capillary is open to atmosphere, the flow measurement can be performed using a soap flowmeter (Celata et al., 2007). However, at these conditions, some research groups, carry out their measurements using the DT technique. This technique cannot be replaced by soap flowmeter measurements when the downstream of the capillary is connected to a constant volume at sub-atmospheric pressures. Studies involving flows in transition and near free molecular regimes require very low downstream pressures. For example, Pitakarnnop et al. (2010) and Ewart et al. (2006) reported flow measurements at downstream pressures of as low as 1,928 Pa and 1,101 Pa, respectively. At such low pressures, a soap bubble and even a soap liquid droplet would quickly evaporate making measurement impossible. For this reason, the liquid used in the DT method must have a very low vapour pressure; typically an oil droplet is used. In their studies, Ewart et al. (2006) used, for example, oil with a vapour pressure of 1.33×10^{-3} Pa.

The liquid droplet is introduced into the capillary typically using a syringe, after which the droplet is allowed to reach constant moving velocity before measurements are taken. The position of the bubble moving in the calibrated part of the capillary is observed visually (Zohar et al., 2002), or with a help of auxiliary instrumentation. The latter includes, the use of opto-electronic sensors (Colin et al., 2004; Pitakarnnop et al., 2010) similar to those used in automated soap flowmeters, or a low power microscope (Harley et al., 1995), or using a high resolution digital camera (Ewart et al., 2006). After measurement, the liquid droplet must be retracted and/or withdrawn from the capillary in order to prepare the system for the next measurement.

Flow rates measured by the DT technique are typically provided in kg/s. Thus, the comparison of minimum flow rates that can be measured with the DT technique and soap flowmeters is not immediately obvious because of different measurement units. Moreover, some research groups provide very low mass flow rates for an individual microchannel by using hundreds of identical microchannels in parallel in a single test section (Shih et al., 1996). As a rule of thumb, the lowest value of the mass flow rate that can be measured by the DT technique in a system with a single microchannel is of the order 10^{-10} kg/s (Morini et al., 2011). However, values much lower than 10^{-10} kg/s have been reported in the literature. For example, Ewart et al. (2006) reported measuring the mass flow of nitrogen as low as 2.68×10^{-12} kg/s. In this case, the measurement was carried out at the pressure of just 1.1 kPa and 296.3 K. Converting this mass flow rate into volumetric flow rate at 1.1 kPa and 296.3 K leads to approximately 0.013 cm^3/min, which is actually greater than 0.005 cm^3/min that can be measured using the SEG soap flowmeter, having the nominal tube size of 50 μL.

In general, the DT technique is associated with greater uncertainty compared to measurements taken using soap flowmeters. Moreover, its implementation is associated with various problems, some of which include (Ewart et al., 2006):

- Difficulty to introduce the drop oil in the calibrated tube without causing a pressure distortion;
- Formation of several drops rather than a single drop in the calibrated tube, which perturbs the pressure in the tube;
- “Explosion” of a droplet causing a pressure jump in the tube;
- Difficulty in precise estimation of the drop/gas interface position and hence difficulty in following the same point of the interface during the experiment.

The first three problems lead to difficulty in maintaining a constant moving speed of the droplet at steady state conditions, which in combination with the fourth problem may result in significant errors in the measured velocity of the liquid droplet. In addition, another problem occurs in the accurate measurement of the inner diameter of the tube (d_t), which weights the most in determining the mass flow rate (Morini et al., 2011). While this problem is also also applicable to measurements with soap flowmeters, it is probably more eminent in case of the DP technique, which utilizes “homemade” rather than commercial calibrated tubes.

3.1.4 Effect of back diffusion on characterization of semi-permeable materials

The influence of back diffusion of air on flow measurements with soap flowmeters has been recognized by Czubryt and Gesser (1968), and more recently by Guo and Heslop (2004). Because of the influence of back diffusion of air, flow measurements should not be taken in the end section of soap flowmeters, in particular when very small flow rates of gases are involved. If the back diffusing air, or more generally any gas, can reach the flow source and then be transported across the flow source, (which is the case when the flow source is a membrane), the effect of back diffusion may lead to a systematic error in gas permeability coefficients determined when using a soap flowmeter. The following discussion is based on the recently published paper by the current authors (Lashkari and Kruczek, 2008B).

Fig. 4 presents a schematic diagram of a typical CP system used for measuring the permeation rate of gas A through a membrane. The gas permeation rate is evaluated based on the gas flow rate measured by a soap flowmeter, which is attached to the permeate side of the membrane. The soap bubble is introduced at the entrance of a calibrated column and is picked up by the flowing gas. Because of the negligible weight of the soap bubble, the speed of the bubble through the calibrated column can be correlated to the volumetric flow rate of the permeating gas. In the system depicted in Fig. 4, the membrane is open to atmosphere of gas B, which is typically air. If A and B are different gases, B may diffuse towards the membrane and then permeate through the membrane. Since the direction of the diffusion and permeation of B is opposite to the direction of the permeation and flow of A, the diffusion and permeation of B are referred to as back diffusion and back permeation, respectively.

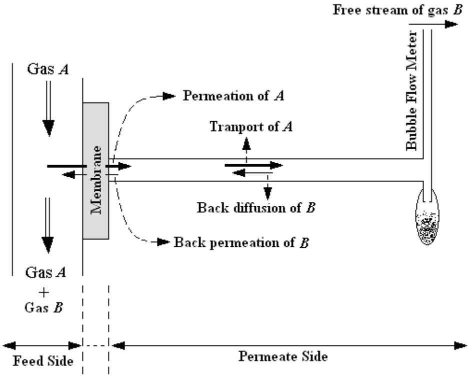

Fig. 4. Measurement of the permeation rate of a gas through a membrane in a constant pressure system. Adapted from Lashkari and Kruczek (2008B).

Treating the membrane in Fig. 4 as a "black box", that is, assuming that the permeability coefficient of A (P_A) is not affected by the presence of B and the permeability coefficient of B (P_B) is not affected by the presence of A in the membrane; the respective fluxes, N_A and N_B, are expressed using Eq. (9):

$$N_A = \frac{P_{m,A}}{L_m}\left(p_{A,f} - p_{A,p}\right) = \frac{P_{m,A}}{L_m}\left(p_f - p_p (x_A)_p\right) \tag{16}$$

$$N_B = \frac{P_{m,B}}{L_m}\left(p_{B,f} - p_{B,p}\right) = \frac{P_{m,B}}{L_m}\left(0 - p_p\left(1 - (x_A)_p\right)\right) = -\frac{P_{m,B}}{L_m} p_p\left(1 - (x_A)_p\right) \tag{17}$$

where: $(x_A)_p$ is the mole fraction of gas A at the permeate side of the membrane. It is important to note that Eq. (16) assumes that the mole fraction of A at the feed side of membrane is equal to unity. This is a reasonable assumption, especially when the feed side is swept with A.

The expression for the permeability coefficient, given by Eq. (10), can be rewritten in a slightly different form, which follows from Eq. (16):

$$P_{m,A} = \frac{L_m N_A}{p_p\left(p_f/p_p - (x_A)_p\right)} \tag{18}$$

In the case of a single gas permeation test in a CP system, the composition of the permeating gas is not measured, and although not explicitly stated, it is simply assumed that $(x_A)_p$ is equal to unity. Moreover, it is assumed that the experimentally measured gas flux through the membrane (N) corresponds to N_A. With these assumptions, the expression for the permeability coefficient given by Eq. (18) becomes:

$$P_{m,A}\Big|_{app} = \frac{L_m N}{p_p\left(p_f/p_p - 1\right)} \tag{19}$$

To distinguish between the permeability coefficients given by Eq. (18) and Eq. (19), the former will be referred to as the actual permeability coefficient and the latter as the apparent permeability coefficient. Given a situation, in which back diffusion and back permeation of B exist, $N \neq N_A$, and $(x_A)_P < 1.0$, consequently $P_{m,A} \neq P_{m,A}\big|_{app}$.

To evaluate the error associated with the apparent permeability coefficient when the phenomena of back diffusion and back permeation are present, it is necessary to realize that for the system depicted in Fig. 4, the experimentally measured gas flux is given by:

$$N = N_A + N_B = Cu \tag{20}$$

where: u is the gas velocity and $C = \sum C_i$ is the total gas concentration. Substitution of Eq. (16) and Eq. (17) into Eq. (20) leads, after rearrangements, to:

$$P_{m,A} = \frac{L_m N}{p_P\left(p_f/p_P - (x_A)_P - \alpha_{BA}\left(1-(x_A)_P\right)\right)} \tag{21}$$

where: $\alpha_{BA} = P_{m,B}/P_{m,A}$. Dividing Eq. (19) by Eq. (21) yields the following expression:

$$\frac{P_{m,A}\big|_{app}}{P_{m,A}} = 1 + \left(1-\alpha_{BA}\right)\frac{1-(x_A)_P}{p_f/p_P - 1} \tag{22}$$

When $p_f > p_p$, it follows from Eq. (22) that:

$$\text{if} \quad \alpha_{BA} < 1 \quad \Rightarrow \quad P_{m,A}\big|_{app} > P_{m,A}$$

$$\text{if} \quad \alpha_{BA} > 1 \quad \Rightarrow \quad P_{m,A}\big|_{app} < P_{m,A}$$

In the limiting case when $p_f >> p_p$, regardless of α_{BA}, $P_{m,A}\big|_{app} \to P_{m,A}$.

To quantify Eq. (22), it is necessary to evaluate the composition of the gas at the permeate side of the membrane. This requires modelling of back diffusion and the knowledge of the mechanism by which the gas is transported through the membrane. In the following analysis the transport equations describing the phenomenon of back diffusion are developed by assuming that the membrane can be treated as a "black box".

For the purpose of modelling, the CP system presented in Fig. 4 is generalized in Fig. 5. Tube 1 represents a bubble flowmeter. The bubble is made at z_1 and moves towards z_0. Tube 2 is a connecting tube between the membrane cell and the bubble flowmeter. There can be more than two tubes between the membrane and the atmosphere, but for the purpose of modelling the case with two tubes is sufficiently representative. Since there is no velocity field except in longitudinal (z-direction), the continuity equation for a constant density fluid is reduced to:

$$\frac{du}{dz} = 0 \tag{23}$$

where *z* is distance from the free stream of B (air), i.e. from the outlet of the bubble flowmeter tube.

It is important to emphasize that for typical velocities in gas permeation experiments the pressure drop through the tubes does not affect the velocity field. This can be verified by applying Bernoulli's equation for typical velocities associated with membrane gas permeation. Since the velocity in a tube of constant diameter is constant, the continuity equation yields:

$$u_1\left(\frac{\pi d_1^2}{4}\right) = u_2\left(\frac{\pi d_2^2}{4}\right) = u_m A_m \tag{24}$$

where *d* is the tube diameter, subscripts 1, 2 and *m* indicate the tube numbers and the membrane, respectively, and A_m is the membrane area available for gas permeation. The velocity across the membrane can be calculated from:

$$u_m = \frac{\sum_i (N_i)_m}{C} \tag{25}$$

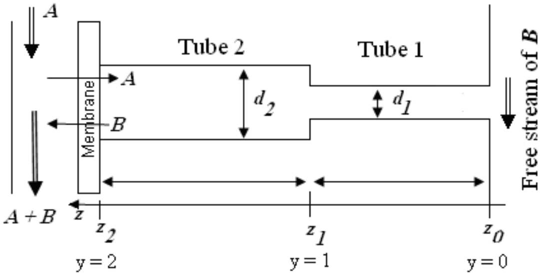

Fig. 5. Schematic representation of a CP system for the purpose of modelling of back diffusion and back permeation. Adapted from Lashkari and Kruczek (2008B).

Combining Eqs. (24) and (25) leads to:

$$u_1 = u_m \frac{A_m}{\left(\pi d_1^2/4\right)} = \frac{\sum_i (N_i)_m}{C} \frac{A_m}{\left(\pi d_1^2/4\right)} \tag{26}$$

Assuming that air consists only of N_2 and O_2, gas permeation experiments with single N_2 and O_2 will represent the examples of back diffusion and back permeation in binary systems. In the experiment with O_2, A = O_2 and B = N_2. For the components A and B in a binary system the continuity equations are:

$$\frac{d(N_A)}{dz}=0 \qquad \frac{d(N_B)}{dz}=0 \tag{27}$$

Applying Fick's first law, the total flux of A in tube *k* is given by:

$$(N_A)_k = -CD_{AB}\frac{dx_A}{dz} + x_A(Cu_k) \tag{28}$$

or

$$\frac{dx_A}{dz} = \frac{u_k}{D_{AB}}(x_A - \xi_A) \tag{29}$$

where D_{AB} is the diffusivity of A in B, ξ_A is a position independent dimensionless parameter defined by Eq. (30), and subscript *k* indicates the tube number.

$$\xi_A = \frac{(N_A)_k}{(N_A)_k + (N_B)_k} = \frac{(N_A)_k}{Cu_k} \tag{30}$$

To obtain the composition profile in the tubes, $x_A(z)$, and thus the gas composition at the permeate side of the membrane, $(x_A)_p$, Eq. (29) must be solved for all tubes. The solution in each tube requires one boundary condition. The composition of the free stream B, which is the composition of air, represents the boundary condition for tube 1. Solving Eq. (29) for tube 1 allows evaluation of the gas composition at z_1, $(x_A)_1$, which represents the boundary condition for tube 2, with which Eq. (29) may be solved in tube 2. Treating the membrane as a black box, ξ_A may be expressed in terms of N_A evaluated from Eqs. (16) and (17) as:

$$\xi_A = \frac{p_f/p_P - (x_A)_P}{p_f/p_P - (x_A)_P - \alpha_{BA}\left(1-(x_A)_P\right)} \tag{31}$$

Therefore, for a binary system and a two-tube configuration presented in Fig. 5 the following equation becomes applicable:

$$\frac{\xi_A - (x_A)_P}{\xi_A - (x_A)_0} = \exp\left(-\frac{u_1}{D_{AB}}\left(l_1 + l_2\left(\frac{d_1}{d_2}\right)^2\right)\right) \tag{32}$$

It is important to note that u_1 in Eq. (32) represents the net velocity of the gas in the bubble flowmeter, a positive number, which can be measured experimentally. In general:

$$\frac{\xi_A - (x_A)_P}{\xi_A - (x_A)_0} = \exp\left(-\frac{u_j}{D_{AB}}l_e\right) = \exp(-Pe) \tag{33}$$

where *Pe* is the Peclet number ($Pe = u_j l_e / D_{AB}$) in which l_e is an equivalent length of the connecting tubes. For *n* tubes in series including soap flowmeter as tube *j*, the general equation for l_e is given by:

$$l_e = \sum_{k=1}^{n} l_k\left(\frac{d_j}{d_k}\right)^2 \tag{34}$$

Eqs. (31) and (33) can be simultaneously solved for the two unknowns $(x_A)_P$ and ξ_A, and then $P_{m,A}\big|_{app}/P_{m,A}$ can be evaluated using Eq. (22).

The model for back diffusion and back permeation was compared with experimental data generated in single gas permeation experiments with oxygen and nitrogen using a homogeneous PPO membrane, in a CP system equipped with fully automated soap flowmeter capable of measuring the flow rates as low as 0.005 cm^3/min (Lashkari and Kruczek, 2008A). The experimental system also allowed sampling of the permeating gas at three different distances from the membrane in order to compare the experimentally determined gas compositions with the model-predicted values.

The experimental results for the apparent permeability and the composition of the permeating gas as a function of feed pressure confirmed the theoretical trends, but some discrepancies were observed. The discrepancy between the experimental and theoretical results was quantified by a dimensionless correction factor (β), with which Eq.(33) becomes:

$$\frac{\xi_A-(x_A)_P}{\xi_A-(x_A)_0}=\exp(-\beta Pe) \tag{35}$$

The correction factor β, determined by minimizing the least square difference between the theoretical and experimental values using a MATLAB simplex method, was less than unity for all experimental runs. In other words, the experimentally observed effects of back diffusion and back permeation were actually greater than the theoretically predicted effects. In general, the discrepancy based on the composition of permeate was greater than that based on the permeability coefficients; also the discrepancy increased with decrease in the membrane thickness. As the membranes thickness decreases, the flux and thus the net velocity of the gas in tube increases. This indicates that the effects of back diffusion and back permeation might be still present at relatively large *Pe*.

From the point of view of membrane characterization by single gas permeation experiments with N_2 and O_2, the effect of back permeation and back diffusion leads to an underestimation of the permeability coefficient of less permeable gas (N_2) and an overestimation of the permeability coefficient of more permeable gas (O_2). Consequently, the ideal selectivity, α_{O_2/N_2}, will be greatly overestimated. The phenomena of back diffusion and back permeation may explain some "inflated" ideal selectivities reported in the literature.

The obtained experimental results by Lashkari and Kruczek (2008B) suggest running gas permeation tests in a CP system at the conditions for which $Pe \geq 10$. It also appears to be more advantageous to maximize the *Pe* number by increasing the length of the tube connecting the membrane cell with the bubble flow meter rather than by increasing the net velocity of the gas in the soap flow meter column via, for example, an increase in feed pressure and/or by using thinner membranes. However, since maximization of the *Pe* number does not guarantee complete elimination of the effects of back diffusion, it might be advantageous to sample permeating gas or gases near the permeate side of the membrane to allow for the analysis of the permeate composition. Negligible concentrations of back permeating gases in the permeate stream near the membrane would increase reliability of the permeability coefficient determined in a CP system. Even if back permeation effects were not negligible, knowing the exact composition of the permeate stream near the membrane would allow for more accurate calculations of permeability coefficients.

3.2 Constant volume technique

In the constant volume (CV) technique flow measurements are carried out at constant volume and temperature conditions, while changes in pressure are monitored simultaneously. Consequently, Eq. (2) simplifies to:

$$Q = \frac{V}{RT}\frac{dp}{dt} \tag{36}$$

As a rule of thumb, the CV technique allows measurements of much lower flows than the CP technique. Therefore, the CV technique has become a very important tool in characterization of microchannels. In the case of membranes, the CV technique not only allows for the measurement of flows that otherwise could not be measured, but also the determination of the diffusivity coefficient. The resolution of the CV technique and thus the lower limit of flow rates that can be measured depend on the resolution of the pressure sensor. For this reason, it is advantageous to carry out CV flow measurements at very high vacuum. This is not however, always possible, particularly in applications involving microchannel characterizations.

3.2.1 Constant volume technique in membrane characterization

The constant volume (CV) technique has been used for characterization of gas permeation through semi-permeable membranes since the introduction of the latter in the mid nineteenth century (Stannett, 1978). Moreover, since the introduction of a time lag method by Daynes nearly a century ago (Daynes, 1920), which was brought to prominence by Barrer (1939), the CV technique has also been widely used for the evaluation of membrane diffusivity. The CV membrane characterization technique is exclusively employed at the highest vacuum possible.

A common experimental technique in CV systems used to determine the diffusivity involves the procedure, in which the inflow and outflow volumes are evacuated to the lowest possible absolute pressure to degas the membrane or the medium to be tested. The inflow volume is then instantaneously pressurized and the resulting pressure response at the permeate side of the membrane is monitored. If, after pressurization, the concentration of the gas at the feed and the permeate faces of the membrane are constant and the latter remains approximately equal to zero during the entire experiment, the pressure in the receiver as a function of time (*t*), is determined by (Barrer, 1939):

$$p(t) = \frac{A_m p_f P_m RT}{V v_{STP} L_m}\left[t - \frac{L_m^2}{6D_m} + \frac{2L_m^2}{\pi^2 D_m} \times \sum_{n=1}^{\infty} \frac{(-1)^{n+1}}{n^2} \exp\left(-\frac{D_m n^2 \pi^2 t}{L_m^2} \right) \right] \tag{37}$$

where v_{STP} is the volume of one mole of gas at standard temperature and pressure conditions. It is important to emphasize that p_f in Eq. (37) corresponds to the pressure gradient across the membrane, which implies that the pressure increase at the permeate side of the membrane is negligible compared to p_f. Eq.(37) is graphically presented in Fig. 6. The last term on the right-hand side of Eq. (36) contains an exponential function with a negative argument, which is proportional to *t*. Consequently, as *t* increases, this term disappears and the pressure response becomes a linear function of time.

$$p(t) = \frac{A_m p_f P_m RT}{V v_{STP} L_m}\left[t - \frac{L_m^2}{6D_m}\right] \tag{38}$$

The term in front of the bracket in the above equation corresponds to the slope in Fig. 6, which represents dp/dt in Eq. (36). Moreover, this term contains the permeability coefficient, thus P_m can be evaluated from the slope in Fig. 6. The extrapolation of the linear part of the pressure response curve into the time axis represents the time lag (θ_m) of tested membrane. Mathematically, the expression for θ_m is obtained by setting $p(t)$ equal to the initial pressure in the receiver, which is assumed to be zero. Therefore:

$$t = \theta_m = \frac{L_m^2}{6D_m} \tag{39}$$

Consequently, the diffusivity of the membrane can be obtained by rearranging Eq. (39) based on the time lag and the thickness of the membrane. Knowing D_m and P_m, allows for the determination of S_m from Eq. (5). Thus, the time lag method allows for the evaluation of the three gas transport coefficients based on the asymptote of the pressure response curve in a single gas permeation experiment.

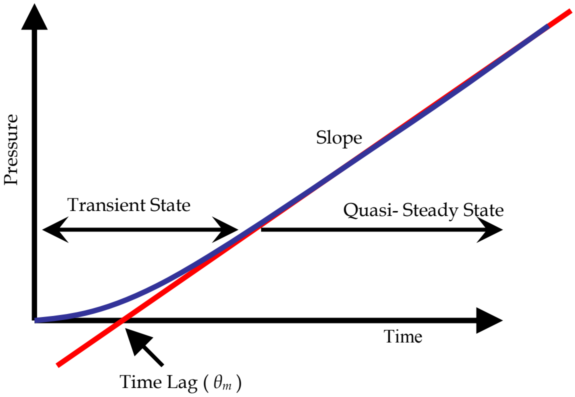

Fig. 6. Expected pressure response of a pressure sensor in a CV system receiver during a time lag experiment.

The heart of the CV system is the receiver, where the gas permeating through the membrane is accumulated and its pressure accurately measured. Early designs of CV systems were based on the Dow gas transmission cell, originally developed in late 1950s (Paul and DiBenedetto, 1965). In that system, the gas accumulates directly under the tested membrane and the volume of the receiver is varied by means of an adapter. It is important to emphasize that the requirement of "constant volume" is not strictly observed in the Dow's cell, because the pressure increase due to gas permeation is measured using a mercury manometer, and as the pressure of the accumulated gas increases, the mercury in the capillary leg is displaced.

Commercial availability of high accuracy, low-range pressure transducers has led to more complex designs of the receiver. Generally, in case of the modern systems, the permeating gas is no longer accumulated directly under the tested membrane, and receiver configurations can be divided into two groups, systems with a single accumulation tank and systems with multiple accumulation tanks (Lashkari and Kruczek, 2010).

An example of a CV system with a single accumulation tank is described by O'Brian et al. (1986). In this system, depending on the anticipated permeation rate, a tank with a correspondingly appropriate volume should be used. However, the range of tank volumes, length and size of tubing used downstream from the membrane are are not commonly provided in the literature. The system described by O'Brian et al. (1986) was modified by Costello and Koros to allow for its use at elevated temperatures; the accumulation tank used in the modified system has volume of 1000 cm^3 (Costello and Koros, 1992). Recently, Al-Juaied and Koros (2006) reported using 1/4 and 1/8 inch tubes and a total receiver volume of 1029 cm^3. Assuming the same size of the accumulation tank in references (Costello and Koros, 1992) and (Al-Juaied and Koros, 2006), 29 cm^3 corresponds to the volume of 1/4 in. and 1/8 in. tubes as well as to the volume associated with valves and fittings downstream from the membrane. CV systems with a single accumulation tank are also used by other research groups (Shishatskii et al., 1996; Bos et al., 1998; Lee et al., 1999).

Unlike in systems with a single accumulation tank, in systems with multiple accumulation tanks can change the receiver volume without exposing the system to atmosphere. The latter is not desirable because re-evacuation of the receiver might be very time consuming. For example, Huvard et al. (1980) reported two weeks as a minimum evacuation time before performing any gas permeation experiments. Stern et al. (1963) provide one of the earliest examples of a system with multiple accumulation tanks, but without any detailed specifications. Based on the schematic diagram provided in this reference, the system consists of three accumulation tanks arranged in parallel. Another example of a three-tank system is described in Kemp (1972), in which two of the tanks are arranged in parallel, while the third tank is in series with the other two. As a result, the volume downstream from the membrane can have five discrete values ranging from 4.77 cm^3 to 108.7 cm^3 (Kemp, 1972). The system reported by Huvard et al. (1980) consists of four accumulation tanks arranged in parallel and 1/4 in. tubes. While the volumes of the accumulation tanks are not reported, according to the schematic diagram, each tank has a different volume. Therefore, the volume of the receiver in that system can have 16 discrete values. Multiple accumulation tanks are also used in the CV system described by Mohammadi et al. (1995), Lin et al. (2000) and Lashkari and Kruczek (2011).

The biggest challenge associated with CV systems operating at a very high vacuum is tightness of the receiver. While operation of the CV systems at high vacuum maximizes the resolution of the measurement, the advantage of high resolution disappears if the tightness of the receiver is compromised. This is because the tightness of the receiver determines the leak rate into the system. Under normal operation protocol, leak rate should be checked before each experiment, and in principle this determined leak rate could be subtracted from the measured flow rate. Nevertheless, when the apparent flow rate is in the order of the leak rate, the reliability of the measurement is compromised. Therefore, whenever possible, it is best to carefully weld tube connections in the receiver, and when welding is not possible

VCR connections with replaceable metal gaskets one should use. The advantages and disadvantages of welding versus VCR, tube fittings are discussed by Moore et al. (2004). All valves in the receiver should be special vacuum valves. The most difficult element to seal in the receiver is the membrane cell. Schumacher and Ferguson (1927) sealed the membrane cell with mercury. Tabe-Mohamadi et al., (1995) used the membrane itself facing two mirror polished plates and reported leak rates below 1.2×10^{-9} cm^3/s. On the other hand, Moore et al. (2004) employed a combination of an o-ring with a self-seal membrane masking to seal the membrane cell, and recommended this method for brittle membranes such as carbon molecular sieve membranes.

3.2.2 Constant volume technique in microchannel characterization

The CV technique in microchannel characterization is used only for the measurement of gas flows emerging from microchannels under a specific pressure gradient. CV systems in microchannel characterization are not used while under very high vacuum, but rather over a wide distribution of pressures ranging from near atmospheric to moderate vacuum pressures. In addition, the receivers used in applications involving flow measurements in microchannels are relatively simple, consisting of a tank with a relatively large volume to ensure quasi-steady state conditions during measurement, a sensitive pressure sensor and, a tube connecting the microchannel with the tank and the pressure sensor. On the one hand, the volume of the receiving tank should be large, but on the other hand, if the pressure in the tank is excessively large, the detection of the pressure rise resulting from the microchannel flow becomes difficult, in particular when approaching atmospheric pressure.

Another difficulty with measurements near atmospheric pressure is the influence of small temperature drifts on flow measurement. To understand this problem, Eq. (36) must be presented more generally:

$$Q=\frac{V}{RT}\frac{dp}{dt}-\frac{pV}{RT^2}\frac{dT}{dt} \tag{40}$$

It is evident from Eq.(40) that the effect of temperature variation, dT/dt, on the measured flow is directly proportional to p.

To address the problem of very low resolutions and temperature fluctuations near atmospheric pressures, Arkilic et al. (1997) developed a two-tank CV system. Both tanks in the modified receiver are located downstream of the microchannel. During the test one tank is used to accumulate the gas flowing out of the microchannel, while the other one remains at constant pressure, thus acting as a reference tank. The main advantage of this is solution comes from the fact that instead of measuring the absolute pressure rise, the pressure difference between the two tanks is measured. Consequently, Eq. (39) becomes:

$$Q=\frac{V}{RT}\frac{d(\varDelta p)}{dt}-\frac{\varDelta pV}{RT^2}\frac{dT}{dt} \tag{41}$$

where Δp is the pressure difference between the reference tank and the working tank. In the case of experiments near atmospheric pressure, Δp at the end of experiments is typically orders of magnitude less than p. Consequently, the sensitivity of the mass flow rate to the tank temperature fluctuations is reduced by several orders of magnitude, and the minimum flow rate that can be measured in this system is also greatly decreased.

Ewart et al. (2006) developed a system that allows flow measurement by both the DP method and the CV method. While downstream pressure for the two methods are overlapping, the tests involving a relatively high vacuum (absolute pressures less than 1 kPa) were exclusively performed using the CV method. At such low pressures the problems are greatly reduced with regards to the sensitivity of pressure measurement by an absolute pressure transducer, and the effect of temperature fluctuations.

Recently, Pitakarnnop et al. (2010) developed a new setup for gas microflows, in which the CV method is applied at both downstream and upstream of the microchannel, which offers a double check and provides the possibility to compare the measured results for the same flow. The system is also equipped with Peltier modules to maintain a constant temperature. In addition, similarly to the system of Ewart et al. (2006), the system of Pitakarnnop et al. (2010) is also capable of flow measurement by the DT method.

Another challenge to the CV method is to achieve a constant mass flow rate, when applied to measure the flow in microchannels. Unlike the DT method, the receiving volume cannot be excessively large. The same is also true for the inflow volume in the case of the system presented by Pitakarnnop et al. (2010. As the outlet of the microchannel is directly connected to the tank, the outlet pressure keeps changing and is uncontrolled. The inlet pressure must be very carefully adjusted with the passage of time to maintain constant pressure difference between the two tanks. This is very difficult to achieve in practice. Thus, the process of gas flow in the microchannel becomes time-dependent with the CV method (Morini et al., 2011).

3.2.3 Resistance to gas accumulation in high vacuum systems

Although not explicitly stated, measurements in CV systems rely on the assumption that there is no resistance to gas accumulation in the receiver. In other words, as a gas molecule enters the receiver at a specific point, it can be found anywhere within the receiver with the same probability. However, this would require an infinite diffusivity of the molecule in the receiver. In reality, the diffusivity of gas molecules accumulating in receivers that are initially at high vacuum is a finite value. In tubes of small cross-sectional area, which are normally an integral part of modern receivers, the Knudsen number (*Kn*) is often much greater than unity and the accumulation of the gas occurs at free or near free molecular regime (Kruczek et al., 2005). The diffusivity of molecules accumulating in a circular tube at these conditions can be evaluated from a semi-empirical formula reported by Loab (1961):

$$D = \frac{pr^2}{8\mu} + \frac{2}{3}r\sqrt{\frac{8RT}{\pi M}}\left(\frac{1 + C_1 p}{1 + C_2 p}\right) \tag{42}$$

where p is the mean pressure in the tube, r is the radius of the tube, μ is the dynamic viscosity of the gas, M is the molecular mass of the gas, and C_1 and C_2 are constants, which are determined by solving the following set of equations:

$$\frac{C_1}{C_2} = \frac{3\zeta\sqrt{\frac{\pi M}{RT}}p}{8\sqrt{2}\mu} \tag{43}$$

$$C_2 - C_1 = 0.6117\sqrt{\frac{M}{RT}}\frac{r}{\mu} \tag{44}$$

The coefficient of slip (ζ) is evaluated using Maxwell's deduction from the kinetic theory of gases (Maxwell, 1879):

$$\zeta = \frac{\mu}{p}\sqrt{\frac{\pi RT}{2M}}\left(\frac{2-f}{f}\right) \tag{45}$$

where f is a fraction of gas molecules, which lose the momentum as a result of adsorption and desorption at the walls of tube. While f depends on the nature of the gas and the tube surface, it is usually close to unity (Stacy, 1923). With f=1, solving simultaneously Eqs. (43) and (44) leads to the following expressions for the constants C_1 and C_2:

$$C_1 = 0.8768\sqrt{\frac{M}{RT}}\frac{r}{\mu} \tag{46}$$

$$C_2 = 1.4885\sqrt{\frac{M}{RT}}\frac{r}{\mu} \tag{47}$$

At very low pressures, regardless of the value of f, Eq. (42) approaches the expression for the diffusion coefficient in a free molecular (Knudsen) flow regime:

$$D \to D_K = \frac{2}{3}r\sqrt{\frac{8RT}{\pi M}} \tag{48}$$

For commonly used 1/4 inch stainless steel tubing with r = 0.193 cm and N_2 at 23°C, the free molecular regime (Kn > 10) exists at pressures less than 0.49 Pa. On the other hand, the diffusivity of N_2 does not differ more than 10% from D_K = 0.6 m^2/s up to 10 Pa (Kruczek et al., 2006).

Application of the time lag method for the characterization of membranes in CV systems requires the receiver to be initially set at as high a vacuum as possible. The actual initial vacuum in the receiver depends on the quality of a vacuum pump used. Using a rotary pump in series with a turbo molecular pump, Checchetto et al. (2004) reported the initial pressures in the range of low 10^{-6} Pa, while Sanchez et al. (2001) in the range of 10^{-7} Pa. Even without a turbo molecular pump, very low initial pressures are possible. For example Li et al. (2001) reported the initial pressure of 0.1 Pa, while Hirayama et al. (1996) of 0.013 Pa.

From the above considerations it is reasonable to assume that accumulation of gases in tubes of a small cross-sectional area can be described using a constant diffusivity of gas. With this assumption and considering the receiver to be a straight cylinder, the resistance to gas transport downstream from the tested medium may be quantified by the position-dependent time lag, using the following expression (Kruczek et al., 2005):

$$\theta(z) = \frac{l^2}{6D} - \frac{(l-z)^2}{2D} \tag{49}$$

where *l* is the length of the cylinder, and *z* is the distance of the pressure sensor from the flow source. Depending on *z*, i.e., the position where the pressure rise is monitored, *θ*(*z*) may be a positive or a negative number. At the limit of *z* = *l*, Eq. (49) simplifies to $\theta(l) = l^2/6D$, which corresponds to the maximum positive value, while at other limit of *z* = 0, Eq. (49) simplifies to $\theta(0) = -l^2/3D$, which corresponds to the maximum negative value.

The difference between *θ*(*l*) and *θ*(0) implies the existence of a constant pressure gradient within the receiver during a quasi-steady state accumulation. Since the pressure within the receiver is constant before the gas starts to flow into the receiver, there must be a transient period, during which the pressure gradient develops; consequently, the pressure response is a function of position within the receiver. In such a transient period, using Eq. (36) for the evaluation of the flow into the receiver could lead to a very significant error. Moreover, since the accumulation of gas leads to an increase in pressure, there should likely be a transition from the free molecular regime to near-free molecular regime, in which the diffusion coefficient increases with pressure. Thus, the developed pressure gradient within the receiver should gradually decrease as the pressure increases. Both of these effects are illustrated in Fig. 7a, in which the pressure gradient within the receiver first develops, and after reaching the maximum value approximately 50 s from the initiation of the experiment, gradually decreases with time, i.e., as the pressure in the receiver increases (Kruczek et al., 2006). This implies that after the initial transient period, the flow rate determined using Eq. (35) continues to be associated with a small systematic error, which decreases however, as the pressure in the receiver increases, and was verified experimentally by Chapanian et al. (2008).

In real systems, the outflow receiver is never just a straight cylindrical tube; it consists of a series of interconnected tanks to vary the volume of the receiver in order to accommodate a wide range of flow rates into the receiver. Since the Knudsen diffusion coefficient is proportional to the internal radius, the resistance to gas accumulation in tanks should be practically negligible. However, the presence of a resistance-free tank in the outflow receiver greatly magnifies the resistance effect in the tube. Assuming a constant diffusion coefficient in the tube connecting the flow source to the resistance-free tank, the following equation for the position-dependent time lag can be derived (Kruczek et al., 2006):

$$\theta(x) = \frac{l^2/D\left(l/6 + V/2A\right)}{1 + V/A} - \frac{(l-x)^2}{2D} - \frac{V(l-x)}{AD} \tag{50}$$

where *V* is the volume of the tank, and *A* is the cross sectional area of the tube. With *V* = 0, Eq. (50) simplifies to Eq. (49). On the other hand, with *V* > 0, because of the third term, time lag tends to be a large negative number, leading to an underestimation of the time lag of the tested medium. The error is magnified as the distance between the pressure sensor and the tank, *l* – *x*, increases. The radius of the connecting tube has a major effect on the error, since *A* is proportional to r^2, while *D* is proportional to *r*.

Experimental verification of the effect of the resistance-free tank is demonstrated by comparing Figs. 7a and 7b, which present the progress of time lag experiments monitored simultaneously by two identical pressure transducers located at different distances from the membrane in two different configurations of the receiver. The results presented in Fig. 7a were obtained in the configuration consisting of only 1/4 inch tube, while those in Fig. 7b in the configuration, assembled with a large accumulation tank at the end of the tube (Kruczek et al., 2006).

The location of the tank at the end of the tube represents the worst case scenario for the resistance in the tube. Installing the tank closer to the flow source while keeping the same total length of tube in the receiver decreases the "magnifying effect" of the tank (Lashkari et al., 2006). The mathematical model that allows evaluation of the resistance effects in any configuration of the receiver, including the configurations with multiple tanks, was recently developed and verified experimentally by Lashkari and Kruczek (2010).

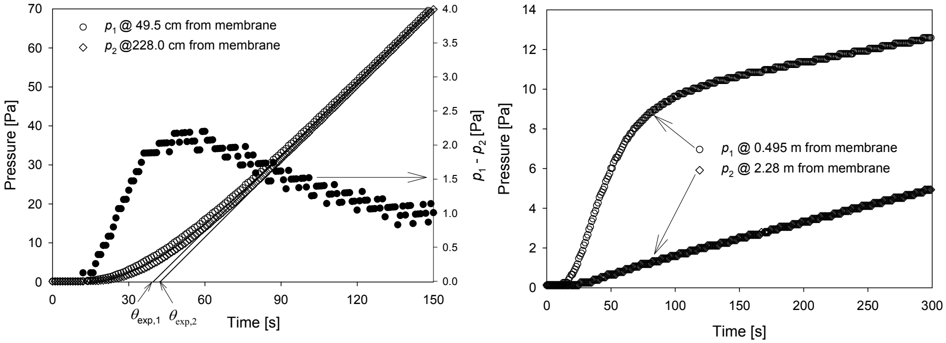

a) b)

Fig. 7. Progress of time lag experiments with a PPO membrane using N_2 at 23°C and at the initial pressure of 0.13 Pa. Experiments monitored simultaneously by two identical pressure transducers installed 0.495 m and 2.28 m from the membrane. Configuration **a):** standard 1/4 inch stainless steel tube of length 2.365 m; feed pressure, p_f = 206.8 kPa. Configuration **b):** standard 1/4" inch steel tube of length 2.415 m with a cylindrical tank of volume V = 2.250 x 10^{-3} m^3 attached at the end of the tube; feed pressure, p_f = 206.8 kPa. Adapted from Kruczek et al. (2006).

The resistance to gas accumulation in outflow receivers that are initially at high vacuum primarily affects time lag of the medium being tested. In the extreme case of very large resistance shown in Fig. 7b, the resulting apparent time lag based on the pressure transducer located 0.495 m from the membrane is a large negative number implying a negative diffusivity, which obviously does not make physical sense. However, the resistance to gas accumulation may also lead to significant errors in the permeability coefficient. In Fig. 7b, because of a large outflow volume, after 300 s from the initiation of the experiment, the pressure does not exceed 14 Pa, yet the pressure gradient between the positions at 0.495 m and 2.28 m from the membrane is nearly 9 Pa. If the gas were allowed to continue to accumulate in the receiver, this pressure gradient would eventually disappear, but during this time the slope, dp/dt at 0.495 m would be lower than that at 2.28 m Consequently, the measured microflows based on Eq. (35) would depend not only on the location of the pressure transducer, but also on the time frame used for the evaluation of the slope.

The problem of resistance to gas accumulation in CV systems used in microchannel characterization is likely negligible. This is not only because these systems are not operated at very high vacuum, but also because the outflow volume cannot be very large due to the problem with the resolution of the pressure measurements. Conversely, in characterization of microchannels by the DT method, it is desired to have the outflow volume as large as possible to maintain a constant pressure gradient over the microchannel. Therefore, if DT measurements are carried out at downstream pressures of 1 kPa or lower, one should perform calculations suggested by Kruczek et al. (2006) to confirm negligible resistance effects.

3.2.4 Design guidelines for new CV systems

Although CV systems are very commonly used in membrane gas separation labs, to our best knowledge, there are no guidelines for their design. Moreover, as shown in the preceding discussion, the resistance to gas accumulation should be taken into consideration when designing a new CV system. This section summarizes the key points of the design process.

Range of rate of pressure increase

The range of rate of pressure increase, i.e., the range of asymptote slopes (dp/dt), is primarily determined by a pressure transducer. The minimum slope, dp/dt_{min}, depends on the resolution of the selected pressure transducer. Since the resolution is inversely related to the linear range of the transducer, the resolution can in principle be increased by selecting a pressure transducer with a very small linear range. However, apart from the resolution of the pressure sensor, the lowest reliable rate of pressure increase also depends on the tightness of the receiver, which governs the leak rate into the receiver. While the determination of the leak rate is a prerequisite before each experiment in a CV system, and the experimentally determined leak rate can be subtracted from the apparent permeation rate, the actual permeation rate determined this way will be associated with a considerable random error if the leak rate is relatively large.

The maximum slope dp/dt_{max}, which determines the upper measurement range may appear to be primarily determined by the linear range of the selected pressure transducer. When performing a time lag experiment in absence of large resistance to gas accumulation, the pressure response becomes a linear function of time after $3\theta_m$, but to minimize the error in determination of the slope of the asymptote, the time lag experiment should be carried out for at least the period corresponding to 4 θ_m, and the permeate pressure after the time corresponding to 4 θ_m and preferably 10 θ_m should be below the upper limit for the linear range of the pressure transducer. On the other hand, considering possible effects of increasing permeate pressure (Lashkari, 2008), it might be advantageous to keep the permeate pressure well below the upper limit for the linear range of the pressure transducer. In addition, if accumulation in the receiver is influenced by the resistance effects, keeping the permeate pressure below 10-20 Pa would minimize the variation of the diffusion coefficient downstream from the membrane, which would allow a better recovery of membrane properties (Lashkari and Kruczek, 2012). Consequently, the upper measurement range might be an order of magnitude lower then that arising from the upper limit of the linear range of the utilized pressure transducer.

Minimum volume of the receiver and minimum permeation rate

The minimum volume of the receiver ($V_{\min}$) along with $dp/dt_{\min}$ is the critical design parameter when the system is to be used for the evaluation of transport properties of barrier materials, because barrier materials are associated with very low permeability coefficients and thus very low gas permeation rates (Q). The latter should still be significantly greater than the maximum leak rate into the receiver. Consequently, it is possible to set a reasonable limit on the minimum permeation rate ($Q_{\min}$). Knowing $Q_{\min}$, the minimum volume of the receiver can be evaluated by rearranging the ideal gas law:

$$V_{\min} = \left(\frac{RT}{v_{STP}} \right) \frac{Q_{\min}}{Z_{\min}} \tag{51}$$

It should be noted that while the absolute temperature (T) is also directly proportional to $V_{\min}$, gas permeation experiments are typically performed at ambient or slightly above ambient (35°C) temperatures.

In practice, $V_{\min}$ is typically determined by the volume of tubing when all tanks are excluded from the outflow volume. In turn, the volume of tubing depends on their length and cross-sectional area. It is important to emphasize that actual $V_{\min}$ is always greater than the volume of tubing because of the presence of dead volumes associated with membrane cells, pressure transducer(s), valves and other fittings. According to Lashkari and Kruczek (2010), the length of tubing should be minimized for the physical dimensions of the accumulation tanks and the pressure transducer, while their diameters should be maximized. In practice, tubing with the diameters of at least 1/2 inch are recommended. On the other hand, without knowing the number and the size of the accumulation tanks it is not possible to estimate the required length of tubes and thus the resulting volume of the system when all tanks are excluded. Therefore, it might be advantageous to have the ability to isolate a section of tubing downstream from the membrane cell with the volume corresponding to $V_{\min}$ determined from Eq. (51) rather, than letting this parameter be determined by the total length of tubing. The section of tubing that determines $V_{\min}$ should of course be equipped with its own pressure transducer. The location of the pressure sensor upstream from accumulation tank(s) is the worst one considering the resistance to gas accumulation, because is it associated with a relatively large negative time lag (Lashkari and Kruczek, 2010). Consequently, it might be necessary to have two pressure sensors in the receiver, one upstream from the accumulation tank(s) for the measurements involving V_{min} and another one downstream from the accumulation tanks for all other measurements.

Maximum volume and maximum permeation rate

In principle, there is no upper limit on permeation rate that could be evaluated in a CV system, because even for very high Q one can find V for which the restrictions on $dp/dt_{\max}$ discussed previously will be observed. However, from the practical point of view there are two important considerations that may allow setting the maximum permeation rate ($Q_{\max}$) and the maximum volume of the receiver ($V_{\max}$).

The major advantage of CV systems compared to constant pressure (CP) systems is the ability of continuously monitor of very low permeation rates. However, when the expected permeation rates are greater than 0.1 cm^3/min and definitely when they are greater than 0.5

cm^3/min, it might be more advantageous to evaluate the diffusion, permeability, and solubility coefficients in a constant pressure system using the theoretical framework presented by Ziegel (1969), rather than using a CV system.

Setting the $Q_{\max}$ along with previously established $Z_{\max}$ will allow determination of $V_{\max}$. Limiting $Q_{\max}$ and thus $V_{\max}$ is also advantageous from the perspective of minimization of the resistance to gas accumulation. Although without knowing the exact configuration of the receiver and the location of the pressure sensor it is not possible to evaluate the resistance effects, knowing $V_{\max}$, and the length and the diameter of tubing corresponding to $V_{\min}$ one can evaluate the position-dependent time lag along the tube using Eq. (49), which is a special case of the general equation derived by Lashkari and Kruczek (2010). To minimize the resistance to gas accumulation it is better to split the volume into more than one accumulation tank. On the other hand, such a split increases the required length of tubing, which in turn, increases the resistance. Consequently, evaluation of the resistance effects for $V_{\max}$ attached to the end of tube of length $l_{\min}$ will provide some rough resistance values, which could be expected in the final design.

The minimum number of accumulation tanks and their arrangement

To determine the number of accumulation tanks we start from rearranging Eq. (51) to determine the maximum flow rate ($Q_{\max,1}$) that can be measured in the previously determined $V_{\min}$:

$$Q_{\max,1} = V_{\min} Z_{\max} \left(\frac{v_{STP}}{RT} \right) \tag{52}$$

If $Q_{\max,1} < Q_{\max}$, it is necessary to increase the volume of the receiver by ΔV_1. Setting $Q_{\max,1}$ to be the minimum permeation rate to be measured in the increased volume of the receiver, the required volume increment can be evaluated from the following equation:

$$V_{\min} + \Delta V_1 = \left(\frac{RT}{v_{STP}} \right) \frac{Q_{\max,1}}{Z_{\min}} \tag{53}$$

The maximum flow rate in the increased volume ($Q_{\max,2}$) is determined from Eq.(53) in which $V_{\min}$ is replaced by $V_{\min} + \Delta V_1$ and the process continues until $Q_{\max,n} \geq Q_{\max}$. At this point: $V_{\min} + \sum_1^n \Delta V_i \geq V_{\max}$. Consequently, following this simple procedure allows evaluation of the number of the required volume increases (n) in the receiver between the predetermined $V_{\min}$ and $V_{\max}$, as well as, the value of each increment (ΔV_i). The number of required volume increases corresponds to the minimum number of accumulation tanks in the receiver, while ΔV_is correspond the volumes of the respective tanks.

Since the accumulation tanks are available in a discrete rather than a continuous size range, incremental volume increases between $V_{\min}$ and $V_{\max}$ according to the above procedure may not be possible. In this case, one should select accumulation tanks with volumes closest but smaller than the respective volumes corresponding to the minimum number of accumulation tanks. This will likely increase the number of the required accumulation tanks and will lead to some measurement overlaps, but at the same time, it will ensure covering the entire range of permeation rates.

It is also important to emphasize that volume increase resulting from adding an accumulation tank is always greater than the actual volume of the added tank because of the necessary extra length of tubing. The volume increment associated with extra tubing should be taken into consideration, in particular when 1/2 inch or larger tubes are utilized.

The tanks can be arranged in parallel or in series. In the case of a series arrangement, the extra volume of tubing associated with each increment can be accurately evaluated. On the other hand, within a parallel configuration, the extra volume of tubing is the same regardless of the number of accumulation tanks utilized in particular configuration (Lashkari and Kruczek, 2010). Moreover, this extra volume of tubing is not known until the number of the required accumulation tanks is established. On the other hand, parallel configuration has one practical advantage over series configuration; the rate of pressure increase in any configuration of the receiver can be monitored using a single pressure transducer installed on the main line regardless of the number of accumulation tanks. In the case of a series configuration, each accumulation tank must be equipped with its own pressure transducer. Therefore, the parallel configuration of accumulation tanks is normally used in multi-tank CV systems. If parallel configuration is selected, and the number and the volumes of the accumulation tanks are established, it is important to verify that covering the entire range of flow measurement, in particular the flow range associated with the first volume increment. This is because of extra length of tubing associated with accumulation tanks. If there are any discontinuities within the flow range, it might be necessary to select smaller tank(s).

After the above design process is completed and subsequently the configuration of the receiver is established, it is now possible to evaluate the anticipated resistance effect using the analytical equations developed by Lashkari and Kruczek (2010). Consequently, it is possible to generate a figure, which maps the position-dependent time lag within the receiver in different possible configurations. If the above guidelines are followed, in particular the 1/2 inch tubes are used and reasonable limits on $Q_{\max}$ and hence $V_{\max}$ are set, the magnitude of the position-dependent time lag should be comparable or even smaller than for the system presented by Lashkari and Kruczek (2012).

Inflow part of CV system

One of the assumptions of the time lag method is that the feed pressure can be increased in a step-wise manner. Favre et al. (2002) investigated the effect of imperfect feed pressure rise on membrane response. They approximated the feed pressure rise by a first order kinetics and concluded that any time delay in the pressure rise would be added to the membrane's time lag. There are couple of simple remedies to reduce the effects of imperfect pressure rise including a time delay in reaching the set value, an overshoot, and a time-dependent pressure decrease. First of all, a relatively large buffer tank should be installed upstream from the membrane. The volume of the buffer tank should be such that when the pressure in the receiver operating in the configuration corresponding to $V_{\max}$ increases to its maximum allowed value, the change in the buffer tank pressure should be negligible. Creating a step change in feed pressure using a gas regulator connected to a pressurized cylinder without a buffer tank creates a problem, because gas regulators have internal dynamics, and are activated with a sudden change in the cylinder pressure during initiation of a time lag experiment. The gas regulator should only be used to fill the buffer tank and then should be disconnected from the inflow volume by means of a regular valve. The buffer tank should also be isolated from the membrane cell by a special vacuum valve. Once the desired pressure is established in the buffer tank, opening this valve initiates the actual time lag experiment. Consequently, using a vacuum solenoid valve is advantageous because it ensures recording a proper “zero time” and allows a sudden and repeatable opening of this valve, which helps to achieve a perfect step change in feed pressure.

The volume between the solenoid vacuum valve and the membrane should be negligible compared to the volume of the buffer tank. This volume should also be connected to the outflow volume to allow evacuation of both sides of the membrane before an experiment. In addition, O’Brien et al. (1986) recommends having an atmospheric pressure rupture disk on the receiver in case of membrane rupture to protect costly pressure transducers installed in the receiver.

4. Conclusion

The measurements of microflows in characterization of microchannels by the CP, or more specifically by the DP and CV methods are challenging. Since the purpose of the characterization of microchannels is to measure the flow under different pressure gradients, the upstream and downstream ends of the tested microchannel are normally connected to finite volume tanks maintained at different pressures. In case of the DT measurements, the volumes of the tanks can be maximized to maintain a relatively constant pressure gradient. Yet, it is difficult to maintain a constant speed of the droplet in the calibrated tube even at presumably constant pressure gradients. In the case of the CV technique, because of a trade-off between the resolution of the pressure measurement and maintaining a constant pressure gradient across the microchannel, accurate flow measurements are even more challenging.

On the other hand, because of the generally very large resistance to gas transport imposed by a membrane, it is much easier to maintain constant pressure gradients during the characterization of membranes. Moreover, since the CV measurements involving membranes are normally carried out at very high vacuum, the problems associated with the resolution of the pressure measurements and temperature fluctuations do not practically exist. The CP systems used in membrane characterization are open to atmosphere, which allows to carry out the flow measurement at truly constant pressure conditions. Despite these “inherent” advantages, the characterization of membranes using the CP and CV techniques is associated with some unique difficulties, which had been recognized only recently.

The measurements of gas permeation rate in open CP systems may be influenced by the phenomena of back diffusion and back permeation. A simple mathematical model derived from first principles, was presented in this Chapter, allowing for a quick assessment if these phenomena are negligible or not. On the other hand, while the theoretical trends related to back permeation and back diffusion are confirmed experimentally, the magnitude of the systematic error and also the range of conditions at which this systematic error exists are considerably greater than the theoretical predictions.

In the case of measurements involving the CV method, while high vacuum conditions eliminate the problems of pressure resolution and temperature fluctuations, they may lead to gas accumulation resistance. This phenomenon primarily affects the experimentally measured time lag, and thus membrane diffusivity, but it also affects the experimental permeability coefficient. A step-by step procedure for the design of new CV systems is very useful to minimize the resistance effects. However, the complete elimination of the resistance to gas accumulation downstream from the membrane may not be possible, in particular when complex configurations of the receiver are involved. It is therefore of primary importance to understand this phenomenon to be able to correct the existing data and to recover the actual properties of the membrane. A similar approach is also applicable in case of the phenomena of back diffusion and back permeation; they must be well understood in order to be able to interpret the data influenced by these phenomena.

5. Acknowledgment

The authors acknowledge the financial support from NSERC Canada. BK acknowledges the warm hospitality of Mr. and Mrs. Młynarczyk during his stay in Poland, where most of this Chapter was written.

6. References

Al-Juaied, M.; Koros, W.J. (2006). Performance of Natural Gas Membranes in the Presence of Heavy Hydrocarbons, *J. Membr. Sci.*, Vol.174, pp. 227-243.

Arenas, A.; Victoria, L.; Ibaňez, J.A. (1995). A Time-Integration-Based Measurement Circuit for a Soap Bubble Flow-Meter Using Optical Fibre Sensors. *Mass. Sci. Technol*. Vol.6, pp. 435-436.

Arkilic, E.B.; Schmidth, M.A & Breuer, K.S. (1998). Sub-Nanomol per Second Flow Measurement Near Atmospheric Pressure. *Experiments in Fluids,* Vol.25, pp. 37-41.

Bailey, B.J.; Ferguson, J.A.; Moses, J.L. (1968). Two Flowmeters Using Electronic Timing *J. Sci. Instrum*. (*J. Phys. E*), Series 2 Vol.1, pp. 562-563.

Barigou, M.; Davidson, J.F. (1993). The Fluid Mechanics of the Soap Film Meter. *Chem. Eng. Sci*., Vol.48(14), pp. 2587-2597.

Barigou, M.; Deshpande, N.S.; Wiggers, F.N. (2003). Numerical Simulation of the Steady Movement of a Foam Film in a Tube. *Trans. Ind. Chem. Eng*, Vol 81, Part A (July 2003) 623-630

Barr, G. (1934). Two Designs of Flow-Meter, and a Method of Calibration. *J. Sci. Instrum*. V.11, pp. 321-324.

Barrer, R.M. (1939). Permeation, Diffusion and Solution of Gases in Organic Polymers. *Trans. Farad. Soc*., Vol.35, pp. 628-643.

Bos, A.; Pünt, I.G.M.; Wessling, M.; Strthmann, H. (1998). Plasticization-Resistanct Glassy Polyimide Membranes for CO_2/CH_4 Separations. *Sep. Pur. Tech*., Vol.14, pp. 27-39.

Celata, G.P.; Cumo, M.; McPhail, S.J.; Tesfagabir, L.; Zummo, G. (2007). Experimental Study on Compressible Flow in Microtubes. *Int. J. Heat Fluid. Flow.* Vol.28, pp. 28-36.

Chapanian, R.; Shemshaki, F.; Kruczek, B. (2008). Error in Measurement of Gas Flow Rate by the Pressure Rise Technique Arising from the Resistance to Accumulation of Gases in Vacuum Tubes. *Can. J. Chem. Eng.*, Vol.86(4), pp. 712-719.

Checchetto, R.; Bazzanella, N.; Patton, B.; Miotello, A. (2004). Palladium Membranes Prepared by R. F. Magnetron Sputtering for Hydrogen Surification. *Surface and Coatings Tech.*, Vol.177-178, p. 73.

Colin, S.; Lalonde, P.; Caen, R. (2004). Validation of a Second-Order Slip Flow Model in Rectangular Microchannels. *Heat Transf. Eng.*, Vol.25(3), pp. 25-30.

Concus, P. (1968). Static Menisci in a Vertical Right Circular Cylinder, *J. Fluid Mech.*, Vol.34(3), pp. 481-495.

Costello, L.M.; Koros, W.J. (1992). Temperature Dependence of Gas Sorption and Transport Properties in Polymers: Measurement and Applications. *Ind. Eng. Chem. Res.*, Vol.31, pp. 2708-2714.

Czubryt, J.J.; H.D. Gesser, H.D. (1968). Part I - Inaccuracy of the Moving Bubble Flowmeter in the Low Flow Rate Region, *J. Gas Chromat.* Vol.6, pp. 528-530.

Daynes, H.A. (1920). The process of diffusion through a rubber membrane. *Roy. Soc. Proc.*, Vol.97, pp. 286-307.

Deissler, R.G. (1964). An Analysis of Second Order Slip Flow and Temperature-Jump Boundary Conditions for Rarefied Gases. *Int. J. Heat Mass Transf.*, Vol.7, pp. 681-694.

Ewart, T.; Perrier, P.; Graur, I.A.; Meolans, J.G. (2006). Mass Flow Rate Measurements in Gas Micro Flows. *Experiments in Fluids.* Vol.41, pp. 487-498.

Ewart, T.; Perrier, P.; Graur, I.A.; Meolans, J.G. (2007). Mass Flow Rate Measurements in a Microchannel, From Hydrodynamic to Near Free Molecular Regimes. *J. Fluid. Mech.*, Vol.584, pp. 337-356.

Exner, F. (1875). Über den Durchgang der Gase durch Flüssigkeitslamellen. *Pogg. Ann. Phys. Chem.*, V.231, p.321.

Favre, E.; Morliere, N.; Roizard, D. (2002). Experimental Evidence and Implications of an Imperfect Upstream Pressure Step for the Time-Lag Technique. *J. Membr. Sci.*, Vol.207, pp. 59–72.

Guo, J.; Heslop, M.J. (2004). Diffusion Problems of Soap-Film Flowmeter When Measuring Very Low-Rate Gas Flow. *Flow Meas. Instrum.* Vol.15, pp. 331-334.

Hadjiconstantinou, N.G. (2003). Comment on Cercignani's Second Order Slip Coefficient. *Phys. Fluids,* Vol.15(8), pp. 2352-2354.

Harley, J.; Huang, Y.; Bau, H.; Zemel, J. (1995). Gas Flow in Microchannels. *J. Fluid. Mech.*, Vol.284, pp. 257-274.

Heslop, M.J.; Mason, G.; Provatas, A. (1995). Comments on the Pressure Produced by a Soap Film Meter. *Chem. Eng. Sci.*, Vol.50(15), pp. 2495-2497.

Hirayama, Y; Yoshinaga, T.; Kusuki, Y.; Ninomiya, K.; Sakakibara, T.; Tamari, T. (1996). Relation of Gas Permeability with Structure of Aromatic Polyimides I. *J. Membr. Sci.*, Vol.111, p. 169.

Huvard, G.S.; Stannett, V.S.; Koros, W.J.; Hopfenberg, H.B. (1980). The Pressure Dependence of CO_2 Sorption and Permeation in Poly(Acrylonitrile). *J. Membr. Sci.*, Vol.6, pp. 185-201.

Jousten, K.; Menzer, H. (2002). A New Fully Automated Gas Flow Meter at the PTB for Flow Rates Between 10^{-13} mol/s and 10^{-6} mol/s. *Metrologia*, Vol.39(6), pp. 519-529.

Kemp, D.R. (1972). The Diffusion Time Lag in Heterogeneous Polymer Membranes. PhD Dissertation, University of Texas at Austin, USA.

Knudsen, M. (1909). Die Gesetze der Molekularstromung und der Inneren Riebungsstromung der Gaze Durch Rohen. *Annu. Phys. (Leipzig).* Vol.28, p.130.

Kruczek, B.; Frisch, H.L.; Chapanian, R. (2005). Analytical Solution for the Effective Time Lag of a Membrane in a Permeate Tube Collector in which Knudsen Flow Regime Exists. *J. Membr. Sci.*, Vol.256, pp. 57-63.

Kruczek, B.; Shemshaki, F.; Lashkari, S.; Chapanian, R.; Frisch, H.L. (2006). Effect of a Resistance-Free Tank on the Resistance to Gas Transport in High Vacuum Tube. *J. Membr. Sci.*, Vol.280, pp. 29-36.

Lashkari, S. (2008). Fundamental Aspects of Membrane Characterization by Constant Volume and Constant Pressure Techniques. PhD Dissertation, University of Ottawa, Canada.

Lashkari, S.; Kruczek, B. (2008A). Development of a Fully Automated Soap Flowmeter for Micro Flow Measurements. *J. Flow Meas. Instrum.* Vol.19(6), pp. 397-403.

Lashkari, S.; Kruczek, B. (2008B). Effect of Back Diffusion and Back Permeation of Air on Membrane Characterization in Constant Pressure System. *J. Membr. Sci.*, Vol.324, pp. 162-172.

Lashkari, S.; Kruczek, B. (2010). Effect of Resistance to Gas Accumulation in Multi-Tank Receivers on Membrane Characterization by the Time Lag Method. Analytical Approach for Optimization of the Receiver. *J. Membr. Sci.*, Vol.360, pp. 442-453.

Lashkari, S.; Kruczek, B. (2012). Reconciliation of Membrane Properties from the Data Influenced by Resistance to Accumulation of Gases in Constant Volume Systems. Desalination, Vol.287 pp. 178-182.

Lashkari, S.; Kruczek, B.; Frisch, H.L. (2006). General Solution for the Time Lag of a Single-Tank Receiver in the Knudsen Flow Regime and its Implications for the Receiver's Configuration. *J. Membr. Sci.*, Vol.283, p. 88-101.

Lee, Y.M.; Ha, S.Y.; Lee, Y.K.; Suh, D.H.; Hong, S.Y. (1999). Gas Separation Through Conductive Polymer Membrane. 2. Polyaniline Membranes with O_2 Selectivity. *Ind. Eng. Chem. Res.*, Vol.38, pp. 1917.

Levy, A. (1964). The Accuracy of the Bubble Meter Method for Gas Flow Measurements. *J. Sci. Instrum.*, Vol.41, pp. 449-453.

Li, X-G.; Kresse, I.; Springer, J.; Nissen, J.; Yang, Y.-L. (2001). Morphology and Gas Permselectivity of Blend Membrane of Polyvinylpyridine with Ethylcellulose. *Polymer*, Vol.42, p. 6859.

Lin, W.-H.; Vora, R.H.; Chung, T.-S. (2000). Gas Transport Properties of 6FDA-Durene/1,4-Phenylenediamine (pPDA) Copolyimides. *J. Polym. Sci., Part B: Polym. Phys.*, Vol.38, pp. 2703.

Loeb, L.B. (1961). The Kinetic Theory of Gases. pp. 278-300. Dover Publications, Inc. New York, USA.

Maurer, J.; Tabeling, P.; Joseph. P.; Willaime, H. (2003). Second-Order Slip Laws in Microchannels for Helium and Nitrogen. *Phys. Fluids.* Vol.15, No.9, pp. 2613-2621.

Maxwell, J. (1879) On stress in rarefied gases arising from inequalities of temperature. *Philos. Trans. R. Soc. London,* Vol.170, pp. 170-231.

McCulloh, K. E.;. Tilford, C.R; Ehrlich, C.D.; Long, F.G. (1987). Low-Range Flowmeters for Use with Vacuum and Leak Standards. *J. Vac. Sci. Technol. A*, Vol.5, pp. 376-381.

Moore, T.T.; Damle, S.; Williams, P.J.; Koros, W.J. (2004). Characterization of Low Permeability Gas Separation and Barrier Materials; Design and Operation Considerations. *J. Membr. Sci.*, Vol.245(1-2), pp. 227-231.

Morini, G.L.; Yang, Y.; Chalabi, H.; Lorenzi, M. (2011). A Critical Review of the Measurement Techniques for the Analysis of Gas Microflows Through Microchannels. *Exp. Therm. Fluid Sci.* Vol.35, pp. 849-865.

O'Brien, K.C.; Koros, W.J.; Barbari, T.A.; Sanders, E.S. (1986). A New Technique for the Measurement of Multicomponent Gas Transport Through Polymeric Films. *J. Membr. Sci.*, Vol.29, pp. 229-238.

Paul, D.R.; DiBenedetto, T. (1965). Diffusion in Amourphous Polymers. *J. Polym. Sci. Part C*, Vol.10, pp. 17-44.

Pitakarnnop, J.; Varoutis, S.; Valougeorgis, S.G.; Baldas, L.; Colin, S. (2010). A Novel Experimental Setup for Gas Microflows. *Microfluid Nanofluid*. Vol.8, pp. 57-72.

Sanchez, J.; Gijiu, C.L.; Hynek, V.; Muntean, O.; Julbe, A. (2001). The Application of Transient Time-Lag Method for the Diffusion Coefficient Estimation on Zeolites Composite Membranes. *Sep. Pur. Tech.*, Vol. 25, p. 467.

Schumacher, E.E.; Ferguson, L. (1927). A Convenient Apparatus for Measuring the Diffusion of Gases and Vapours Through Membranes. *J. Am. Chem. Soc.* Vol.49, pp. 427-28.

Shih, J.C.; Ho, C.; Liu, J.; Tai, Y. (1996). Monatomic and Polyatomic Gas Flow Through Uniform Microchannels. *ASME DSC*. Vol.(59), pp. 197-203.

Shishatskii, A.M.; Yampol'skii, Yu.P.; Peinemann, K.-V. (1996). Effects of Film Thickness and Density on Gas Permeation Parameters of Glassy Polymers. *J. Membr. Sci.*, Vol.112, pp. 275-285.

Stacy, L.J. (1923). A Determination by the Constant Deflection Method of the Value of the Coefficient of Slip for Rough and for Smooth Surfaces in Air. *Phys. Rev.*, Vol.21, p. 239.

Stannett, V.T. (1978). The Transport of Gases in Synthetic Polymeric Membranes — A Historic Perspective. *J. Membr. Sci.*, Vol.3(2), pp. 97-115.

Stern, S.A.; Gareis, P.J.; Sinclair, T.F.; Mohr, P.H. (1963). Performance of a Versatile Variable-Volume Permeability Cell. Comparison of Gas Permeability Measurements by the Variable-Volume and Variable-Pressure Methods. *J. Appl. Polym. Sci.*, Vol.7, 2035-2051.

Tabe Mohammadi, A.; Matsuura, T.; Sourirajan, S. (1995). Design and Construction of Gas Permeation System for the Measurement of Low Permeation Rates and Permeate Compositions. *J. Membr. Sci.*, Vol.98, pp. 281-286.

Zohar, Y.; Lee, S.Y.K.; Li, W.Y.; Jiang, L.; Tong, P. (2002). Subsonic Gas Flow in Straight and Uniform Microchannel. *J. Fluid Mech.* Vol.472, pp. 125-151.

Zolandz, R.; Fleming, G.K. (1992). Gas Permeation, In: *Membrane Handbook* H. Sirkar (Ed.), , Van Nostrand Reinhold, New York, USA.

Ziegel, K.D.; Frensdorff, H.K.; Blair, D.E. (1969). Measurement of Hydrogen Transport in Poly-(Vinyl Fluoride) Films by the Permeation-Rate Method. *J. Polym. Sci.: Part A.*, Vol.2(7), pp. 809-819.

Part 2

Biphasic Flow Measurement

2

Gas-Liquid Two-Phase Flow Rate Measurements by Flow Division and Separation Method

Dong Wang
XI'an Jiaotong University
People's Republic of China

1. Introduction

In this chapter we shall introduce a new and practical method for two-phase flow rate measurement, which is known as flow division and separation method. As its name suggested, a two-phase flow is measured by diverting a small fraction of the total stream to a division loop and metering it with the separation means. This method has been developed in Xi'an jiaotong university since the end of last century, and extensively studied in laboratory, some of the meters have been successfully applied in engineering. At first we briefly introduce the flow division technique in single phase flow, then we discuss how this method can be used in gas-liquid two-phase flow measurements, further more we shall give three detail examples of this kind of two-phase flow meters.

2. Flow measurement by flow division technique

The rate of flow in a pipe can be measured by a flowmeter installed in the identical pipe, this kind of flowmeter is called the full bore flowmeter which has the same size of diameter as the flow tube. However as the flow tube becomes very large, the full bore flowmeter will be extremely expensive or even impossible to build. In this case, the flow division technique can be a very convenient choice. In addition to this, the flow division technique can also be used to solve the difficult problem of two-phase flow measurement.

2.1 Flow division technique in single phase flow

Flow division technique, also called flow ratio technique (DeCarlo, 1984), have been widely used in single phase flow measurements, whose main feature is to use a small size meter to measure a large volume flow in large lines. This kind of flow meter is usually called "bypass flow meter", or "shunt flow meter" or "proportional flow meter". As shown in Fig.1, a bypass flow meter consists of three major portions (Fenelon,1994), a main flow path, a bypass loop (flow division branch) and a restriction. The restrictive element is positioned in the main flow path and the bypass flow loop is arranged to cross the restrictive element, so that its inlet and outlet is located at the upstream and downstream of the restrictive element respectively. The function of the restrictive element is to create a pressure drop between the upstream and downstream of the restriction which will cause a portion of total flow to enter into the bypass loop. A small size flow meter is installed in the bypass flow loop to meter the flow quantity or flow rate passing through the bypass loop. The total flow quantity or flow rate can be inferred from the metered value since a definite ratio exists between the flow rate in bypass loop and the total flow rate.

From Fig.1 we can also see that the bypass loop and the main flow path have a common inlet and a common outlet i.e. they are in parallel to each other (Munson, 2002). In accordance with the nature of parallel loops, the pressure loss of these two loops must be equal (Munson,2002). The pressure loss in these two loops include friction and local resistance which can be express as

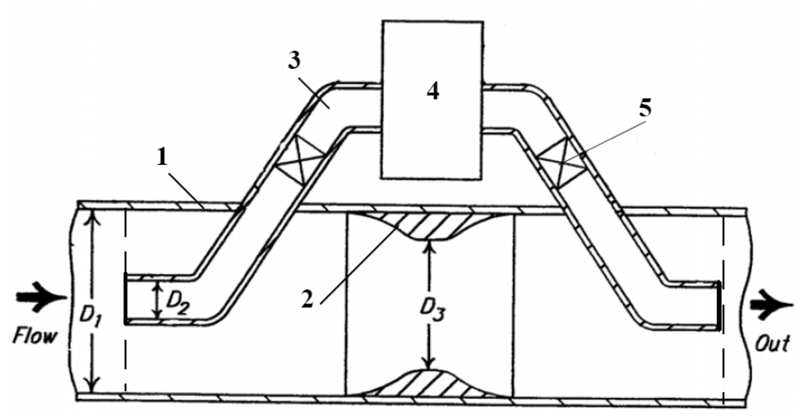

1. Main flow path; 2. Restrictive element; 3. Bypass loop; 4. Flow meter; 5. Valve

Fig. 1. Schematic represent of a bypass flow meter

$$\Delta P_2 = \left[\sum \lambda_2 \frac{l_2}{D_2} + \sum \xi_2\right] \frac{1}{2\rho}\left(\frac{M_2}{A_2}\right)^2 \tag{1}$$

$$\Delta P_3 = \left[\sum \lambda_3 \frac{l_3}{D_3} + \sum \xi_3\right] \frac{1}{2\rho}\left(\frac{M_3}{A_3}\right)^2 \tag{2}$$

Where Δ P is the pressure loss, λ is Darcy friction factor, l is tube length, D is tube inner diameter, ξ is local loss factor, ρ is the density of fluid, M is mass flowrate, A is tube cross section area, Symbol Σ represents summation; Subscript "2" represents the main flow path and the subscript "3" represents the bypass loop. Since $\Delta P_2 = \Delta P_3$, we can obtain the ratio of M_2 to M_3 from equation (1) and (2)

$$\frac{M_2}{M_3} = \frac{A_2}{A_3}\sqrt{\frac{\sum \lambda_3 \frac{l_3}{D_3} + \sum \xi_3}{\sum \lambda_2 \frac{l_2}{D_2} + \sum \xi_2}} \tag{3}$$

As the total flow rate M_1 equals to the sum of M_2 and M_3, therefore the ratio of M_3 to M_1 can be derived from equation (3)

$$\frac{M_3}{M_1}=\frac{1}{1+\frac{A_2}{A_3}\sqrt{\frac{\sum\lambda_3\frac{l_3}{D_3}+\sum\xi_3}{\sum\lambda_2\frac{l_2}{D_2}+\sum\xi_2}}} \tag{4}$$

Equation (4) clearly shows that the ratio of flow rate passing through the bypass loop to the total flow is dependent on the structure parameters of these two loops. By properly setting the resistance devices in these two loops, a constant ratio can be obtained. In practice the ratio should be calibrated by experiment, and a bypass flow meter will have an equivalent precision as the full bore meter.

The ratio of M_3 to M_1 can vary from 1 to $2.5\text{x}10^{-4}$, hence the flow meter in the bypass loop can be greatly reduced in size. We can use a small size flow meter or flow sensor to meter a large volume flow in a large pipe. Thus the capital cost and operation cost can be significantly reduced. This is the main advantage of a bypass flow meter.

The flow meter incorporated in bypass loop can be a flow quantity meter for measuring the quantity of flow (Hirst, 1951; Hodgson,1932; Kidder, 1934; Peranio, 1967;Thomson, 1895a, 1895b), or a flow rate meter for measuring the rate of flow.

The flow rate meters used in the bypass loop can be any types, but we usually select the meters which have a relative large metering range, for example, it can be a rotameter (Rlkuta,1969; Stenberg,1962), a Coriolis mass flow meter (Kane, 1994; Kalotay,1994;Van Cleve,1999), or a thermal (calorimetric) mass flowmeter (Adams,1969; Baker,1969, 1971,1977; Hawk,1984;Kronberger,1952; Laub,1956; Sato,1983). Therefore a bypass flow meter will also have a large metering range. At the same time, the flow meter or a flow sensor will also have a higher sensitivity than the full bore flow meter because of its small size. For instance, a small size Coriolis effect flow sensor is more sensitive than a large one because of its thinner and more flexible flow tube which is more suitable for the generation of meaningful Coriolis forces (Kalotay,1994).

A bypass flow meter's metering range and precision can be further expanded and improved if a variable constriction is used. Fig.2 is an example of variable constriction flow meter (Bahrton,1996). The significant feature of the variable constriction in Fig.2 is that a moveable conical body is introduced in the orifice. When the total flow is very low, the conical body will be pressed to the left by the spring so as to decrease the flow area of the orifice or completely close the orifice, so that all of the flow, or at least a large part of the total flow will enter into the bypass loop and metered by the flowmeter. On the contrary, when the flow is large, the conical body will be forced to the right by the fluid so as to increase the flow area of the orifice, so that a smaller part of total flow will pass through the bypass loop. As a result the dynamics (the ratio of maximum flow rate to the minimum flow rate) of the bypass meter can be expanded to 2500:1 which is much larger than a full bore flow meter. It can also be seen from Fig.2 that in any case the flow passing through the bypass loop can always fall in the optimum measuring arrange of the flow meter by adjusting the restriction, and this will improve the precision of the flow meter. Similar structure can also be found in references (Connet,1928; Olin,1984).

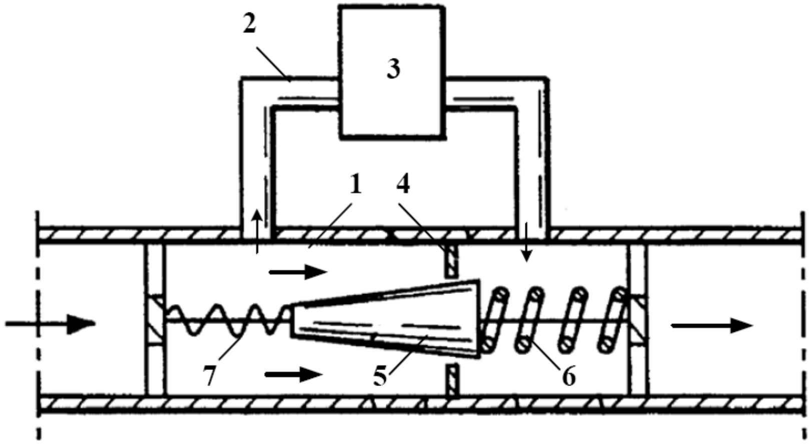

1. Main flow path; 2. Bypass loop; 3. Flowmeter; 4. Orifice plate; 5.Connical body; 6,7. Spring

Fig. 2. Bypass flowmeter with a variable constriction

The restrictive element in a bypass flow meter can be also a Venturi tube (Van Cleve,1999), a nozzle(Baker,1971), a pitot tube (Baker,1977) or other resistance devices.

2.2 Recent development in two-phase flow measurement

Two-phase flow rate measurement is still a difficult problem in science and engineering. Traditional solution is to separate the two-phase mixture into single phase flows first, and then measure the flow rate of each phase with single-phase flow meters. In this method, usually a large separator vessel is required to complete the separation of two-phase flow, and both the capital and operating cost of equipments tend to be high. Also, in practice, the measurements derived from this process are subject to many errors（Thorn et al ,1997）. During the last couple of decades, a number of techniques have been studied to measure the two-phase flow rate. Nearly all the conventional flow meters have been tried to meter the two-phase flow(Bates and Ayob ,1995; Cha et al ,2002; Chisholm ,1974; Jung et al ,2009; Kriiger et al,1996; Lin,1982; Murdock,1962; Skea and Hall,1999; Steven,2002; Steven and Hall,2009). Experiments show that the measurement errors will increase rapidly as the amount of second phase appeared in the flow increases. At the same time, the response of a single phase flowmeter to the two-phase flow depends on not only the flowrate but also on the phase fraction. For instance, under a certain flowrate, the higher the gas quality, the larger the differential pressure passing through an orifice. Therefore, a single phase flowmeter is not capable of measuring the flowrate and phase fraction simultaneously and a combination with other measuring devices is necessary. A lot of combined methods have been developed to measure the two-phase flowrate and phase fraction (Huang et al ,2005; Geng et al ,2007; Meng et al ,2010; Meribout et al ,2010; Oliveira et al ,2009; Reis and Jr ,2008; Sun ,2010; Zhang et al ,2010; Zheng et al ,2008).

These combined methods mentioned above can work well within their respective metering ranges, however, the measurement error would increase and the instruments may even fail to work once beyond their narrow rated ranges. One of the major reasons that cause the larger measuring error and the failure of measurement is that a two-phase flow is always in violent fluctuation. Fluctuation is an inherent feature of two-phase flow that makes the instruments unsteady and unreliable. Nevertheless some researchers consider it as useful information to determine the phase fraction or flowrate of a two-phase flow (Beg and Toral ,1993; Ferreira ,1997; Wang and Tong ,1995; Xu et al ,2003). A separation means for two-phase flow measurement that does not employ large separator may be a good choice (Liou ,1995; Turkowski ,2004).

2.3 Two-phase flow measurement by flow division and separation method

From section 2.1 it has been known that the flow division technique is a reliable method for measuring the single phase flow rate. Its main advantage is to use a small size meter to measure the total flow in a large flow pipe. If this method can be used in gas-liquid two-phase flow, then we can use a small size separator in the bypass loop to separate the two-phase mixture passing through the bypass loop into single phase gas and liquid and consequently measuring them by conventional single phase flowmeters, thus the problem of two-phase flow rate measurement can simply be solved. However, there is a key problem which must be solved before this technique can be successfully used in two-phase flow, that is how to divert a portion of two-phase mixture, which will have the same components as the total flow and be proportional to the total flow, to the bypass loop. We can not simply place the inlet end opening of the bypass loop in the main flow as in the case of single phase flow, because a two-phase fluid is not a homogenous medium, on the contrary, it always presents different flow pattern at different flow conditions. Hence a special distributor must be employed between the main and bypass loop. Fig.3 shows a schematic representation of a flow division type two-phase flow measurement system (Wang & Lin, 2002). The measuring process is that, first, a small portion (1%—20%) of the total two-phase flow is extracted by a distributor, then it is separated by a small compact separator, after that the separated gas and liquid flows are metered by the single phase flowmeter respectively, in the end, the two metered flows are returned to the main stream. The total gas flow rate M_G and total liquid flow rate M_L are determined by the following equations

$$M_G = \frac{M_{G3}}{K_G} \tag{5}$$

$$M_L = \frac{M_{L3}}{K_L} \tag{6}$$

Where M_{G3} and M_{L3} is the metered gas and liquid flow rate respectively, K_G and K_L represents the gas and liquid extraction ratio respectively. For an ideal distributor, K_G and K_L should be a constant so that the determinations of total flow rate of each phase would be much simpler. Apparently, it is difficult for a real distributor to keep the extraction ratio being constant in any condition. In fact, as long as K_G and K_L could be relatively stable within a quite wide range, the distributor could be used. From Fig.3 it can also been seen that the flow rate of the stream entering into the separator is only 1%—20% of the total flow, so the size of separator can be reduced at least 1%—20% times compared with the traditional separating method in which all the two-phase mixture is separated, and the size of a two-phase flow meter may nearly approach that of common single flow meter. In the following section we shall introduce three different distributors.

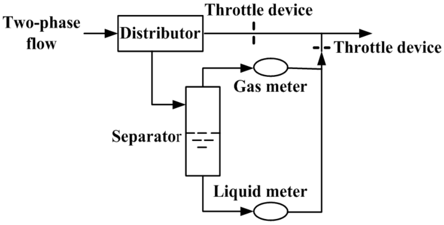

Fig. 3. Schematic representation of a flow division type two-phase flow measurement system

2.3.1 Rotation drum distributor

Fig. 4 shows the schematic drawing of the drum distributor (Wang & Lin, 2002). The core part of a rotational drum distributor is the rotational drum. The outline of the drum is a cylinder, the inside space is equally segregated into a series of small flow channels which twisted around the drum axis. The outputs of the most channels are directed to the down stream part of the pipe, only a few channels, which are selected as the extraction channels, are connected to the separator (to the bypass loop).

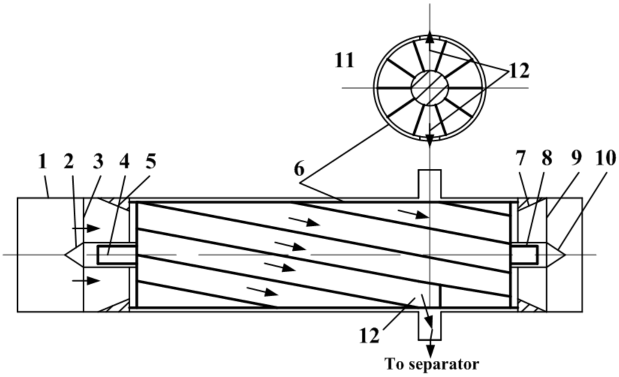

1. Shell; 2,10. Bearing seat; 3,9. Bracket; 4,8. Shaft; 5. Front guide cone; 6. Rotation drum; 7. Back guide cone; 11. Normal channel; 12. Extraction channel.

Fig. 4. Schematic drawing of a rotational drum distributor

As two-phase mixture passes through channels, the drum will be forced to run at a high speed around its axis by the fluid. With the running of the drum, the entrance of each channel will continuously scan over every point on the cross section in front of the drum. If each channel has the same characteristics of geometry, friction and output pressure, and the rotation speed is high enough, then the flow of fluid at any point on the cross section in front of the drum would not be influenced by the rotating of the rotational drum, and would have the same possibility to enter each channel. In other words, the flow would be considered as steady flow within a drum running period and the time duration Δt, during which the fluid at any point of the cross section in front of the drum flowing into a channel within a drum rotation period, will be equal, that is

$$\Delta t = \frac{T}{n} \tag{7}$$

Where T is the drum rotation period; n is the total number of the channels inside the drum.

The amount of gas and liquid passing through each channel in a drum rotation period will be

$$\Delta M_G = \int_A \Delta t \alpha_i u_{Gi} \rho_G dA = \Delta t \rho_G \int_A \alpha_i u_{Gi} dA = \Delta t M_G \tag{8}$$

$$\Delta M_L = \int_A \Delta t (1-\alpha_i) u_{Li} \rho_L dA = \Delta t \rho_L \int_A (1-\alpha_i) u_{Li} dA = \Delta t M_L \tag{9}$$

Where ΔM_G and ΔM_L is the amount of gas and liquid passing through each channel in a drum rotation period respectively; α_i is the local void fraction and u_{Gi}, u_{Li} is the local gas and liquid velocity on the cross section in front of the drum respectively; ρ_G and ρ_L is the gas and liquid density respectively; A represents the cross section of the pipe in front of the drum. M_G and M_L is the total gas and liquid flow rate respectively.

Equation (8) and (9) also mean that ΔM_G and ΔM_L is equal to the amount of total flow of each phase passing through the cross section of the pipe in front of the drum within time Δt respectively. The drum distributor seemingly acts as a time controlled switch which equally directs the total flow into each channel. As long as the rotation period of drum is short enough, the accuracy of Equation (8) and (9) will be all right.

The average gas flow rate m_G, and liquid flow rate m_L passing through each channel will be

$$m_G = \frac{\Delta M_G}{T} = \frac{\Delta t}{T} M_G = \frac{M_G}{n} \tag{10}$$

$$m_L = \frac{\Delta M_L}{T} = \frac{\Delta t}{T} M_L = \frac{M_L}{n} \tag{11}$$

If z channels are selected as the extraction channels, which are connected to the separator, then the sum of gas flow rate M_{G3} and liquid flow rate M_{L3} of the bypass stream is

$$M_{G3} = \frac{z}{n} M_G \tag{12}$$

$$M_{L3} = \frac{z}{n} M_L \tag{13}$$

The gas extraction ratio K_G, and liquid extraction K_L is

$$K_G = \frac{M_{G3}}{M_G} = \frac{z/n M_G}{M_G} = \frac{z}{n} \tag{14}$$

$$K_L = \frac{M_{L3}}{M_L} = \frac{z/n M_L}{M_L} = \frac{z}{n} \tag{15}$$

Equation (14) and (15) show that the extraction ratio of the rotational drum distributor is simply dependent upon the number of extraction channels and independent of the flow patterns. In the experiment of this study, n, the total number of channels, is 10, z, the number of extraction channels, is 2. According to Equation (14) and (15), the extraction ratio should be

$$K_G = K_L = \frac{2}{10} = 0.2 \tag{16}$$

Equation (14) – (16) are obtained for a perfect rotational drum distributor. There are some factors which should be considered when use them to a real rotational drum distributor. These include the size of the gap between the drum and the shell, the rotating speed of the drum and the geometrical departure from the ideal shape during the manufacturing and the assembling process. All these effects on the extraction ratio will be determined by experiments.

Two different drums were used in the experiments in order to examine the effect of gap size between the shell and the drum on the extraction ratio. One drum has 0.75 mm gap size, and another one has 0.25 mm gap size. The experiments were carried out in an air-water two-phase flow loop in Xi'an Jiaotong University as shown in Fig.5.

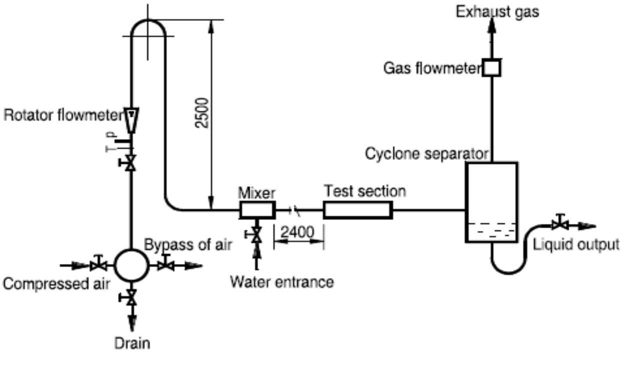

Fig. 5. The air-water two-phase flow experimental loop schematic

A gas rotameter was installed vertically upstream of the mixer for air flow rate adjustment, the precise gas flow rate was given by the vortex flow meter installed at the top of cyclone separator at the outlet end of the loop. The gas flow rate of the extracted (bypass) stream was also metered by a vortex flow meter. The water flow rates, both the total water flow rate and the extracted (bypass) water flow rate, were metered at the point of liquid output in the water leg of the cyclone separator and of the separator used in the bypass loop respectively by using the weight—time method. The duration of time during which water is collected was about 10 – 120 s, depending upon the flow rate of the water. An assessment was carried out on the uncertainty on each of the measured parameters. They were all within ±1.5%. From this the accuracy of the extraction ratio was determined and found to be ±1.5% for liquid extraction ratio K_L, and ±2% for gas extraction ratio K_G. The separator used in the bypass loop in this experiment was simply a vertically installed cylinder made from Plexiglas pipe, mounted internally with a multi-hole plate in the cross section of the cylinder just above the entrance of the bypass stream. The inner diameter and height of the separator were 70 and 350 mm respectively. The straight pipe between the mixer and the test section has 30 mm ID and 2400 mm total length, and is made from Plexiglas pipe through which the flow patterns can be observed.

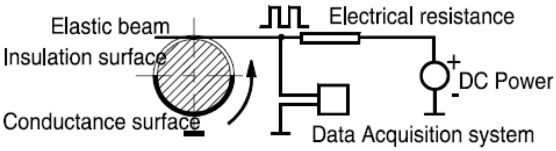

Fig. 6. The rotation speed measuring circuit

In order to determine the effect of rotation speed of the drum on extraction ratio, a simple electrical circuit as shown in Fig. 6 was used to measure the rotation speed of the rotational drum. A short portion (about 3 mm wide) of the drum shaft was selected as one part of the circuit. Half of the outer surface of the shaft was coated with a thin layer of plastic to form the insulation surface, and the other half was a polished metal surface. An elastic beam made from thin copper – beryllium plate, is contacted to the shaft at one end, and is connected to the electrical resistance at the other end. With the running of the shaft, the elastic beam contacts alternatively with insulation surface and conductance surface. Thus, a square electric current pause is generated in the circuit for each cycle. The square wave signal can be seen on the screen of the data acquisition system, and the frequency of the square wave represents the drum rotation speed. If some water is appeared on the insulation surface, the amplitude of square wave signal will be reduced a little, but the shape and frequency of the square wave will not be changed any more, even the pipe is full of water.

Extraction ratio were measured in the following experiment range: gas superficial velocity varied between 4 and 40 m/s; water superficial velocity ranged from 0 to 0.28 m/s; flow patterns occurring during experiments included stratified flow, wave flow and annular flow. A typical experimental results of the extraction ratio are shown in Fig. 7, data symbol S, W and A represents the flow pattern of stratified, wave and annular flow respectively. These results were obtained with the drum having 0.25 mm gap size between the shell and the drum. From these results it is seen that both the gas extraction ratio and liquid extraction ratio are very close to the theoretical value—0.2 as the extracted (bypass) liquid flow rate is high, but as the extracted liquid flow rate is low, the liquid extraction ratio becomes higher than 0.2, while the gas extraction ratio becomes lower than 0.2. For the liquid extraction ratio, this phenomena could be explained by the fact that some of the liquid will preferentially leak into the separator through the gap between the shell and the drum, rather than through the flow channels in drum as two-phase flow passing through the distributor. Therefore the actual liquid flow rates extracted are a little more than the theoretical values (predicted with Eq. (13)). This liquid leakage is generally quite small compared to the total liquid flow rate extracted when the liquid flow rate is high, so the extraction ratio is close to 0.2; but when the liquid flow rate is low, the liquid leakage will not be a small value compared to the total liquid flow rate, and the liquid extraction ratio K_L will be much higher than 0.2. The larger the gap is, the more apparent this tendency will be, as shown in Fig. 8, which was obtained with the drum having 0.75 mm gap size. Thus if the leakage could be effectively controlled by reducing the gap size between the drum and shell as far as possible or by other means, the stability of K_L would be improved significantly.

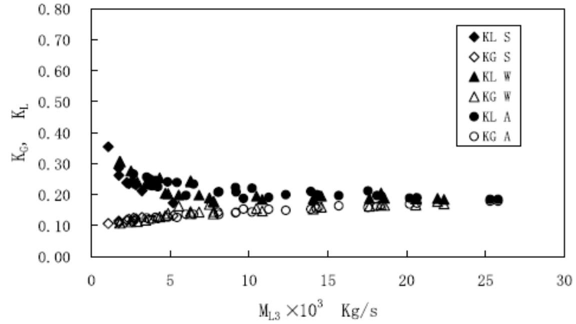

Fig. 7. Experimental result of extraction ratios (0.25 mm gap size)

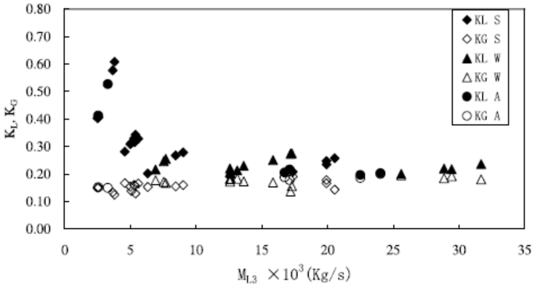

Fig. 8. Experimental result of extraction ratios (0.75 mm gap size)

For the gas extraction ratio K_G, the explanation is that the resistance to the air flow in the main flow loop is low compared to the bypass loop as the liquid flow rate is low, so some gas that should flow into the bypass loop will remain in the main loop, and the extraction ratio will be lower than 0.2; with the increase of the liquid flow rate, the resistance to the air flow in the main flow loop will increase, this make more gas flow into the bypass loop, and the gas extraction ratio increases gradually. Since the total resistance in main loop (and also bypass loop) comprises two parts: the resistances in drum and after the drum, it is easy to balance the first part of total resistance in main loop with that in bypass loop (as every flow channel of the drum nearly has the same geometry), and yet it is not easy to balance the second part in main loop with that in bypass loop, so it is the unbalance of the second part of total resistance in main loop and in bypass loop that causes the variation of K_G. If the second part of total resistance in both loops could be restricted within a very small fraction compared to the first part (or total resistance), the variation of K_G would be reduced remarkably. From Fig. 7 and Fig. 8 it can also be seen that flow regime do not have significant effect on the extraction ratios in the experimental range. The effect of rotation speed of the drum on the extraction ratio is shown in Fig.9, where V_{SL} represents superficial liquid velocity in the straight pipe. These data were obtained at arbitrary liquid and gas flow rates which cover the range of experiment. Although significant variations of extraction ratios can be seen in Fig. 9, any definite relationship between the variations and rotation speed of the drum can't be seen except the data of K_L at low liquid superficial velocity V_{SL} < 0.028 m/s. The extraction ratios, K_G and K_L, are only dependent upon the superficial liquid velocity. At the same nominal superficial liquid velocity, K_G (or K_L) is nearly unchanged over the span of rotation speed. All the higher value points of K_L and lower value points of K_G occur at the condition of low superficial liquid velocity V_{SL} < 0.028 m/s, the reason for this has been explained above. The value of K_L at low superficial liquid velocity V_{SL} < 0.028 m/s increases with increasing rotation speed, this can be further explained by the fact that the drum is driven by the fluid to be measured, so the rotation speed is nearly proportional to the gas flow rate at low superficial liquid velocity. Therefore, the increase in rotation speed means the increase in gas flow rate that will cause a higher pressure difference between the inlet and exit of the drum distributor, and of course a higher liquid leakage through the gap between the shell and the drum and finally a higher value of K_L. It is the gas flow rate that affects the value of K_L at low superficial liquid velocity. The rotation speed of drum does not have significant effect on the extraction ratios in the experimental range.

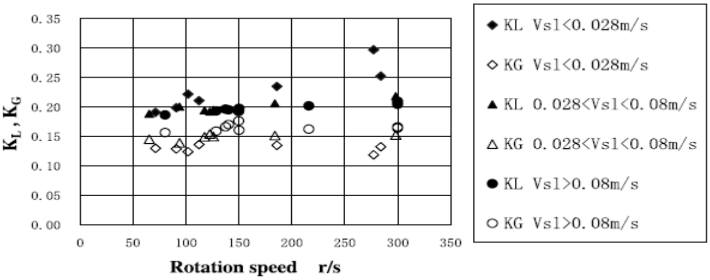

Fig. 9. Effect of rotation speed on extraction ratios (0.25 mm gap size)

Figs. 7 and 8 can also be considered as the extraction ratio calibration curves. By using these calibration values of K_G and K_L, the total gas flow rate and liquid flow rate can be determined according to Equation (5) and (6) respectively. The average error of flow rate measurement in the experiments were about ±6.2% and ±5.1% for gas and liquid respectively when the drum gap size was 0.75 mm; and ±5.6%, ±3.4% when the drum gap size was 0.25 mm.

2.3.2 The wheel – Fluid rooms distributor

Two type of wheel—fluid rooms distributors are schematically shown in Fig.10 and Fig.11 respectively (Wang et al, 2012).

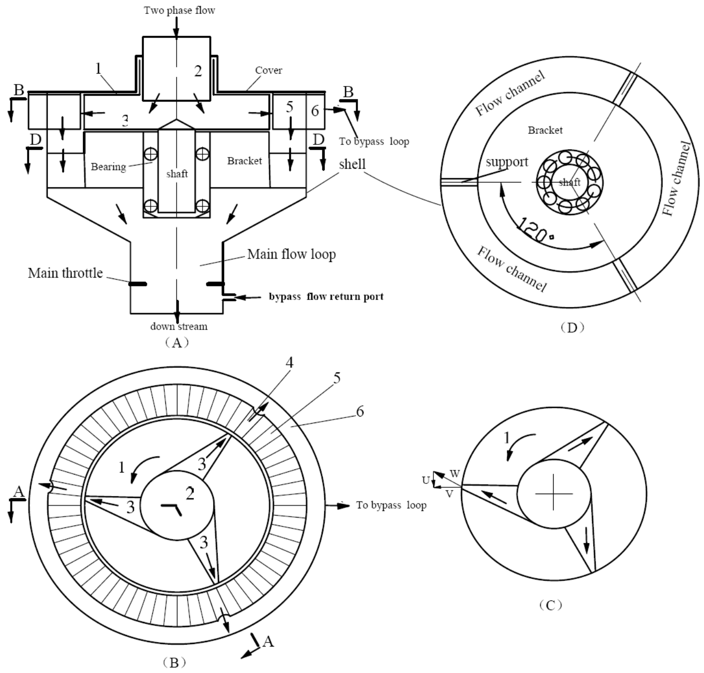

1.Wheel; 2.Entrance of flow; 3.Flow path; 4.Bypass fluid room; 5.Main fluid room; 6.Header of bypass flow

A. Rotated sectional view A-A; B. Sectional view B-B; C. Velocity triangle; D. Sectional view D-D

Fig. 10. The wheel—fluid rooms distributor-passive type

From Fig.10 it can be seen that the main body of the distributor consists of two parts: a wheel and a number of fluid rooms (Fig.10B). The wheel is located at the center of the distributor, and the fluid rooms equally surround the wheel. These fluid rooms are divided into two groups, one is connected to the main flow loop through their bottom (Fig. 10A), which is named as main fluid rooms; the other is connected to the bypass loop through the header of bypass flow (Fig.10B,A), which is called bypass fluid rooms. In Fig.10 the number of bypass fluid rooms is 3 and they are arranged 120 degrees from one to another around the wheel (Fig. 10B). As shown in Fig. 10A, the wheel is vertically installed in the bracket with a shaft and two bearings. The planform of bracket is shown in Fig. 10D. The wheel can rotate about its center axis, and is flow driven. In Fig.10A, the cover of distributor is made from Plexiglas plate for an easy observation of the wheel rotation. The fluid entrance of the distributor is located at the center of the cover, from where a short tube, which is fixed into the cover is inserted into the wheel center. There are 3 flow paths that equally surround flow entrance extending to the edge of the wheel (Fig.10B). As two-phase mixture flow downwards into the center of wheel (Fig.10A), the fluids will pass through the 3 flow paths within the wheel (Fig. 10B) and form 3 jets at the exit of the path. A reaction force will act on the wheel when the jets leave, which has a component in the tangency direction of wheel and push the wheel to rotate around the shaft at a high speed. The velocity triangle of the jets is shown in Fig.10C, where w is the relative velocity of the fluids, U is the wheel linear velocity at the edge, and V is the absolute velocity of fluids. It can be seen that V is nearly in the radial direction of the wheel, which means that the fluids can flow directly into the fluid rooms without impacting with the side wall of fluid rooms, and this will reduce the pressure loss of the distributor. With the rotation of wheel, the total two-phase flow is conducted alternately into main flow loop and bypass loop through their corresponding fluid rooms.

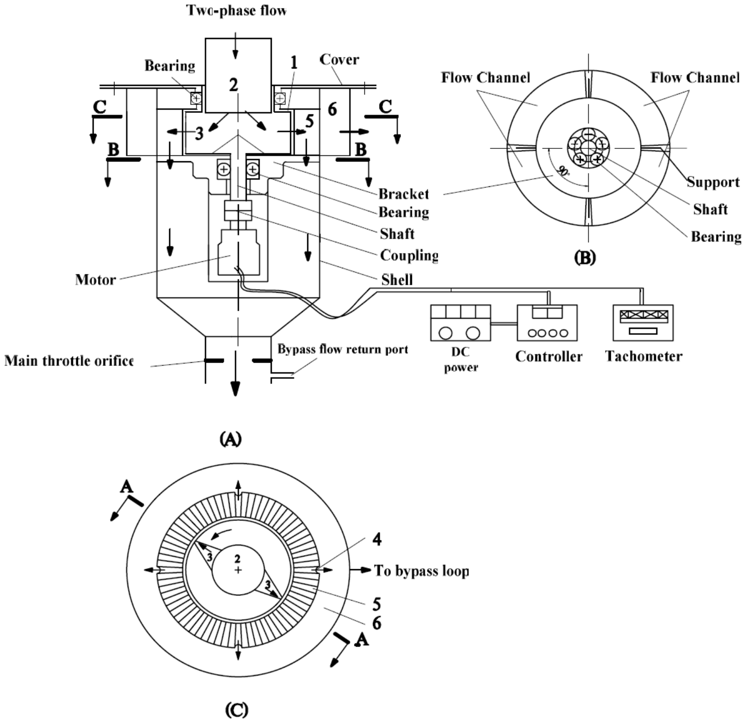

1.Wheel; 2.Entrance of flow; 3.Flow path; 4.Bypass fluid room; 5.Main fluid room; 6.Header of bypass flow

A. Rotated sectional view A-A; B. Sectional view B-B; C. Sectional view C-C

Fig. 11. The wheel－fluid rooms distributor-active type

Fig.11 is similar to Fig.10, only the wheel is driven by a motor and the rotation speed of the wheel is controlled by adjusting the electrical current to the motor. There are totally 4 bypass fluid rooms arranging 90 degrees from one to another around the wheel (Fig.11C). The number of flow paths within the wheel is 2 (Fig.11C). This distributor is designed for low velocity condition when the fluid can not drive the wheel steadily.

To be similar to a rotational drum, the wheel can evenly distributes the total flow to each fluid room during rotation, hence the relationship between M_{1j} and M_{3j} (where M is flowrate, j represents an arbitrary phase, gas or liquid, 1 presents total flow and 3 is the bypass flow) in the distributor mentioned above can be obtained based on the mass conservation within one period of rotation of the wheel. The amount of an arbitrary phase flowing to the bypass loop is

$$\Delta m_j = m \times \frac{T \times M_{1j}}{n} = T \times M_{3j} \tag{17}$$

where n is the total number of the fluid rooms, which is equal to 60 in Fig.10 and 72 in Fig.11; m is the number of bypass fluid rooms, which is 3 in Fig.10 and 4 in Fig.11 respectively; T represents the rotation period of the wheel.

Rearranging Equation (17), the extraction ratio will become

$$K_j = \frac{M_{3j}}{M_{1j}} = \frac{m}{n} \tag{18}$$

Equation (18) shows that the extraction ratio depends only on the ratio of bypass fluid room number to the total fluid room number and is independent of the speed of rotation. The rotation period changes with the flow rate, while the extraction ratio will still remain constant. We can change the value of the extraction ratio by altering the value of m or n. In the present study, for the passive distributor of Fig.10, m=3, n=60, according to Equation (18), the theoretical value of extraction ratio K_j is 0.05; and m=4, n=72 ,K_j=0.0556 for the active distributor of Fig.11. It should be pointed out that Equation (17)—(18) are only correct under the isokinetic sampling condition, i.e. the flow to each fluid room (refer to Fig.10B or Fig.11C) must be equal (let it equal to q), hence the bypass flow rate should equal to mq, the main flow rate be (n-m)q and the total flow rate be nq. In order to meet this requirement, the resistance in bypass flow loop and main flow loop must be properly controlled. The pressure loss due to friction and local resistance in these two loops can be written as below based on homogeneous flow model (Butterworth et al, 1978)

$$\Delta P_3 = \left[\sum \psi_3 \lambda_3 \frac{l_3}{D_3} + \sum \xi_3\right] \frac{1}{2\rho_L}\left(\frac{M_3}{A_3}\right)^2 \left[1 + X_3\left(\frac{\rho_L}{\rho_G} - 1\right)\right] \tag{19}$$

$$\Delta P_2 = \left[\sum \psi_2 \lambda_2 \frac{l_2}{D_2} + \sum \xi_2\right] \frac{1}{2\rho_L}\left(\frac{M_2}{A_2}\right)^2 \left[1 + X_2\left(\frac{\rho_L}{\rho_G} - 1\right)\right] \tag{20}$$

Where $\triangle P$ is the pressure loss, Ψ is correction factor, λ is Darcy friction factor, l is tube length, D is tube inner diameter, ξ is local two phase flow loss factor, ρ_L is the density of liquid phase, ρ_G is the density of gas phase, M is mass flowrate, A is tube cross section area, and X is the gas quality; Symbol Σ represents summation; Subscript "2" represents the main flow loop and the subscript "3" represents the bypass flow loop. Although Equation (19) and (20) are derived from the homogeneous flow model, they have been corrected by experimental data and several correlations about Ψ and ξ have been established for engineering application, especially in China and Russia (Lin et al, 2003).

From Fig.3 it can be seen that the bypass flow loop and the main flow loop have a common inlet and a common outlet i.e. they are in parallel to each other (Munson 2002), in accordance with the nature of parallel loops, the pressure loss of these two loops must be equal (Munson 2002). In isokinetic sampling case, X_2= X_3=X_1, where X_1 is gas quality of total flow, and the fluid densities are also equal. If we neglect the possible small difference of static head between two loops, the left hand sides of Equation (19) and (20) are equal. From

Equation (18), (19) and (20), a relationship of resistances between two loops for isokinetic sampling can be obtained

$$\frac{1}{1+\frac{A_2}{A_3}\sqrt{\frac{\sum\psi_3\lambda_3\frac{l_3}{D_3}+\sum\xi_3}{\sum\psi_2\lambda_2\frac{l_2}{D_2}+\sum\xi_2}}}=\frac{M_3}{M_3+M_2}=K \tag{21}$$

Where M_3 is the mass flowrate of bypass flow, and M_2 is the mass flow flowrate of main flow. This means that the resistance in two loops should be adjusted according to Equation (21) once an expected extraction ratio is selected. To make this work become easier, a main throttle device and a smaller throttle device are installed in main loop and bypass loop respectively. These two devices produce the major pressure loss in the corresponding loop, and Equation (21) can be met by merely adjusting these two throttle devices. In this case the pressure loss due to friction and other local resistances can be neglected, Equation (21) can be simplified as

$$\frac{1}{1+\frac{A_2}{A_3}\sqrt{\frac{\xi_3}{\xi_2}}}=\frac{M_3}{M_3+M_2}=K \tag{22}$$

Where ξ_3 and ξ_2 are the two-phase resistance factors of throttle devices in the bypass loop and main loop respectively. If both throttle devices belong to the same type (orifice or nozzle) then the value ofξ_3/ξ_2 will only depend on the size of these two devices. It will be verified by experiments.

The distributor and measurement system (bypass flow loop) were vertically installed in the left leg of an inverted U-shape pipe, as show in Fig.12. The inner diameter of the pipe was 50 mm, and made from Plexiglas pipe for flow pattern observation purpose. The separator was a cyclone type with an inner diameter of 60 mm. And there was a layer of stainless steel mesh on the top of cyclone cylinder to further remove the small water particle mixed with the gas. The gas flowmeter in the bypass loop was a thermal mass flowmeter (Proline t-mass 65F) with an inner diameter of 15 mm, made by E+H instrument company. and with a measurement accuracy of ±1%. The liquid flow rate was measured with a YOKOGAWA electromagnetic flow meter (ADMAG AE) with an inside diameter of 5 mm and an accuracy of ±0.5% FS.

The two phase flow experimental loop is shown in Fig.13. There were 100 pipe diameters length of straight pipe section upstream of the test section. Air and tap water were used as the working fluids in the experiments. The total air flow rate was metered using a YOKOGAWA vortex flow meter (YF102) with a accuracy of ±1% FS. The total water flow rate was measured with two orifice flow meters with a accuracy of ±1% FS, for lower flow rates and higher flow rates respectively. Since the flow patterns in the inverted U tube were always under an unsteady condition and very difficult to define, we observed the flow regimes at the entrance of inverted U tube i.e. at the horizontal line. The flow pattern occurring during the experiments included stratified flow, stratified wave, slug flow and annular flow. Though the flow pattern observed in horizontal line were not exactly the flow regime in the inverted U tube before the distributor, it could reflect the effect of flow patterns on the measurement.

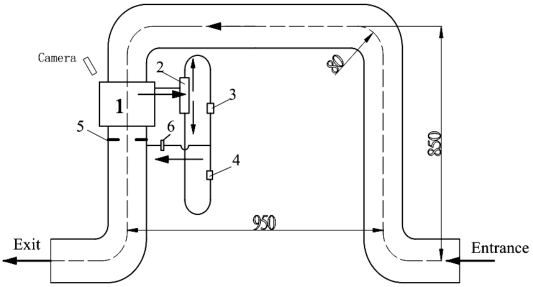

1. Distributor; 2.separator; 3.gas flow meter; 4. liquid flow meter; 5.main throttle; 6.throttle

Fig. 12. Test section

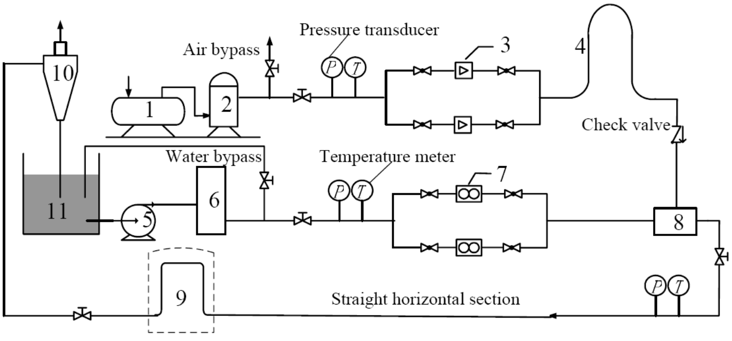

1.Compressor; 2.compressed air vessel; 3.gas flow meter; 4.invertied U tube; 5.Pump; 6. Water vessel; 7.water flow meter; 8.mixer; 9.test section; 10.cyclone separator; 11.water tank

Fig. 13. Two phase flow experimental loop

The electronic signals from instruments and transducers were connected to NI6023E data acquisition system and recorded by a computer. The acquisition frequency was 1kHz and the recording length was 120s. The average values were calculated after the recording. After that the air and water flowrates of total flow and bypass flow were able to be determined, and the real extraction ratio could also be calculated according to Equation (5) and (6). The uncertainty of extraction ratio was less than 1.4% according to the error theory (Taylor, 1982).

For the passive distributor of Fig.10, the wheel was driven by the two-phase flow, and the rotation speed was counted by a high speed video camera recording through the transparent cover of the distributor. Experiments showed that the rotation speed of the wheel was approximately proportional to the velocity of the two-phase mixture. The range of rotation speed of the wheel was 400 to 2000 r/min (T=0.15～0.03 s) with the gas superficial velocity ranged from 8 m/s －22m/s, and the liquid superficial velocity ranged from 0.02－0.2m/s. The wheel was not able to rotate steadily when the gas superficial velocity was below 7 m/s（at the same time the flow pattern transforms to stratified flow and slug flow.） The flow patterns appeared in this experiment was mainly annular flow. The maximum pressure loss of the distributor was less than 10kpa.

For the active distributor of Fig.11, the wheel was driven by a motor, and the rotation speed was controlled by adjusting the electrical current to the motor. The speed range was 100－700 r/min. The gas superficial velocity range was 1.5 m/s － 8m/s, and the liquid superficial velocity was in the range of 0.02～0.45m/s. The flow patterns occurred in the experiment included stratified flow, slug flow and stratified wave. The maximum pressure loss of the distributor was less than 6kpa.

For the passive distributor of Fig.10, the theoretical value of extraction ratio was 0.05, hence the size of the throttle devices in the bypass loop and main loop should be determined by this value according to Equation (22). Both devices selected were orifice plates. In order to determine their size, we first set the diameter of main loop orifice to 20 mm, then determined the diameter of bypass loop orifice by a tentative method. As the diameter equaled to 4.1 mm, experimental data showed that Equation (22) was met, i.e. the real extraction ratio was nearly equal to 0.05 as shown in Fig.14. Where K_L and K_G are the liquid and gas extraction ratios determined by experiments, U_{SL} is the superficial liquid velocity and U_{SG} is the superficial gas velocity. It can be seen that K_G and K_L are very close to the theoretical value of 0.05 and independent of liquid and gas superficial velocity. The average value of K_G was 0.0506, and the standard deviation was 0.00079; the average value of K_L was 0.0498, and the standard deviation was 0.00166. The maximum difference between K_G and the theoretical value was less than 4%, and the maximum difference between K_L and the theoretical value was less than 6%.

For the active distributor of Fig.11, the theoretical value of extraction ratio was 0.0556, we determined the size of orifices with the same method mentioned above. The diameter of main loop orifice was 25 mm, and the diameter of sample loop orifice was 5 mm. the real extraction ratios are shown in Fig.15. It can be seen that when U_{SL} is lager than about 0.1 m/s, K_G and K_L are very close to the theoretical value of 0.0556 and independent of gas and liquid superficial velocity. The average of K_G was 0.0560, and the average of K_L was 0.0559. But as U_{SL} is less than about 0.1 m/s, both K_G and K_L will deviate below the theoretical value, and the lower the gas and liquid velocity, the smaller the K_G and K_L. This can be explained by the fact that as the superficial velocity of liquid and gas become lower, the dynamic pressure of the jets from the flow path of the wheel (refer to Fig.11C) will become smaller, at a certain point (critical value), the dynamic pressure is not high enough to overcome the resistance of fluid rooms to enable the jets to completely flow into the bypass flow header, and some fluid will preferentially flow back to the main flow loop. Fig.16 shows that this critical value is 400 Pa, and it can also be seen that nearly all points fall on the same line. Based on this critical value we can determine the lowest effective working point of the distributor.

Fig.17 shows the effect of rotation speed on the extraction ratios. It can be seen that K_G is not affected by the rotation speed, but K_L increases with the rotation speed as U_{SL} is less than about 0.1 m/s, due to centrifugal force.

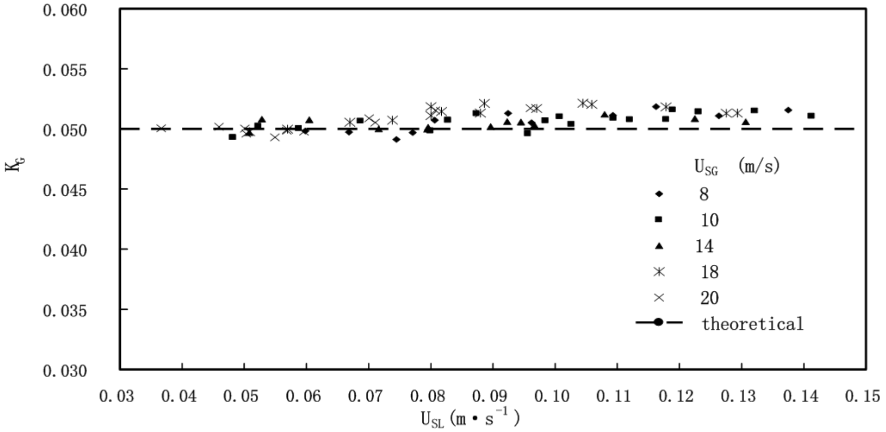

(A)

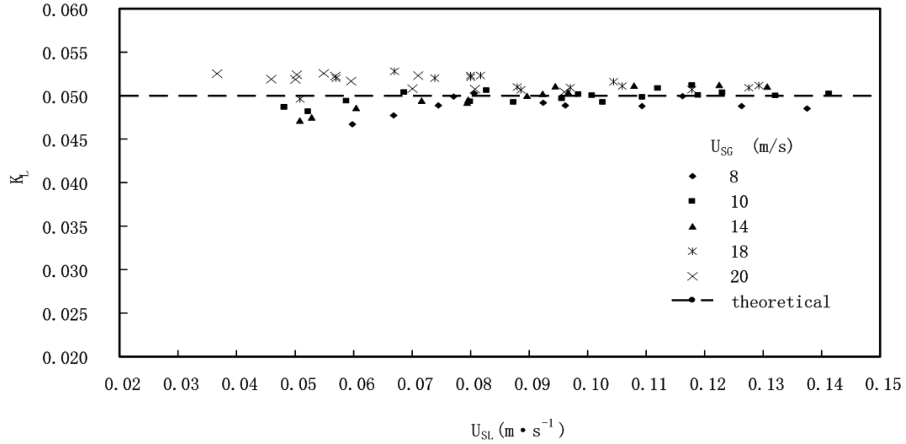

(B)

A: Gas extraction ratio B: Liquid extraction ratio

Fig. 14. Extraction ratios of the passive distributor of Fig.10

Fig.18 shows the effect of flow patterns on the extraction ratios of the active distributor of Fig.11. In the experiments the most frequently occurred flow pattern was slug flow which is the most unsteady flow, from Fig.18 we can see that both K_G and K_L are very close to the theoretical value for all slug flow and some stratified wave data, however, K_G and K_L will drift below the theoretical value as the pattern is stratified flow and for partial stratified wave data. The reason is that in these two patterns both the gas and liquid superficial velocity are lower as compared with other patterns, the jet's dynamic pressure in the wheel is below the critical value of 400 Pa, so some fluids which should flow to bypass loop flow to the main loop. Therefore we can say that it is the jet's dynamic pressure or fluid velocities that affects the K_G and K_L.

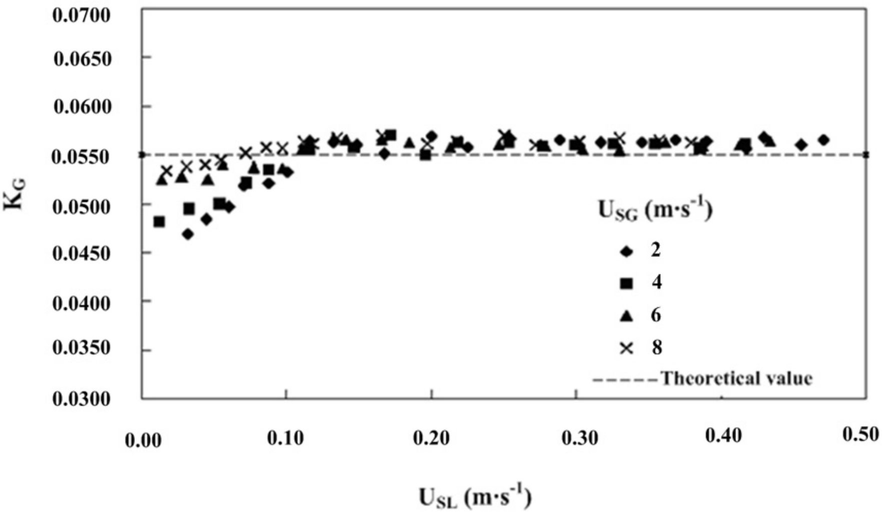

(A)

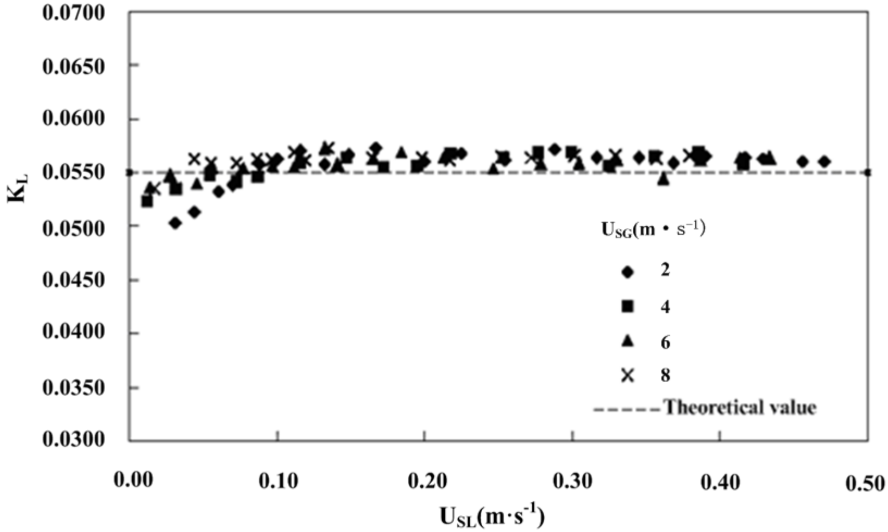

(B)

A: Gas extraction ratio B: Liquid extraction ratio

Fig. 15. Extraction ratios of the active distributor of Fig.11

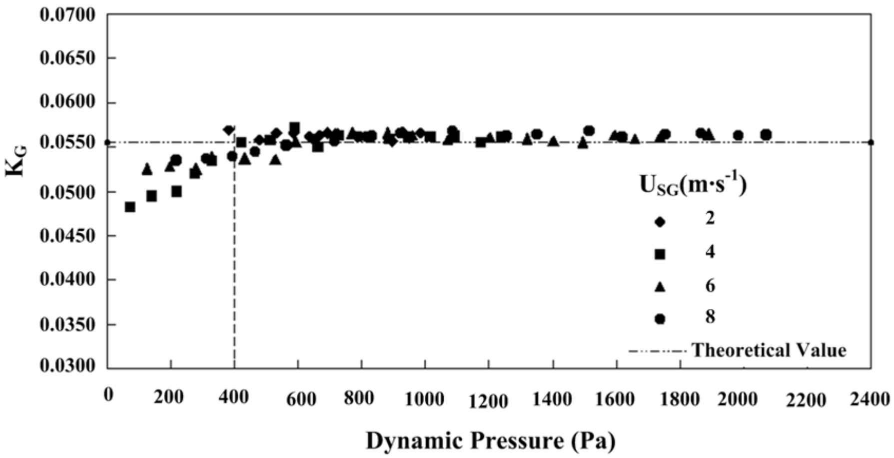

(A)

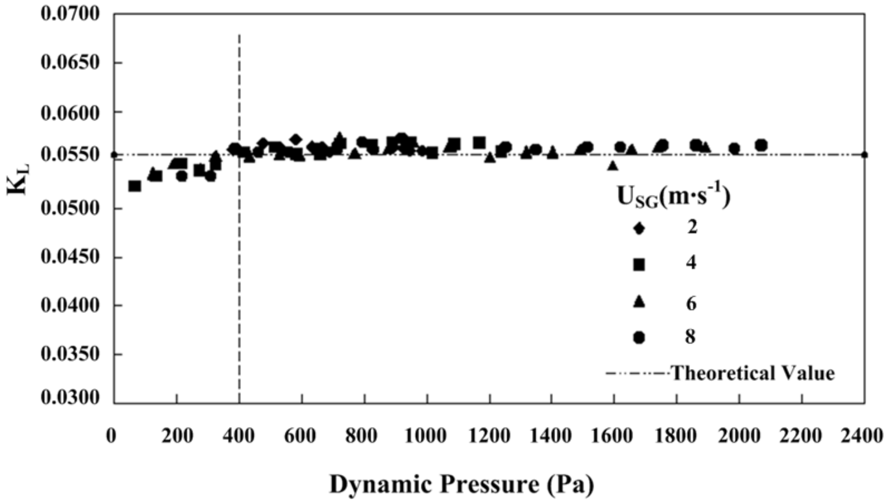

(B)

A: Gas extraction ratio B: Liquid extraction ratio

Fig. 16. Relation between extraction ratios and the jet dynamic pressure

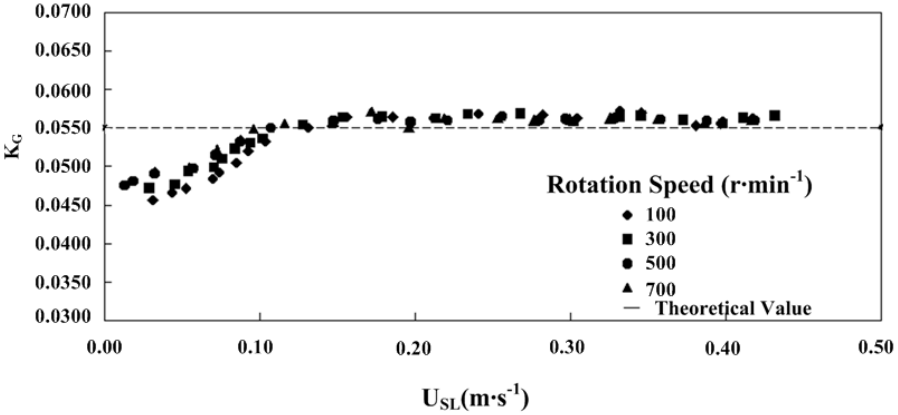

(A)

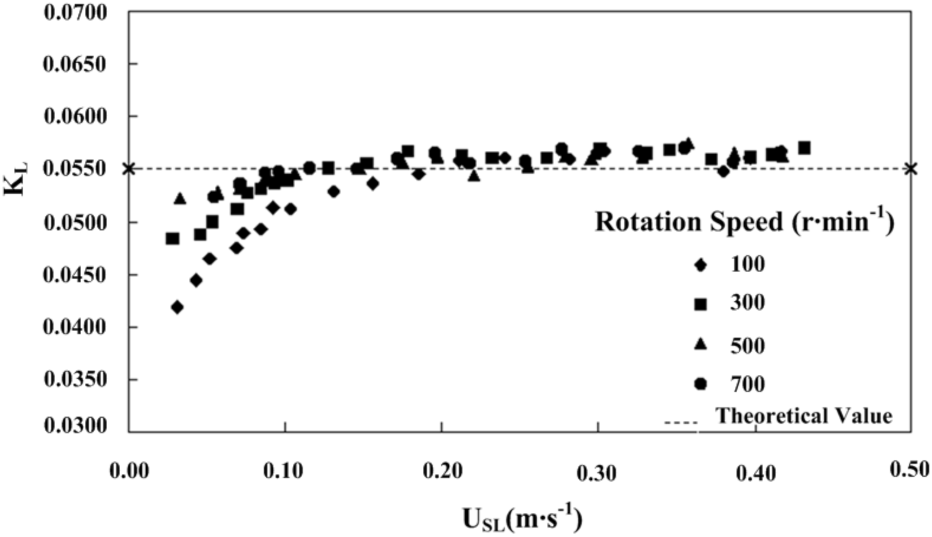

(B)

A: Gas extraction ratio B: Liquid Extraction ratio

Fig. 17. The effect of rotation speed on extraction ratios

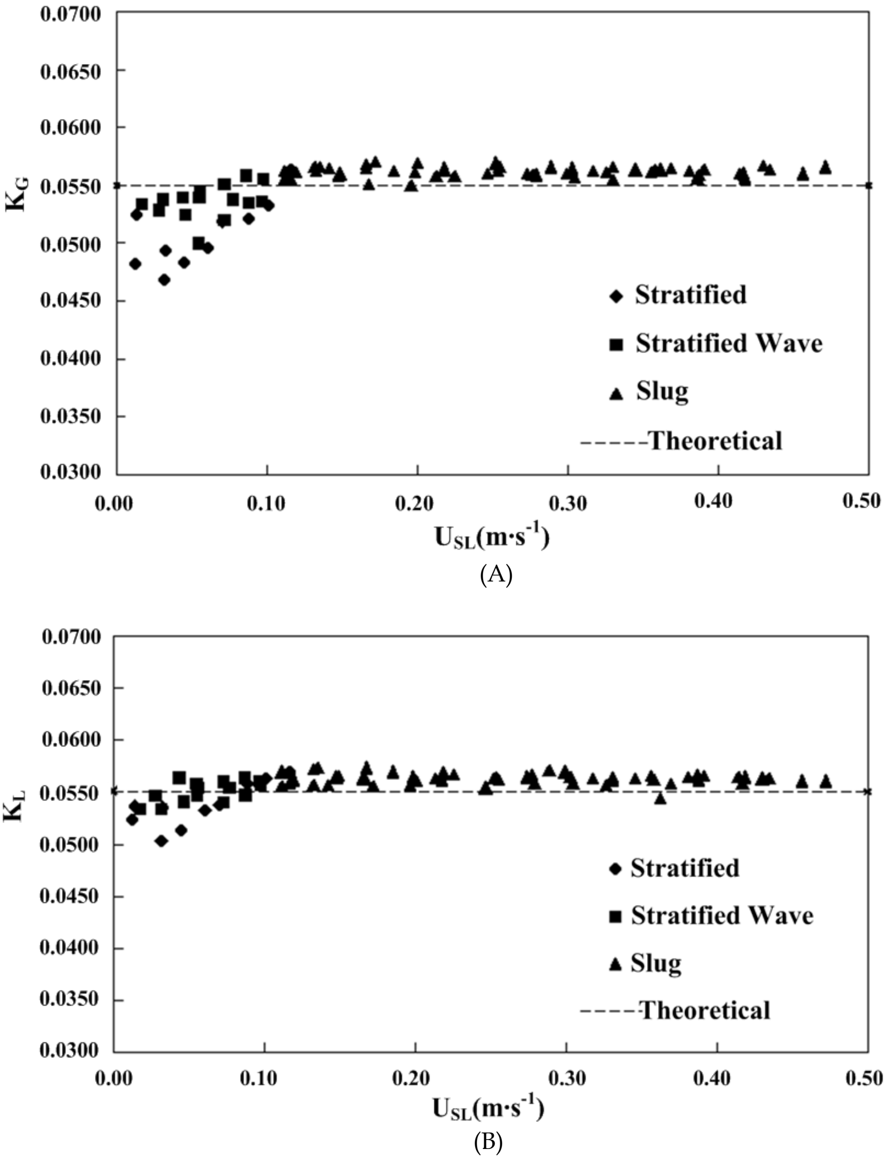

A: Gas extraction ratio; B: Liquid Extraction ratio

Fig. 18. The effect of flow pattern on extraction ratios

From Fig.14 and Fig.15 we have observed that both K_G and K_L are very close to the theoretical values, i.e. gas and liquid were drawn with the same proportion, so we certainly can expect that the bypass fluid will have the same components as the total flow, and this assumption was proved by the experiments. Comparisons of the gas quality of sample flow with that of total flow show that the gas quality of sample flow is very close to that of total flow in the experiments, the maximum difference between them is less than 1.3%. This demonstrates that the bypass fluid is an excellent representative of the total flow.

The calibrated values of K_G and K_L which are constants and independent of flowrates can be used to determine the total liquid and gas flow rates M_{1L} and M_{1G} according to Equation (5) and (6) after the bypass flow rate M_{3L} and M_{3G} have been metered. Fig.19 and Fig.20 present the measurement error of total gas and liquid flowrate of two-phase flow respectively. It can be seen that the total flow rates measurements error is less than ±5% ，and the large errors occurred at low flowrates. Therefore we can conclude that this method is reliable.

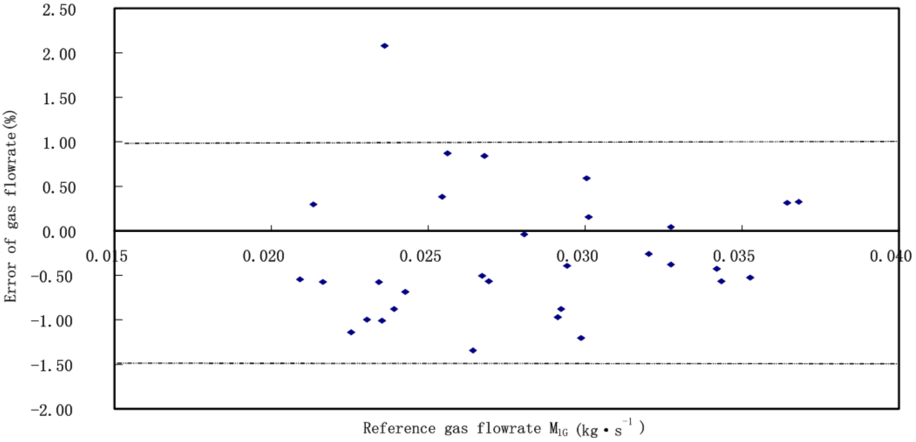

(A)

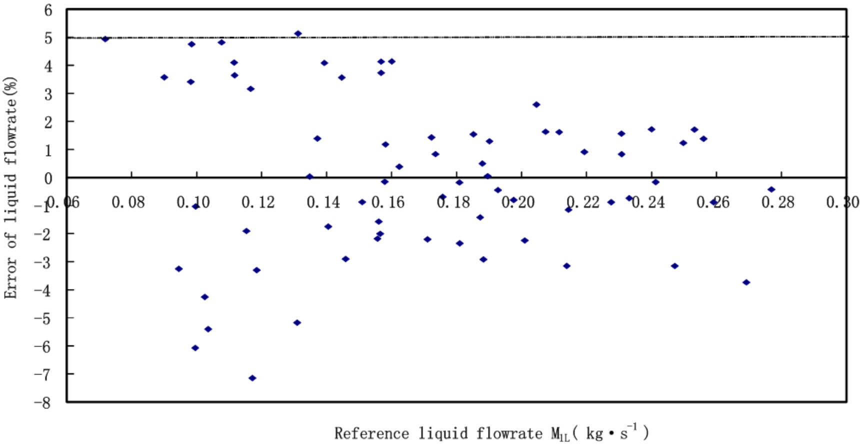

(B)

A: Gas flow B: Liquid flow

Fig. 19. Error of total flowrate measurements of the passive distributor of Fig.10

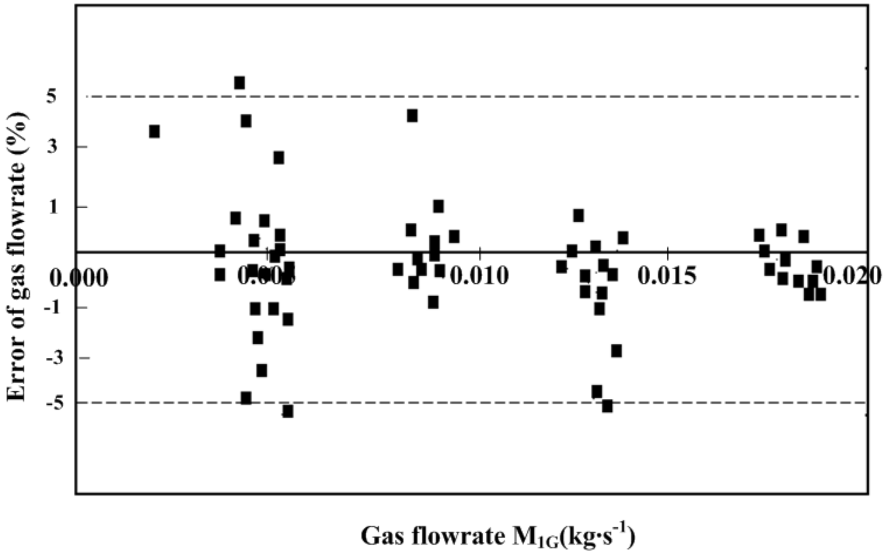

(A)

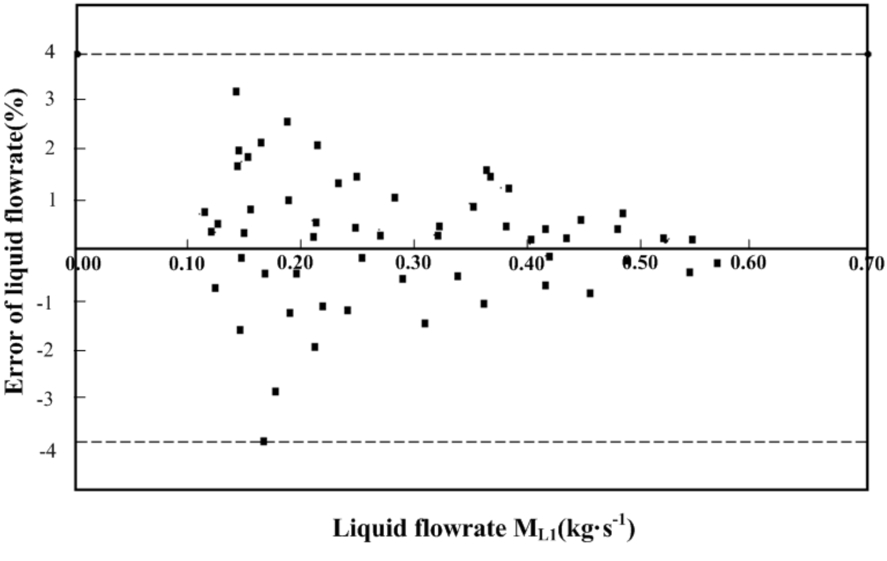

(B)

A: Gas flow B: Liquid flow

Fig. 20. Error of total flowrate measurements of the active distributor of Fig.11

2.3.3 Static distributor for high pressure steam-water two-phase flow

In high pressure steam-water flow condition, it is more suitable to use a static distributor that does not contain any moving parts. A distributor used in this study is shown in A-A section view of Fig.21 (Wang et al, 2011).

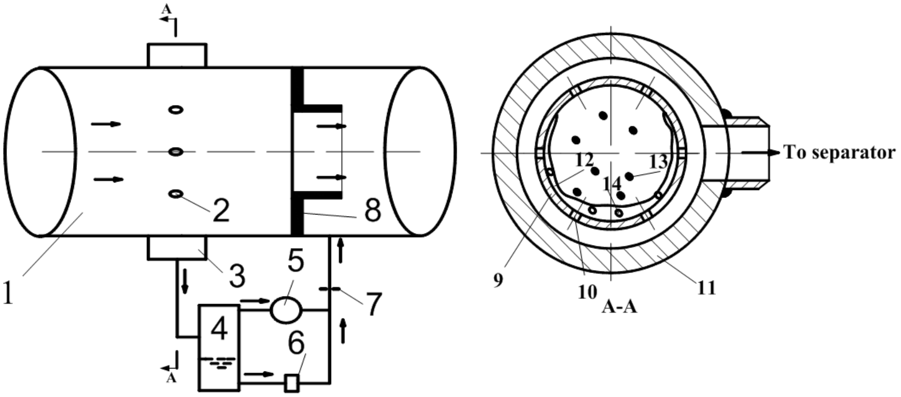

1. main pipe; 2,10.division holes; 3.collection ring; 4.separator; 5.steam meter; 6.water meter; 7.throttle device; 8.main loop throttle device; 9.pipe wall;11.the wall of collection ring;12.water film;13.water droplet;14.steam bubble

Fig. 21. Static distributor and flow division system

The static distributor consists of 6 small division holes that are evenly spaced around the circumference of the main pipe and a collection ring surrounding the pipe wall. The inside diameter of the main pipe was 50 mm, and the thickness of the pipe wall was 3 mm. The inner diameter of the collection ring was 70 mm, and the diameter of the division hole was 3.5 mm. The separator is a cyclone type with inner diameter of 42 mm. Both the steam meter and water meter were venturi tubes with throat diameter of 7.4 mm and 4.4 mm respectively. The throttle device was a thick orifice plate with diameter of 3.5 mm. The restriction in main loop was a nozzle with diameter of 28 mm.

To be equivalent to equation (5) and (6), the total steam and water flow rates are determined by the following equations

$$M_s = \frac{M_{ss}}{K_s} \tag{23}$$

$$M_w = \frac{M_{sw}}{K_w} \tag{24}$$

Where, M_s is the total steam flow rate; M_w is the total water flow rate; M_{SS} is the bypass steam flow rate metered by steam meter; M_{SW} is the bypass water flow rate metered by water meter; K_s is the steam extraction ratio; K_w is the water extraction ratio. Referring to Fig.21, we can also see that the fluid flowing to the division (bypass) loop comes from a region near the wall where the water proportion is higher, and therefore more water will enter the division loop, i.e. K_w will be larger than K_s, and it is beneficial to the measurement of water flow rate in the condition of flow with high steam volume fraction.

Equation (23) and (24) are only the definition of extraction ratios, the real values of K_s and K_w are dependent on the resistance relation between the division (bypass) loop and the main loop, and also on the distribution characteristic of the division loop. From Fig.21 we can see that the division (bypass) loop and the main loop have a common inlet and a common outlet, i.e. they are in parallel. In accordance with the nature of parallel loops (Munson, 2002), the pressure losses of both loops are equal

$$\Delta P_m = \Delta P_s \tag{25}$$

Where, ΔP_m is the pressure loss in the main loop; ΔP_s is the pressure loss in the division (bypass) loop.

ΔP_m and ΔP_s can be calculated based on the separated flow model (Lin, 1982)

$$\sqrt{\Delta P_m} = \sqrt{\Delta P_{ms}} + \theta_m \sqrt{\Delta P_{mw}} \tag{26}$$

$$\sqrt{\Delta P_s} = \sqrt{\Delta P_{ss}} + \theta_s \sqrt{\Delta P_{sw}} \tag{27}$$

Where, ΔP_{ms} and ΔP_{mw} are the pressure losses when steam phase and water phase flows in the main loop alone respectively; ΔP_{ss} and ΔP_{sw} are the pressure losses when steam phase and water phase flows in the division loop alone respectively; θ is the correction factor which depends on the pressure (Lin, 1982).

In accordance with the single phase flow pressure loss calculation method (Munson, 2002), we can write down the following equations

$$\Delta P_{ms} = \left[\sum \lambda_m \frac{l}{d_m} + \sum \xi_m\right] \frac{1}{2\rho_s} \left(\frac{M_{ms}}{A_m}\right)^2 \tag{28}$$

$$\Delta P_{mw} = \left[\sum \lambda_m \frac{l}{d_m} + \sum \xi_m\right] \frac{1}{2\rho_w} \left(\frac{M_{mw}}{A_m}\right)^2 \tag{29}$$

$$\Delta P_{ss} = \left[\sum \lambda_s \frac{l}{d_s} + \sum \xi_s\right] \frac{1}{2\rho_s} \left(\frac{M_{ss}}{A_s}\right)^2 \tag{30}$$

$$\Delta P_{sw} = \left[\sum \lambda_s \frac{l}{d_s} + \sum \xi_s\right] \frac{1}{2\rho_w} \left(\frac{M_{sw}}{A_s}\right)^2 \tag{31}$$

Where, λ is the Darcy friction factor, l is the tube length, d is the tube inner diameter, ξ is the local loss factor, ρ_w is the density of water, ρ_s is the density of steam, M is the mass flowrate, A is the tube cross section area, the symbol Σ represents summation; subscript "m" represents the main loop and the subscript "s" represents the division loop.

Based on mass conservation, we can write down the flow rates relation of the total flow with that in the main loop and the division (bypass) loop

$$M_s = M_{ms} + M_{ss} \tag{32}$$

$$M_w = M_{mw} + M_{sw} \tag{33}$$

Let X_m be the steam quality of the main loop, X_s be the steam quality of division loop, and neglect the little difference between θ_m and θ_s i.e. $\theta_m=\theta_s=\theta$, then substituting equations (23)-(24) and (26)-(33) into (25), one can obtain

$$\frac{K_0}{K_s}-1=\theta\left(1-\frac{K_0}{K_w}\right)\sqrt{\frac{\rho_s}{\rho_w}}\left(\frac{1}{X_s}-1\right) \tag{34}$$

Where K_0 is the extraction ratio in the case of single phase flow, which can be calculated by the following equation or determined by experiments

$$K_0=\frac{A_s\sqrt{\sum\lambda_m\frac{1}{d_m}+\sum\xi_m}}{A_s\sqrt{\sum\lambda_m\frac{1}{d_m}+\sum\xi_m}+A_m\sqrt{\sum\lambda_s\frac{1}{d_s}+\sum\xi_s}} \tag{35}$$

Equation (34) is known as the resistance equilibrium equation because it is derived from the resistance relation, however, it alone cannot yet determine the values of K_s and K_w, therefore another additional equation must be developed, and equation (34) is the first equation for extraction ratios. Define K_m as the mass extraction ratio

$$K_m=\frac{M_{ss}+M_{sw}}{M_s+M_w}=\frac{1}{\frac{X_s}{K_s}+\frac{1-X_s}{K_w}} \tag{36}$$

For a given structure of the main loop and the division loop, K_m is usually a constant in the case of single phase flow, however in the condition of two phase flow, K_m may vary with the flow rate and steam quality, therefore the value of K_m/K_0 is the function of flow rate and steam quality

$$\frac{K_m}{K_0}=F(M,X_S) \tag{37}$$

The function $F(M,X_S)$ reflects the distribution characteristic of division loop, and can only be determined by experiments.

Experiments were carried out in an once-through boiler for steam flooding in Keramay oilfield, Xinjiang China. Fig.22 is the schematic representation of the experimental systems. The experimental setup was horizontally installed at the test section. The length of the straight horizontal pipe between the sampler separator and test section was 3 meters, and the length of division steam pipe was 0.68 meters. All the pipe and test section were properly insulated with mineral fiber. The heat loss rate in the main pipe and division loop, based on a heat transfer calculation, were less than 0.15kw/m and 76w respectively, and the steam condensation due to heat loss were less than 0.41kg/(m • h) and 0.13kg/h respectively, both were insignificant compared to the steam flow in the pipe.

The flow rate to the once-through boiler was adjusted by changing the rotation speed of the piston pump with a frequency converter, and metered by a calibrated orifice flow meter at the entrance of the boiler which has an accuracy of 1.3%. In accordance with the nature of once-through boiler, the flowrate throughout the boiler must keep a constant in the condition of steady state, because in the steady state the amounts of fluids (water and steam) within the boiler have reached their stable values, no additional fluid will accumulate or be removed from the boiler, i.e. the input must equal to the output. So the flowrate passing through the test section can be measured by the orifice flow meter at the entrance of the boiler under steady state.

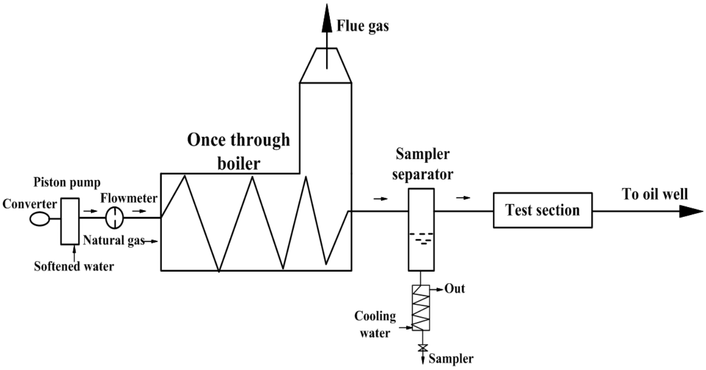

Fig. 22. Schematic representation of the experimental setup

The output steam quality of the boiler was carefully controlled by adjusting the flow rate of natural gas entering the furnace. The value of steam quality at the boiler output was determined based on the fact that the salts dissolved in the softened water (Na_2SO_4, Na_2SiO_3, et al.) still remain in water after the evaporation process in boiler, hence, according the salts conservation, we can write down the following equations

$$M \cdot S_i = M \cdot (1 - X) \cdot S_o \tag{38}$$

$$X = \frac{S_o - S_i}{S_o} \tag{39}$$

Where，S_i is the salts concentration of softened water at the input of the boiler; S_o is the salts concentration of condensed water at the output of the boiler, i.e. at the sampler separator. The sampler separator of Fig.22 is a small vessel connected to the steam pipe which is used to collect some water from the steam-water flow by gravitational effect, but not designed to separate the whole steam-water flow. A very small amount of water(less than 8kg/h) is drained from the sampler separator and then cooled by cooling water, this is the sampler of condensed water.It should be noted that equation (38) and equation (39) are correct only in the condition of steady state of the boiler operation. Due to this reason we had to wait for 2-3 hours after an adjustment of boiler parameters (flowrate or quality) to ensure that a steady state had been reached before the measurements of flowrate and steam quality were able to be taken.

Equation (39) is not convenient to use because it is not an easy task to measure the salts concentration directly in oilfield. The salts concentration measurements are usually replaced by that of electrical conductivity in oilfield based on the principle that in the case of low salts concentration (far below their solubility), the molar conductivity (the conductivity per unit of concentration) tends to be a constant(Aguado, 2006), hence the conductivity of water is proportional to the salts concentration, so Equation (39) can become as

$$X = \frac{C_o - C_i}{C_o} \tag{40}$$

Where, C_i is the softened water conductivity at the input of the boiler; C_o is the condensed water conductivity at the output of the boiler, i.e. at the sampler separator.

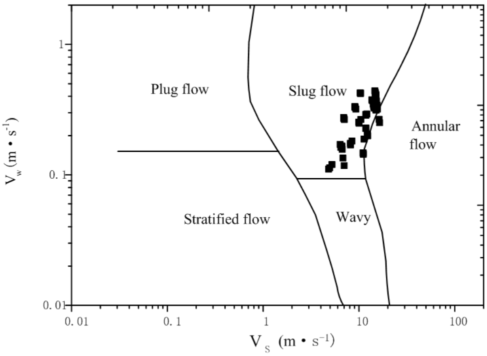

Fig. 23. Experimental range

Equation (40) has been successfully used to measure steam quality in oilfield for many years. During the experiments,both C_i and C_o were measured by a portable conductivity meter with an accuracy of 0.5%, according to error theory, the error of steam quality from Equation (40) is 0.6%. For the sake of boiler safety, the lowest steam quality allowed was 0.60, and the highest steam quality allowed was 0.82 and this range of steam quality is enough to cover the quality usually encountered in oilfield. The flow rate range was 2000kg/h to 8000kg/h, and pressure range was 7.6MPa to 16MPa. Fig.23 showed the experiments range in the Mandhane map (Collier,1981), where V_s represents the superficial steam velocity, and V_w the superficial water velocity. From Fig.22 we can see that the experiment points were mainly located on the borders of slug flow, annular flow and wavy flow which are the most frequently occurring regimes in the steam pipe line for the steam flooding and other industries.

The static pressure of the test section was measured by a Rosemount 3051 pressure transmitter, and both the steam venturi tube and water venture tube differential pressures in the division loop was measured by a Rosemount 3051 differential pressure transmitter respectively. These three transmitters' signals were connected to an industrial computer which automatically converts the signals to numerical data and calculate the bypass steam and water flow rates.

Before the normal two phase flow experiments, a single phase water flow experiment was conducted to determine the value of K_0 (the extraction ratio in single phase case), the result was K_0=0.01350. During the two phase experiments, the pressure and bypass steam and water flow rates were automatically recorded by the computer, and the extraction ratios was able to be calculated according to equation (23) and (24) once the flow rate of the boiler and the steam quality were measured. The results of extraction ratios is shown in Fig. 24, where the horizontal axis represents the right term of equation (34), and the vertical axis represents the left term of equation (34). From Fig.24 it can be seen that a liner relationship exists between the ordinate and the abscissa, and all the experimental points fall on the same line, it means that the equation (34) is correct and independent of flow rate. From these data we can also obtain the value of θ=1.6259.

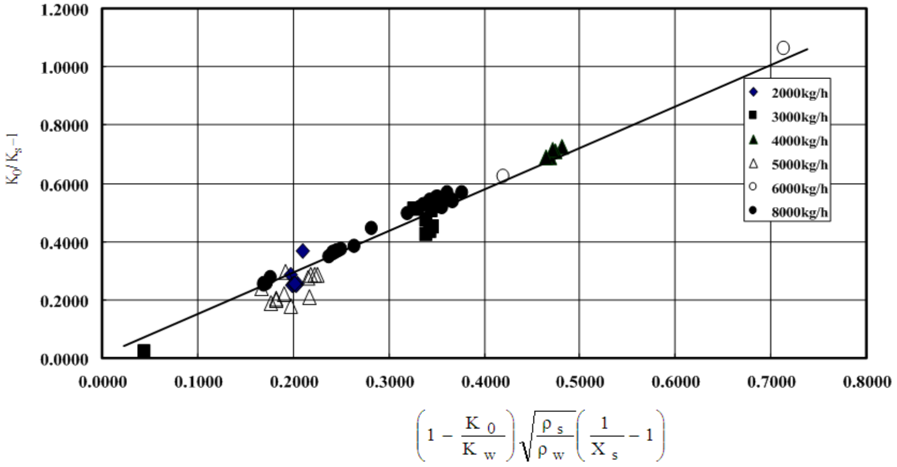

Fig. 24. Experimental results of extraction ratios

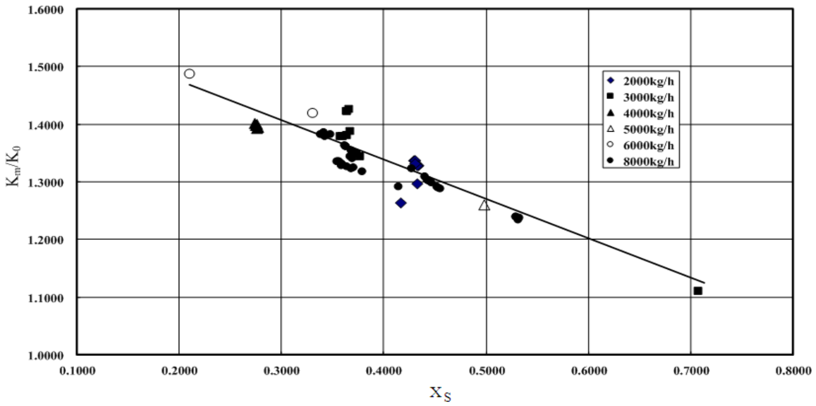

Fig. 25. Relationship between K_m and X_s

Fig.25 showed the relationship between the mass extraction ratio K_m and steam quality of bypass loop X_s for various mass flow rates. It can be seen that a simple linear relation exists between them, and all the experimental data fall on the same line, this means that flow rate M has little effect on the $F(M,X_s)$. From these data the actual form of $F(M,X_s)$ in equation (37) can be determined

$$\frac{K_m}{K_0}=F(M,X_S)=1.6090-0.6919X_s \tag{41}$$

Substituting equation (41) into equation (36) one can obtain

$$\frac{K_0}{K_s}X_s+\frac{K_0}{K_w}(1-X_s)=\frac{1}{1.6090-0.6919X_s} \tag{42}$$

Equation (42) is the second equation of extraction ratios and is called the distribution equation because it reflects the distribution nature of bypass loop.

The extraction ratios K_s and K_w can now be determined by solving equation (34) and (42), and then the total steam and water flow rate M_s and M_w(or the total flow rate M and quality X) can be measured once the bypass steam and water flow rate M_{ss} and M_{sw} are metered, these works are automatically done by the computer which is connected to the pressure and different pressure transmitters. Table 1 give some measurement results, where the reference flowrates represent values metered by the orifice flowmeter at the entrance of the boiler, the reference mass quality is obtained by conductivity method. From Table 1 it can be seen that the maximum error of flow rate measurements is less than ±2.5%, and the maximum error of quality measurements is less than ±3.5%. The water extraction ratio K_w is 3~5 times more than steam extraction ratio K_s.

No	Flow rate (kg/h)			Mass quality			Extraction ratio	
	Measured	Reference	Error(%)	Measured	Reference	Error(%)	K_s	K_w
1	2120	2100	0.95	0.7236	0.7200	0.36	0.01075	0.03677
2	3430	3420	0.29	0.7975	0.8000	-0.25	0.01325	0.02195
3	3930	4000	-1.75	0.6980	0.6628	3.52	0.007828	0.04072
4	4890	4850	0.82	0.6403	0.6517	-1.14	0.006811	0.04552
5	5160	5150	0.20	0.7788	0.8140	3.52	0.01096	0.04587
6	6130	6150	-0.33	0.6636	0.6473	1.63	0.006541	0.04489
7	7438	7529	-1.21	0.7651	0.7758	-1.07	0.008774	0.05089
8	7540	7600	-0.79	0.7746	0.7541	2.05	0.008852	0.04667
9	7880	8070	-2.35	0.7564	0.7403	1.61	0.008750	0.04242
10	7990	8070	-1.00	0.7837	0.7886	-0.49	0.09423	0.04783

Table 1. Measurement results of flow rate and mass quality

3. Conclusion

Flow division techniques have been widely used in single phase flow measurements, whose main feature is to utilize a small size meter to measure a large volume flow in large lines. In addition to this, a bypass flow meter usually has a much wider metering range, a better precision and a lower price. Further more, when we apply this technique in two-phase flow, an even more important advantage will appear: a small size separator can be used in the bypass loop to separate the two-phase mixture and consequently measuring them by conventional single phase meters, thus the problem of two-phase flow rate measurement can simply be solved. However a special distributor must be employed to ensure that the bypass flow will have the same components as the total flow and be proportional to the total flow. Three different kinds of distributors have been studied in this chapter.

The rotational drum is a flow driven distributor whose extraction ratio is equal to the ratio of extraction channel number to the total flow channel number and independent of flow patterns. The gap size between the drum and the shell has a significant effect on the real extraction ratios. When the gap size is equal to 0.25 mm, a much stable extraction ratio can be obtained. The measurements error of total flow is less than ±5.6%. Experiments also showed that the drum rotation speed has no effect on the measurement.

The wheel-fluid rooms distributor is much simpler in structure. The wheel can be driven either by the flow or by a motor and the rotation speed has no effect on the measurements. The extraction ratio can be as low as 0.05 (and 0.0556) and depends only on the ratio of bypass fluid room number to the total fluid room number. The superficial gas velocity can be as low as 1.5 m/s, and the measurement error of total flow rate is within ±5% in the above experimental ranges.

The static distributor was specially designed for the high pressure steam-water two-phase flow measurements where any moving parts in the apparatus may reduce the reliability of the meter. Although the static distributor can not keep the extraction ratio as a constant as the rotational drum or the wheel- fluid rooms distributor does, two independent equations about the extraction ratios have been derived from the resistance equilibrium relation between the main loop and bypass loop, and the distribution function respectively. Thus the extraction ratios can be determined by solving these two equations. The extraction ratios were as small as 0.007-0.05 which is very important to the development of high pressure two-phase flow meter. The experiment points were mainly located on the borders of slug flow, annular flow and wavy flow in the Mandhane map. The error of flow rate measurements is less than ±2.5%, and the error of quality measurements is less than ±3.5%.

4. Acknowledgment

The authors express their great thanks to National Natural Science Foundation of China for financial support (No.50776071 and No.50376051), and also to Dr. Y B Yang and Ms R P Wang for their careful language revision.

5. References

Adams, M. M. (1969). Electric thermal flowmeter. Us Patent :3425277

Aguado, D. ; Montoya, T. ; Ferrer, J. & Seco, A. (2006).Relating ions concentration variations to conductivity variations in a sequencing batch reactor operated for enhanced biological phosphorus removal. *Environmental Modelling & Software,* Vol.21,No.6, (March 2005), pp.845-851，ISSN: 1364-8152

Bahrton, G. (1996). Flowmeter with a variable constriction. Us Patent :5554805

Baker, W. C. (1969). Fluid flow measuring appratus. Us Patent :3443434

Baker, W. C .(1971). Fluid flow measuring appratus. Us Patent :3559482

Baker, W. C. (1977). Fluid flowmeter. Us Patent :4041757

Bates, C. J. & Ayob, R. (1995). Annular two-phase flow measurements using phase Doppler anemometry with scattering angles of 30° and 70°. *Flow Meas. Instrum.* Vol.6,No.1,(January 1994), pp.21-28,ISSN: 0955-5986

Beg, N. A.&Toral, H. (1993). Off-site calibration of a two-phase pattern recognition flowmeter. *Int. J. of Multiphase Flow*,Vol.19, No.6,pp.999-1012, ISSN: 0301-9322

Butterworth, D. & Hewitt, G. F. (1978). *Two-phase flow and heat transfer*, Oxford University Press,pp.49, ISBN:0-19-851715-7, Oxford, UK.

Cha, J. E. ; Ahn, Y. C. & Kim, M. H. (2002). Flow measurement with an electromagnetic flowmeter in two-phase bubbly and slug flow regimes. *Flow Meas. Instrum.* Vol.12,No.5, (January 2002), pp.329–339, ISSN: 0955-5986

Chisholm, D. (1974). Pressure drop during steam/water flows through orifices *J. Mech. Eng. Sci.* Vol.16, No.5, pp.353-355, ISSN: 0022-2542

Collier, J. G.(1981).*Convective Boiling and Condensation* (second edition),McGRAW-HILL International Book Company, pp. 6-21, ISBN :0-07-011798-5, Berkshire,England

Connet, F. N. (1928). Proportionate meter. Us Patent :1681762

DeCarlo, J. P. (1984). *Fundamentals of flow measurement*, Instrument Society of America, pp.195-199, ISBN : 0-87664-627-5, North Carolina, USA

Fenelon, P. J.(1994). In-line parallel proportionally partitioned by-pass metering device and metering device and method. Us patent :533496

Ferreira, V. C. S. (1997).Differential pressure spectral analysis for two-phase flow through an orifice plate. *Int. J. Pres. Ves. & Piping,* Vol.73, No.1, pp.19-23, ISSN: 0308-0161

Geng, Y. F.;Zheng. J. W. & Shi, G. (2007). Wet Gas Meter Development Based on Slotted Orifice Couple and Neural Network Techniques. *Chin. J. Chem. Eng.* Vol.15,No. 2,pp. 281-285, ISSN: 1004-9541

Hawk, C. E. (1984). High temperature mass flowmeter. Us Patent :4475387

Hirst, C. D. (1956). Proportional water meter.Us Patent :2750797

Hodgson, J. L. (1932).Flow quantity meter.Us Patent :1870849

Huang, Z. Y.; Xie, D. L., Zhang, H. J. & Li, H. Q. (2005). Gas–oil two-phase flow measurement using an electrical capacitance tomography system and a Venturi meter. *Flow Meas. Instrum.* Vol.16,No.2 ,pp.177-182, ISSN: 0955-5986

Jung, S. H.; Kim, J. S.; Kim, J. B. & Kwon, T. Y. (2009). Flow-rate measurements of a dual-phase pipe flow by cross-correlation technique of transmitted radiation signals. *Applied Radiation and Isotopes* ,Vol.67,No.7, pp.1254-1258 , ISSN: 0969-8043

Kalotay, P. Z. (1994). In-flow Coriolis effect mass flowmeter. Us Patent :5347874

Kane, M. (1994). Hydrodynamic fluid divider for fluid measuring device. Us Patent :5297426

Kidder, H. H. (1934). Water meter for pipe line systems. Us Patent :1954386

Kriiger, G. J.; Birke, A. & Weiss, R. (1996). Nuclear magnetic resonance (NMR) two phase mass flow measurements. *Flow Meas. Instrum.*,Vol.7,No.1,pp. 25-37, ISSN: 0955-5986

Kronberger, H. (1952). Arrangement for measuring or indicating the flow of fluids. Us Patent :2586060

Laub, J. H. (1956). Thermal flowmeter. Us Patent :2729976

Lin, Z. H. (1982). Two-phase flow measurements with sharp-edged orifices. *Int. J. Multiphase Flow,* Vol.8, No.6, pp. 683-693, ISSN: 0301-9322

Lin Z. H., Wang S. Z. and Wang D.(2003). *Gas-liquid two-phase flow and boiling heat transfer,* Xi'an Jiaotong university Press, pp.63-187, ISBN:7-5605-1656-4,Xi'an,China.

Liou, K. T. (1995). Multiphase flow separation and measurement system. Us patent:5390547

Meng, Z. Z.; Huang, Z. Y.; Wang, B. L.; Ji, H. F.;Li, H. Q. & Yan, Y. (2010). Air_water two-phase flow measurement using a Venturi meter and an electrical resistance tomography sensor. *Flow Meas. Instrum.* Vol.21, No.3, pp.268-76, ISSN: 0955-5986

Meribout, M.; Nabeel, A. R. ;Ahmed, A. N.; Ali, A. B. ; Khamis, A. B. & Adel, M. (2010).Integration of impedance measurements with acoustic measurements for accurate two phase flow metering in case of high water-cut. *Flow Meas. Instrum,* Vol.21,No.1 ,pp.8-19, ISSN: 0955-5986

Munson, B. R.; Yang, D. F. & Okiishi,T. H.(2002). *Fundamentals of fluid Mechanics* (Fourth Edition), John Wiley & Sons Inc., pp.475-510, ISBN:0-471-44250-X, New york,USA

Murdock, J. W. (1962). Two-phase flow measurements with orifices . *J. Basic Eng.* Vol.84, No.4, pp. 419-33, ISSN: 0021-9223

Olin, J. G. (1984). Multirange flowmeter. Us Patent :4461173.

Oliveira, J. L. G.; Passos, J. C.; Verschaeren, R. & Geld, C. V. D. (2009). Mass flow rate measurements in gas-liquid flows by means of a venturi or orifice plate coupled to a void fraction sensor. *Experimental Thermal and Fluid Science*,Vol.33, No.2 pp. 253-60, ISSN: 0894-1777

Peranio, A, (1967). Shunt flow meter. Us Patent :3314290

Reis, E. D. & Jr, L. G. (2008). On the measurement of the mass flow rate of horizontal two-phase flows in the proximity of the transition lines which separates two different flow patterns. *Flow Meas. Instrum.*,Vol.19, No.5,pp.269-82, ISSN: 0955-5986

Rlkuta, S. (1969). Flow meter of the area type. Us Patent :3603148

Sato, K. (1983). Gas flow measuring appratus. Us Patent :4381668

Skea, A. F. & Hall, A. W. R. (1999). Effects of water in oil and oil in water on single-phase flowmeters. *Flow Meas. Instrum.* Vol.10, No.3, pp. 151-157, ISSN: 0955-5986

Stenberg, N. K. (1962). Rate of flow indicator. Us Patent :3066530

Steven, R. & Hall, A. (2009). Orifice plate meter wet gas flow performance. *Flow Meas. Instrum.*Vol.20, No.4, pp.141-51, ISSN: 0955-5986

Steven, R. N. (2002). Wet gas metering with a horizontally mounted Venturi meter. *Flow Meas. Instrum.* Vol.12, No.5, pp. 361-72, ISSN: 0955-5986

Sun, Z. Q. (2010). Mass flow measurement of gas–liquid bubble flow with the combined use of a Venturi tube and a vortex flowmeter. *Meas. Sci. Technol.* Vol.21, No.5, pp. 055403:1-7, ISSN:0957-0233

Taylor, J. R. (1982). *An introduction to error analysis The study of uncertainties in physical measurements*, University Science Books,pp.57, ISBN: 0-935702-10-5, California, USA

Thomson, J. (1895a). Proportional water meter.Us Patent :535639

Thomson, J. (1895b). Proportional water meter.Us Patent :535642

Thorn, R.; Johansen, G. A. &Hammer, E. A. (1997). Recent development in three-phase flow measurement. *Meas. Sci. Technol.,* Vol.8, No.7, pp.691-701, ISSN:0957-0233

Turkowski, M. (2004). Simple installation for measurement of two-phase gas-liquid flow by means of conventional single-phase flowmeters. *Flow Meas. Instrum.*,Vol.15, No.5,pp.295-99, ISSN: 0955-5986

Van, C. C. B. (1999). Bypass type Coriolis effect flowmeter. Us Patent :5861561

Wang, D. & Lin, Z. H. (2002). Gas-liquid Two-phase Flow Measurement Using ESM. *Experimental Thermal and Fluid Science* ,Vol.26,No.6 ,pp.827-32, ISSN: 0894-1777

Wang, D.; Liang, F. C.; Zhang, X. G. & Lin, Z. H. (2012). Multiphase flow measurements by full batch sampling. *Int. J. of Multiphase Flow*, Vol.40, No.4, pp.113-125, ISSN: 0301-9322

Wang, D.; Tan, J. P. & Lin, Y. (2011). High pressure steam water two-phase flow measurement by flow division and separation method. *Proceedings of the 7th international symposium on measurement techniques for multiphase flows,* Tianjin China, 9, 2011

Wang, W. R. & Tong, Y. X. (1995). A new method of two-phase flow measurement by orifice plate differential pressure noise. *Flow Meas. Instrum.* Vol.6,No.4, pp.265-270, ISSN: 0955-5986

Xu, L. J. ; Xu, J.; Dong, F. & Zhang, T. (2003). On fluctuation of the dynamic differential pressure signal of Venturi meter for wet gas metering. *Flow Meas. Instrum.* Vol.14,No.4, pp.211-7, ISSN: 0955-5986

Zhang, F. S.; Dong, F. & Tan, C. (2010). High GVF and low pressure gas_liquid two-phase flow measurement based on dual-cone flowmeter. *Flow Meas. Instrumen.* Vol.21, No.3, pp. 410-417, ISSN: 0955-5986

Zheng, G. B.; Jin, N. D.; Jia, X. H. ; Lv, P. J. & Liu, X. B. (2008). Gas-liquid two phase flow measurement method based on combination instrument of turbine flowmeter and conductance sensor. *Int. J. of Multiphase Flow*, Vol.34, No.11, pp.1031-1047, ISSN: 0301-9322

3

Measurement of Two-Phase Flow Structure in a Narrow Rectangular Channel

Daisuke Ito and Horst-Michael Prasser
ETH Zurich
Switzerland

1. Introduction

The flow channel of the fluids in the nuclear reactor core and the heat exchanger is relatively small. In order to understand the two-phase flow phenomena in the narrow channel, many interesting studies have been carried out, for example, mini capillaries (Wong, et al., 1995, Han & Shikazono, 2009), rectangular channels with small gap (Mishima, et al., 1993, Xu, et al., 1999, Hibiki & Mishima, 2001) and rod bundles with tight-lattice geometry (Tamai et al., 2006, Sadatomi et al., 2007, Kawahara et al., 2008). Especially, a triangle tight-lattice rod bundle has been adopted as a fuel rod configuration in high conversion boiling water reactor (Iwamura et al., 2006, Uchikawa et al., 2007, Fukaya et al., 2009). This has a narrow gap of about 1mm in the coolant channel. Therefore, two-phase flow in the tight-lattice bundle or narrow channel should be clarified for thermal-hydraulic analysis of high conversion reactor. In the past several years, the acquisition of experimental data and the modelling of the flow in tight-lattice rod bundle have been done. Tamai et al. (2006) evaluated the effect of the gap width and the power profile from the pressure drop measured in tight-lattice 37 rod bundles. Sadatomi et al. (2007) studied the void fraction characteristics in double subchannels with tight-lattice array and the data was compared with some correlations and subchannel codes. Furthermore, their group estimated the wall and the interfacial friction forces from the measured void fraction and pressure drop using the same subchannel (Kawahara et al., 2008). However, the advanced measurement techniques of the spatio-temporal phase distribution and velocity field are required for the high accurate analysis of the flow.

For the void fraction distribution measurement, the radiation methods have been developed to evaluate the flow in the bundle. Kureta (2007a, 2007b) developed a neutron radiography method for three-dimensional tomographic imaging of two-phase flow. The three-dimensional flow structures in the tight-lattice rod bundle were visualized. Although the spatial void fraction distribution can be obtained by the neutron imaging method, it is difficult to measure the time variation with high temporal resolution. In addition, there are some limitations of the uses. Thus, the authors focused on two-phase flow measurement using electrical conductance. Wire-mesh sensor (WMS), which uses the difference of electrical conductance between gas and liquid phases, has received attention as cross-sectional void fraction distribution measurement method (Prasser et al., 1998). To apply the WMS measurements to the flow in the rod bundle, a lot of electrode wires have to be installed over the small cross section and there are several intrusive effects to the flow (Ito et al., 2011a). Therefore, a novel void fraction measurement method with the electrodes on the wall of the flow channel was developed for two-phase flow in the narrow channel (Ito et al. 2010b). The wire electrodes were fixed on the opposing walls of the narrow channel and the conductance in the narrow gap was measured. As a result, three-dimensional void fraction distributions can be obtained. On the other hand, a liquid film sensor based on the electrical conductance measurements was developed (Damsohn & Prasser, 2009). This can estimate the liquid film thickness distribution on the wall in a flow channel. In addition, this sensor was applied to the annular flow measurement in the double subchannels of a square-lattice bundle. The liquid film behavior in the rod bundle was well visualized (Damsohn & Prasser, 2010). Thus, the novel measurement method for two-phase flow in the narrow channel has been developed by combining the void fraction detection and liquid film sensor (Ito et al., 2011c). The instantaneous distributions of the liquid film thickness on a wall and the void fraction in the gap were measured simultaneously by this method.

In this chapter, the measurement principle of the novel technique is described, and the measurements in a narrow rectangular channel with a gap width of 1.5mm are carried out by using two liquid film sensors. The liquid film thicknesses on two channel walls and the void fraction in the gap are estimated from the measured electrical conductance. In addition, the void fraction is recalculated by considering the film thickness and interfacial area concentration is obtained by reconstructing the gas-liquid interfacial structure. Furthermore, the individual bubble parameters are obtained by time-revolved reconstruction of the flow.

2. Measurement method

2.1 Principles

The liquid film sensors are installed on walls opposing each other. Fig.1 shows the schematics of simultaneous measurement of the liquid film thickness and void fraction in the narrow gap. When the gap is filled in water, the current exited by a transmitter electrode is acquired by nearby receiver electrodes on each liquid film sensor, as shown in Fig.1 (a). The small bubble comes near the electrodes as shown in Fig.1 (b), and then the conductance corresponding to the bubble size is measured by the receivers on both walls. Although the bubble larger than the measurement region prevents the current flowing to opposing electrode, the smaller electrical current is measured by exited sensor itself. This is caused by the existence of liquid film layer. Therefore, the presence of bubbles can be understood by the conductance between two sensors and the film thickness between bubble and the channel wall can be estimated by that on the sensor. Repeating these processes for all transmitter and receiver electrodes on two liquid film sensors, two dimensional distributions of liquid film thickness and void fraction are obtained.

2.2 Liquid film sensors

The liquid film thickness on the sensing surface is measured from the conductance between transmitter and receiver electrode lying next to each other. The simplified electrical scheme for film thickness measurement is shown in Fig.2. The transmitted pulse signal is sent to every transmitter electrode by switching the circuit of transmitting side at high speed. Then, the signal which is propagated into the liquid film covering the electrodes is detected by the

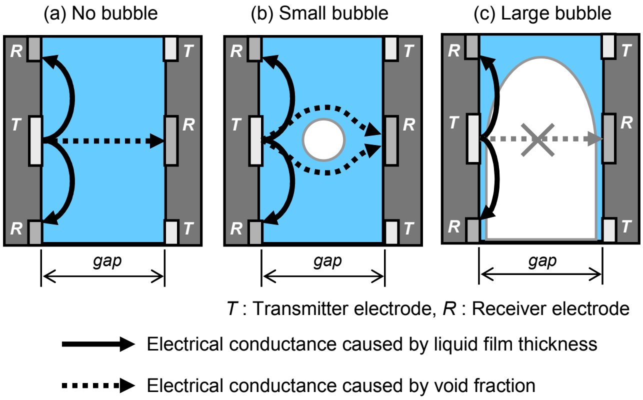

Fig. 1. Schematics of the simultaneous measurements of liquid film thickness and void fraction

receiver electrodes. Consequently, the conductance at each measurement point is obtained as two-dimensional distribution.

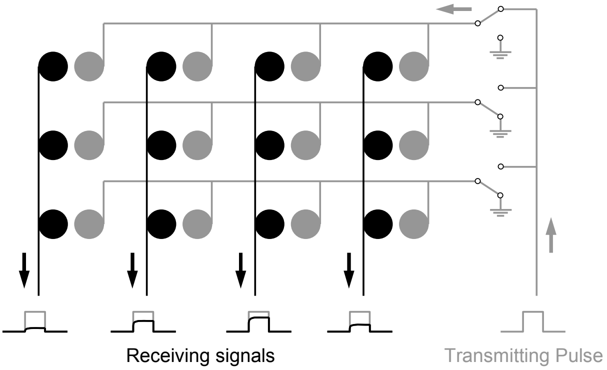

Fig. 2. Simplified electric circuit for liquid film thickness measurement (gray circle: transmitter electrodes, black circle: receiver electrodes, Damsohn & Prasser, 2009)

The electrode arrangement of the film sensor is illustrated in Fig.3. The sensor consists of transmitter, receiver and ground electrodes. The distance between measuring electrodes and ground spots is 1mm. Both transmitter and receiver electrodes have a diameter of 0.5mm and the ground spots have a diameter of 0.9mm. The total elementary cell of electrodes has the lateral dimensions of 2mm, which is equivalent to the spatial resolution of the measuring matrix, i.e. each measuring point corresponds to a surface area of 2×2mm^2.

2.3 Estimation of liquid film thickness and void fraction

In order to estimate the liquid film thickness from the measured electrical conductance, a calibration of the sensor is needed. The dependency of the conductance as function of film thickness is non-linear. Furthermore, the instrument constant can vary between individual

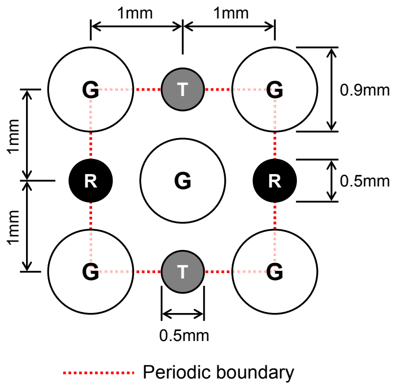

Fig. 3. Geometry of the electrodes of the liquid film sensor used in this study

measuring points due to manufacturing tolerances. In this study, nonconductive cylindrical rollers with the grooves ranging from 100 to 1000μm are applied. They are rolled over the sensor immersed in water. The final signal from the electronic unit is recoded when the roller passes above the electrodes. In this way, the sensor is calibrated together with the signal acquisition electronics. Dimensionless currents are calculated from the ratio of the value measured for a certain known film thickness and the saturation value. The latter is obtained from a measurement with a thickness of the water layer bigger than the sensibility range of the sensor, i.e. a thickness, at which the measured signal converges to the asymptotic one for an infinite water layer. The calibration results of two sensors used in this study are plotted in Fig.4 (a). The horizontal axis is the dimensionless current and the vertical one is film thickness. It is found that the two sensors have different characteristics, but the difference is a very little. In addition, the conductance is almost saturated above a thickness of 600μm. Hence, the applied film sensors can measure the thickness less than about 600μm.

A polynomial calibration function based on a fourth-order polynomial function is adapted to obtain the film thickness from the measured conductance. The denominator of the function is a second order polynomial serving to reflect the asymptotic behavior of the measuring signal. The coefficients of the function are fitted to match the calibration values. So the film thickness is estimated by the following equation.

$$\delta = \frac{a_1 x^4 + a_2 x^3 + a_3 x^2 + a_4 x + a_5}{(x - b_1)(x - b_2)} \tag{1}$$

where

$$x = \frac{\sigma_{film}}{\sigma_L} \tag{2}$$

σ_{film} is a measured conductance and σ_L is that at saturation condition of liquid phase. In the polynomial equation, b_1 and b_2 are the poles of the calibration function. The coefficients a_1 to a_5 are estimated individually for each measurement point in the two-dimensional sensor matrix. The results of the polynomial fit are also shown by the dashed lines in Fig.4(a).

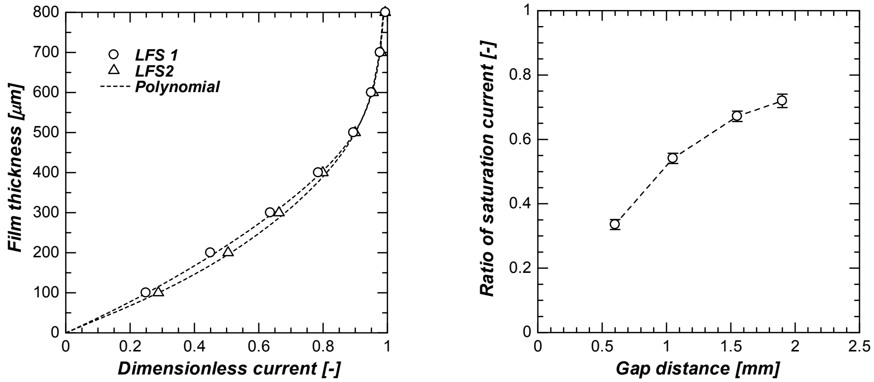

(a) Liquid film thickness estimation (b) Saturation current between two sensors

Fig. 4. Calibration results

In the measurement, the conductance at saturation condition is measured with another sensor because the sensors are fixed in the flow channel. Since the electrodes of the opposing sensor are connected to ground potential when the film conductance is detected, the saturation conductance is influenced by the distance between two sensors. In case of the narrow gap, the conductance with another sensor becomes much smaller than that without it. Therefore, the effect of the gap distance to the conductance is measured and plotted in Fig.4 (b). The horizontal axis is the distance between two sensors and the vertical axis is a ratio of the saturation conductance between with and without the opposing sensor. It is clear that the saturation conductance depends on the distance between the sensors and greatly decreases when the gap becomes narrower. In the gap of 1.5mm, the decreasing ratio of the conductance is about 67%. Thus, in the film thickness estimation, this ratio is multiplied to the saturation conductance σ_L in Eq. (2).

In the estimation of the void fraction, the linear approximation between the void fraction and the measured conductance is applied, and so the void fraction is calculated by the following equation.

$$\varepsilon = 1 - \frac{\sigma_{gap}}{\sigma_L} \tag{3}$$

where σ_{gap} is a measured conductance between two sensors and σ_L is a saturation conductance when the flow channel is completely filled by liquid phase (water). In previous studies with WMS and μWMS, they used also the same expression to estimate the void fraction, and they obtained accurate results.

3. Experimental setup

The scheme of the test channel is given in Fig.5. The rectangular narrow channel is constructed by flanging distance plates with the desired thickness between the opposing channel walls. The length of the test channel is 1,450mm and the width is constant over height. In this study, the gap s=1.5mm and the channel width w=32mm. The flow is a vertical upward air-water flow. Water is supplied from the lower part of the channel, and the flow rate is monitored by a rotameter. The temperature of the water is maintained at 20-22°C. Air is injected from an orifice with 1.0mm diameter in the front wall at a height of 170mm from the water inlet and a center point of channel width. The air flow rate is controlled by a mass flow controller. The air-water mixture passes through the test section and exits from the upper part of the channel. The measurement section is located at a height of 900mm from the air inlet.

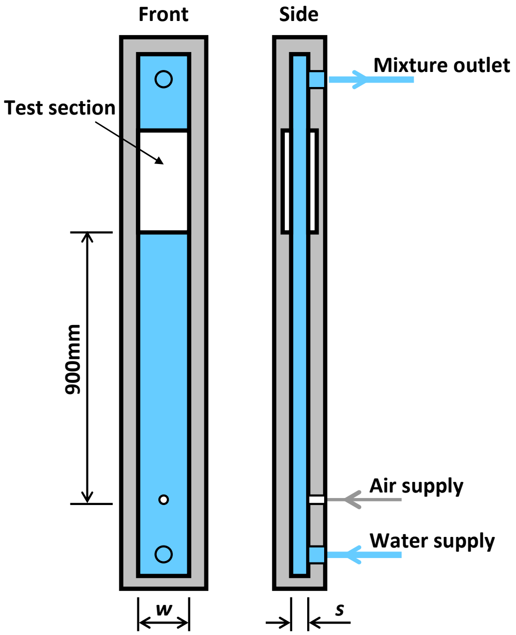

Fig. 5. Schematic diagram of the experimental flow channel

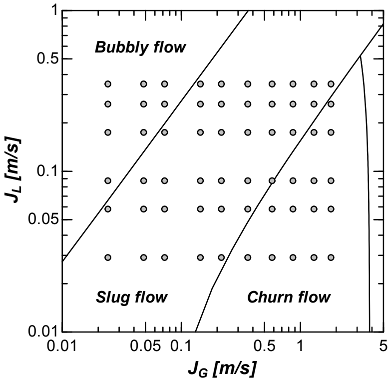

Fig. 6. Flow conditions and two-phase flow regime map for the narrow rectangular channel with a gap of 1.5mm (Hibiki & Mishima, 2001)

As mentioned above, a pair of film sensors is installed on both front and back walls of the channel. Both sensors together form a measuring matrix of 32 transmitters and 128 receivers with a total number of 4,096 measurement points. At this size of the sensor matrix, the applied wire-mesh sensor electronics unit allows to run the measurement at a speed of 5,000Hz. In the result, 2×16×64 (=2,048) points are available for the measurement of the liquid film thickness, and other 2×16×64 (=2,048) points are used for the void fraction measurement. The spatial resolution of both sensors is 2×2mm^2. Therefore, the instrumented area has the dimensions of 32×128mm^2.

The measurements are performed at 60 points with various superficial gas and liquid velocities. The flow conditions are plotted in flow regime map which has been developed for two-phase flow in narrow rectangular channels by Hibiki & Mishima (2001), as shown in Fig.6. The superficial gas velocity is varied from 0.024m/s to 1.8m/s and the superficial liquid velocity is changed from 0.029m/s to 0.35m/s. According to this map, bubbly, slug and churn flows can be created in the channel. Each measurement acquires data for 10 seconds.

4. Results and discussion

4.1 Liquid film thickness between bubbles and the channel wall

4.1.1 Measured instantaneous distributions

The instantaneous distributions of the measured film thickness and void fraction are shown in Fig.7, 8 and 9. The values of the film thickness and void fraction are represented by the colormap. Fig. 7 shows the result of the bubbly flow. The bubbles in the measurement area can be seen not only in the void fraction distribution but also in the liquid film thickness one. In the slug flow, the shape of a Taylor bubble is estimated as shown in Fig. 8. It is found that the liquid film thickness between the Taylor bubble and the wall is small. On the other hand, the gaseous structure becomes complex and the liquid film behaviors are significant in the churn flow in Fig. 9. The film thickness distribution on the gas phase can be visualized by the simultaneous measurement of the liquid film and void fraction.

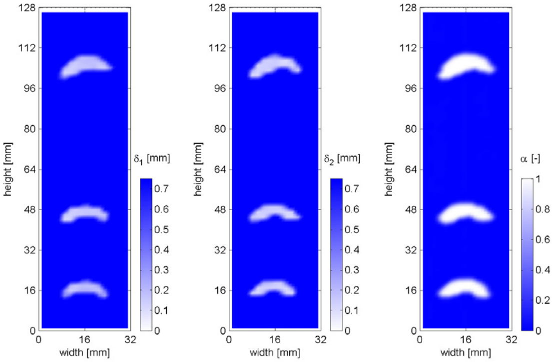

Fig. 7. Instantaneous distributions of liquid film thicknesses and void fraction measured in bubbly flow at J_L=0.35 m/s and J_G=0.024 m/s

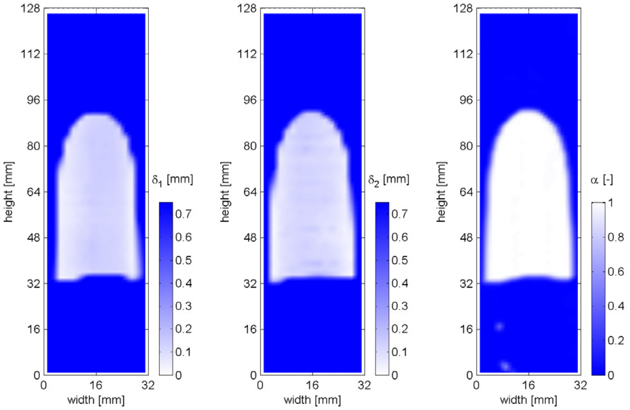

Fig. 8. Instantaneous distributions of liquid film thicknesses and void fraction measured in slug flow at J_L=0.17m/s and J_G=0.22m/s

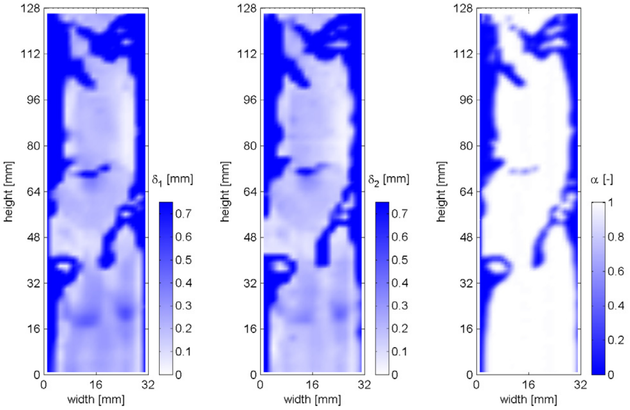

Fig. 9. Instantaneous distributions of liquid film thicknesses and void fraction measured in churn flow at J_L=0.058m/s and J_G=1.8m/s

When the bubble larger than the measurement volume comes between the electrodes opposing each other, the electrical conductance in the gap should be almost zero. So the measured void fraction is 100% at the point. However, the actual void fraction differs from the measured value because of the existence of the liquid film layer. For example, when the liquid film thicknesses are 150μm on the both walls and the local void fraction obtained from the conductance is 100% at a given point, the actual void fraction in the narrow gap is calculated as $(s\text{-}\delta_1\text{–}\delta_2)/s$ = (1,500-2×150)/1,500 = 80%. As a result, there is a large difference of 20%. This difference increases as the film thickness is larger. Thus, more accurate void fraction estimation can be available by considering the liquid film thickness. This is described in Section 4.2. In this study, the void fraction estimated from the electrical conductance is used as a measure of bubble existence.

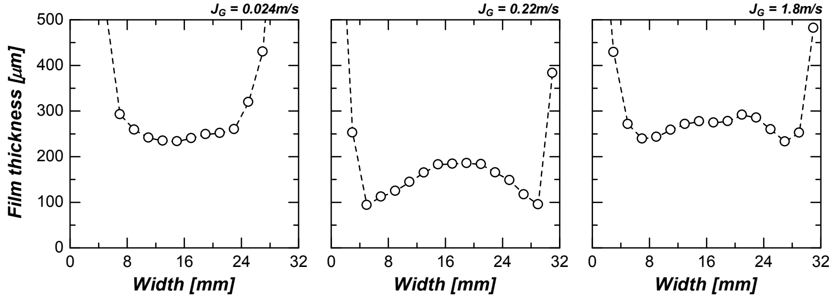

Fig. 10. Time averaged profiles of liquid film thickness between bubbles and wall at z=64mm at J_L=0.17m/s

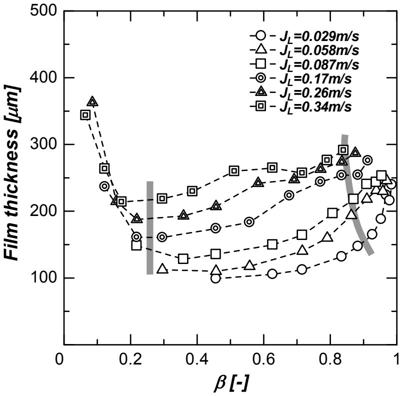

Fig. 11. Mean film thickness between bubbles and wall at different flow conditions (gray lines represent the flow transitions from bubbly to slug flow and from slug to churn flow)

4.1.2 Time-averaged film thickness

To understand the liquid film behavior between the bubble and the channel wall, the film thickness at a point with large void fraction is extracted, and the film thickness is averaged. In this process, the threshold of the void fraction is set to 50%. Fig.10 shows the time-averaged profiles of film thickness at a horizontal measurement line (z=64mm). These results are at the same superficial liquid velocity, and each profile is the results in the bubbly, slug and churn flow, respectively. In bubbly flow (J_G=0.024m/s), the bubbles flow in the middle of the channel width and the thickness profile is almost the flat. However, the Taylor bubbles in slug flow at J_G=0.22m/s have thick film in the center and thin film at the side. This is because the bubble entrains the liquid into this region. The film thickness in annular flow becomes large, but the profile is similar as the slug flow.

The spatio-temporal averaged film thickness for whole flow conditions is shown in Fig.11. The horizontal axis is the volumetric quality which means the ratio of gas flow to total flow rate. In addition, the gray heavy line represents the transition criteria from bubbly to slug flow and from slug to churn flow. These criteria are obtained from the Hibiki-Mishima map shown in Fig.6. In bubbly flow with low volumetric quality, the film thickness is large because there are many small bubbles, which are located a bit far from the sensor surface. In addition, the thickness decreases as superficial gas velocity increases. The film thickness grows gradually in the transition from slug to churn flow. Furthermore, the thickness increases with superficial liquid velocity in slug and churn flows.

4.2 Reconstruction of gas-liquid interfaces

Two phase flow in the narrow channel has thin film between the bubble and the channel wall, as described above. Therefore, the gaseous phase cannot be filled completely in the gap. Thus, the size of gaseous phase in the gap is estimated from the measured data of both liquid film thickness and void fraction to investigate the flow structure and to visualize the interfacial structure. Here, the bubble thickness Δ_b is the width of the gaseous phase in the gap direction. So the bubble thickness in the half gap is defined by the following equations.

$$\Delta_{b,1} = \begin{cases} \dfrac{s}{2} - \delta_1 & (\varepsilon > 50\%) \\ \dfrac{s}{2} \times \varepsilon & (\varepsilon \leq 50\%) \end{cases} \tag{4}$$

where δ and ε are the film thickness and void fraction measured at the same point, respectively. The void fraction value of 50% is used as a threshold to evaluate the film behavior between bubbles and the wall. When the void fraction is above the threshold, the bubble thickness is estimated by subtracting the film thickness from the gap width. On the other hand, the thickness is calculated from the void fraction value below the threshold. The bubble thickness of another wall side is also calculated in the same way. So the bubble thickness in the gap is obtained by adding each thickness, $\Delta_b = \Delta_{b,1} + \Delta_{b,2}$. As a result, the position of the gas-liquid interface can be determined in the test area and the interfacial structure is reconstructed.

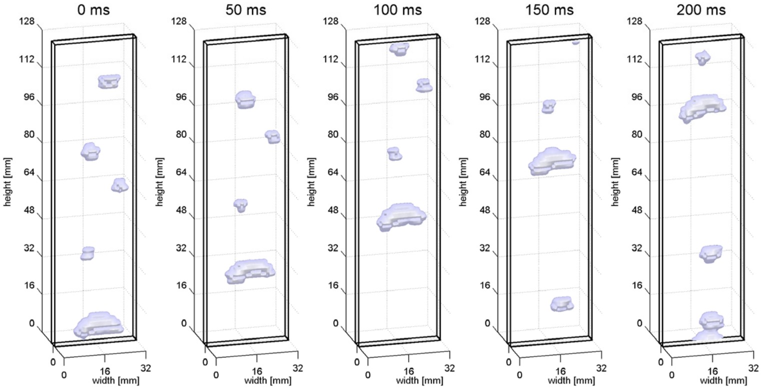

Fig. 12. Spatial reconstructed images of gas-liquid interfaces at J_L=0.35m/s and J_G=0.024m/s

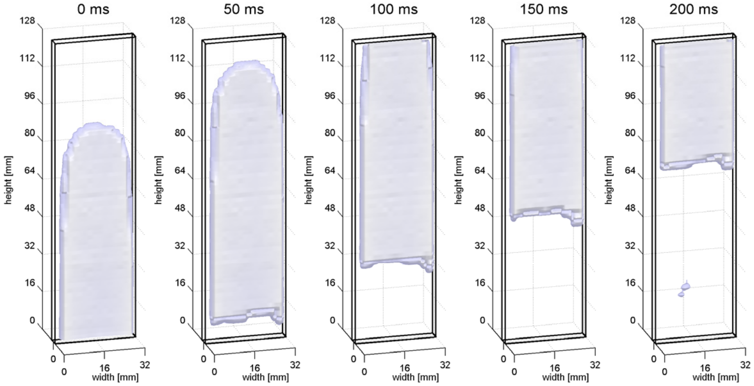

Fig. 13. Spatial reconstructed images of gas-liquid interfaces at J_L=0.17m/s and J_G=0.22m/s

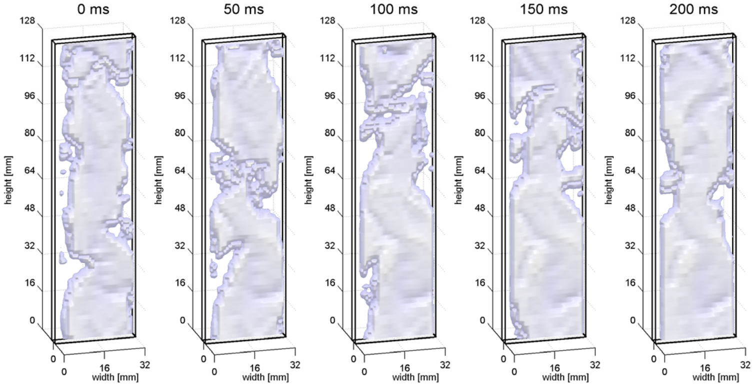

Fig. 14. Spatial reconstructed images of gas-liquid interfaces at J_L=0.058m/s and J_G=1.8m/s

The typical images of the spatial reconstruction of the bubbly, slug and churn flows are shown in Fig.12-14, respectively. In the bubbly flow, the three-dimensional bubble shape and its variation can be found as shown in Fig. 12. The images of Taylor bubble are shown in Fig. 13. The frontal and rear shapes of the bubbles can be seen. In addition, it is shown that the gaseous phase and the liquid film behaviors are observed in the churn flow in Fig.14. From these results, three-dimensional structures of the flow can be visualized by reconstructing the interfaces.

4.3 Void fraction and interfacial area concentration

In gas-liquid two-phase flow, the void fraction and interfacial area concentration is important to represent the flow characteristics. Thus, these parameters are estimate from the measured data. As stated above, the void fraction measured from the electrical conductance doesn't involve the effect of film thickness behavior. Therefore, the void fraction in the gap is recalculated from the bubble thickness as

$$\alpha = \frac{\Delta_{b,1} + \Delta_{b,2}}{s} = \frac{\Delta_b}{s} \tag{5}$$

where *s* is the gap width.

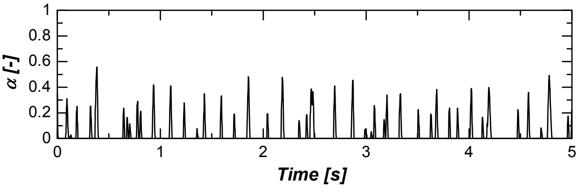

(a) Bubbly flow at J_L=0.35m/s and J_G=0.024m/s

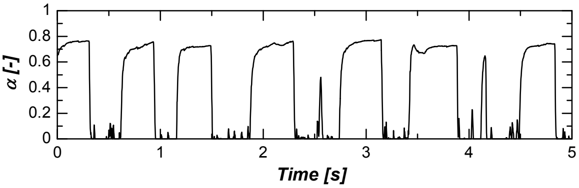

(b) Slug flow at J_L=0.17m/s and J_G=0.22m/s

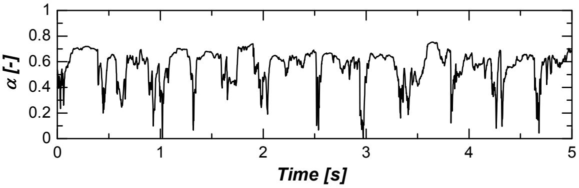

(c) Churn flow at J_L=0.058m/s and J_G=1.8m/s

Fig. 15. Time-series profiles of the cross-sectional averaged void fraction for bubbly, slug and churn flows

The time-series profiles of the cross-sectional averaged void fraction are shown in Fig. 15. The void fraction has a peak when the bubble passes through the test section, as shown in Fig. 15 (a). In the result of slug flow, the length and passing frequency of bubbles can be found. The void fraction doesn't reach 100% in even churn flow because the liquid film thickness is large. However, the large variation of the void fraction is detected in churn flow.

Fig.16 represents the void fraction data plotted against the volumetric quality for different superficial liquid velocity. The solid and dashed straight lines represent the homogeneous model ($\alpha = \beta$) and Ali et al.'s correlation (Ali et al., 1993), respectively. The latter is expressed as follows,

$$\alpha = 0.8\beta \tag{6}$$

This correlation was proposed for the narrow rectangular channels with gaps of 0.778 and 1.465mm. In addition, the dashed curve in Fig.16 is Kawahara et al.'s correlation (Kawahara et al., 2002) for circular micro channel with 100μm in diameter, as expressed in Eq.(7).

$$\alpha = \frac{0.03\beta^{0.5}}{1-0.97\beta^{0.5}} \tag{7}$$

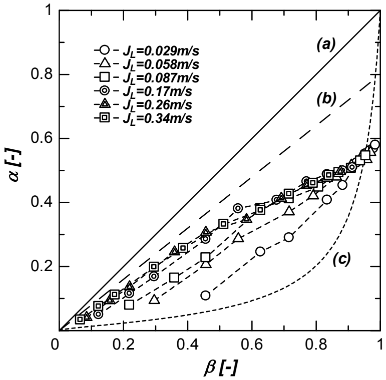

Fig. 16. Void fraction and the comparison previous correlations; (a) homogeneous model, (b) Ali et al., (c) Kawahara et al.

In the comparison with Ali et al.'s correlation, the void fraction data is underestimated. this The correlation was proposed from the void fraction measured from the electrical conductance between two walls. Therefore, the liquid film thickness between the bubbles and the wall is not considered in the correlation. Thus, the difference of the void fractions becomes larger when the liquid film behaviours dominate the flow structure. On the other hand, Kawahara et al.'s correlation which shows good agreement in the void fraction data in the micro channels doesn't agree with the current data. However, the data gets close to Kawahara et al.'s correlation by decreasing superficial liquid velocity. Due to slower liquid phase velocity, the interval between the gas bubbles increases. So the void fraction decreases at lower superficial liquid velocity.

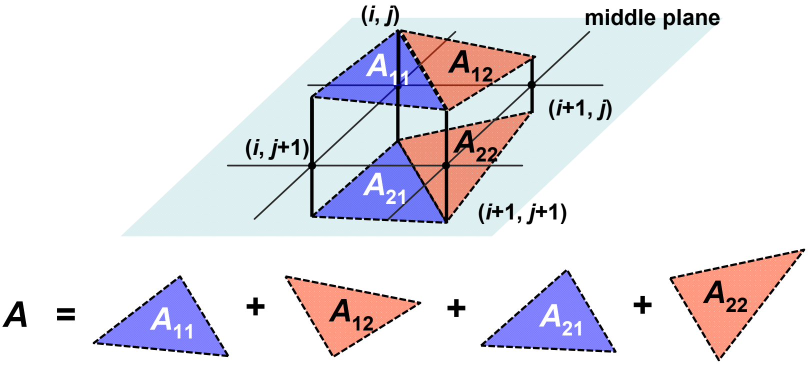

Fig. 17. Estimation of interfacial area from bubble width

The estimating method of the interfacial area is illustrated in Fig.17. The area is calculated by Heron's formula which estimates the area from the length of three sides of a triangle. In this estimation, four triangles are produced from four bubble thicknesses on each wall side, and the interfacial area formed by four measurement points is estimated as a sum of the area of their triangles. Then, the interfacial area concentration is calculated as

$$a_i = \frac{A}{s\Delta x\Delta z} \tag{8}$$

where A is the area obtained in Fig.17, and Δx and Δz are the lateral and axial spacings between two measuring points, respectively.

The estimated results of the interfacial area concentration for each flow condition are shown in Fig.18. it is obvious that the interfacial area concentration increases as the volumetric quality increases. With increasing superficial liquid velocity, the interfacial area concentration becomes larger. This is because the film behavior is large and the interface increases at higher superficial liquid velocity.

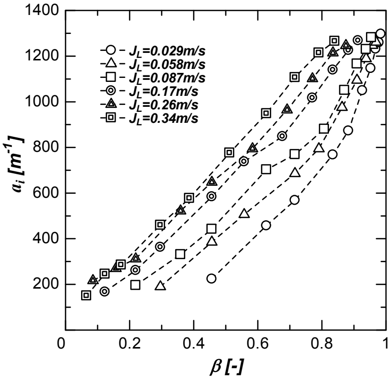

Fig. 18. Interfacial area concentration

4.4 Time-resolved bubble parameters

4.4.1 Time-resolved images

The spatial resolution is 2mm square for the spatial reconstructed results shown in Fig.19(a). As a result, the outline of the bubble is a little bit coarse, as shown in Fig.19(a). Here, the time-resolved reconstruction of the flow is conducted by using the high temporal resolution of the present method. The data in a horizontal measurement line at a given axial position is reconstructed in the time direction. The bubble in Fig.19(b) is obtained by time-resolved reconstruction at the position z=64mm in Fig.19(a). In this reconstruction, the axial resolution of bubble interface is improved, especially, bubble nose and tail.

The typical results of time-resolved reconstruction are shown in Fig.20. The data in the measurement line at z=64mm is reconstructed and the void fraction estimated by Eq. (5) is plotted by a colormap. These results show the flow transitions with the growth of superficial gas velocity at J_L =0.056 m/s and J_L =0.26m/s. The time-series two-phase flow structure is visible by this way. There are a lot of bubbles in bubbly flow (J_G =0.024m/s,

J_L =0.26m/s) and the detailed shape of Taylor bubble is estimated. In the spatial reconstruction, only the bubble less than the test area can be represented the whole bubble shape. However, even long Taylor bubbles are reconstructed in the time-series. In churn flow, the time variations of the gaseous structure and film behavior are found at J_G =1.8m/s.

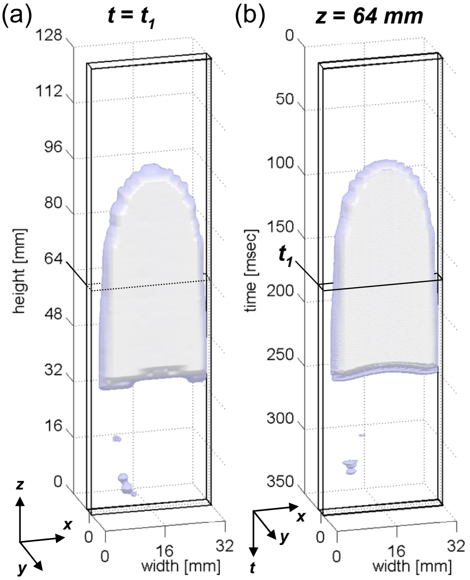

Fig. 19. Spatial and time-resolved reconstruction of Taylor bubble

To estimate the bubble size from the time-resolved data, the interfacial velocity is needed. Because the axial time axis has to be converted to spatial axis. If the interfacial velocity is assumed to be equal to the velocity of bubble, the individual bubble velocity can be used to estimate the bubble volume.

4.4.2 Bubble velocity

The cross-correlation method is applied to estimate the bubble velocity from the data. The schematics of the velocity estimation are shown in Fig. 21. For this estimation, the time-resolved void fraction data of two measurement line at different axial positions is used. In the void fraction distributions, the bubbles and liquid phase are separated by using a threshold of void fraction, and the bubbles are identified Therefore, the bubble travelling time τ between two lines is estimated by cross-correlating the void fraction data, and the bubble velocity is calculated by the following equation.

$$u_b = \frac{d}{\tau} \tag{9}$$

where d is a distance between two measurement lines.

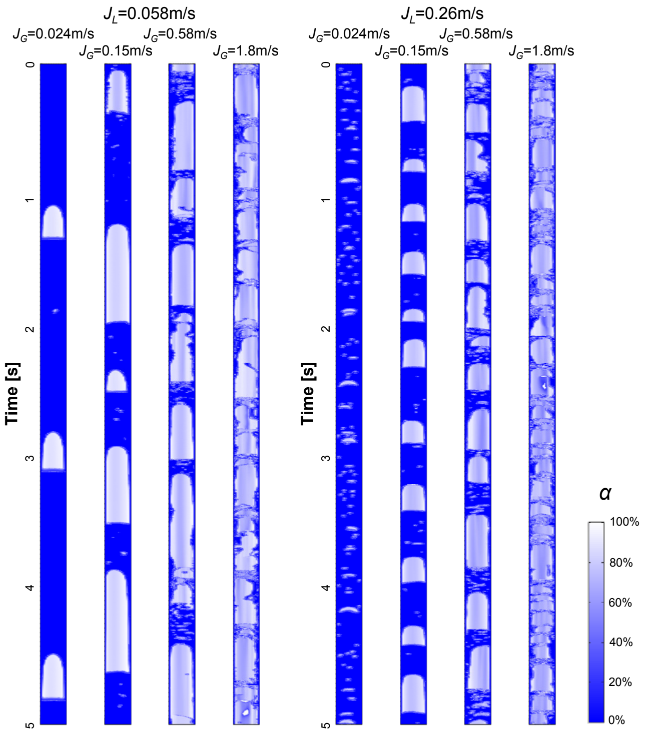

Fig. 20. Time-resolved images of the void fraction at z=64mm

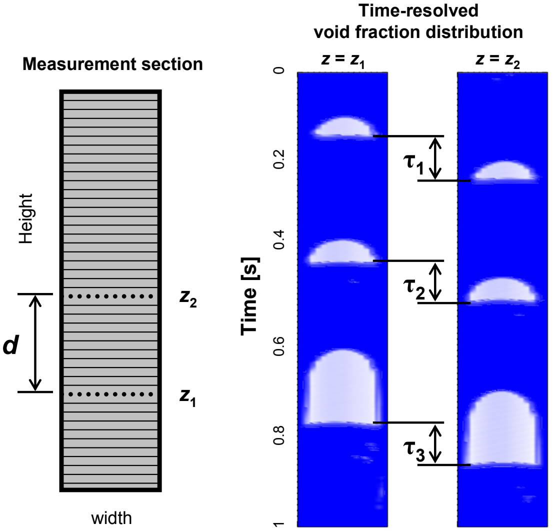

Fig. 21. Estimating method for individual bubble velocity with cross-correlation method

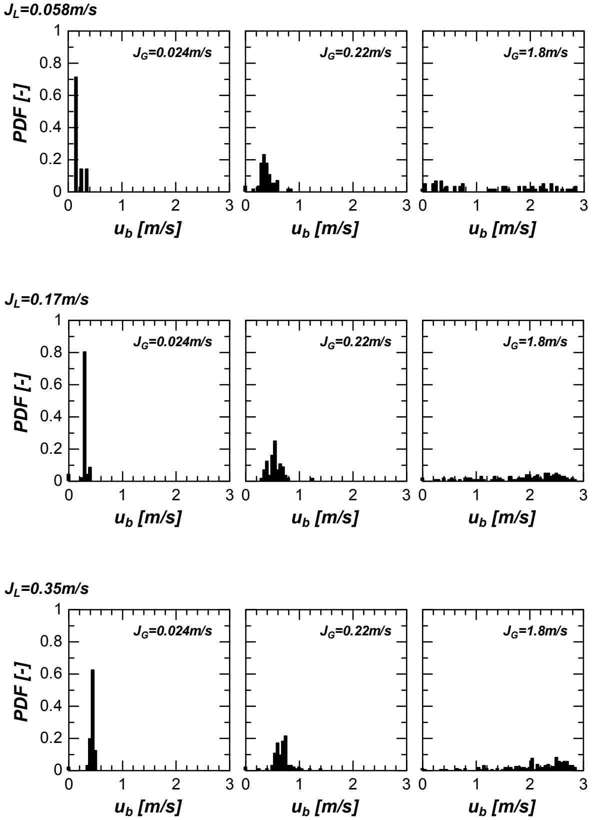

Fig. 22. Bubble velocity distributions for different flow conditions

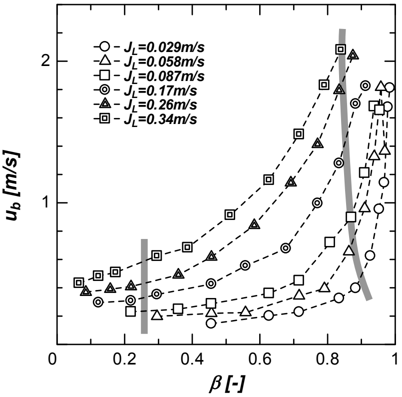

Fig. 23. Mean bubble velocity (gray lines represent the flow transitions from bubbly to slug flow and from slug to churn flow)

The probability density function (PDF) of the estimated bubble velocity at different flow conditions is shown in Fig.22. These results are broadly-divided into bubbly (left), slug (middle) and churn (right) flows. The profile has the pointed peak at low superficial gas velocity. When the superficial gas velocity increases, the peak moves to high velocity side and becomes smooth. In annular flow at J_G =1.8m/s, the profiles are almost flat and there are many bubbles with higher velocity than 1.0m/s. It is also found that the bubble velocity increases as superficial liquid velocity increases in bubbly and slug flow. The mean bubble velocity is plotted against the volumetric quality in Fig.23. The bubble velocity at each flow regime depends on the superficial liquid velocity. At low superficial liquid velocity, the growth of the velocity with the volumetric quality is not so large in slug flow. In contrast, the bubble velocity at higher superficial liquid velocity increases greatly. The velocity in churn flow increases rapidly with the volumetric quality.

4.4.3 Bubble size

The bubble size of individual bubbles is estimated from time-resolved void fraction data and bubble velocity calculated above. The volume of bubble is calculated by integrating the local void fraction belonging to the bubble, as follows.

$$V_b = s\Delta x\Delta t \cdot u_b \sum \alpha \tag{10}$$

where Δx is the lateral spacing between the electrodes and Δt is the time interval between two frames. The corresponding equivalent diameter is calculated using the volume as

$$D_{eq} = \sqrt[3]{\frac{6V_b}{\pi}} \tag{11}$$

As a result, the bubble diameter for individual bubbles passing through the measurement line is obtained.

The bubble size distributions are presented in Fig.24. These distributions are at the same flow conditions as the bubble velocity distributions in Fig.22. In the spatial reconstruction of the bubble, the bubble size less than the measurement area can be estimated due to the limitation of the area, i.e. $D_{eq,max}$=22.7mm for 128×32×1.5mm^3. However, the size of larger bubble is obtained by the time-resolved reconstruction, as shown in Fig.24. In the results, the bubble size increases with the increase of superficial gas velocity because of the flow transition to slug and churn flow. Furthermore, the size decreases with the growth of superficial liquid velocity in bubbly and slug flows. The bubble diameter is averaged and the mean diameter for each flow condition is shown in Fig.25. The averaged bubble size increases as the volumetric quality increases in bubbly flow. In slug flow, there is a large difference of bubble size, since the number of bubbles is less during the measurement at low superficial liquid velocity. Although more than 100 bubble are measured at high superficial liquid velocity condition for 10 seconds, the sampled bubbles are only 6 at J_L =0.029 and J_G =0.024m/s. Churn flow has not only huge bubbles but also many small bubbles between large gas bubbles, and so the averaged value of the bubble size is not so large.

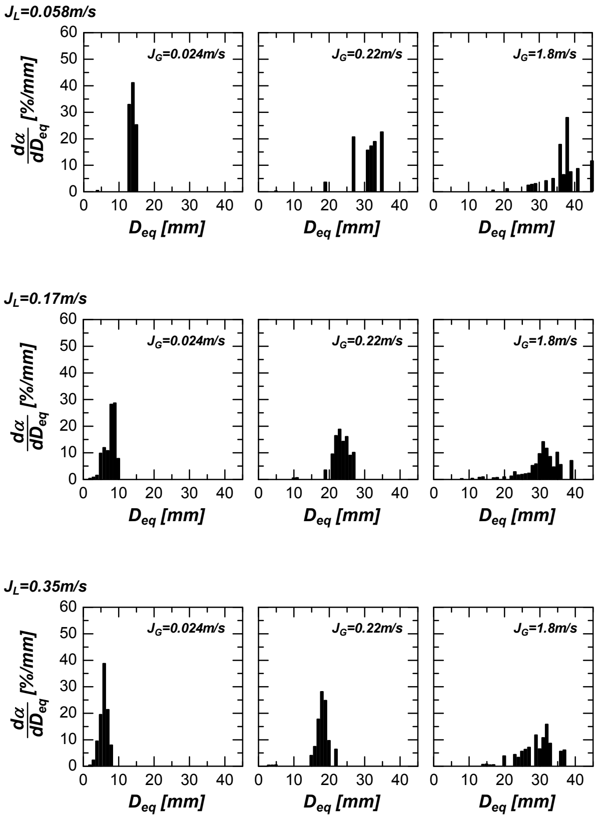

Fig. 24. Bubble size distributions for different flow conditions

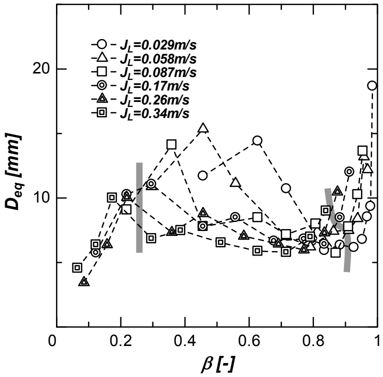

Fig. 25. Mean bubble size (gray lines represent the flow transitions from bubbly to slug flow and from slug to churn flow)

5. Conclusion

A novel measurement method for two-phase flow structure in narrow channel was described and an upwards air-water flow in a narrow gap was studied by the help of liquid film sensors. The liquid film thickness distributions between bubbles and the wall were determined on a two-dimensional domain and with high temporal resolution. The arrangement of sensors on both front and back walls of the test channel allowed measuring film thickness and void fraction simultaneously. Bubbly, slug and churn flows in a narrow rectangular channel with a gap of 1.5mm were measured and the characteristics of film behavior were investigated by averaging the thickness. The gas-liquid interfacial structure was reconstructed spatially by estimating the thickness of gaseous phase at each measurement point. Since the void fraction measured from the electrical conductance cannot be affected by the film behavior, the void fraction was recalculated from the spatial reconstructed data. In addition, the interfacial area concentration was also estimated from it. Finally, the time-resolved reconstruction was carried out in order to evaluate the bubble parameters (velocity and size), and the probability density function and time averaged quantities were estimated.

This technique can be applied to various flow channels such as the rod bundle geometries and micro capillaries. The measuring methods presented here offer the possibility to obtain data for the clarification of the multidimensional flow structure in a narrow channel. Furthermore, these data is also available for the validation of the CFD codes.

6. References

Ali, M.I., Sadatomi, M. & Kawaji, M. (1993). Adiabatic two-phase flow in narrow channels between two flat plates, *The Canadian Journal of Chemical Engineering*, Vol. 71, pp.657-666, ISSN: 0008-4034

Damsohn, M. & Prasser, H.-M. (2009). High-speed liquid film sensor for two-phase flows with high spatial resolution based on electrical conductance, *Flow Measurement and Instrumentation*, Vol.20, pp. 1-14, ISSN: 0955-5986

Damsohn, M. & Prasser, H.-M. (2010). Experimental studies of the effect of functional spacers to annular flow in subchannels of a BWR fuel element, *Nuclear Engineering and Design*, Vol.240, No.10, pp. 3126-3144, ISSN: 0029-5493

Fukaya, Y., Nakano, Y. & Okubo, T. (2009). Study on high conversion type core of innovative water reactor for flexible fuel cycle (FLWR) for minor actinide (MA) recycling, *Annals of Nuclear Energy*, Vol. 36, pp.1374-1381, ISSN: 0306-4549

Han, Y. & Shilazono, N. (2009). Measurement of liquid film thickness in micro square channel, *International Journal of Multiphase Flow*, Vol.35, pp.896-903, ISSN: 0301-9322

Hibiki, T. & Mishima, K., (2001). Flow regime transition criteria for upward two-phase flow in vertical narrow rectangular channels, *Nuclear Engineering and Design*, Vol.203, pp.117-131, ISSN: 0029-5493

Ito, D., Prasser, H.-M., Kikura, H. & Aritomi, M. (2011). Uncertainty and intrusiveness of three-layer wire-mesh sensor, *Flow Measurement and Instrumentation*, Vol. 22, pp. 249-256, ISSN: 0955-5986

Ito, D., Kikura, H. & Aritomi, M. (2011). Micro-wire-mesh sensor for two-phase flow measurement in a narrow rectangular channel, *Flow Measurement and Instrumentation*, Vol.22, pp.377-382, ISSN: 0955-5986

Ito, D., Damsohn, M., Prasser, H.-M. & Aritomi, M. (2011). Dynamic film thickness between bubbles and wall in a narrow channel, *Experiments in Fluids*, Vol. 51, No.3, pp. 821-833, ISSN: 1432-1114

Iwamura, T., Uchikawa, S., Okubo, T., Kugo, T., Akie, H., Nakano, Y.& Nakatsuka T. (2006). Concept of innovative water reactor for flexible fuel cycle (FLWR), *Nuclear Engineering and Design*, Vol.236, pp.1599-1605, ISSN: 0029-5493

Kawahara, A., Chung, P.M.-Y. & Kawaji, M. (2002). Investigation of two-phase flow pattern, void fraction and pressure drop in a microchannel, *International Journal of Multiphase Flow,* Vol. 28, pp.1411–1435, ISSN: 0301-9322

Kawahara, A., Sadatomi, M. & Shirai, H. (2008). Two-Phase Wall and Interfacial Friction Forces in Triangle Tight Lattice Rod Bundle Subchannel, *Journal of Power and Energy Systems*, Vol.2, No.1, pp.283-294, ISSN: 1881-3062

Kureta, M. (2007). Development of a Neutron Radiography Three-Dimensional Computed Tomography System for Void Fraction Measurement of Boiling Flow in Tight Lattice Rod Bundles, *Journal of Power and Energy Systems*, Vol.1, No.3, pp.211-214, ISSN: 1881-3062

Kureta, M. (2007). Experimental Study of Three-Dimensional Void Fraction Distribution in Heated Tight-Lattice Rod Bundles Using Three-Dimensional Neutron Tomography, *Journal of Power and Energy Systems*, Vol.1, No.3, pp.225-238, ISSN: 1881-3062

Mishima, K, Hibiki, T & Nishihara, H. (1993). Some characteristics of gas-liquid flow in narrow rectangular duct, *International Journal of Multiphase Flow*, Vol.19, No.1, pp.115-124, ISSN: 0301-9322

Prasser, H.-M., Böttger, A. & Zschau, J. (1998). A new electrode-mesh tomograph for gas–liquid flows, *Flow Measurement and Instrumentation*, Vol.9, pp. 111-119, ISSN: 0955-5986

Sadatomi, M., Kawahara, A., Kudo, H. & Shirai, H. (2007). Effects of Surface Tension on Void Fraction in a Multiple-Channel Simplifying Triangle Tight Lattice Rod Bundle-Measurement and Analysis, *Journal of Power and Energy Systems*, Vol.1, No.2, pp.143-153, ISSN: 1881-3062

Tamai, H., Kureta, M., Ohnuki, A., Sato, T. & Akimoto, A. (2006). Pressure Drop Experiments using Tight-Lattice 37-Rod Bundles, *Journal of Nuclear Science and Technology*, Vol.43, No.6, pp.699-706, ISSN: 0022-3131

Uchikawa, S., Okubo, T., Kugo, T., Akie, H., Takeda, R., Nakano, Y., Ohnuki, A. & Imamura, T. (2007). Conceptual Design of Innovative Water Reactor for Flexible Fuel Cycle (FLWR) and its Recycle Characteristics, *Journal of Nuclear Science and Technology.*, Vol.44, No.3, pp.277-284, ISSN: 0022-3131

Wong, H., Radke, C.J. & Morris, S. (1995). The motion of lung bubble in polygonal capillaries. Part 1. Thin films, *Journal of Fluid Mechanics*, Vol.292, pp.71-94, ISSN: 0022-1120

Xu, J.L., Cheng, P. & Zhao, T.S. (1999). Gas-liquid two-phase low regimes in rectangular channels with mini/micro gap, *International Journal of Multiphase Flow*, Vol. 25, pp.411-432, ISSN: 0301-9322

4

Development of Capacitance Void Fraction Measurement Method for BWR Test

Hironori Watanabe[1], Hidesada Tamai[1],
Takashi Satoh[1], Mitsuhiko Shibata[1] and Toru Mitsutake[2]
[1]Japan Atomic Energy Agency, Tokai-mura, Ibarakiken
[2]Tosiba, Isogoku Yokohama-shi Kanagawaken
Japan

1. Introduction

In the study of two phase flow, void fraction (volume ratio of gas phase to total volume) in the flow channel is important physical value, so many measurements technique have been applied.

In the study of the atomic energy, X-ray, or γ-ray technique have been adopted for measure void fraction under high temperature and high pressure condition.

But in these techniques, real time measurement is difficult and measurement system is complex, therefore practical method have been expected.

In the measurement of the void fraction for BWR thermo- hydraulic test, following measurement under high pressure and high temperature conditions is necessary.

1. Measurement is available for even though pure water
2. Measurement is available
3. Measurement is available for all void fraction regions
4. Measurement is available in real time

Authors have developed capacitance measurement method (C method) that is electric void fraction measurement method to solve above theme.

Applying C method to BWR thermo-hydraulic test and Modified Light Water Reactor develop test had been performed at JAEA.

In former part of this article, we showed clarified measurement characteristic by C method to atmospheric condition, measurement effectiveness in pure water and measurement region can be expanded.

In latter part, we showed adopted electrode•signal cable for high pressure condition and attained measurement of void fraction on the condition of BWR.

To confirm propriety of C method, we compared measured datum by C method with datum by quick shut method, consequently characteristic function can apply to high pressure conditions.

Symbol

$A_{X\text{-}s}$:Projeited Area of Flow Channel [m^2]
C :Capacitance[F]
C^* :Rasio of Capacitance[−]
$C(\alpha)$:Capacitance at Void Fractionα[F]
d :Inner Diameter of Pipe[m]:
I :Current[A]
j_g :Volume Flux of Gas Phase[m/s]
j_l :Volume Flux of Liquid Phase[m/s]
R :Resistance[Ω]
t :Time[s]
z :Coodinates in the Flow [m]
α :Void Fraction[−]
ρ :Density[kg/m^3]
BWR :Boiling Water Reactor
FBR :Fast Breeder Reactor
SG :Steam Genarator
QSV :Quick Shut Valve

Attached letter

$a=0, \ell$:Liquid Phase 100%
$a=100, g$:Gas Phase 100%

2. C method of void fraction measurement (atmospheric condition)

2.1 Principle of measurement by C method

At first we measured resistance of two phase flow in the flow channel and confirmed that resistance has the relation of definite hyperbolic function (R method) to void fraction both in the atmospheric condition and high temperature and high pressure condition (7MPa). (1)(2)

But there had been the theme that resistance measurement method (R method) do not fit for discontinuity of liquid phase because conductive pass is cut off at high void fraction region(more than 70%).

To solve disadvantage in R method, we developed C method, in C method high frequency AC power charged a pair of electrode.

In C method, it was experimentally confirmed that characteristic curve concluded to definite hyperbolic function, provided capacitance component in the two phase flow is separately measured making use of that phase is different between capacitance and resistance(3) (4). C method has the advantage in measurement sensitivity compared R method as frequency of AC power changes to higher response current increase.

2.2 Test facility for void fraction measurement characteristics test

4x4 rod bundle simulating BWR fuel rod arrangement is installed in the Rectangular test section.

Fig.1 shows characteristic test facility for 4x4 rod bundle. Air-Bubble was introduced from lower nozzle through porous plate to gain uniform small bubble.

Void fraction was regulated by needle valve for inlet air. Void fraction was measured from the water volume in the test section between quick shut valves. Electrode is to measure impedance of two phase flow between a pair of electrode, we adopted different shape for most suitable shape for flow channel (faced plate, plate and rod, rod and rod).

In the test to charge high frequency AC to electrode installed inner wall of the test section, we adopted high frequency type impedance meter (LCR meter) and measured capacitance in the two phase flow.

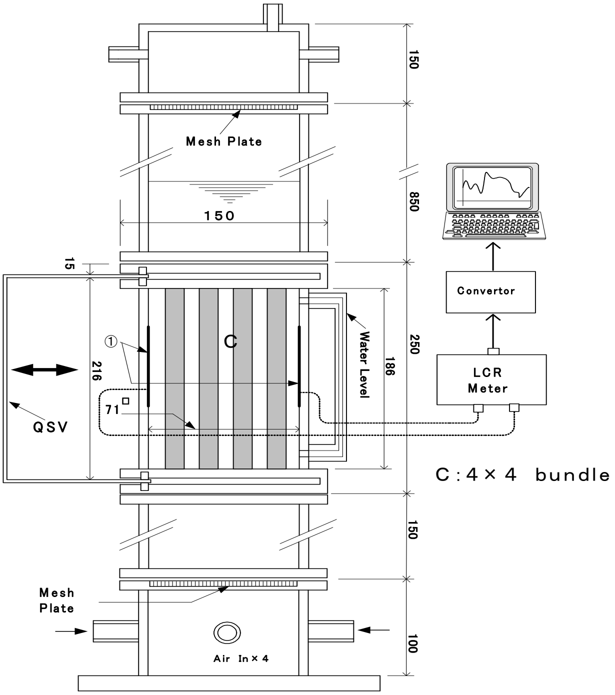

Fig. 1. Void fraction test facility with 4x4 bundle

2.3 Frequency response characteristic of test section

Fig.2 shows the frequency response characteristic of the test section by C method. In C method measurement sensitivity improved as the response current increase proportionally to 1/ (ωC).

On the other hand, more than definite frequency wide band, measured result (capacitance) becomes unstable due to resonance of AC current so 1MHz band was selected. Moreover multiple frequency of supplied AC (50Hz in this district) was avoided to prevent phasing interaction. So 1.01MHz was adopted as measurement frequency, consequently performed stable measurement.

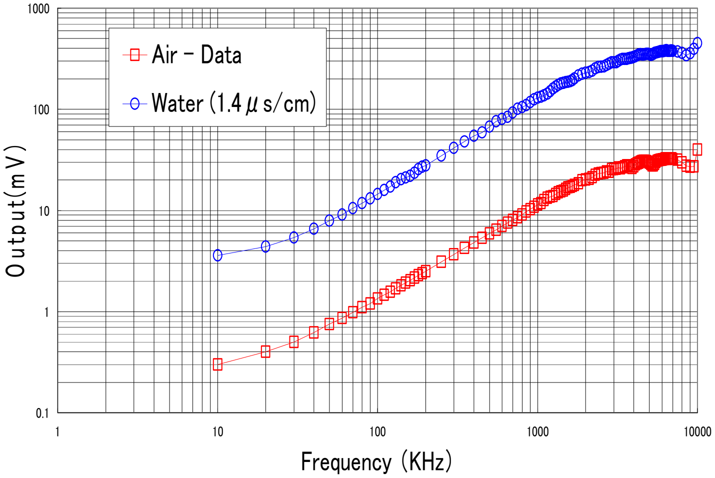

Fig. 2. Frequency characteristics

2.4 Void fraction measurement characteristic test result

Fig. 3 shows measurement result of C and R in the two phase flow with measurement characteristic function (hyperbolic curve).

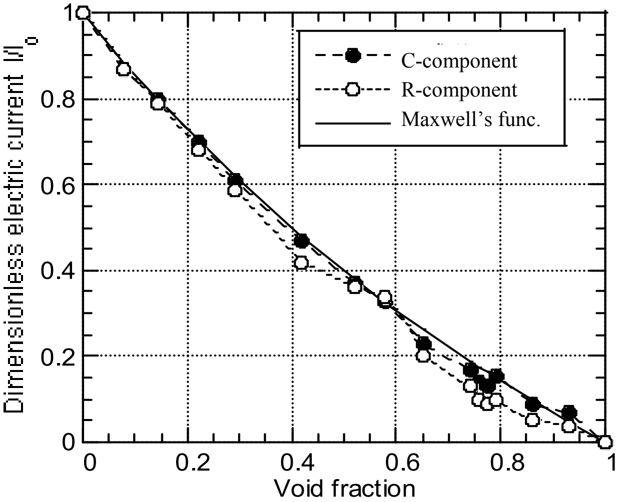

Fig. 3. Void fraction measurement of 4x4bundle (Atmospheric pressure)

This function introduced by Maxwell is expressed with solid curve, and both results agreed to this curve, especially, C measurement result agreed to over all regions, so Maxwell's function was adopted for measurement characteristic function trough tests.

Maxwell's formula(5) is shown in (1).

Formula (1) indicates that relation between current ratio of I (two phase flow) to Io (liquid phase flow) and void fraction is definite hyperbolic function while charging voltage kept constant.

Void fraction can obtain from formula (2) for R measurement and formula (3), (4) for C measurement respectively. Formula (2), (3) are transformed from (1).

$$\frac{I}{I_{\alpha=0}} = \frac{1-\alpha}{1+0.5\alpha} \text{ (Maxwell's formula)} \tag{1}$$

$$\alpha = \frac{R - R_{\alpha=0}}{R + 0.5R_{\alpha=0}} \text{ (R method)} \tag{2}$$

$$\alpha = \frac{1 - C^*}{1 + 0.5C^*} \text{ (C method)} \tag{3}$$

$$C^* = \frac{C(\alpha)\text{-}C_{100}}{C_{\alpha=0} - C_{\alpha=100}} \tag{4}$$

3. Void fraction measurement test under high temperature and high pressure condition (7MPa)

With C method we performed void fraction measurement under high temperature and high pressure condition(6) (7) (8) by using measurement characteristic function showed at formula (3), (4) applying advanced BWR thermo-hydraulic test facility.

3.1 Advanced BWR thermo-hydraulic test facility

Advanced BWR (Tight-lattice Reduced Moderation Water Reactors) thermo-hydraulic test facility contains 37 e rods bundle in flow shroud made of ceramic. (9)A pair of opposite circular electrode made of stainless steel was attached to inner wall of ceramic flow shroud.

Fig.4 shows structure of test section and out line of the void fraction measurement system.

We measured capacitance between a pair of electrode in the two phase flow by LCR meter as described in 2.2.

3.1.1 Electrode

We developed Mineral insulator (MI) sheath type electrode to keep insulation and resistance to high temperature and high pressure condition (9).

Fig.5 shows over view and arrangement of MI sheath type electrode. Sensor part of electrode is circular SUS plates (6mm diameter, 1mm thickness). Sheath is SUS pipe filled with ceramic inside.

Electrodes were attached to the measurement nozzles of the test section at 3 different elevations with 2mm interval oppositely to another electrode.

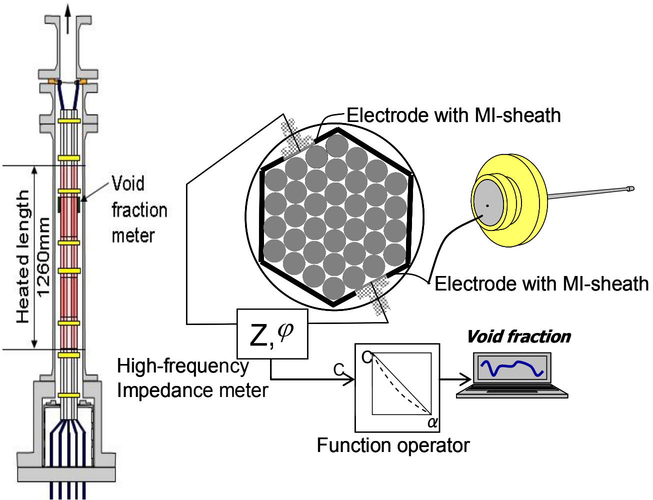

Fig. 4. 37 Bundle and measurement system

As to durability of electrode in the high temperature and high pressure condition, crack by the thermal stress was prevented as thermal expansion coefficient among composed materials are almost equal, consequently we could gain long life of MI sheath type electrode through autoclave test.

Signal cable was insulated from MI sheath to prevent leakage of measured signal current. Insulating points are following 3.

- Ceramic tip of cone shape was inserted between sheath and signal cable.
- Ceramic pipe was inserted in the half part of sheath (To cancel the capacitance by insulator between sheath and signal cable)
- In the welding of sheath and ceramic, intermediate material (Kovar-Alloy) was adopted as Kovar can be weld with sheath and ceramic.

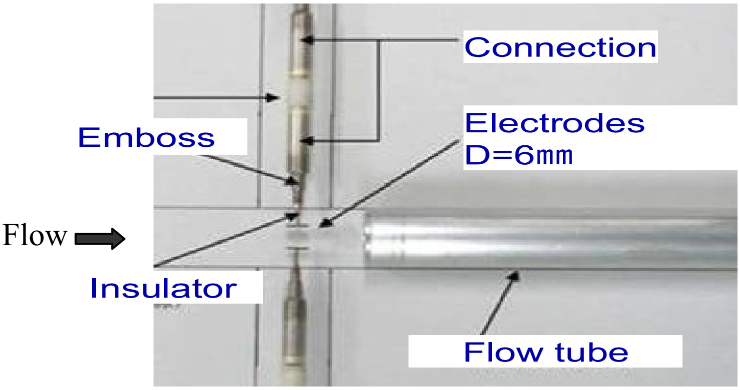

Fig. 5. MI sheath type electrode

3.1.2 Measurement Hi frequency of AC Power

In C method, measurement frequency of AC power should be optimized therefore we adopted 1MHz as stable frequency band as showed at 2.3.

3.1.3 Data acquisition of Liquid phase flow and Gas phase flow

In measurement initial capacitance data of liquid phase flow (Cl) and Gas phase flow (Cg) need to be input into signal conditioner as set up data.(Formula(4) claims Cl and Cg)

- C measurement of liquid phase (Cl) C measurement of the liquid phase were performed at 2MPa，4MPa，and 7MPa as steady test conditions.

At transient condition of temperature measured C should be correct as C changes with temperature changes.

- C measurement of the gas phase (Cg) In practical measurement Cg means void fraction is 100% and inner wall of the flow channel is wet condition.

In calibration test, Cg condition was realized as follows. Water level dropped enough and electrode exposed by accumulating steam in the test section by shutting of out let valve. Cg condition was confirmed from measured ΔP.

3.2 Response test of void fraction measurement

The response signal characteristics of void fraction measurement system were obtained with the advanced BWR thermo-hydraulic test facility. The results are shown in Fig.6.

From Fig.6, it was known that the measured void fraction follows to power with good response under the transient conditions while heating power of rod bundle is increasing and flow rate of recirculation water is constant. Void fraction measured elevation are 1200mm , this elevation is top in the heating part (Void signal 1), and 900mm in the heating part (Void signal 2). From Fig.6, it was clarified that void fraction measurements can perform in real time way by C method.

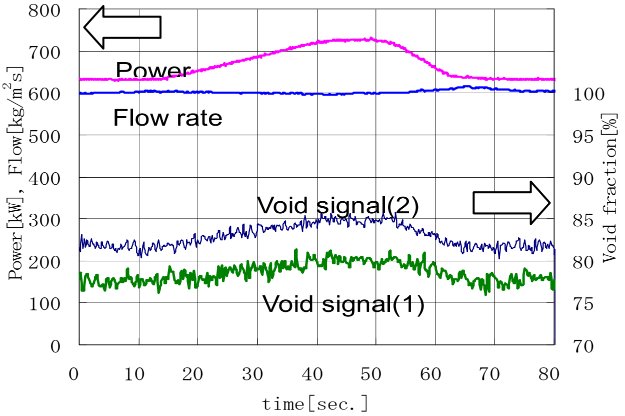

Fig. 6. Response of measurement system (7.2MPa pressure, 600kg/m^{2}s mass velocity)

3.3 Void fraction measurement result

Pressure 2MPa, 7MPa

Void fractions were successfully measured applying C method to advanced BWR thermo-hydraulic test facility (10) (11) (12). Fig.7 shows void fraction measurement result under heating power transiently controlled as to every mass flow rates of the recirculation water is constant at 2MPa pressure condition.

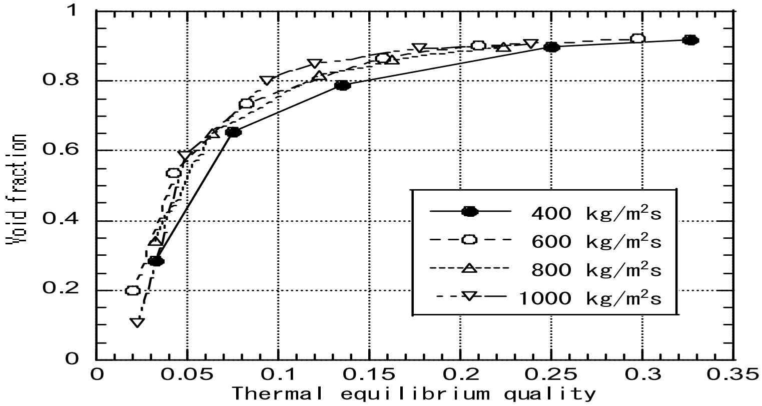

Fig. 7. Void fraction Measurement (2MPa pressure)

From measured result it were showed that with the increasing of mass flow rate of recirculation water 、measured void fraction becomes decrease and this result agreed to the usual knowledge. In this test measured maximum void fraction is 92%. This result shows C method enable to measure large void fraction region with stability. Fig.8 shows void fraction measurement result, in the condition of pressure changed to 7.2MPa in former test. Result shows that with increasing quality void fraction following increase rationally.

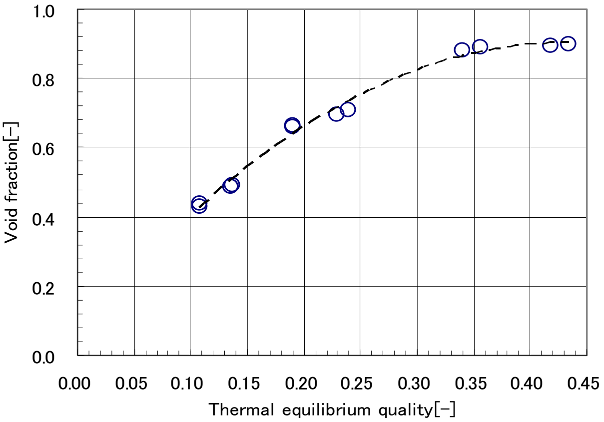

Fig. 8. Vo id fraction measurement (7.2 MPa pressure, 600 kg/m2s mass velocity)

4. Propriety of C method under high temperature (pressure 2MPa)

To confirm propriety of C method, we practically confirmed application of formula (3), (4) to high temperature and high pressure condition, we compared measured result by C method with measured result by quick shut method under the high pressure condition. At the result it was confirmed that C method is available for high temperature and high pressure conditions as well as atmospheric condition. Following is about calibration test for propriety. We adopted two type test section for calibration test. Test section for C method contains heating 37 rods bundle and test section for quick shut method contains non heating 19 rods bundle (Injected steam and water).

Comparison test was performed under 2MPa condition. Dimensions of the both test sections showed in the following.

Measurement method	C-method	Q.S. method
Number of rods	37	19
Outer rod diameter[mm]	13	12
Rod gap[mm]	1.3	
Hydraulic diameter[mm]	4.34	4.25

Configuration of 37 rods bundle is honeycomb 4 peripheries, and 19 rods bundle is honeycomb 3 peripheries respectively. Effect on the void fraction measurement due to the difference in the hydraulic diameter between 2 test sections was evaluated to be small though calculated result by Drift flux void fractional computing function.(Void fraction change is less than 1% provided quality is more than 5%)

But effect on the void fraction distribution due to heating form of the rod bundle was observed in the measured result.

4.1 Test facility for void fraction measurement by quick shut method

In the quick shut method two phase flow was instantly shut by Quick Shut Valve (QSV) and volume of the water in the test section is measured by differential pressure meter. For practical, Q.S.V is quick shut rotary disk installed to the shaft droved by high pressured air, synchronized actuate time is 0.05 second.

Fig.9 shows the structure of quick shut test section. Test section is composed of two sections to evaluate error of void fraction measurement, upper section is half length of lower section.

Correct void fraction was obtained from difference of the measured void fractions in the two sections, as void fractions correspond to gap between bundle and QSV was canceled.

4.2 Calibrated result of C method by Q.S method

Fig.10 shows measured result by C method and by Q.S method.

In Fig.12, measured void fraction by C method were showed with △ (solid line）, measured void fraction by Q.S method were showed with ○ (broken line) , and difference between C and Q.S approximated logarithmic function were showed with solid line for reference.

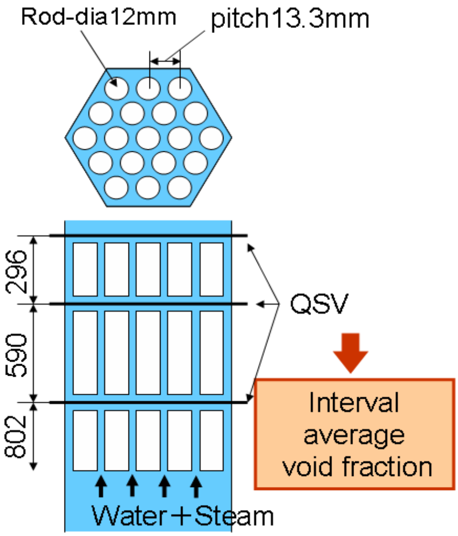

Fig. 9. Test section with quick-shut valve (QSV) for void fraction measurement

Moreover Fig.12 (10) shows that obtained two relational functions between void fraction and quality are equivalent function.

From minute view, measured void fraction by C method is a little larger than measured void fraction by Q.S method. Difference in the measured void fraction was largest at near 0.05 of the quality, difference becomes close up gradationally according to increasing in void fraction and range of difference was 4%～8%. The cause of the difference in the void fraction was considered that heating condition in the test section is different. 37 rods bundle is heating bundle and 19 rods bundle is non-heating bundle. In heating rods bundle it was observed that void fraction distribution was comparatively uniform. Contrary in non- heating rod bundle it was observed that void fraction distribution was large at the central flow channel and small at the near of the wall. With above reason, it is considered that measured void fraction by Q.S method is a little small than measured void fraction by C method under the region of less than 0.15 of quality. From calibration test C method is considered to be available in the condition of high temperature and high pressure as well as atmospheric condition in conclusion.

Moreover Fig.10 (13) shows that obtained two relational functions between void fraction and quality are equivalent function. From minute view, measured void fraction by C method is a little larger than measured void fraction by Q.S method. Difference in the measured void fraction was largest at near 0.05 of the quality, difference becomes close up gradationally according to increasing in void fraction and range of difference was 4%～8%. The cause of the difference in the void fraction was considered that heating condition in the test section is different. 37 rods bundle is heating bundle and 19 rods bundle is non-heating bundle. In heating rods bundle it was observed that void fraction distribution was comparatively uniform. Contrary in non- heating rod bundle it was observed that void fraction distribution was large at the central flow channel and small at the near of the wall. With above reason, it is considered that measured void fraction by Q.S method is a little small than measured void fraction by C method under the region of less than 0.15 of quality. From calibration test C method is considered to be available in the condition of high temperature and high pressure as well as atmospheric condition in conclusion.

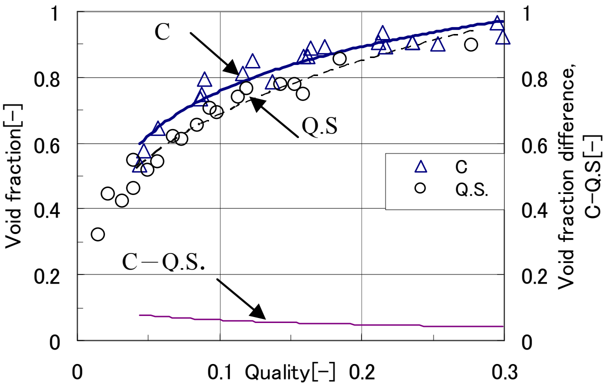

Fig. 10. Compared result between C and Quick-shut valve method void fraction method s (2MPa in pressure, 400～2000kg/m^{2}s in mass flux) (10)

5. Conclusion

We developed C method for practical void fraction measurement, applied to the high temperature and high pressure condition and following results were obtained.

In C method measurement relational function between void fraction and capacitance in the two phase flow was confirmed to be definite hyperbolic function (Formula (3),(4)) through tests under different temperature and pressure conditions.

In C method void fraction measurement is available in the pure water as well as conductive water and measurement region is almost 0～100%.

In C method void fraction measurement under the condition of high temperature and high pressure up to 7MPa pressure was achieved by developed MI sheath type electrode. C method was applied following thermo-hydraulic tests.

BWR stability test, BWR Critical Heat Flux test, and Reactivity Initiated Accident test.

6. Acknowledgments

As to perform void fraction measurement test we would like to express cordial thanks to Dr Kazuyuki TAKASER, Akira OHNUKI (Now MHI Co., LTD) in Research Group for Thermal and Fluid Engineering, Dr Masatoshi KURETA in Research Group for Nuclear Sensing and members in Mechanical Engineering and Electronics Section in Department of Engineering Services in Japan Atomic Energy Agency (JAEA) respectively. As for making test facility we express cordial thanks to ART KAGAKU Co., LTD (Precise test section) and SUKEGAWA ELECTRIC CO., LTD (MI sheath type Electrode).

7. References

[1] Watanabe, H., Iguchi, T., Kimura, M. and Anoda, Y., Development of quick-response area averaged void fraction meter, *JAERI-Research 2000-043* (2000) ·

[2] Watanabe, H., Iguchi, T. and Kimura, M. , Development of conductance-type void fraction meter, *JSME annual meeting*, No.4(2002), pp.233- 234 ·

[3] Watanabe, H., Mitsutake, T., Kakizaki, S. and Takase, K, Experimental study on feasibility of capacitance void fraction meter, *Transactions of the Japan Society of Mechanical Engineers, Series B*, Vol. 74, No.742 (2008), pp. 435-436

[4] Watanabe, H., Mitsutake, T., Kakizaki, S. and Akimoto, H, Electro-void fraction meter development and application to tight lattice rod assembly within reduced moderation water reactor, *Proceedings of the 9th National symposium of power and energy systems*(2004), pp.69-70 ·

[5] Maxwell, J.C., *A treatise on electricity and magnetism,*3rd ed · ,(1954), Vol · 1, Chapter 9, Article 314, Dover, New York

[6] Watanabe, H., Mitsutake, T., Kakizaki, S. and Akimoto, H, Electro-void fraction meter development and application to tight lattice rod assembly within reduced moderation water reactor, *Proceedings of the 9th National symposium of power and energy systems*(2004), pp.69-70 ·

[7] Watanabe, H., Mitsutake, T., Kakizaki, S. and Takase, K, Experimental Study on Capacitance Void Fraction Meters for High Temperature and High Pressure Conditions, *Transactions of the Japan Society of Mechanical Engineers, Series B*, Vol. 76, No.769 (2010), pp. 1379-1385

[8] Kureta, H., Yoshida, H., Tamai, H., Ohnuki, A. and Akimoto, H., Thermal-Hydraulic Estimation in Tight-Lattice Rod Bundles for Development of the Innovative Water Reactor for Flexible Fuel Cycle, *Progress in Multiphase Flow Research 3*, (2008), pp.99-109.

[9] Watanabe, H., Mitsutake, T., Kakizaki, S. and Takase, K, Experimental study on feasibility of capacitance void fraction meters, *Proceedings of the 13th National symposium of power and energy systems* (2007), pp.77-78 ·

[10] Kureta, H., Yoshida, H., Tamai, H., Ohnuki, A. and Akimoto, H. ، Thermal-Hydraulic Estimation in Tight-Lattice Rod Bundles for Development of the Innovative Water Reactor for Flexible Fuel Cycle, *Progress in Multiphase Flow Research 3*, (2008), pp.99-109.

[11] Cimorelli, L and Evangelisti, R., The application of the capacitance method for void fraction measurement in bulk boiling conditions, *International Journal of Heat and Mass Transfer*, Vol · 10(1967), pp · 277-288 ·

[12] Inoue, A., Kurosu, T., Aoki, T., Yagi, M., Mitsutake, T. and Morooka, S., Void fraction distribution in BWR fuel assembly and evaluation of subchannel code, *Journal of Nuclear Science and Technology* Vo. 32, No.7(1995), pp.629-640.

[13] Tamai, S, Takase, K., Shibata, M. and Hayafune, H. ، Flow instability experiments on steam generator with straight double-walled heat transfer tube for FBR (2) Experimental Results under High Pressure Conditions, *2007 Fall Meeting of the Atomic Energy Society of Japan, K58,* (2007).

Part 3

Gas Flow Measurement

5

Experimental Procedure for Rotating Ventilated Disk

Kannan M. Munisamy
Dept. of Mechanical Engineering, College Of Engineering
Universiti Tenaga Nasional, Kajang
Malaysia

1. Introduction

This chapter illustrates experimental procedure and rig development for a ventilated brake disk. Ventilated brake disk is the state of the art technology in automobile braking system. It is well known that the braking capability of brake disk is affected by the rate at which heat is dissipated through forced convection. The rapid increase and decrease of the brake disk temperature could lead to catastrophic failure of the brake disk due to high thermal strains. Heat transfer property enhancement in any ventilated disk design is an important interest to researches. The heat transfer analysis can be conducted experimentally or numerically. Experiment can be carried out on vehicle testing and in laboratory testing procedures. This chapter describes a method for laboratory testing procedure for vehicle disk brake design heat transfer property evaluation.

A rotating test rig is described with unique outflow measurement casing design to restrict outflow with minimum leakage. The casing is important to measure the total air metered through the ventilated disk passage due to inductive air flow. The chapter includes the test procedure and the post processing of the data collected. The devices, such as infrared sensors, thermocouples, flow meter, magnetic speed pick-up and pressure transducers are all connected to Data Acquisition System (DAQ), where the signals are converted to raw data files. The data acquisition module and graphical outputs are shared during the transient recording. The stationary but rotating test rig allows designer to eliminate cross wind effect and other fittings in the car wheel components to focus on the blade geometrical aspect alone. The immobility of the test rig makes it easier to measure the flow pass through and heat transfer from the disk brake.

2. Brake disk experimental rig

A preliminary experimental rig is initially developed to measure the amount of air metered into the ventilated brake disk and the pressure between the rotating blades. The inlet velocity is measured by taking the velocity integral in the inlet ducting using pitot-static tube. Schematic diagrams of the test rig with the components positions shown in picture below. The initial test rig was worth the effort to minimize lead time in designing the rotating test rig with DAQ system and sophisticated measuring equipment.

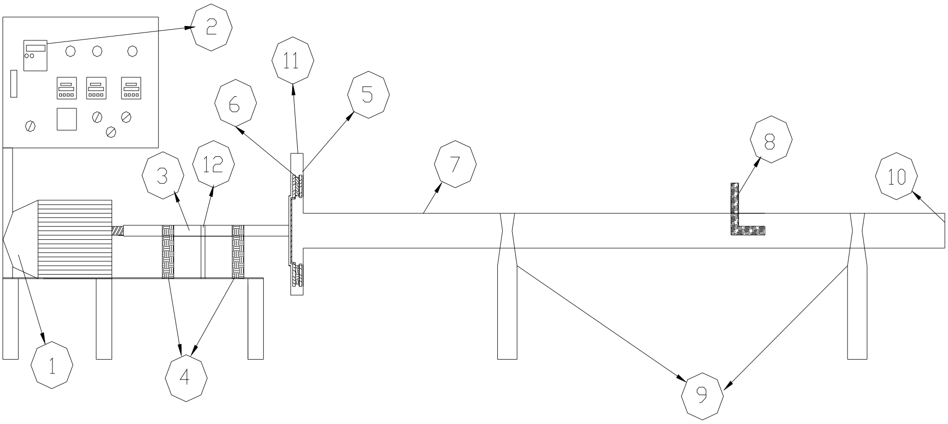

Part No.	Description	Part No.	Description
1	Single Phase Motor	7	Inflow Ducting
2	Motor Speed Controller	8	Pitot-tube Manometer
3	Connecting Shaft	9	Ducting Support
4	Bearing	10	Inflow
5	Disc Brake Casing	11	Outflow
6	Ventilated brake disc specimen	12	Magnetic speed pick-up

Fig. 1. Schematic of Experimental Rig and the Main Components

Test rig shown above used to predict the flow range using pitot tube which is labeled as no. 8. The upgraded version of the experimental rig has ability to measure sophisticated measurements, such as total flow rate, surface temperature and pressure which collected by DAQ. The enhanced version of test rig circuit drawing shown in Fig to observe the position of the measuring device which placed at the test specimen. Moreover the brief explanation of the thermocouple location also has been discussed in Table . There are Pt-type, K-type and infrared type thermocouples involved in the measurements of temperature.

ID	Thermocouple	Location
A	Pt1	R = 125mm
B	Pt2	R = 110mm
C	Pt3	R = 95mm
D	Pt4	R = 125mm
E	Pt5	R = 110mm
F	Pt6	R = 95mm
G	Pt7	Inlet, R = 60mm
H	Pt8	Outlet, R = 130mm
I	K1	Ambient

Table 1. Position of Thermocouple

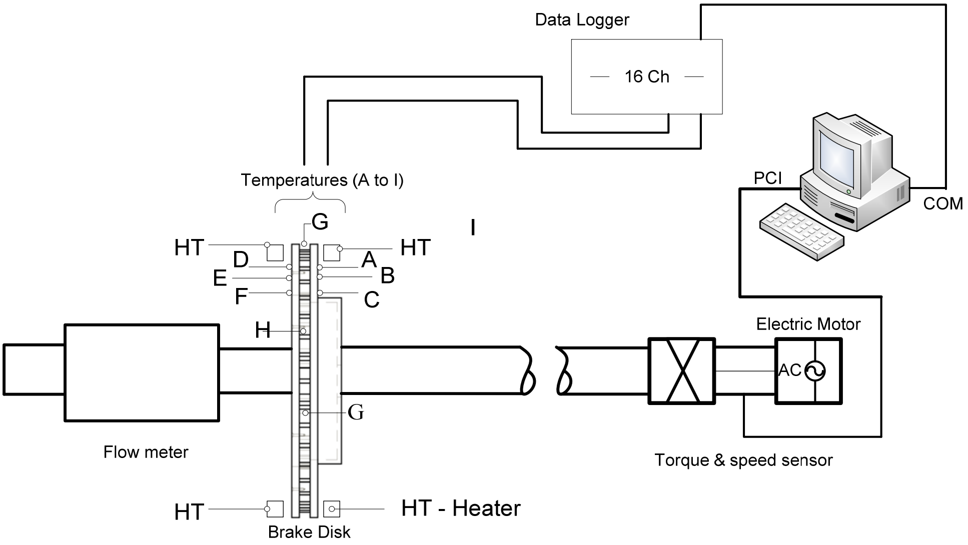

Fig. 2. Ventilated brake disk experimental rig

Fig. illustrates the photographic view of the upgraded experimental rig used. The Fig. show the overall view of the test rig with long intake duct to ensure developed flow at the flow meter. The Figure (a) shows the long air flow ducting to ensure a fully developed flow passes through the flow meter. Figure 3(b) shows the disk brake stationary casing and the manual display of the parameter measurements. The design shows the custom-made Aluminum material casing that guides the outflow radially out and axially directed in through the center of the brake disk with almost zero leakage. The ventilated brake disk of 255mm diameter is fitted with only 1mm clearance between rotating disk and the casing. The tube around the casing is to measure the outlet static pressure.

3. Error analysis

Experiments are basically done to verify some statement, by determining objectives, methodology and research are carried out also at first, followed by progress, results, and analysis with discussion and finally conclusions are made. These are the basic steps on how an experiment is being conducted, and there are no limitations for sub-stages to be included in each step. Specifically, analysis can be categorized to few sub-stages, such as measuring and obtaining some data, tabulate it and plotting a graph based on table. Besides that, error analysis is vital part and it’s divided into two fraction; random error and systematic error. These analysis are done mainly to shirk wrong analysis as well provide good accuracy during collecting data from the measurement device.

3.1 Random error

Random errors are errors in measurement that lead to measured values being inconsistent when repeated. The word random indicates that they are inherently unpredictable, and

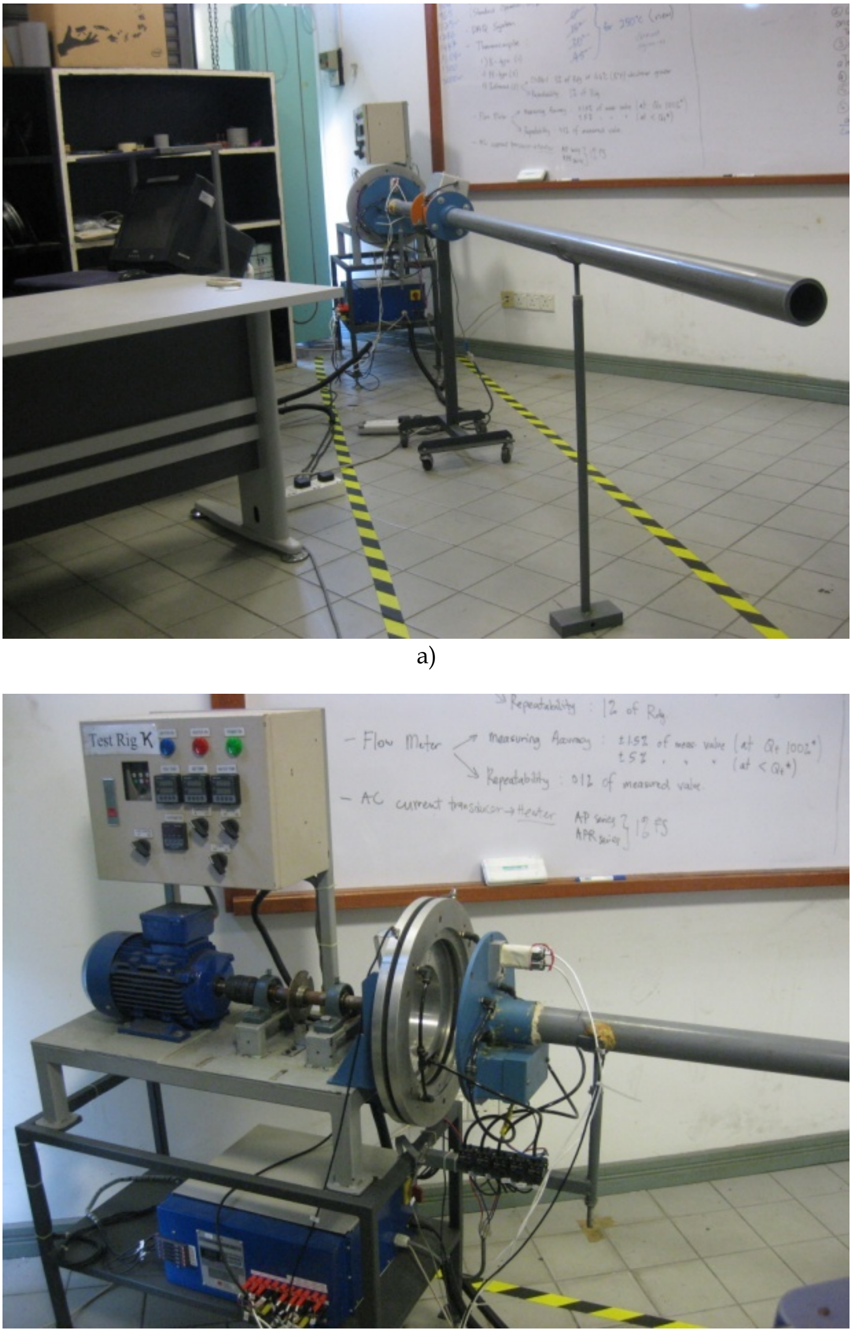

a)

b)

Fig. 3. Photographs of the upgraded experimental rig

have null expected value, namely, they are scattered about the true value, and tend to have null arithmetic mean when a measurement is repeated several times with the same instrument. Random errors are also can be defined as an error that results from unpredictable variations from one or more influenced quantities. Random error is mainly caused by unpredictable fluctuations in the data of a measurement apparatus, or in the human interpretation of the instrumental reading; these fluctuations may be in part due to interference of the environment with the measurement process. The concept of random error is closely related to the concept of precision. There are no way of perfect experiment to be done without any random error, but the higher the precision of a measurement instrument in an experiment, the smaller the variability (standard deviation) of the fluctuations in the readings.

3.2 Systematic errors

Systematic errors are also known as bias error in measurement which leads to the situation where the mean of many separate measurements differs significantly from the actual value of the measured attribute. Often of several different types of measurement are prone to systematic errors. Sources of systematic error may be imperfect calibration of measurement instruments and sometimes imperfect methods of observation can be either zero error or percentage error.

Systematic errors may also be present in the result of an estimate based on a mathematical model or physical law. For instance, the estimated oscillation frequency of a pendulum will be systematically in error if slight movement of the support is not accounted for. Systematic errors can be either constant, or be related (e.g. proportional or a percentage) to the actual value of the measured quantity, or even to the value of a different quantity.

3.3 Comparison of random errors and systematic errors

Many are still confused between random and systematic errors. Random error will always appear in a measurement and being caused by unpredictable fluctuations in the readings of a measurement apparatus or with experiment conductor’s interpretation of the instrumental reading.

On the other side, systematic error is quite predictable, and always either constant or proportional to the true value. It can be eliminated if the cause of the systematic error can be identified. Systematic errors are caused by imperfect calibration of measurement instruments or imperfect methods of observation, and always affect the results of an experiment in a predictable direction. Inversely for random errors, its unpredictable criteria makes the error hardly identified, yet eliminate it. Example, distance measured by radar will be systematically overestimated if the slight slowing down of the waves in air is not accounted for. Incorrect zeroing of an instrument leading to a zero error is an example of systematic error in instrumentation.

4. Measurement devices error analysis

To gather all information regarding systematic errors, user manuals for all equipment were researched. Below is the table describing the channels representing hardware, basic description about the function of the hardware and systematic errors.

CHANNEL	HARDWARE	DESCRIPTION	ERRORS (SYSTEMATIC)
0	Infrared temperature sensor	To measure temperature at outer radius of disc	OS 136 – 1 : 3% of reading or 44°C (8°F) whichever greater. Repeatability: 1% of reading.
1	Infrared temperature sensor	To measure temperature at inner radius of disc	OS 136 – 1 : 3% of reading or 44°C (8°F) whichever greater. Repeatability: 1% of reading.
2	Control panel	Contains controller for tachometer, and power on/off for heater	-
3	-	-	-
4	-	-	-
5	Pt-type temperature sensor	To measure temperature of radiation of disc at top left	Class A : Tolerance ± 0.06% @ 0C Class B : Tolerance ± 0.12 % @ 0C
6	Pt-type temperature sensor	To measure temperature of radiation of disc at top right	Class A : Tolerance ± 0.06% @ 0C Class B : Tolerance ± 0.12 % @ 0C
7	K-type temperature sensor	To measure temperature of air flow through ducting	Linear from 0 °C to +400 °C (3 °C ± 3% of reading)
8	-	-	-
9	Pt-type temperature sensor	To measure temperature of radiation of disc at bottom	Class A : Tolerance ± 0.06% @ 0C Class B : Tolerance ± 0.12 % @ 0C
10	Pressure Tapping / Transducer	To measure pressure change at left inlet of disc	Hysteresis Error 0.5% of FS – Standard Operation, 0.1% of FS High Resolution Mode – Zero Shift.
11	Pressure Tapping / Transducer	To measure pressure change at right inlet of disc	Hysteresis Error 0.5% of FS – Standard Operation, 0.1% of FS High Resolution Mode – Zero Shift.
12	Pressure Tapping / Transducer	To measure pressure change at right outlet of disc	Hysteresis Error 0.5% of FS – Standard Operation, 0.1% of FS High Resolution Mode – Zero Shift.
13	Pressure Tapping / Transducer	To measure ambient pressure	Hysteresis Error 0.5% of FS – Standard Operation, 0.1% of FS High Resolution Mode – Zero Shift.
14	Pressure Tapping / Transducer	To measure pressure change at left outlet of disc	Hysteresis Error 0.5% of FS – Standard Operation, 0.1% of FS High Resolution Mode – Zero Shift.
15	Flow meter	To measure air flow rate through ducting	± 1.5% of measured value (at Qt 100%), ± 5% of measured value (at <Qt*)

Table 2. Table of representative channel, description and systematic error for hardware in Disc Brake Experimental Rig

As in

Table channel 3, 4 and 8 are not connected to any hardware, and might be used in future if more measurement is needed. Similar brand and model is used for each type of sensors, so similar errors are obtained. When calculating for combined errors for certain formulas or equations, the errors for standard operation is chosen. The errors also selected when the variables are in 100% condition, example for flow meter which having two condition of error selection. The first condition of ±1.5% of measured value is chosen because flow rate is 100%, which indicating no disturbance in the flow. For pressure transducer, 0.1% error is chosen in calculation of error analysis, because the Experimental Rig is assumed working under standard operation. Other errors are taken directly, which had given in the respective user manuals that suitable for all kind of condition.

4.1 Pitot-static measurement

The flow measurement is first measured using pitot-static tube. The schematic of the experimental rig illustrated in Fig. . As shown, to constraint the flow through the disk specimen, a custom-made brake disk casing is fabricated. In order to measure the air inflow velocity, an circular duct was built. Additional tapping is also made on the brake disk casing to tap the inlet and outlet pressure between the disk blades in radial direction. This experimental rig can be tested using various brake disk specimen with constant outer diameter. Another constraint to this test rig is the maximum revolution shall go up to 2600 rpm which is equivalent to 320km/h road speed.

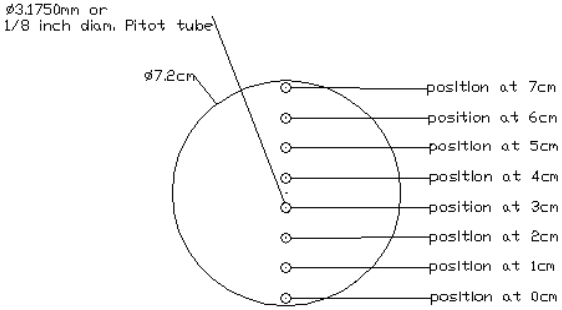

Fig. 4. Traversed Pitot tube positioning at 8 radial points in pipe cross-section

The experimental rig is mainly developed to measure the amount of air metered into the ventilated brake disk and the pressure between the rotating blades. The inlet velocity is measured in the by taking the velocity integral in the inlet ducting. The screen which keeps the flow attached in a ducting is not needed because there is no sudden change in the diameter of the ducting (Mehta, (34)). Then, the entrance length l_e was calculated with reference to Munson et. al. (35)

$$\frac{l_e}{D} = 0.06R_e \tag{1}$$

$$\frac{l_e}{D} = 4.4R_e^{\frac{1}{6}} \tag{2}$$

The equation 1 is for laminar flow and equation 2 is for turbulent flow. The highest Reynolds Number is turbulent. Thus, equation 2 is used to calculate the entrance length. The entrance length l_e of a 2.5m ducting is constructed for the pitot - static tube velocity measurement. Fig shows the pitot - static tube measuring position. The velocity in traverse direction (see Fig is measured using pitot tube with reference to the BS1042. Then, the flow rate is calculated using multiple-application trapezoidal rule. An incline liquid manometer is used to measure the small static pressure difference.

5. Oscillation flow meter (model: DOG)

This device works without any moving parts. An orifice in the lower section generates a flow resistance through which part of the flow is fed into the measuring head. There is then a spontaneous oscillation of the gas in the measuring head. The oscillation frequency is proportional to the flow velocity and consequently to the volume flow. Since the relationship between the flow through the measuring head and the flow through the measuring casing is constant the oscillation frequency also remains directly proportional to the overall volume flow through the device. A hot wire sensor determines the oscillations in the measuring head. A signal transducer feeds the sensor with power supply and amplifies and scales the oscillations. This flow meter manufactured by Kobold. Flow meter's technical information listed as below:-

Measuring accuracy	± 1.5% of measuring value at Q_t 100%
Repeatability	0.1% of measured value
Temperature	maximum -20 to 120 °C
Materials	
Housing	Stainless Steel 1.4571
Orifice	Stainless Steel 1.4436
Sensing Element	PolyphenyleneSulfida (PPS)
Sensor	Platinum
Gaskets	Silicone

6. Infrared temperature sensor (model OS136 series)

This model is a low cost, super compact infrared transmitter. It measures temperature via non contact, and provides an analog output proportional to the measured temperature. This unit has a fixed Emissivity of 0.95 which makes it easy to measure temperature. The range is larger than the optical field of view of the transmitter. The design, 19mm OD x 89mm length is ideal to measure temperature in confined, and hard to reach places (shown in Fig). This transmitter can operate in an ambient temperature of 0 °C to 70 °C. There is a warm up period of 2 minute after power up. This flow meter manufactured by Omega Engineering. Its technical information listed as below:-

Measuring Accuracy	3% of Reading
Repeatability	1% of Reading
Temperature	maximum -18 to 204 °C
Laser Wavelength	630 – 670 nm
Operating Distance	Up to 9.1 m

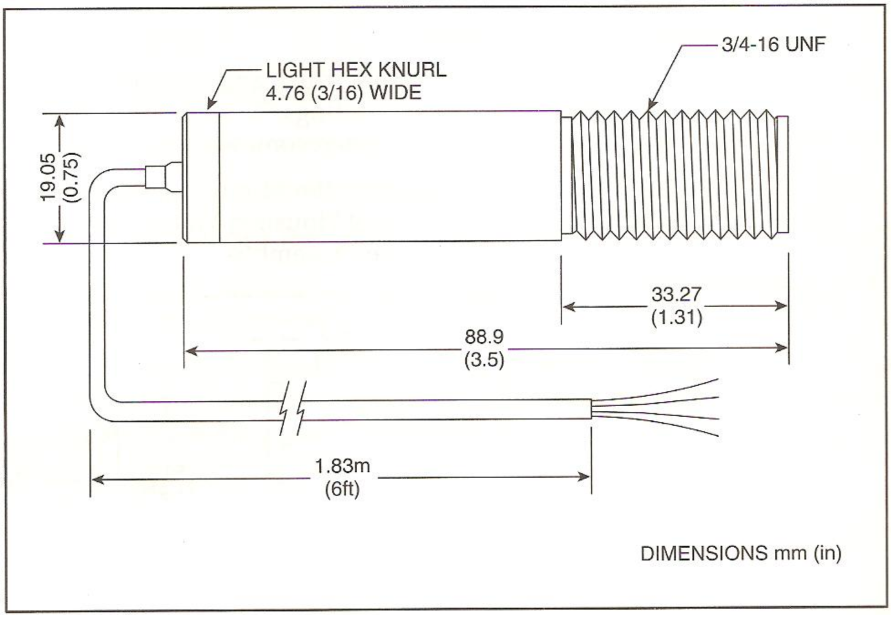

Fig. 5. Infrared Temperature Sensor housing dimension

7. Calculation of convective heat transfer coefficient

The cooling results from test rig were used to determine the convective heat transfer coefficient. The radiation heat transfer was deducted from the disc total heat transfer coefficient and heat conduction to shaft is neglected as the disk brake housing was insulated. At steady state the disk temperature is recorded T_d. The disk temperature will vary in accordance to the convective heat transfer performance of the ventilated blades. The heater is set to be on constant heat flux mode. Thus the heat transfer coefficient is calculated as below:

$$h_c A_W (T_d - T_\infty) = Q_{heater} \tag{3}$$

The equation 3 indicates the heat transfer coefficient, h_c calculated at steady state heating of the brake disk.

8. Error analysis for non-dimensional groups

Error analysis is important to be done for the equations because few variables are involved, which carrying their own errors. So calculation is necessary in order to determine new error for important equation, which later on used in future application. In this sub-chapter, every detail of calculation, together with its example will be showed. All the calculation below are based on Eq 3.11 & 3.16 of textbook of Experimentation and Uncertainty Analysis for Engineers, 2nd edition, By Hugh W.Coleman and W. Glenn Steele. Pg 51. (Coleman and Steele December 1998)

8.1 Non-dimensional number, Cw

$$\mathrm{Cw} = \frac{Q}{\mu R} \tag{4}$$

Where

Cw: Non-dimensional number
R: Radius of disc brake = 0.1275m
Q: Air flow rate
μ: kinematic viscosity of air = 1.1516E-05 m²/s

$$\frac{U_{Cw}^2}{Cw^2} = \left(\frac{Q}{Cw} \bullet \frac{\partial Cw}{\partial Q}\right)^2 \left(\frac{U_Q}{Q}\right)^2 + \left(\frac{\mu}{Cw} \bullet \frac{\partial Cw}{\partial \mu}\right)^2 \left(\frac{U_\mu}{\mu}\right)^2 + \left(\frac{R}{Cw} \bullet \frac{\partial Cw}{\partial R}\right)^2 \left(\frac{U_R}{R}\right)^2$$

$$\frac{U_{Cw}^2}{Cw^2} = \frac{U_Q^2}{Q^2} + \frac{U_\mu^2}{\mu^2} + \frac{U_R^2}{R^2}$$

μ andR are constant, uncertainties related to these constants are equals to zero, so it can be omitted from the equation

$$\frac{U_{Cw}^2}{Cw^2} = \frac{U_Q^2}{Q^2} = 1.5\%$$

8.2 Reynolds number, Re

$$\mathrm{Re} = \frac{\boldsymbol{V_{rot} R^2}}{\boldsymbol{\mu}} \tag{5}$$

Where

Re: Reynolds Number
V_{rot}: rotational speed
R: radius of the disc brake = 0.1275m
μ: kinematic viscosity of air = 1.1516E-05 m²/s

$$\frac{U_{Re}^2}{Re^2} = \left(\frac{V_{rot}}{Re} \bullet \frac{\partial Re}{\partial V_{rot}}\right)^2 \left(\frac{U_{V_{rot}}}{V_{rot}}\right)^2 + (2)^2\left(\frac{R}{Re} \bullet \frac{\partial Re}{\partial R}\right)^2 \left(\frac{U_R}{R}\right)^2 + \left(\frac{\mu}{Re} \bullet \frac{\partial Re}{\partial \mu}\right)^2 \left(\frac{U_\mu}{\mu}\right)^2$$

$$\frac{U_{Re}^2}{Re^2} = \frac{U_{V_{rot}}^2}{{V_{rot}}^2} + (2)^2\frac{U_R^2}{R^2} + \frac{U_\mu^2}{\mu^2}$$

Since R, V_{rot} and μ are constant, uncertainties related to these constants are equals to zero, so it can be omitted from the equation

$$\frac{U_{Re}^2}{Re^2} = 0\%$$

8.3 Head rise, Hr

$$\mathrm{Hr} = \frac{\boldsymbol{P_1 - P_\infty}}{\boldsymbol{\rho g}} \tag{6}$$

Where

P_1 - P_∞: Pressure Difference
ρ : density = 1.17 kg/m³
g : gravity constant = 9.81 m²/s

$$\frac{U_{Hr}^2}{Hr^2} = \left(\frac{\mathrm{P1-P\infty}}{Hr} \bullet \frac{\partial Hr}{\partial \mathrm{P1-P\infty}}\right)^2 \left(\frac{U_{\mathrm{P1-P\infty}}}{\mathrm{P1-P\infty}}\right)^2 + \left(\frac{\rho}{Hr} \bullet \frac{\partial Hr}{\partial \rho}\right)^2 \left(\frac{U_\rho}{\rho}\right)^2 + \left(\frac{g}{Hr} \bullet \frac{\partial Hr}{\partial g}\right)^2 \left(\frac{U_g}{g}\right)^2$$

$$\frac{U_{Hr}^2}{Hr^2} = \frac{U_{\mathrm{P1-P\infty}}^2}{\mathrm{P1-P\infty}^2} + \frac{U_\rho^2}{\rho^2} + \frac{U_g^2}{g^2}$$

Since ρ and g are constant, uncertainties related to these constants are equals to zero, so it can be omitted from the equation

$$\frac{U_{Hr}^2}{Hr^2} = \frac{U_{\mathrm{P1-P\infty}}^2}{\mathrm{P1-P\infty}^2} = 0.1\%$$

8.4 Pressure rise, Pr

$$\mathrm{Pr} = \frac{\boldsymbol{Hr.\ g}}{\boldsymbol{V_{rot}^2 .\ R^2}} \tag{7}$$

Where
Pr: Pressure rise
Hr: Head rise
g: gravity constant = 9.81 m²/s
Vrot: rotational speed
R: radius of the disc brake = 0.1275m

$$\frac{U_{Pr}^2}{Pr^2} = \left(\frac{\mathrm{Hr}}{Pr} \bullet \frac{\partial Pr}{\partial \mathrm{Hr}}\right)^2 \left(\frac{U_{\mathrm{Hr}}}{\mathrm{Hr}}\right)^2 + \left(\frac{\mathrm{g}}{Pr} \bullet \frac{\partial Pr}{\partial \mathrm{g}}\right)^2 \left(\frac{U_g}{g}\right)^2 + \left(\frac{V_{rot}}{Pr} \bullet \frac{\partial Pr}{\partial V_{rot}}\right)^2 \left(\frac{U_{V_{rot}}}{V_{rot}}\right)^2 + \left(\frac{\mathrm{R}}{Pr} \bullet \frac{\partial Pr}{\partial \mathrm{R}}\right)^2 \left(\frac{U_{\mathrm{R}}}{\mathrm{R}}\right)^2$$

$$\frac{U_{Pr}^2}{Pr^2} = \frac{U_{\mathrm{Hr}}^2}{\mathrm{Hr}^2} + \frac{U_{\mathrm{g}}^2}{\mathrm{g}^2} + \frac{U_{V_{rot}}^2}{{V_{rot}}^2} + \frac{U_{\mathrm{R}}^2}{\mathrm{R}^2}$$

Since g, V_{rot} and R are constant, uncertainties related to these constants are equals to zero, so it can be omitted from the equation

$$\frac{U_{Pr}^2}{Pr^2} = \frac{U_{\mathrm{Hr}}^2}{\mathrm{Hr}^2} = 0.1\%$$

8.5 Nusselt number, Nu

$$\mathrm{Nu} = \frac{\boldsymbol{C1 - C2\ [T_d^4(r) - T_{heater}^4]}}{\boldsymbol{T_d(r) - T\infty}} \tag{8}$$

Where

Nu: Nusselt number
C_1: constant from equation $C1 = \lambda air\left(\frac{\partial T(r)}{\partial x}\right)$

C_2: constant from equation $C2 = \frac{\sigma F \varepsilon_d \varepsilon_H}{1 - F^2(1 - \varepsilon_d)\varepsilon_H}$

T_d: temperature of disc

T_{heater}: Temperature of heater

T_∞ : Ambient temperature

C1 and C2 are constants obtained from literature review, so uncertainties for these constants are equals to zero and error analysis calculation for these constants are assumed zero

$$\frac{U_{Nu}^2}{Nu^2} = \left(\frac{\mathrm{C1}}{Nu} \bullet \frac{\partial Nu}{\partial \mathrm{C1}}\right)^2 \left(\frac{U_{\mathrm{C1}}}{\mathrm{C1}}\right)^2 + \left(\frac{\mathrm{C2}}{Nu} \bullet \frac{\partial Nu}{\partial \mathrm{C2}}\right)^2 \left(\frac{U_{\mathrm{C2}}}{\mathrm{C2}}\right)^2 +$$

$$(4)^2 \left(\frac{Td(r) - Theater}{Nu} \bullet \frac{\partial Nu}{\partial Td(r) - Theater}\right)^2 \left(\frac{U_{Td(r) - Theater}}{Td(r) - Theater}\right)^2 + \left(\frac{\mathrm{Td(r) - T\infty}}{Nu} \bullet \frac{\partial Nu}{\partial \mathrm{Td(r) - T\infty}}\right)^2 \left(\frac{U_{\mathrm{Td(r) - T\infty}}}{\mathrm{Td(r) - T\infty}}\right)^2$$

$$\frac{U_{Nu}^2}{Nu^2} = \frac{U_{\mathrm{C1}}^2}{\mathrm{C1}^2} + \frac{U_{\mathrm{C2}}^2}{\mathrm{C2}^2} + (4)^2 \frac{U_{Td(r) - Theater}^2}{Td(r) - Theater^2} + \frac{U_{\mathrm{Td(r) - T\infty}}^2}{\mathrm{Td(r) - T\infty^2}}$$

$\frac{U_{Nu}^2}{Nu^2}$= (16) (0.0006) + (0.0006)
= 0.0096 + 0.0006
= 0.0102
= 1.02%

9. Disk brake experimental rig procedure

The test rig developed with established test procedure. The incorporation of the hardware and the software is described briefly below. Measuring devices such as infrared sensors, flow meter and pressure transducers are all connected to Data Acquisition System (DAQ), which receives reading in raw data. Device Manager and Wavescan 2.0 software's used in this experimental procedure to capture data in real time. The chart in Fig. illustrates the test procedure. The steady state highest temperature value is recorded for the supplied power input at the heater. Then cooling temperature rate can be measured.

Device Manager software used to capture and convert data into spread sheet. The general description of the steps can be found in the flow chart Fig. Firstly, the Device Manager is opened and synchronized. Then all 16 channels are checked to be functioning in good condition as in Fig. The output window with 16 channels turned on can be seen in Fig. After the data capturing is started the window will look like in the Fig. Once the data capturing stopped the data can be converted into spread sheet for further exploitation with the button shown in Fig.

10. Results for a disk brake sample

The experimental rig can be exploited in accordance to the research problem statement by the researcher. The results that were obtained for a study on straight blade ventilated brake disk are shared below. The Figure 12 shows the mass flow rate obtain from the gas flow meter. In this particular study it is even validated against pitot static tube measurement done at multipoint inside the air flow duct. The figure 13 shows the heat transfer coefficient calculated from the experimental analysis is presented against the disk brake rotation speed. The results are checked with numerical data labeled "CFD" for computational fluid dynamics. Following that the no-dimensional parameter Nusselt number if also plotted against rotational Reynolds number. The raw data from the experimental is at the discretion of the researcher to be post-processed in any convenient way for critical analysis.

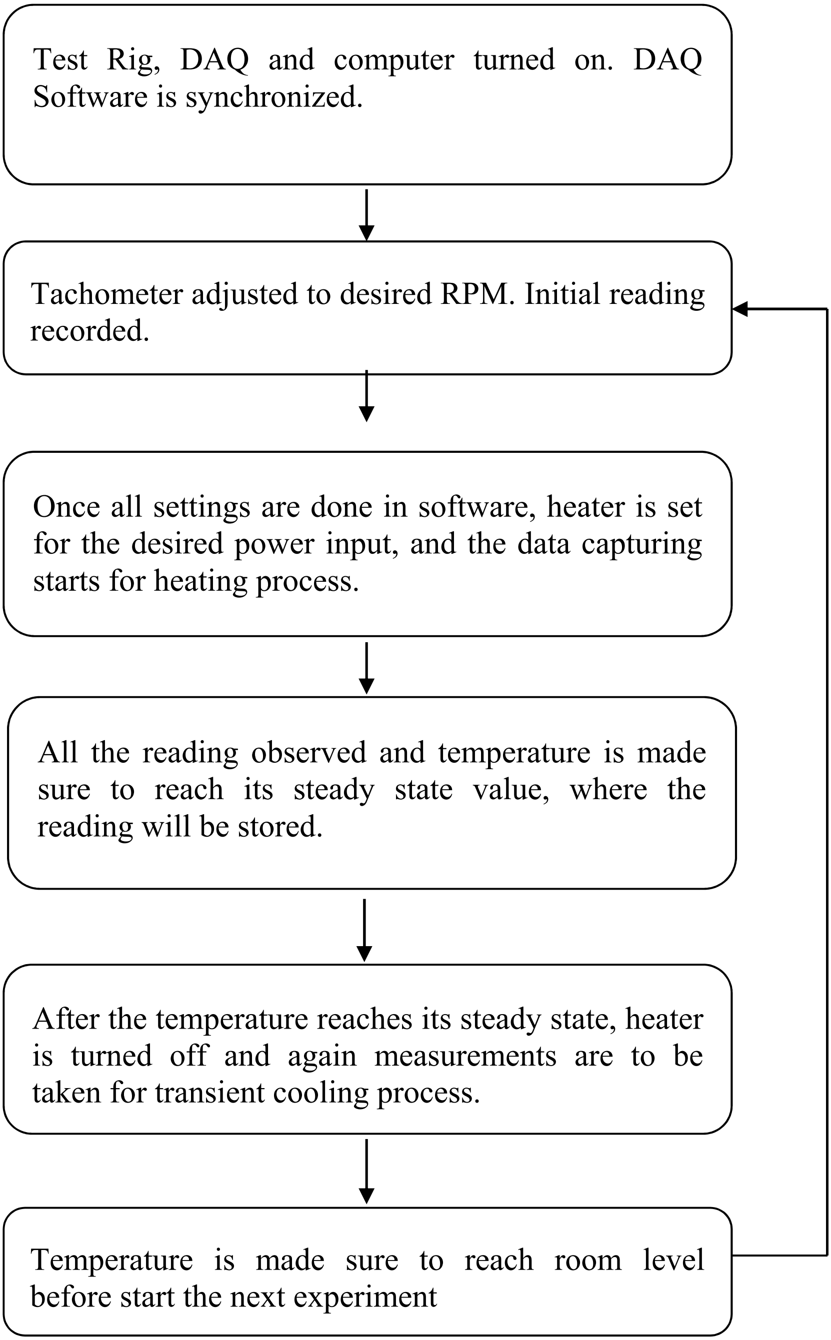

Fig. 6. Flow chart of procedures for Experimental Rig of Disc Brake

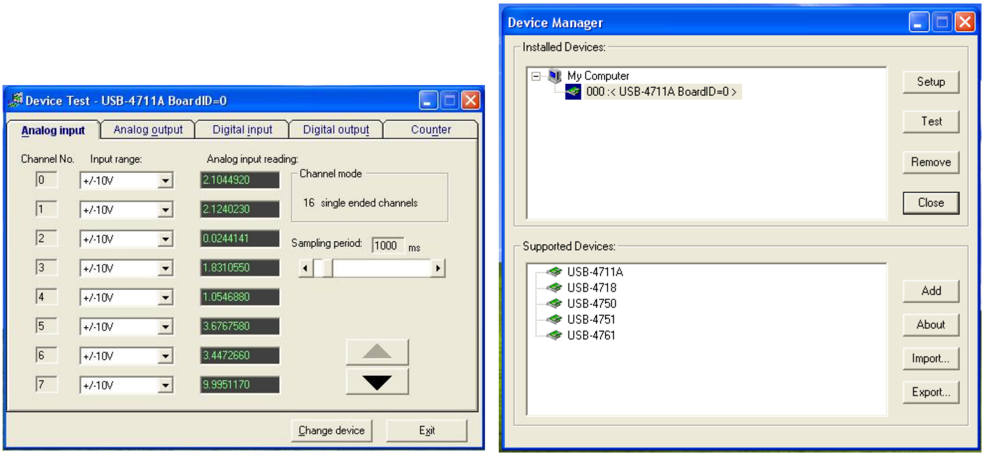

Channel No.	Input range:	Analog input reading:
0	+/-10V	2.1044920
1	+/-10V	2.1240230
2	+/-10V	0.0244141
3	+/-10V	1.8310550
4	+/-10V	1.0546880
5	+/-10V	3.6767580
6	+/-10V	3.4472660
7	+/-10V	9.9951170

Channel mode: 16 single ended channels

Sampling period: 1000 ms

Installed Devices:
- My Computer
  - 000 :< USB-4711A BoardID=0 >

Supported Devices:
- USB-4711A
- USB-4718
- USB-4750
- USB-4751
- USB-4761

Fig. 7. Device Manager and Device Test

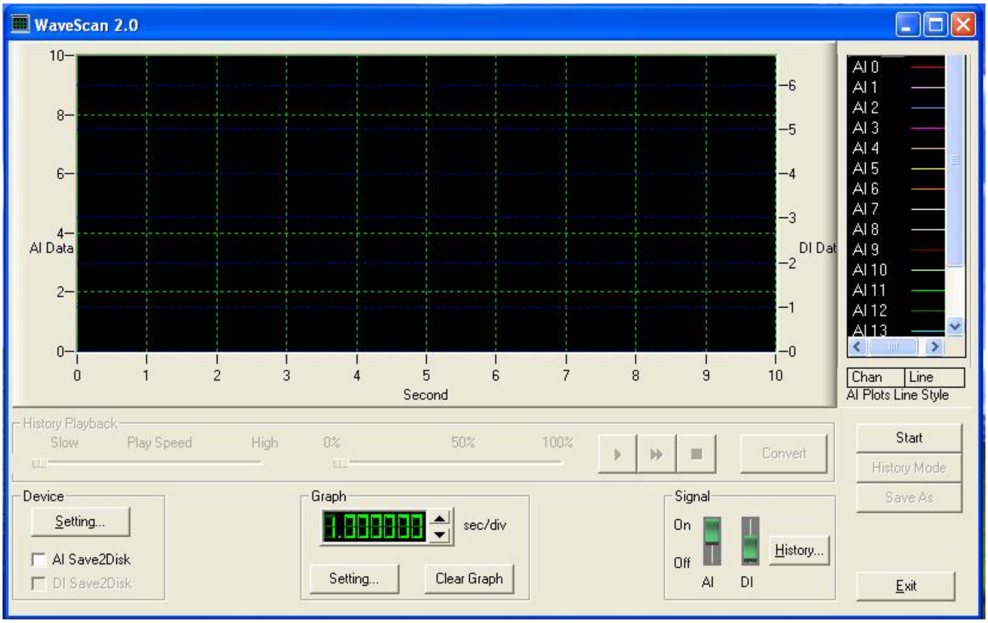

Graph: 1.000000 sec/div

Fig. 8. Analog Signal and channels can be seen on top right side of box

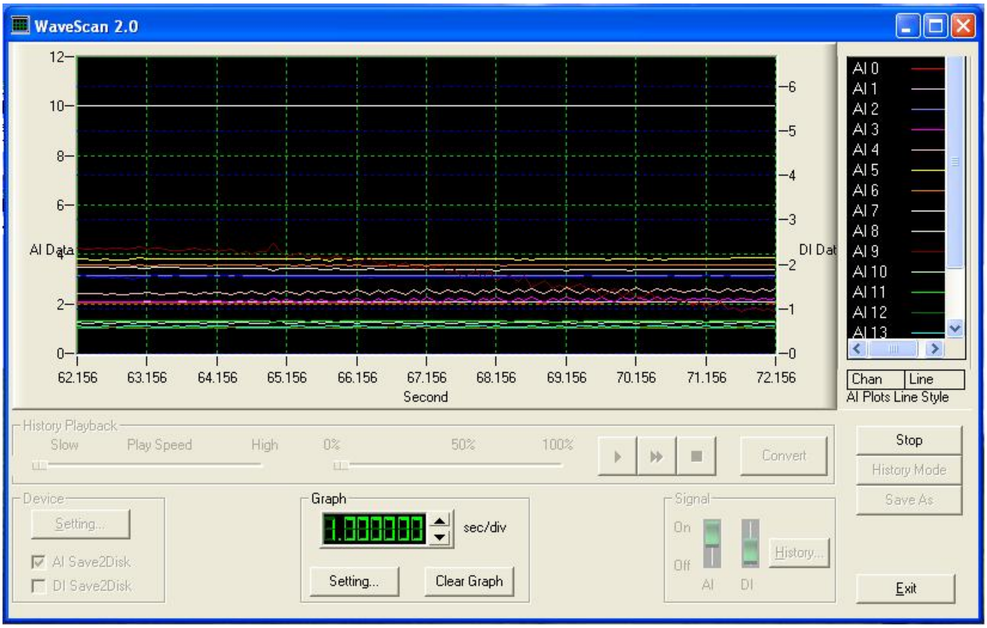

Fig. 9. Raw results with analog signal upon capturing started for all channel

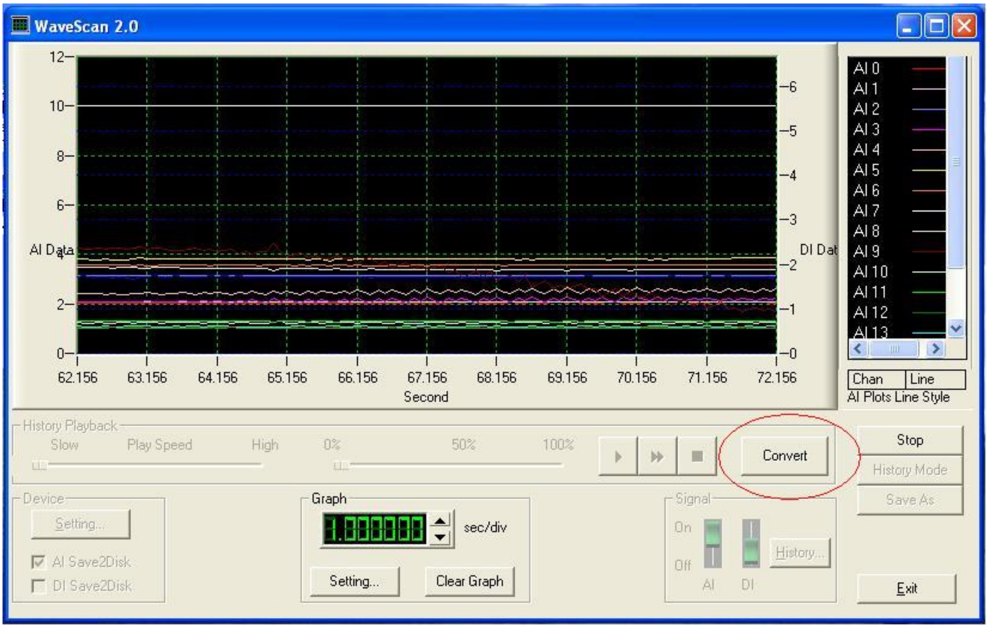

Fig. 10. Wavescan box appeared to convert (in red circle) raw data to spread sheet format

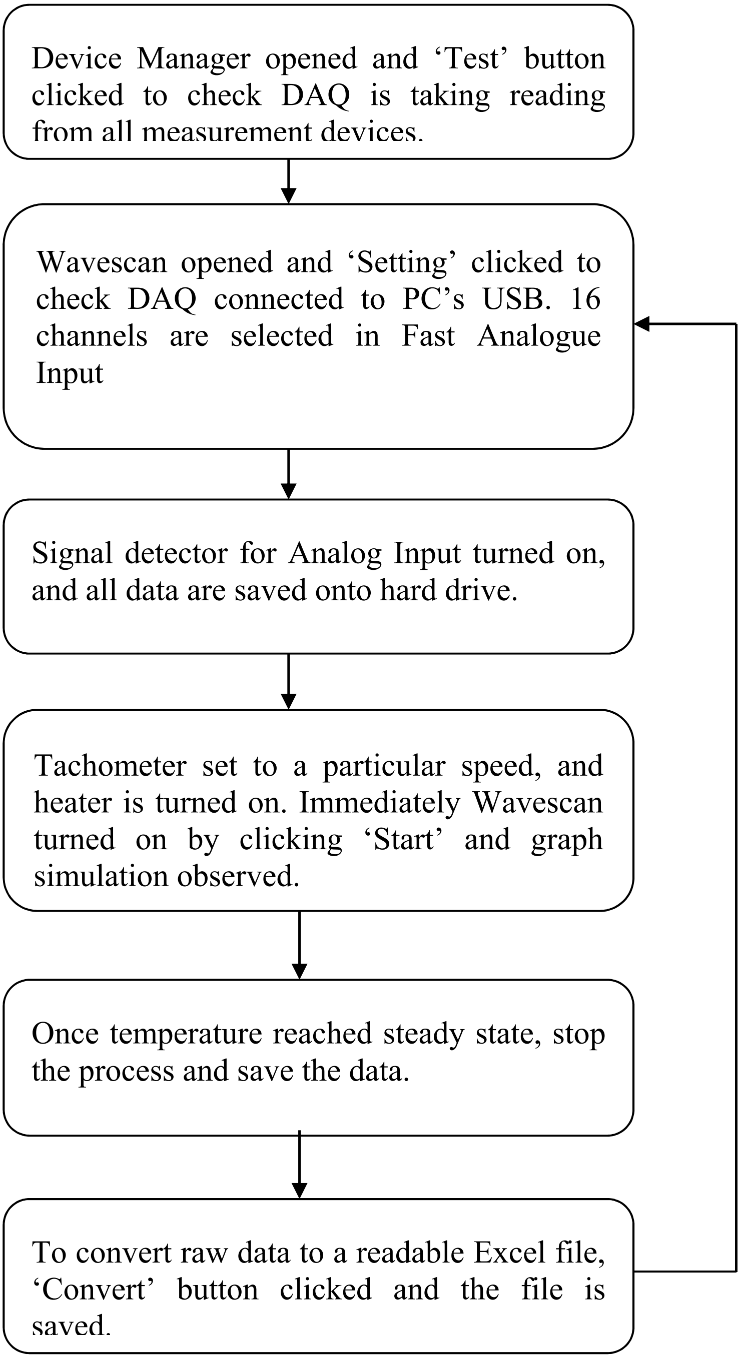

Fig. 11. Flow chart of software evaluation procedures

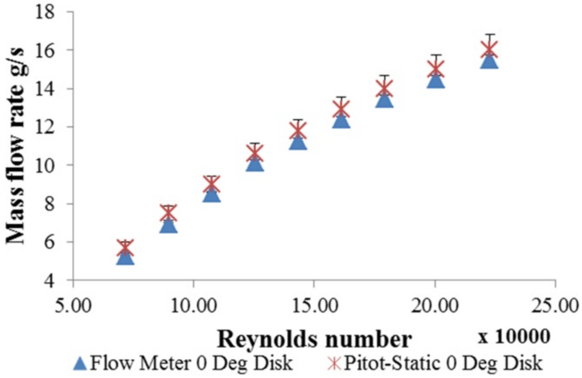

Fig. 12. Mass flow rate measured using flow meter and pitot-static manometer for straight blade brake Disk

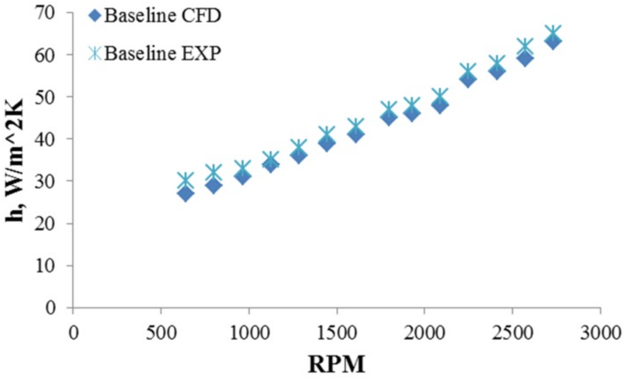

Fig. 13. Validation of CFD modeling with experimental of heat transfer coefficient for baseline brake disk for all rotational speed

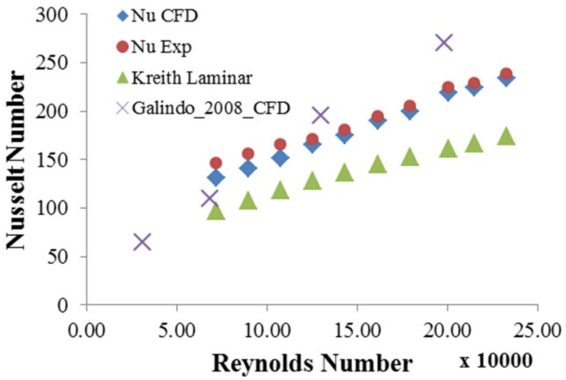

Fig. 14. Validation of CFD modeling with experimental of average Nusselt number for baseline disk brake specimen

11. Conclusion

The experimental rig is a control environment to focus on the heat transfer enhancement of the disk brake alone. The parameters like mass flow rate and Nusselt number is used for classification of the trend of heat transfer characteristics.

For instance for the above Figure 14 nusselt number plot, an expression can be derived with with curve fitting R^2 value less than 1.

For the low speed region where Reynolds number < 2.4×10^5 the Nusselt is correlated with Reynolds number with the relationship is given by:

$$Nu = \frac{h_c d_o}{2k} = 0.5 \left(\frac{\omega d_o^2}{4\nu}\right)^{0.50} \tag{9}$$

The Nusselt number against Rotational Reynolds number is given for references.

For the laminar flow condition, the Kreith et. al. (7) correlation is given in equation 10:

$$Nu = \frac{h_c d_o}{2k} = 0.36 \left(\frac{\omega d_o^2}{4\nu}\right)^{0.5} \tag{10}$$

The best fit is given by power of 0.5 for laminar flow condition which agrees well with Kreith (Kreith, Taylor, and Chong, 1959) as in the equation 10.

The experimental procedure described in this chapter can be cost effective to design an improved brake disk for industrial application on vehicles. The rig also demonstrates confident results to be used as significant contribution in disk brake heat transfer area.

12. References

Coleman, Hugh W., and W. Glenn Steele. *Experimentation and Uncertainty Analysis for Engineers*. New York: John Wiley & Sons, December 1998.

Kreith, F., Taylor, J.H., and Chong, Heat and mass transfer from a rotating disk, Journal of Heat Transfer, 1959, ol 81,pp 95-195

Mehta, R. D., and P. Bradshaw. "Technical notes, design rules for small low speed wind tunnels." (The aeronautical journal of the royal aeronautical society) 1979: 443-449.

Munsun, B. R., D. F. Young, and T. H. Okishi. "Fundamentals of fluid mechanics." (John wiley & Sons Inc) 1998.

6

The LDV and PIV Study of Co-Rotating Disks Flow with Closed Shroud

Shen-Chun Wu*
Department of Aviation Mechanical Engineering,
China University of Science And Technology, Taipei,
Taiwan

1. Introduction

The co-rotating disks system is applied to a wide range of industrial machinery. This study focuses on co-rotating disks of magnetic disk storage devices. Although numerous experimental and numerical studies have been given to the relevant flow field, the flow physics has not been completely elucidated as a result of its inherent complexity. Consequently, investigating the flow field in detail is required. Many studies have analyzed this flow type; however, for the sake of brevity, only the most relevant works are cited in this work.

Stewartson (1953) first investigated flow between un-shrouded co-rotating disks using theoretical analysis combined with flow visualization and obtained an analytic solution. However, variation in experimental parameters and detailed experimental data were lacking. Lennemann (1974) performed experiments in water to visualize flow between co-rotating disks. Using aluminum particles as light scattering agents, Lennemann visualized a laminar core of fluid extending from the hub to the periphery of the disks that rotated at about 80% of the disk rotation speed. Szeri et al. (1983) examined flow between un-shrouded co-rotating disks in detail. Laser Doppler Velocimetry (LDV) was employed in measuring only circumferential and radial velocities. The measured velocity profile indicated that fluid exists in solid body rotation. Also using LDV, Chang et al. (1989) determined the mean velocity and root mean square value of velocity fluctuation. One year later, Chang et al. (1990) investigated this flow numerically. Abrahamson et al. (1988, 1989) utilized a hot film probe to measure velocity spectra. Their experimental results indicated that the spectra converged at a single frequency. The peak energy at integral normalized frequency was obtained by dividing the measured spectra frequency by 75% of the rotating speed of the disks. The authors also utilized added bromothymol blue to co-rotating disk water to clearly show that the polygon shapes were correlated with circumferentially periodic and axially aligned flow vorticity. Schuler et al. (1990), who also employed LDV to measure the co-rotating flow in an enclosure, elucidated the solid body rotation region near the hub. Their power spectra analysis results were in agreement with those obtained by Abrahamson; however, their study presented only one measured point. Tzeng and Humphrey (1991) measured the flow between shrouded co-

---

[*] Corresponding Author

rotating disks using the LDV technique in airflow. The velocity time sequence had distinct sinusoidal-like oscillations. Humphrey and Gor (1993) visualized the flow between disks in an experimental apparatus similar to that used by Schuler et al. by illuminating micro-sized mineral oil droplets on a laser sheet. Humphrey et al. (1995) numerically analyzed the unsteady flow motion utilizing a time-explicit algorithm. Iglesias and Humphrey (1998) confirmed the existence of a symmetrical pair of counter-rotating vortices in the cross-stream (r-z) plane via numerical results. Herrero et al. (1999) continued this line of research. Randriamampianina et al. (2001) carried further analyzed co-rotating disk flow numerically. Wu and Chen (2002) examined large-scale structures between shrouded co-rotating disks. Two LDVs and a phase-averaged technique scheme were applied to examine the coherent structures. Based on reconstructed streamline patterns, three distinct flow regions were quantitatively identified. Using the same apparatus and technique, Wu and Chen (2003) examined shrouded co-rotating disks, and measured density points that were four times of that obtained one year before. The measured instantaneous velocity (phase-averaged) fluctuations were also applied to calculate Reynolds stresses for exploring turbulent flow dynamics. Wu et al. (2006) examined the flow between a pair of enclosed co-rotating disks using LDV. A systematic measurement with wide Re ranging from 10^4 to 10^6 was conducted, and the effect of Re on the flow structure was investigated. They performed a power spectra analysis and developed an equation for calculating the number of outer region vortices. Wu, (2009) examined the coherent flow between enclosed co-rotating disks using PIV. The core region revealed that a pair of circular flow structure acts like an annular chain to surround the large-scale vortex. This finding was not reported in the literature.

Flow visualization techniques (Lennemann et al., 1974; Abrahamson et al., 1989; Humphrey and Gor, 1993) or point-wise velocity measurements (Chang et al., 1989; Schuler et al., 1990; Wu and Chen, 2002, 2003; Wu et al., 2006; Wu, 2009) were applied in early experimental studies. However, a complete experiment conducted in both the $r-\theta$ plane and the $r-z$ plane was still not found. Point-wise experimental techniques, such as LDV or Hot Wire Anemometer (HWA), were limited to acquiring time-averaged velocity. Although phase-averaged measurement results were obtained, those results were not instantaneous. Thus, the present effort attempts to complement this work with planar velocity measurements via PIV, permitting structural and instantaneous interpretation of the kinematical behavior for this flow type. PIV reveals instantaneously and quantitatively the global structures in a two-dimensional or three-dimensional flow field without disturbing the flow, and are extremely effective and necessary. Consequently, this work utilizes the LDV and PIV technique. In addition, flow visualization image in each plane is employed to examine the flow structure established based on the velocity measurements.

2. Experimental method and apparatus

In this work the parameters of a 3.5-inch hard disk are adopted as the reference to determine the dimensions of the test configuration and the values of the relevant flow parameters for the enclosure co-rotating disk pair flow via dynamic similarity.

2.1 Flow facility

Fig. 1 schematically depicts the investigated geometry. The experimental model comprised a motorized test section fixed to an inertial test stand. Two rigid disks were concentrically clamped to a hub. The disks were made of transparent Plexiglas and had a thickness of 10mm. The spacer (D) measuring 17.4mm in diameter and having a radius of R_1=59.4mm, was used to separate the disks in the spindle axis direction (z direction). Measurements were performed at the middle of the test section. The test section shroud was also made of transparent Plexiglas with an axisymmetric inner wall and a radius of $R_3 = R_2 + a$ = 189.5mm. Flow visualization in the $r-\theta$ plane was also limited to the inter-disk mid-plane. In this work, dimensionless axial distance of disks was set at S =0.09, and the Reynolds number was Re=5.25×10^5. The values of Re and S correspond to the rotation speed of about 12000 rpm for the next generation hard disk and general disk space. An approximate dynamic similarity is ensured by setting $Re_{(model,\ water30^\circ C)} = Re_{(prototype,\ air30^\circ C)}$. Pure water was utilized as the working fluid to attain high Reynolds number at relatively low model disk rotation speed of Ω = 133rpm.

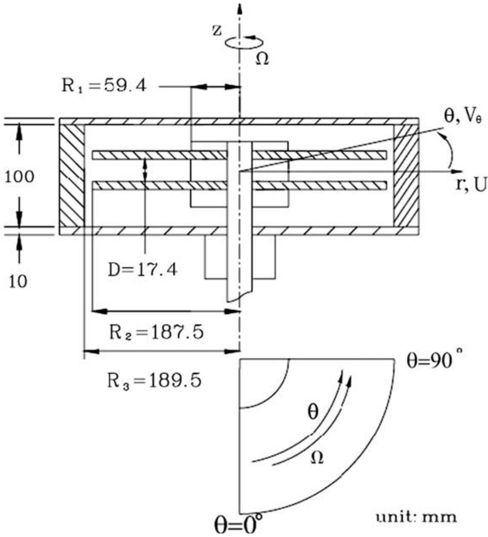

Fig. 1. Sketch of configuration coordinate system and of the test section.

2.2 LDV system

The principle and practice of LDV have been introduced elsewhere, e.g. Durst et al. (1981). The LDV systems with direct relevance to the present study are introduced here. Two laser velocimeters, an LDV and a Phase Doppler Particle Analyzer (PDPA), were utilized in order to carry out phase-averaged measurements. The schematic of the optical arrangement is shown in Fig. 2. The two component fiber-optic LDV system worked in a forward scattering mode during the measurements. The optical module consisted of the following components: a TSI Model 9201 Colorburst Multicolor Beam Separator, four Model 9271 couplers, an argon-ion laser (Coherent Innova 90, 2W), a probe with front collimating lens of 350 mm focal length, a single-mode polarization-preserving fiber, a Bragg cell, two pinhole filters and two photomultiplier optics sections. The associated electronics included two photomulipliers, two electronic frequency shifters, three TSI 1990C counter processors, a TSI-MI990 buffer interface. The PDPA system consisted of five major components:

transmitter, receiver, signal processor, motor controller box, and a computer. The Aerometrics model XMT-1100-4S transmitter was used to generate two equal intensity laser beams and to focus them to an intersection point that formed the measurement region. The transmitters contained a Spectra-Physics model SP-106, 10mW, and polarized helium-neon laser. Optical components within the transmitter served to focus, partition, and collimate the laser beam. A beamsplitter with radial diffraction grating helped to produce a frequency shift on measured particle signals. The Aerometrics model MCB-7100-1 motor controller was used to monitor and control the frequency shift. The receiver model RCV-2100 collected the light scattered from seeding particles. The receiver was then connected to the PDP-3100 signal processor with 2 μs resolution to process the Doppler signals. The analog output of the PDP-3100 signal processor was transmitted to the TSI counter processor. Pure water was used as the working fluid in the experiment. MgO particles with a diameter of about 1.2 μm, were adopted as seeding material in the LDV measurements.

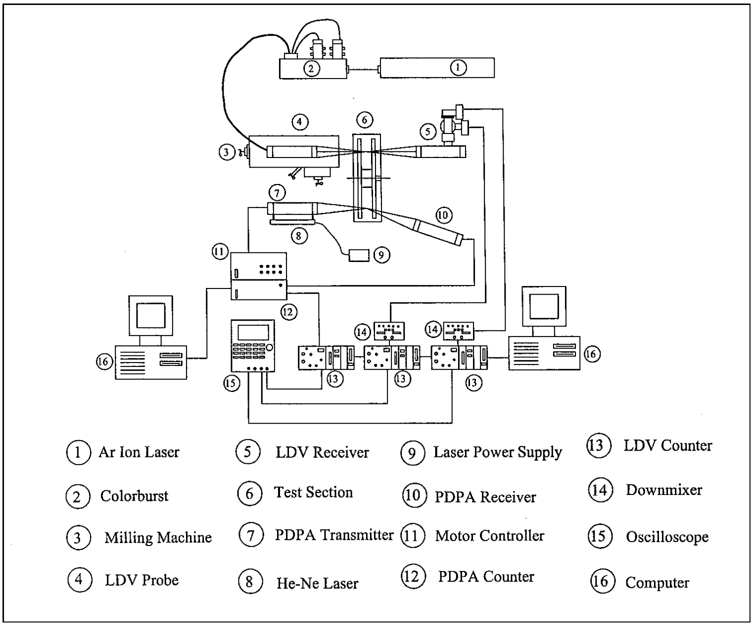

Fig. 2. Sketch of LDV experimental apparatus.

3. Measurement technique and data reduction

During the measurements, the PDPA probe was fixed at a specific position (r*=0.75, Z/H=0.5) where the circumferential velocity power spectra had peak values. To investigate the vortical structures, all of the LDV measurements were made in a quarter of the center plane between the two co-rotating disks. In the measurement domain there were totally 4096 points. The PDPA probe was kept at the specific position as phase reference while the LDV probe was translated in the measurement domain by a three-axis translation stage with an uncertainty of 0.02 mm. Doppler burst signals detected from PDPA and LDV were transferred to the LDV counters, which worked in coincident mode under the control of the

TSI MI-990 interface module. A coincident time window length (0.1 ms) was set in the MI-990 interface module to test the synchronization of burst signals detected by PDPA and LDV. The burst signals were processed to compute the Doppler shift frequency, as the time intervals of signals detected by PDPA and LDV were lower than the coincident time window length. Data of Doppler shift frequency was then transferred to a personal computer via a DMA interface card. The velocity values were further calculated and then the time sequence was stored. The coincident data rate was kept at about 2000 Hz as the measurement was made, which was high enough to resolve the periodic motion of vortical structure with 5.08Hz of frequency in the present study. In each measurement, more than 20,000 samples of time sequences of reference point and measuring points were collected, respectively. All of the time histograms of velocity, whether circumferential or radial component, were measured with respect to the same phase reference point. Measurement examples using the phase-averaged method are shown in Fig. 3. A cycle was built between two adjacent crests of time series of U_{ref}, and was then divided into ten phases of equal time interval with phase one and phase ten corresponding to the crests. Velocity values of U_r and V_θ corresponding to each phase instant defined by U_{ref} were sampled and averaged, respectively. In order to investigate periodic flow fields, a decomposition of velocity proposed by Hussain and Reynolds (1972) was adopted here, a time varying velocity u can be decomposed into a global mean component $\overline{u}$, a periodic mean component $\tilde{u}$ and a random fluctuation component u'. This triple decomposition can be written as follows:

$$u = \overline{u} + \tilde{u} + u' \qquad (1)$$

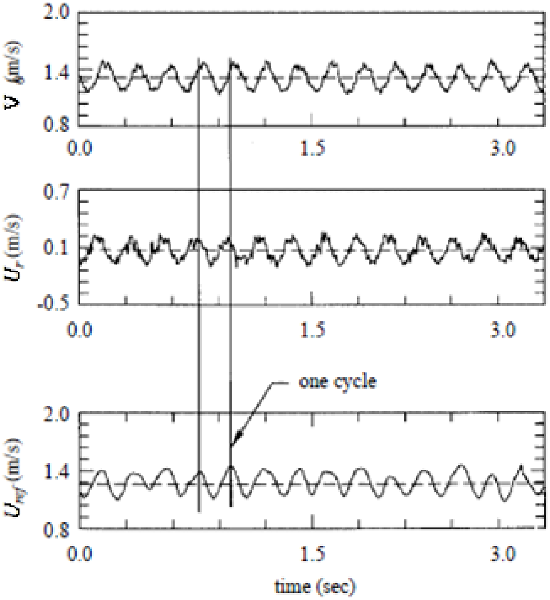

Fig. 3. Typical time records of the circumferential and radial velocity at r*=0.40

The bias of calculating global mean velocity was corrected by the method provided by McLaughlin and Tiederman (1973). In situ calibration was carried out with an oscilloscope and the maximum velocity bias was estimated to be less than 2%. Uncertainties of the phase-averaged velocity and Reynolds stresses were estimated statistically. The maximum uncertainty for phase-averaged velocity was about 4.5% at the 95% probability level. A typical value was about 1.2%.

3.1 PIV system

PIV is a non-intrusive technique for simultaneously measuring velocities at numerous points in a flow field. The fluid was seeded with tracer particles to illuminate the region under investigation. An image of the illuminated region was captured and then, a second image was taken shortly after. Appropriate analysis of these images produced an instantaneous velocity vector map. The PIV theory was introduced by Adrian (Adrian, 1984). At that time, due to hardware limitations, a single photographic frame was exposed numerous times and analyzed using an auto-correlation technique. However, enhanced photographic speed recording soon facilitated capturing separate frames for analysis using cross-correlation (Keane and Adrian, 1992). The cross-correlation technique is generally impractical for high-speed flows; the time interval between video frames is sufficiently long that any correlations between particle positions are lost (Willert, 1991). Auto-correlation, conversely, permits spacing of exposures as close as the light source allows without overlapped particle images.

The PIV system appears in Fig. 4 present the PIV system. For PIV measurements, double pulsed Nd:Yag lasers supplied the pulsed laser sheet (power, 170mJ/pulse) to illuminate the flow field being measured. Thus, the pulse duration and delay resolution were 50 ns. Each laser had a nominal repetition rate of 10Hz, and could emit double-pulsed lasers. Polycrystalline particles (particle diameter is about 30μm, density is 0.98 g/ml) were utilized as PIV tracers in the flow field. A Nikon F4 camera was employed to capture PIV images. A laser-sheet head, 1.5 mm thick, was mounted on an optical table, and generated a laser-light sheet that intersected the camera optical axis perpendicularly. The twin Nd:Yag lasers and camera were controlled via a synchronizer. The experimental system recorded 30 velocity fields per second. Each velocity field was obtained from a pair of consecutive images; the second image in the pair was captured 1ms after the previous image via a frame straddling approach. The PIV images captured by the camera were digitized by a scanner, and then transferred to a computer for image processing. The spatial resolution of the images was as high as 2400×1600 pixels.

The PIV image was transferred to a computer for gray scaling. The processed image with 256 gray levels was then divided into several small interrogation areas for quantifying the average particle displacement within each of them. The images were divided into 64×64 pixel interrogation areas, and 50% overlap grids were employed for the PIV image processing. Commercial software (TSI Insight) was used to process the PIV image and to compute the velocity vectors through the auto-correlation algorithm. Since the vortex structures or velocity reversals would not be presented in the laboratory frame, the velocity field could thus be calculated without directional ambiguity from a single double-exposed PIV image.

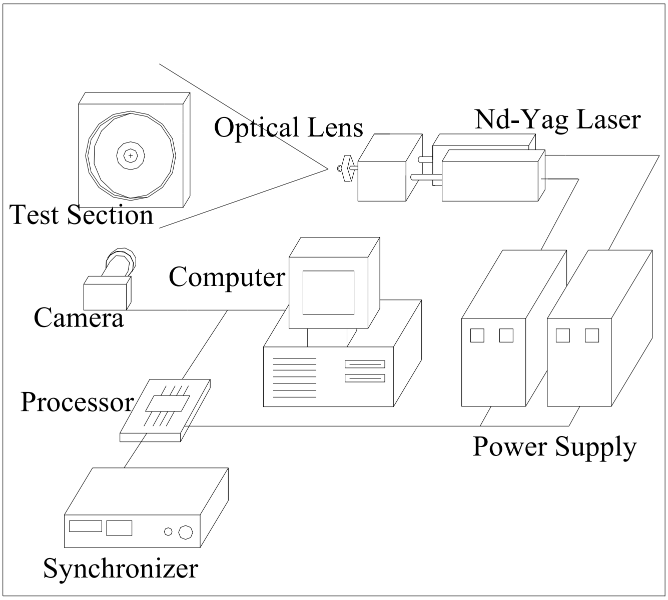

Fig. 4. Sketch of PIV experimental apparatus.

The accuracy of velocity measurements was estimated, depending on the ability to determine the displacement of a particle (Adrian, 1991). Here, a parabolic interpolation method was used to search for the peak of the autocorrelation function with sub-pixel accuracy, and hence the uncertainty of the vector-processing algorithm was reduced to 0.03 pixels. The time interval between two pulsed lasers was chosen to give the particle displacement of not less than 6 pixels, to keep a relative error below 0.5%. For a typical flow velocity of 1.5 m/s, this error corresponds to a velocity error of 70.75 cm/s. However, there are a number of other aspects in PIV measurements that can affect the accuracy of measurements due to imperfections in the apparatus, the particular PIV parameters used, and the nature of the flow being measured. In order to ensure the reliability of PIV measurements, a calibration based on the comparison of the measurement results of LDV and PIV was applied. Here, the time average of the instantaneous velocity measured by PIV was compared with the mean velocity measured by LDV. The deviation between two velocity data was found to be within 3%.

3.2 Flow visualization

Flow visualization was performed to confirm the flow field division identified by the velocity measurements. Fig. 5 presents the experimental apparatus for flow visualization in both the $r-\theta$ plane and the $r-z$ plane. To visualize the flow structure in the $r-\theta$ plane, a flow visualization technique that displays particle distribution was used. Briefly, a light sheet generated by the laser from the Ar+ system illuminated magnesium oxide particles. Particle diameter was 1.0μm and density was 1.5–5.5 g/ml, resulting in a Stokes number of 10^{-6}. The particles were injected into the flow field adjacent to the hub using an injector inserted through the enclosure. Near the hub where the flow was in solid body rotation, the particles accumulated and reflected the light sheet to illuminate the region. Away from the hub where the flow mixing rates were high, the few particles penetrating from the bright region were diluted rapidly.

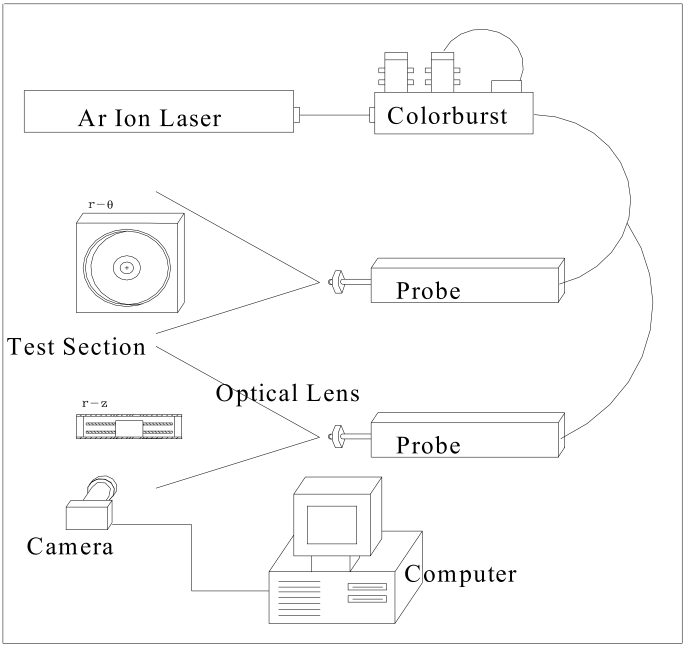

Fig. 5. Sketch of flow visualization experimental apparatus.

The flow visualization in the $r-z$ plane emphasizes the region near the enclosure where the flow exhibits a complicated pattern. To visualize the above mentioned flow motion, Rhodamin B was injected near the enclosure. As a result, the fluid in this cross stream flow contained more dyes than the flow near the hub where the fluid was in solid body rotation around the hub center. When illuminated by the light sheet, the flow regions where the dyes were in abundance appeared bright and the near hub region appeared dark. With the concentrations used, this method might obtain the impressions of the cross-stream flow motion. A useful consequence of this method is that the different dye concentrations help one to distinguish between regions of different flow region.

4. Results and discussion

4.1 LDV measurement

4.1.1 Mean velocity profiles

Fig. 6 shows the normalized mean circumferential velocity component measured as a function of the radial position along the symmetrical plane, midway between the two disks (z=0). The mean values have been normalized by the local disk speed. A horizontal dashed line was plotted to represent the local disk speed U/rΩ=1. The dashed line manifests the solid body rotation. Fig. 6 shows that the velocity of the fluid begins to deviate from the solid body rotation at the position of about r *=0.35 in the present study. Included for comparison are also the results measured by Abrahamson and colleagues (1989) (Re=4:5×10^5) and Tzeng and colleagues (1991) (Re=7.9×10^4). The circumferential velocity begins to deviate from the solid body rotation at nearly the same dimensionless radial position of about 0.45 in the results measured by Abrahamson (1989) and Tzeng and their colleagues (1991). The difference is caused by the larger axial distance of the disks in the present work. The dimensionless axial distance in the other studies was fixed at S/D= 0.05, whereas the value adopted in this study was S/D= 0.12. The axial distance of the disks in the studies of Abrahamson (1989) and Tzeng (1991) and their colleagues was so small as to prevent the inflow with momentum deficit from penetrating a greater distance inside. For comparison, the experiments were also performed at S/D=0.05. As can be seen, good agreement can be found between the present results and those of Abrahamson (1989) and Tzeng (1991) and their colleagues.

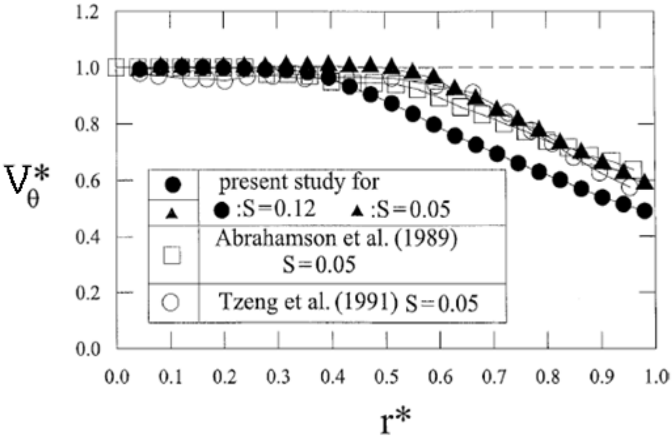

Fig. 6. Radial profiles of the circumferential mean velocity.

4.1.2 Power spectra

Fig. 3 shows the measured time-resolved circumferential and radial velocities at the midplane between the two disks at r *= 0.395. These time sequences display distinct sinusoid-like oscillations. The Fourier spectra of radial and circumferential velocities at several radial positions were calculated. The results of radial and circumferential velocity power spectra were presented as examples in Fig. 7 and 8. The actual frequencies of the spectra were normalized by 0.75 times the disk rotational frequency. The spectral results show peaks in energy at an integral normalized frequency of f *= 3. Abrahamson and colleagues (1989) reported similar results. In addition to the spectral frequency, Fig. 7 shows a plot of spectral intensity as a function of radial position. For radial velocity, the spectral intensity increases with r* and reaches a maximum value at about r*=0.47; it then begins to decrease to as weak a value as r*~ 1. The radial velocity is most energetic at r*~0.5, and its spectral intensity displays good symmetry to r*~0.5.

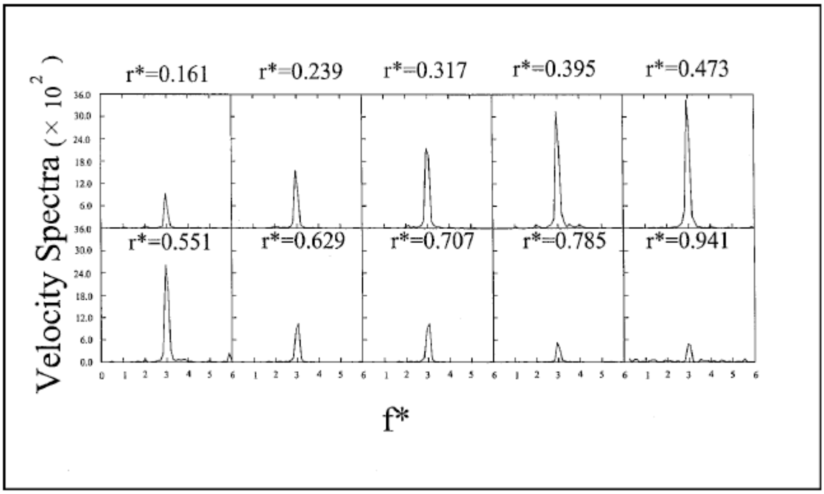

Fig. 7. Normalized spectra of circumferential velocity fluctuation at various radial positions.

It is to be noted that the distribution of spectral intensity for circumferential velocity (as shown in Fig. 8) is quite different from that of radial velocity. There are two local maximums of circumferential power spectra intensity. The first local maximum value takes place near the point r*= 0.4. It is also the most energetic spot for circumferential velocity because the highest value of the circumferential spectral intensity arises there. It recalls the point at the interface of the inner and outer regions, as discussed previously. The second local maximum occurs at r *= 0.72. It is located at the center of the vortical structure. Thus, it is clear that the circumferential velocities are more energetic at the interface of the inner and outer regions and also near the center of the vortical structure.

Streamline patterns at different phases

Fig. 9a shows the vector fields, and Fig. 9b shows the streamline patterns for one of the 10 phases, as observed with a 0.75 Ω reference speed. Fig. 8 shows the streamline patterns as observed with a 0.75 Ω reference speed. The streamline patterns at different phases during the passage of one vortex are demonstrated as an example. Some other reference speeds were also tested. The test results reveal that the vortical structure could not be recognized at a higher reference speed. On the contrary, the vortical structure is located in the solid-body rotation region at a lower reference speed. This phenomenon is obviously unreasonable. The appropriate rotational speed was found to be (0.75±0.05) Ω in the present case. A similar reference velocity was found by other researchers, such as Abrahamson and colleagues (1989). In their work, the camera was mounted on a motor that followed the rotation of the disks. The vertical structure could not be observed under a fixed-reference frame. Three distinct regions can be distinguished from the streamline patterns in Fig. 10.

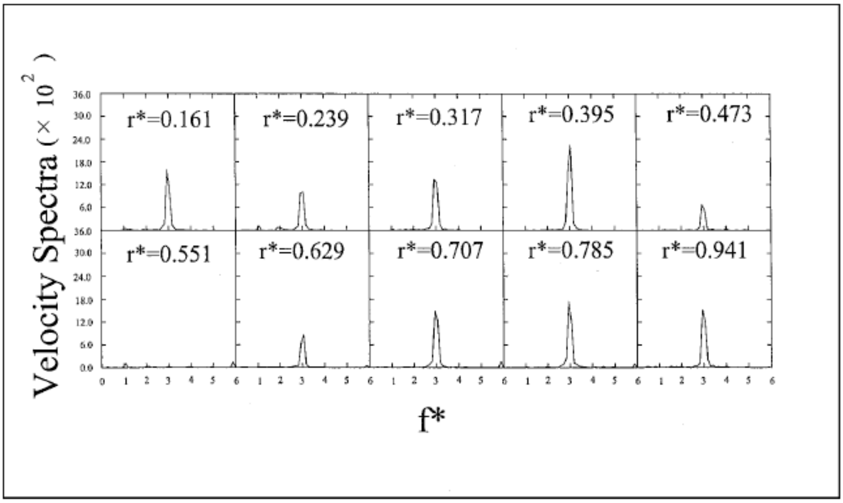

Fig. 8. Normalized spectra of circumferential velocity fluctuation at various radial positions.

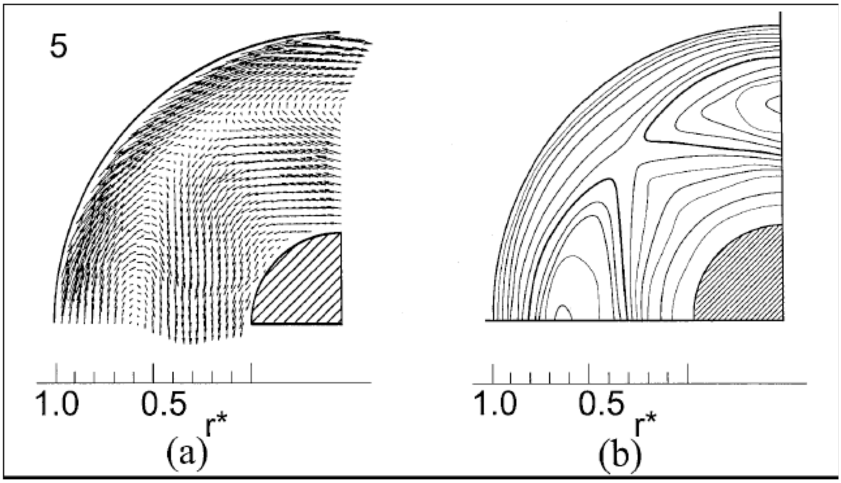

Fig. 9. Velocity vector and streamline patterns. (a) Velocity vector, observed at a reference velocity of 0.75Ω. (b) Streamline pattern, observed at a reference velocity of 0.75Ω.

The inner solid-body rotation region ranges from r*= 0 to 0.35; the outer vortical structure region from r *~0.35 to 0.9; the shrouded boundary layer region from r *=0.9 to 1. It is noted that there seems to be no radial flow across the boundary between the rotating disks and the outsides of the disks, as shown in Fig. 10.However, because the centrifugal force acts on the rotating fluid, there must exist radial inflow and outflow. The inflow and outflow regions rotate in the same direction as the disks, forming a periodic flow field (Mochizuki, 1993). Extended experiments have been carried out in the cross stream (r-z) plane (Wu, 2000). The experimental results show that there is indeed radial flow. However, the circumferential components are much larger than the radial ones, so the radial flow is not clearly observed from the phase-averaged measured data.

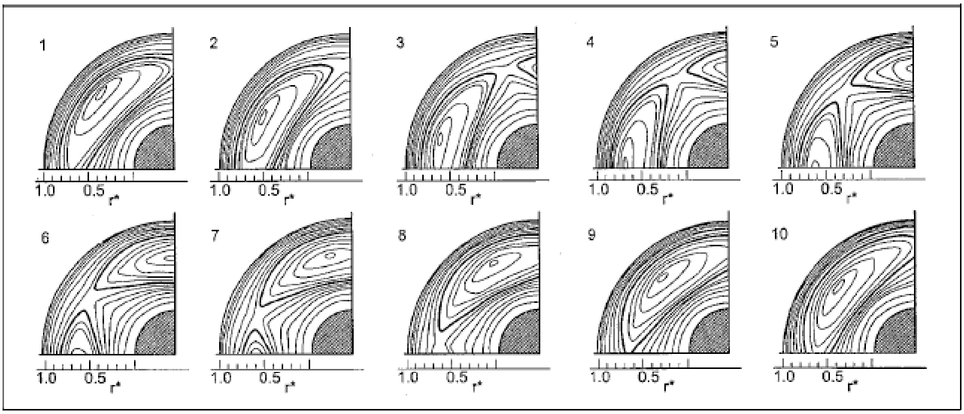

Fig. 10. The streamline patterns at various phases at a reference velocity of 0.75Ω and a contour interval of 0.2.

Although only a quarter of the frame was reconstructed, the number of the vortical structure can be easily determined to be 3. This integer is the same as the normalized frequency found in the power spectra analysis, as shown in Fig. 7 and 8. These findings demonstrate that the velocity oscillations result from the periodic passage of flow structure. The center of the vortex is located at r*= 0.72. In addition, the radius of the inscribed circle of the vortical structure is found to be the same as thatcalculated by the formula $Ri=R_2((N-\pi A)/(N+\pi A))$, as proposed by Tzeng and colleagues (1991), where $\pi A = N - fs/\Omega$. The oscillatory frequency fs measured is 9.9 Hz, and the number of the vertical structure N is 3 in the present study. The inscribed circle radius calculated by the formula is thereby Ri=108.7 mm. In Fig. 9, the inscribed circle of each phase was drawn to find its radius, and the average value of the 10 radii was taken. The inscribed circle of the polygonal structure with the average radius intersects the dimensionless radial position at $r^*=(r-R_1)/(R_2-R_1)=0.4$, corresponding to r = Ri = 110.7 mm. There is little difference between the calculated and measured values.

4.2 PIV measurement

Fig. 11(A)-1 presents the instantaneous velocity field at Re= 5.25×10^5 ($\Omega = 133$ rpm and f_n =2.22Hz). The radial velocity profile along $\theta = 0^o$ is found to increase with increasing r (from the hub) until about $r^* = 0.5$ and then decrease near the shroud. The fluids within $r^* = 0.5$ are primarily moved by the rotating disks. Beyond $r^* = 0.5$, shroud shear stress increases gradually and, hence, impacts fluid velocity. No structure would be found in the laboratory frame (Fig. 11(A)-1). By subtracting a reference velocity from the original circumferential velocity, a rotating reference frame is simulated to reveal the vortex structure. The camera frame rate is controlled to identify the reference velocity. When the frame rate is 1.66Hz (75% of the disk rotation rate) and reference velocity is 0.75Ω, the motion of vortex structure is frozen, i.e., the vortex in sequence pictures are almost on the same rotation phase.

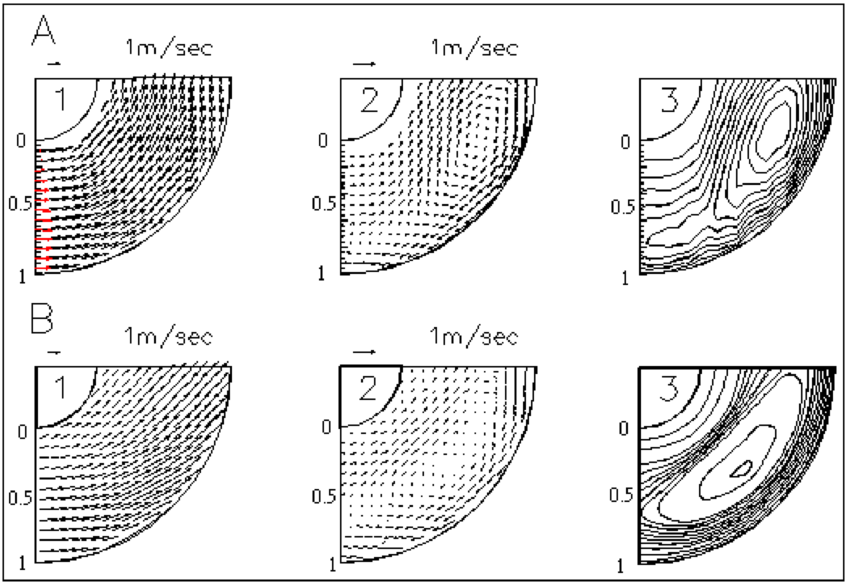

Fig. 11. Procedure for reconstructing the flow patterns with a simulated rotating reference frame. Stream line pattern A：PIV，B：LDV.

Above results demonstrates that the vortex structure rotates at 75% of disk rotation velocity and can be observed correctly by an observer moving at this reference velocity. Fig. 11(A)-2 presents the velocity field with this reference frame. Then Fig 11(A)-3 presents the streamlined pattern of the reference frame obtained by integrating results (as Fig. 11(A)-2). The inner flow region surrounding the hub is a polygon shape. Beyond the inner region is the outer region containing circumferentially periodic large-scale vortex structures.

Abrahamson et al. (1991) also identified an outer region that is dominated by large-scale vortex structures. These structures are almost evenly distributed around a circle, approximately two-thirds of the distance between the hub and the shroud, and generally span the radial of the outer region. Here, the rotating reference velocity is set at 70–80% of the disk rotation speed, and a reference velocity higher or lower than 70–80% of the disk rotation speed would cause the vortex center to deviate from the radial location again.

To exhibit the periodic variation characteristics of the flow, the measured data was processed using the phase averaged method(Eq.1). Fig. 11(B)-1 shows the processed velocity field. The principle associated with method was utilized by Wu and Chen (2002). Fig. 11(B)-3 presents the integrated streamline pattern for the rotating reference frame.

Although the grid finenesses in Fig. 11(A)-3 and Fig. 11(B)-3 are similar, the streamlines in Fig. 11(B)-3 are smoother. Moreover, unlike the results for the phase-averaged LDV measurements that reveal a symmetrical vortex (Fig. 11(B)-3), the vortex front revealed by

PIV measurements has the shape of an arc with a pointed rear section. Fundamentally, LDV is a point measurement technique. When combined with a phase average process, LDV can obtain the global mean and periodic mean components ($u=\overline{u}+\tilde{u}$), and generally not the fluctuation term (u') if the data rate in a cycle is not sufficiently high. The vortex identified by PIV measurements acquires the vortex structure; whereas its irregular shape exhibits the perturbation of instantaneous velocity.

Appropriate PIV measurements can obtain the complete and instantaneous velocity components and, hence, provide the real flow information. To acquire the whole field velocity by LDV, time-consuming point-by-point measurements are required. Moreover, an additional laser is required to freeze the flow using a phase-averaging method and, hence, measuring work becomes extremely complicated. However, PIV can measure the whole field velocity effectively. Additionally, time resolved PIV measurements can be achieved by controlling the camera frame rate; an advantage cannot be realized with LDV.

4.3 Flow visualization-the $r-\theta$ plane

The flow visualization photograph taken at the instant before the particles injected near the hub diffuse uniformly and streamlines constructed from measured velocity vector field are depicted in Fig. 12. Note that in flow visualization particles are injected once and the injector is then removed. After several seconds, the particles diffuse to fill the inner region. The flow visualization image in the $r-\theta$ plane clearly reveals two regions. The existence of a partition between the inner and outer regions is verified by the accumulation of most particles in the inner region for several minutes. The inner region is bright as the particles bounded there strongly reflect the illuminating light. Beyond the inner region, only few particles exist and have a diffuse, grainy distribution. The triangular boundary of the inner

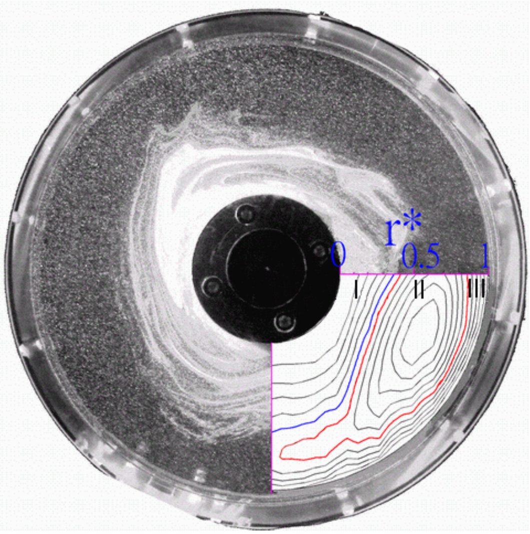

Fig. 12. Flow visualization photograph and stream line in the $r-\theta$ plane ($\mathrm{Re}=5.25\times10^5$, S=0.09).

region rotates at a speed slightly slower than the disks. Furthermore, the radius of the inscribed circle of the triangle intersects the radial coordinate axes at about r*=0.39. Fig. 11(A)-3 is also inserted on the right lower corner of Fig. 12. It is seen that for the present co-rotating disk flow, periodic vortex structures rotate at about 75% of disk rotation speed. Consequently, the outer region and shroud region can be identified.

The above flow visualization is performed to verify the division of the flow field based on PIV measurements. Based on the reconstructed flow patterns obtained by PIV and flow visualization (Fig. 12), the flow field is divided into three regions: (I) inner region (solid body rotation region) (0.04<r*<0.39); (II) outer region (vortex region) (0.39<r*<0.75); and, (III) shroud region (0.75<r*<1).

4.4 Flow visualization-the $r-z$ plane

The flow visualization in the $r-z$ plane is also conducted. In Fig. 13(A), due to the solid body rotation, the injected dyes can not penetrate near the hub, resulting in a dark solid body region (Fig. 13(C) sub-region 1st). When illuminated by the light sheet, the boundary layers (Fig. 13(C) sub-region 4 th) on both the upper and lower disk surfaces are clearly observed. The fluids from the boundary layers are redirected in the axial direction adjacent to the enclosure wall, and hence cause a thin shroud shear layer (Fig. 13(C) sub-region 8 th) on the wall surface. These two axial flows collide and merge on the enclosure wall, and they are subsequently pumped radically inward by the adverse pressure gradient force. In order to balance the mass flux, the Ekman layer (Fig. 13(C) sub-region 6th) is induced to replace the outward flow through the boundary layers and hence maintain the cross-stream circular flow(Fig. 13(C) sub-region 5th). As a result, an axial flow layer appears slightly outer than the solid body region and spans the distance between two disks. This flow layer is designated as a detached shear layer (Fig. 13(C) sub-region 3rd) resulting from the different rotations in the solid body region and in the Stewartson flow region (Fig. 13(C) sub-region 7th). The flow field in the $r-\theta$ plane can be divided into three regions. The radial extents of these three (I II III) regions are also indicated in the top of Fig. 13(C) in order to make a comparison of the flow regions in the $r-\theta$ plane with the regions in the $r-z$ plane.

4.5 Velocity distribution

Fig. 13(B) shows the normalized radial and circumferential velocity distribution at different radial positions respectively. The flow performs solid body (region I; Fig. 13(C) sub-region 1st) rotation between r*=0.04 and r*=0.39, as can be easily seen. The boundary layer (Fig. 13(C) sub-region 4th) starts to grow at r*=0.39 and develop gradually along the radial direction toward the shroud. At this moment, note that the fluid in this flow is dominated by the rotating centrifugal force, adverse pressure caused by the static shroud and the Coriolis force induced by the rotation of these two forces. Within the interface between inner and outer regions, the fluid is first affected by adverse pressure force and is no longer subject to solid-body rotation. The above mentioned three forces affect the flow obviously. The fluid is first dragged by the Coriolis force to flow toward the face of disk. Then, the fluid near the disk affected by the centrifugal force flows radically outward and hence forms the boundary layer there. Since the centrifugal force grows along the radial direction, the boundary layer also becomes thicker, as shown in Figs. 13(A) and 13(B). However, within the

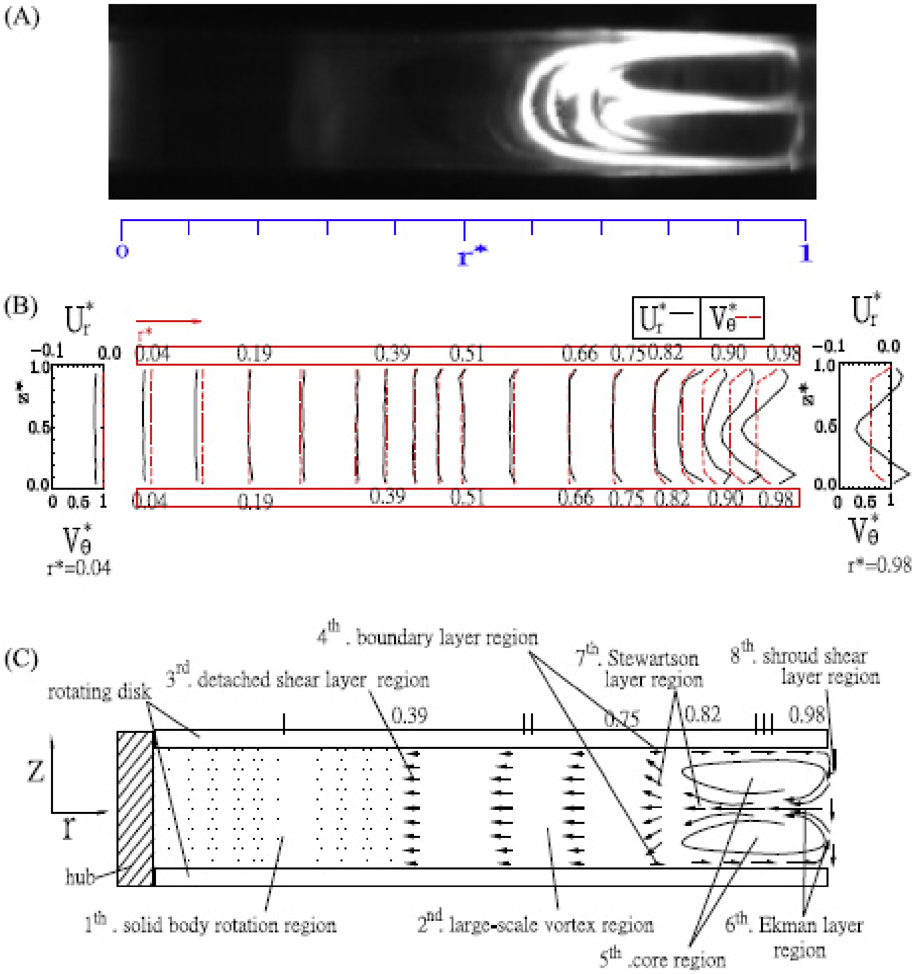

Fig. 13. (A) Flow visualization, (B) velocity distribution (LDV), and(C) sketched characteristics and divisions of flow field in the $r-z$ plane ($\mathrm{Re}=5.25\times10^5$, S=0.09).

region very close to the shroud (r*=0.98), the adverse pressure induced by static shroud strongly impacts the flow. The centrifugal force causes the fluid along the disk to flow outward, while the adverse pressure causes the fluid placed in the middle of two disks to flow inward. The imbalance of these two forces creates two symmetric circular flow (Fig. 13(C) sub-region 5th) appearing near the shroud. In the flow field, the circumferential flow velocity is much higher than the radial one, hence, the radial extent where the fluid backflow from the shroud is restricted to be near the shroud and within the region where the adverse pressure can affect (about beyond r*=0.75). This region (0.75<r*<1.0) within which the influence of boundary effect is obvious is referred to as shroud region (region III) . In the $r-z$ plane, experimental results indicate the flow structure can be divided into six sub-regions.

4.6 Integrating each plane results

According to the PIV measured velocity field, flow visualization and the prior LDV measured velocity field, the flow between disks can be identified into three regions which in fact consist of eight sub-regions. The flow patterns are sketched in Fig. 13(C), and each sub-region is described respectively as follow:

i. **Inner region** ($0.04<r^*<0.39$): The dimensionless circumferential velocity remains constant and the flow performs **solid body rotation**. (solid body rotation region also is sub-region 1st)
ii. **Outer region** ($0.39<r^*<0.75$): The dimensionless circumferential velocity declines radially outward and the **large-scale vortex** structures are observed in this region (the vortex structure is sub-region 2nd). Within the vortex region, there are boundary layers on the face of both disks. The **detached shear layer region** (sub-region 3rd) resides between the solid body rotation region and the vortex region. The **boundary layer region** (the boundary layers on both disks are the sub-region 4th) starts at $r^*=0.39$ on the disk surface and gradually develops to the disk edge.
iii. Shroud region ($0.75<r^*<1$): The flow is three-dimensional in this region. In the core of the flow field, the fluids flow inward by the adverse pressure gradient and induce a pair of circular flow. The core region is the sub-region 5th, which contains both the upper and lower circular flow, but not includes the other parts of the circular flow. The sub-region which is not inclusive in sub-region 5th is the Ekman layer region (sub-region 6th). The circular flow structure acts like an annular chain to surround the outer-region vortex. As the result, the vortex would not be flung out of the outer region by the centrifugal force, and hence cause the vibration of the whole flow field. The Stewartson layer region (sub-region 7th), where three vortices compromise mutually, locates between the vortex region and the shroud boundary-layer region. Besides, the shroud shear layer region (sub-region 8th) lies between disk edge and shroud. In addition, the circumferential velocity (Fig. 13(B)) component in the 5th core region reveals that a pair of circular flow structure acts like an annular chain to surround the 2nd sub-region large-scale vortex. This finding is also not reported in the literature. Among these sub-flow regions the 5th to 7th flow regimes are not identified previously.

4.7 The phase velocity

Fig. 14 presents normalized mean circumferential velocity (marked with ●) distribution along the radial direction on the mid-plane measured by PIV. The flow field is easily divided into two regions. First, the normalized mean circumferential velocity remains about 1, from $r^*=0$ to $r^*=0.39$. This region is the solid body rotation region. Second, from the location $r^*=0.39$ to $r^*=0.98$, the normalized mean circumferential velocity decreases from 1 to approximately 0.54. Abrahamson et al. (1989), who performed a similar study, defined the first region as the inner region and the second region as the outer region.

At this point it should be mentioned that the vortex structures rotate at 75% of the angular velocity of the disks (mentioned in the Introduction), and the disk rotating period Ω is 133rpm. By controlling the camera frame rate, the phase-resolved PIV measurement is achieved. Here, the velocity fields at different phases are measured and the camera time interval is set at 1/15 of the vortex structure rotation period. (A vortex is divided into 5 phases). A synchronizer controls the laser repetition rate and camera frame rate. However, the camera cannot take repeated images using such a short interval. To achieve this sampling interval, the trigger time is shifted one period for each run.

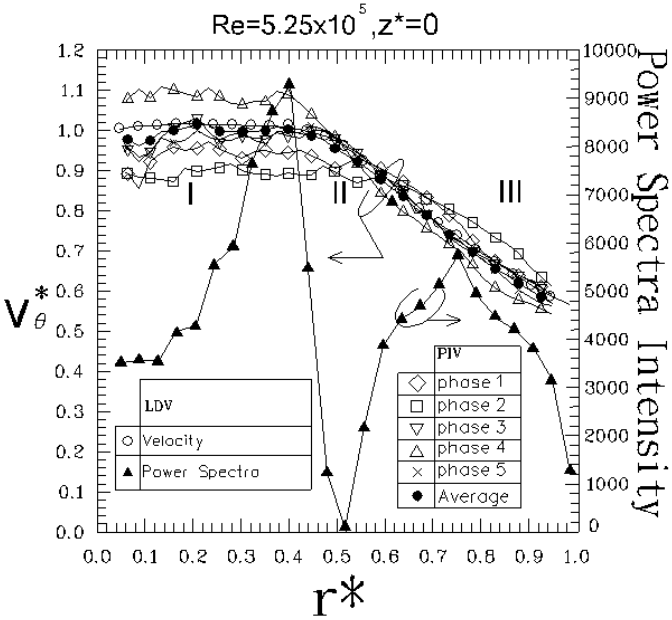

Fig. 14. PIV measured radical profiles of the circumferential phase velocity and LDV measured power spectra.

Fig. 14 shows the radical profiles of velocity from the hub to the shroud under the same time interval and along the same radial position ($\theta = 0$). The normalized velocity near the hub has a small range of perturbations in the radial direction. The fluid is dominated by rotating centrifugal force, adverse pressure caused by the static shroud and the Coriolis force. At the interface between inner and outer regions, the fluid starts to be influenced by the adverse pressure force and leaves solid-body rotation. Boundary layers develop along the surface of each disk beyond the solid body region. Fluid in the boundary layer is pumped radically outward by a combination of centrifugal force and Coriolis force.

Experimental data indicates that at a certain radial location, the normalized circumferential velocity begins declining. However, the locations of the normalized circumferential velocity begin declining at different time steps. Based on above result, the polygon inner region is compressed by the vortices. When the vortex center moves toward the sampling line ($\theta = 0$), the boundary of inner region is flattened inward toward the hub. Therefore, the normalized circumferential velocity near the hub arises as a result of the reducing channel. Conversely, when a vortex leaves the sampling line, the velocity near the hub continually declines due to the expanding inner region. As indicated by the velocity profile labeled with a △ in Fig. 14, a vortex center bypasses the sampling line, and the normalized circumferential velocity remains larger than 1 as it moves form the hub outward to r^* =0.39. Contrary to this, as the inner region vertex bypasses the sampling line (profile labeled with a □), the normalized circumferential velocity is slightly less than the disk speed and maintains its value until r^* =0.60.

The periodic passage of the vortex structure affects the normalized circumferential velocity (Fig. 14).The velocity profiles rise or fall at different time steps, and the increases and decreases in the inner and outer regions are opposed to each other. When the vortex center moves close to the sampling line (θ=0°), the inner region boundary is flattened inward toward the hub. Therefore, the normalized circumferential velocity near the hub arises due to the reducing channel and increases continually. Until the vortex center arrives, the dimensionless circumferential velocity peaks. Conversely, when a vortex leaves the sampling line, the velocity near the hub continually decreases due to the expanding inner region. In the outer region, fluid velocity increases or decreases periodically in a manner that is opposite to that in the inner region.

However, this flow behavior was not observed with the LDV-measured velocities (marked with a ○) (Wu and Chen 2003). The fluid in the inner region coincides with rotating disk speed. The radial location at which velocity starts to decline is fixed at r^* = 0.39. The mean velocity profile measured by LDV is in agreement with the global mean velocity profile measured by PIV (marked with a ●). Experimental data indicate that LDV measurement can only show time-averaged results, and cannot exhibit the periodic perturbation of velocity.

4.8 Power spectra

The velocity time history recorded by LDV is also utilized for power spectrum analysis. Two local maxima of spectral intensity can exist (Fig. 14). The first maximum is located at r*=0.39, whereas the second local maximum is at r*=0.75, indicating that circumferential velocity has increased energy at these two locations. Notably, the spectral intensity is almost zero at r*=0.51, implying that circumferential velocity does not oscillate at this location.

The normalized mean circumferential velocity starts declining at r*=0.39 (Fig. 14). Instantaneous velocity profiles also indicate that this location is sometimes in the inner region, and sometimes in the outer region. Consequently, the radial gradient of velocity varies markedly, and the velocity value changes periodically due to passing vortices. The radial gradient of velocity also varies violently at about r*=0.7, the location of vortex center. When a vortex passes the sampling line, its self-rotation causes the fluids at each side of the vortex center to accelerate in opposite directions, resulting in strong variation in radial gradient velocity. Furthermore, as the vortex passes or leaves the sampling line, the velocity value also varies periodically. Notably, the profiles of velocities intersect at about r*=0.51, where spectra intensity approaches zero. Comparatively, at the position where spectra intensity achieves a maximal value, the amplitudes of velocity change significantly.

Power spectra analysis provides periodic information, such as the distribution of spectra intensity and the primary flow frequency, as long as the grids of LDV measurements are adequately refined. However, spectra intensity distribution cannot be explained effectively by the global mean velocity profile measured by LDV. The phase velocity measurements provide the physical explanation of the cyclic variation in the 1st solid body rotation region reported previously by LDV.

5. Conclusions

Six major conclusions may be drawn.

1. By using two laser Doppler velocimeters and the phase averaged method, the temporal vortical structure in the flow between corotating disks can be quantitatively reconstructed. The detailed flow information, including the mean, periodic, and random terms, provides a basis for numerical verification.
2. The power spectral analysis shows that all the peaks in the energy are at the same integral normalized frequency. The value of the normalized frequency is the same as the number of the vortical structure observed in the reconstructed streamline patterns. This indicates that the flow oscillations result from the periodic passage of the flow structure.
3. Both laser (LDV, PIV) measurements and flow visualization in the r- θ plane show that the flow feature between the co-rotating disks can be divided into three regions: (I) Inner region: solid body rotation region ($0.04<r^*<0.39$), (II) Outer region: vortex region ($0.39<r^*<0.75$), and (III) Shroud region: shroud shear layer region ($0.75<r^*<1$). Among them the shroud region is quantitatively identified for the first time.
4. In the $r-z$ plane, the flow structure is found to consist of six sub-flow regions. Combining the flow patterns in the $r-\theta$ and $r-z$ planes, the complex 3-D flow explored can be divided into eight sub-regions, namely 1st solid body rotation region, 2nd large-scale vortex structure region , 3rd detached shear layer region ,4th boundary layer region, 5th core region, 6th Ekman layer region, 7th Stewartson layer region, and 8th shroud shear layer region. The (5th to 7th) three sub-flow regions are identified in the present study.
5. The large-scale vortex structure is not flung out of the above-mentioned 2nd sub-region by the centrifugal force since the circular-pair flow structure in the core region acts like an annular chain to surround it.
6. The periodical variation of circumferential velocity or the cyclic variation of the inner solid body rotation reported previously by authors' LDV spectra results can be explained by the present PIV phase velocity measured results.

6. Acknowledgement

There are so many thanks for the Department of Mechanical Engineering National Taiwan University of Prof. Yau-Ming Chen, who has had the long-term support and assistance to my papers.And also thanks for the subvention from National Science Council.

7. Nomenclature

a	Clearance between disks and shroud (mm)
D	Displacement between disks (mm)
f^*	Normalized frequency
f_n	Natural frequency of flow (Hz)
fs	Dominant frequency of power spectra(Hz)
f_n	Natural frequency of flow (Hz)

N	Number of vortices
R_1	Radius of hub (mm)
R_2	Radius of disk (mm)
R_3	Radius of shroud (mm)
Ri	Radius of inscribing circle of polygon structure
Re	Reynolds number, $R_2\Omega/\nu$
r	Radial coordinate (mm) (mm) (mm) (mm)
r^*	$(r- R_1)/ (R_2-R_1)$
S	D/ R_2
$U; u$	Velocity(mm/s)
U_r	Radial velocity (mm/s)
Uref	Circumferential velocity of the reference point(mm/s)
$U_r{}^*$	Normalized radial velocity $U_r/r\Omega$
V_θ	Circumferential velocity (mm/s)
$V_\theta{}^*$	Normalized circumferential velocity $V_\theta/r\Omega$
$\overline{u}$	Global mean of u
$\tilde{u}$	Periodic fluctuation away from $\overline{u}$
u'	Random fluctuation away from $\tilde{u}$
z	Axial coordinate (mm)
z^*	z/D

8. Greek symbols

Ω	Rotating velocity of disk (rpm)
θ	Periphery coordinate (degree)
ν	Kinematic viscosity (mm^2/s)

9. Reference

Abrahamson, S. D., Eaton, J. K., and Koga, D. J., The Flow between Shrouded Corotating Disks, Phys. fluids A, 1 (1989)241-251.

Abrahamson, S. D., Koga, D. J., and Eaton J. K., Flow Visualization and Spectral Measurements in a Simulated Rigid Disk Drive, IEEE Trans. Comp. Hybrids and Manuf. Tech., 11(4) (1988)576-584.

Abrahamson, S. D., Eaton, J. K., and Chang, C., Flow Structure in Head-Disk Assemblies and Implications for Design, Adv. Info. Storage Syst., 1(1991)111-132.

Adrian, R. J., Image shifting technique to resolve directional ambiguity in double-pulsed velocimetry, Applied Optics, 25 (1986)3855-3858.

Adrian, R.J., Particle-imaging Techniques for Experimental Fluid Mechanics, Annu. Rev. Fluid Mech., 23(1991)261-304.

Adrian, R. J., and Yao, C. S., Development of Pulsed LASER Velocimetry (PLV) for Measurement of Turbulent Flow, In Proc. Symp. Turbul., ed. X. Reed, G. Patterson, J. Zakin, Rolla: Univ. No. 380 (1984) 170-186.

Chang, C.J., Humphrey, J.A.C., and Greif, R., Calculation of Turbulent Convection Between Corotating Disks in Axisymmetric Enclosures, Int. J. Heat Mass Transfer, 33 (1990)2701-2720.

Chang, C. J., Schuler, C. A., Humphrey J. A. C., and Greif R., Flow and Heat Transfer in the Space between Two Corotating Disks in an Axisymmetric Enclosure, J. of Heat Transfer, 111 (1989) 625-632.

Herrero, J., Giralt, F., and Humphrey, J. A. C., Influence of the Geometry on the Structure of the Flow between a Pair of Corotating Disks, Phys .of Fluids, 11 (1999)88-96.

Humphrey, J. A. C., Chang, C. J., Li, H. and Schuler C. A., Unobstructed and Obstructed Rotating Disk Flows: A Summary Review Relevant to Information Storage Systems, Adv. Info. Storage Syst., 1(1991)79-110.

Humphrey, J. A. C., and Gor, D., Experimental Observation of an Unsteady Detached Shear Layer in Enclosed Corotating Disk Flow, Phys. Fluids, 5(1993) 2438-2442.

Humphrey, J. A. C., Schuler C. A., and Weber, D. R., Unsteady Laminar Flow Between a Pair of Disks Corotating in a Fixed Cylindrical Enclosure, Phys. Fluids, 7(1995)1225-1240.

Hussain, A.K.M.F. and Reynolds, W.C., The Mechanics of an Organized Wave in Turbulent Shear Flow. Part 3. Theoretical Models and Comparisons with Experiments," J. Fluld Mech., 54(1972)263-288.

Iglesias, I., and Humphrey, J. A. C., Two- and Three-Dimension Laminar Flows Between Disks Co-rotating in a Fixed Cylindrical Enclosure, Int. J. Numer. Meth. Fluids, 26, (1998)581-603.

Keane R.D., and Adrian, R.J., Theory of cross-correlation of PIV images, Applied Scientific Research, 49 (1992)191-215.

Lennemann, E., Aerodynamic Aspects of Disk Files., IBM J. Res. Develop., 18(1974)480-488.

Perry, A. E. and Watmuff, J. H., The Phase-Averaged Large-scale Structures in Three Dimensional Turbulent Wakes, J. Fluid Mech., 103(1981)33-51.

Randriamampianina, A., Schiestel, R., and Wilson, M., Spatio-temporal Behavior in an Enclosured Corotating Disk Pair, J. Fluid Mech., 434 (2001)39-64.

Schuler, C. A., Usry W., Weber, B., Humphrey, J. A. C. and Greif, R., On the Flow in the Unobstructed Space between Shrouded Corotating Disks, Phys. Fluids , 2 (1990)1760-1770.

Stewartson, K., On the Flow between Two Rotating Coaxial Disks, Proc. Camb. Phil. Soc., 3(1953)333-341.

Szeri, A.Z., Schneider, S.J., Labbe, F. and Kaufamn, H.N., Flow between Rotating Disks (Part 1, Basic Flow), J. Fluid Mech., 34(1983)103-132.

Tzeng, H. M., and Humphrey, J. A. C., Corotating Disk Flow in an Axisymmetric Enclosure with and without a Bluff-body, Int. J. Head and fluid flow, 12(1991) 194-201.

Willert, C. E., and Gharib, M., Digital Particle ImageVelocimetry, Exp. in Fluids, 10 (1991) 181-193.

Wu, S. C., The flow between corotating disks with/without an obstruction in a cylindrical enclosure, Ph.D. diss., National Taiwan University,2000.

Wu, S.C., and Chen, Y.M., Phase-Averaged Method Applied to Periodic Flow between Shrouded Corotating Disks, International Journal of Rotating Machinery, 8 (2002) 413-422.

Wu, S.C., and Chen, Y.M., The Dynamic Behavior of the Coherent Flow between Shrouded Co-rotating Disks, Journal of the Chinese institute of engineers, 26 (2003) pp. 47-56.

Wu, S.C., Tsai ,Y.S., Chang, Y.M. and Chen, Y.M., Typical Flow between Enclosed Corotating Disks and its Dependence on Reynolds Number, Journal of the Chinese institute of engineers, 29 (2006) 841-850.

Wu, S.C., A PIV Study of Co-rotating Disks Flow in a Fixed Cylindrical Enclose, Experimental Thermal and Fluid Science, 33(2009), 875-882.

Part 4

Indirect Flow Measurement

7

Flow Measurement Methods Applied to Hydro Power Plants

Gustavo Urquiza[1], Miguel A. Basurto[1], Laura Castro[1],
Adam Adamkowski[2] and Waldemar Janicki[2]
*[1]Research Center on Engineerging and Applied Science (CIICAp)
from the Autonomous University of Morelos State (UAEM), Morelos
[2]The Szewalski Institute of Fluid-Flow Machinery,
Polish Academy of Science, Gdansk
[1]México
[2]Poland*

1. Introduction

Efficiency and maximal power output are two of the most important goals to analyze in hydraulic turbines. Turbines normally operate in variable head conditions; therefore, tests to analyze performance are frequently realized for a selected number of power plant heads. Usually it is limited to three heads: low, medium and high. The efficiency of water turbines is most frequently expressed using the weighted average efficiency or arithmetic mean efficiency, calculated from the measured results in the examined heads. To perform the calculation of efficiency is necessary to know several parameters such as kinetic and potential energy of water due to the position, because of this is required to know the flow rate entering the turbine. The flow rate of water through the turbine (Q) is determined by the volume of water flowing in time unit. The measurement of this quantity is one of most difficult tasks in water turbine tests. Three basic methods of flow rate measurement and results of them will be presented in this chapter.

2. Pressure-time method (Gibson)

One of the basic methods for flow rate measurement applied in hydropower plants is pressure-time method, commonly called the Gibson method. It consists in flow rate measurement by integration of pressure difference between two pipeline cross-sections during fast shut-off. Selected experiences in developing and utilizing the method are presented in this section, which covers cases of flow rate measurements in pipelines of more complex geometry, e.g. curved penstocks. The calculation procedure that provides the possibility to analyze the influence of measurement system components (pressure difference transducer, length and diameter of tubes connecting the pressure taps with a transducer) on measured flow rate has been already developed as the main element of this methodology. Furthermore, utilizing the Gibson method to flow rate measurement through water turbines requires know the leakage rate flow through closed guide vanes, i.e. through the blade interspaces. The procedure for estimating this rate is presented in this section. Practical application of Gibson method requires preparation of special measurement devices, often installed inside the large-size penstocks and with no possibility to approach the pipeline from the outside. During years 03-09 this method was successfully applied for efficiency tests of units that were carried out at many hydropower plants in Poland and Mexico by the authors of this chapter.

2.1 Theory

This method is based on the water hammer phenomenon taking place in a closed pipe. It was introduced by Norman Gibson (1923), who used the work conducted by Jukowsky in 1898 concerning the water-hammer theory. Gibson's method measures a static pressure difference, between two cross-sections of the penstock as result of momentum variation caused by a quick closing of the wicked gates of the turbine. The flow rate is then obtained by integration, within a proper time interval. Gibson method is recommended by the international standard IEC 41:1991 as well as its European equivalent EN 60041. In the measurement conditions recommended by the standard, the accuracy of the measurement is better than +/-1.5 to 2.3% and it does not stay away from the accuracy of other basic methods for flow measurement. There are three principal versions of the Gibson method:

i. Direct measurement of the pressure difference between two hydrometric sections of the penstock by means of a transducer of pressure difference, whereas the measuring penstock segment between the sections is straight and has a constant diameter – this version could be called the classical.
ii. Separate measurement of pressure variations in two hydrometric sections of the penstock is used – version with separate measurement sections.
iii. Pressure change measurement in one hydrometric section of the penstock and referring these changes to the constant pressure in an open reservoir of the liquid to which the penstock is directly connected – version with single penstock measurement section.

To derive a relationship that calculates the volumetric flow rate Q must be considered a closed pipe with a flow section area A which may change along its length.

Scheme of measuring section on turbine penstock is shown in Figure. 1. Next has to be considered that the water flow must be stopped. Taking into account one segment of length L, limited between sections 1-1 and 2-2 has to be assumed that the velocity and pressure distributions in those sections are constant. Also it is assumed and that the fluid density and the flow section area do not change with water hammer effect.

With these assumptions done, the relation between the parameters of the one-dimension unsteady flow between two selected sections of the pipe can be described using energy balance equation:

$$\alpha_1 \frac{\rho Q^2}{2A_1^2} + p_1 + \rho g z_1 = \alpha_2 \frac{\rho Q^2}{2A_2^2} + p_2 + \rho g z_2 + \Delta P_f + \rho \int_0^L \left(\frac{dQ}{dt} \right) \frac{dx}{A(x)} \tag{1}$$

Where ρ is water density, p_1 and p_2 are static pressures in sections 1-1 and 2-2 of the pipe, respectively (see Fig. 1), z_1 and z_2 are hydrometric levels of sections 1-1 and 2-2, α_1, α_2 are

Coriolis coefficient (kinetic energy correction coefficient) for sections 1-1 and 2-2, respectively, and finally, ΔP_f is the pressure drop caused by friction losses between sections 1-1 and 2-2. The fourth term on the right-hand side of the above equation represents the hydraulic friction losses in the pipe segment. In the Gibson method, the pressure drop caused by friction is determined from a square flow rate function, written as:

$$\Delta P_f(t) = K_f Q(t)\left|Q(t)\right|,$$

Where K_f = constant.

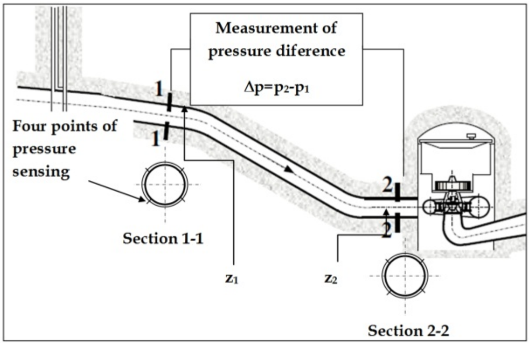

Fig. 1. Penstock and measuring sections in Gibson's method.

The term at final of equation (1) is the unsteady term, which takes into account the time-history of change of the volumetric flow rate $Q=VA$, recorded during the time period of the water hammer effect. This term represents the effect of fluid inertia in the examined conduit segment. To clarify these considerations some quantities are presented to group terms of equation (1):

- static pressure difference between measuring sections 2-2 and 1-1 related to a reference level:

$$\Delta p = p_2 + \rho g z_2 - p_1 - \rho g z_1 \tag{2}$$

- dynamic pressure difference between conduit sections 2-2 and 1-1:

$$\Delta p_d = \alpha_2 \frac{\rho Q^2}{2A_2^2} - \alpha_1 \frac{\rho Q^2}{2A_1^2} \tag{3}$$

- geometrical modulus of the penstock segment of a length L:

$$C = \int_0^L \frac{dx}{A(x)} \tag{4}$$

Then we arrive at the differential equation in the form:

$$\rho C \frac{dQ}{dt} = -\Delta p - \Delta p_d - \Delta P_f \tag{5}$$

After integrating equation (5) for the time interval (t_0, t_k), in which the flow changes from initial to final conditions, was obtained the flow rate difference between those conditions. Then it is assumed that flow rate at final condition (Q_k) is knew, i.e. after the cut-off device has been closed, allowing the following expression to be applied for the computation of the volumetric flow rate at initial condition (before starting the water flow cut-off):

$$Q_0 = \frac{1}{\rho C}\int_{t_0}^{t_k}\left[\mathit{\Delta} p(t) + \mathit{\Delta} p_d(t) + \mathit{\Delta} p_f(t)\right] dt \; + Q_k \qquad (6)$$

The water flow rate at final condition is different from zero due for instance to water leaks through the closing device, so this will be called leakage flow Q_k and its determined by the empirical equation:

$$Q_k = \mu A_s \sqrt{\frac{2\mathit{\Delta} p_k}{\rho}} \qquad (7)$$

2.2 Instrumentation

In order to obtain high accuracy of the measurement, proper selection of the measuring device range is very important. This should correspond well at measured pressure. High-class pressure transducers of various types are nowadays widely available on the market. These are electro-mechanical devices, in which the mechanical effect caused by the pressure is converted to an electric signal. Their advantages include:

- Easy connection at electronic system of measurement data acquisition,
- Negligible flow of liquid through a manometer connector, which secures fast and precise reaction to pressure changes,
- Easy determination of average values of the fluctuating pressure using the data acquisition system,
- Easy recording of the time-history of rapid pressure changes in steady-state and transient conditions using available electronic equipment.

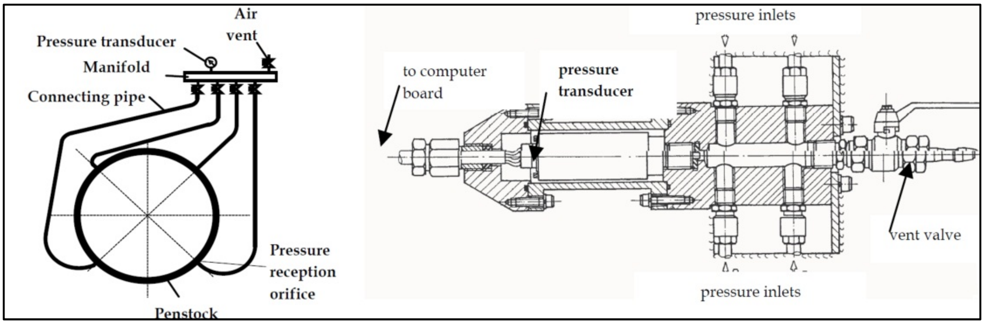

Fig. 2. Scheme of sensing points on penstock and waterproof manifold installed.

2.3 Example

To exemplify the results obtained by this method, some graphics of results are showed. Mainly the graphics of pressure difference vs. time, and efficiency curve calculated vs. mechanical power (figs. 3-5, Castro L. (2011))

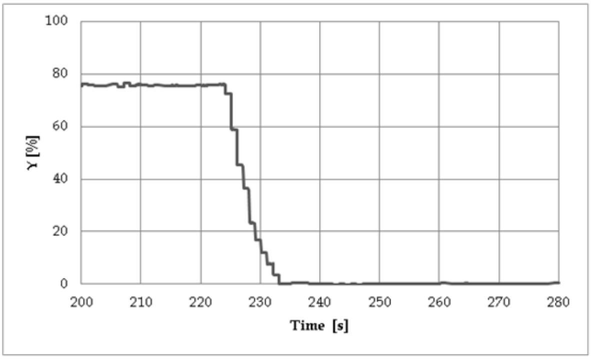

Fig. 3. Differential pressure measured vs. time during closing of the wicked gate

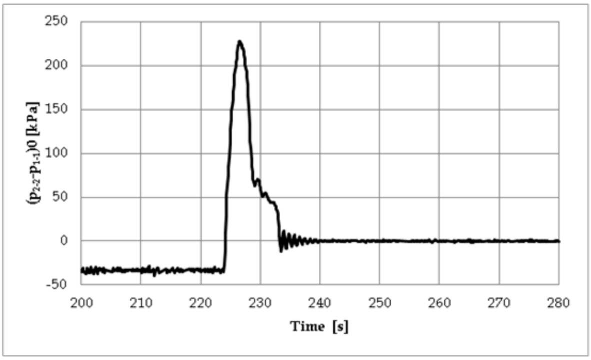

Fig. 4. Pressure difference vs. time during closing of the wicked gate

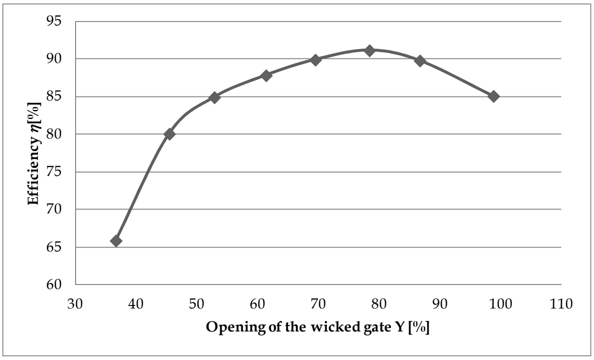

Fig. 5. Efficiency calculated vs. closure percentage of the wicked gate

In table no.1 are showed some or the results obtained in measurements, were the $Q_{turbine}$ is the total volumetric flow, obtained from the addition of Q_{gib}, Q_k and $Q_{cooling}$, the last one, is the flow of water used for cooling air from the electric generator.

Test Number	Opening of the wicked gate Y [%]	Mechanical Power P_{mech} [MW]	Gibson Flow Rate Q_{Gibson} [m³/s]	Leakage Flow Q_k [m³/s]	Cooling Flow $Q_{cooling}$ [m³/s]	Total Flow $Q_{turbine}$ [m³/s]	Net Head H_n [m]	Efficiency η_t [%]
1	98.8	31.65	88.97	0.7	0.0	89.67	42.40	85.10
2	86.7	30.71	81.30	0.7	0.0	82.00	42.64	89.80
3	78.4	29.03	75.44	0.7	0.0	76.14	42.75	91.16
4	69.5	26.05	68.03	0.7	0.0	68.73	43.09	89.91
5	61.4	22.63	60.29	0.7	0.0	60.99	43.18	87.84
6	52.9	19.02	52.20	0.7	0.0	52.90	43.27	84.92
7	45.5	15.72	45.41	0.7	0.0	46.11	43.52	80.08
8	36.7	10.14	34.98	0.7	0.0	35.68	44.10	65.89

Table 1. Results from the measurements by Gibson's method.

In the examined case, the efficiency measurements performed for one hydropower station head with the aid of the Gibson method, were used for determining the efficiency curve of the turbine and the hydro-unit, and for calibrating the measuring system based on the Winter-Kennedy method. Once calibrated, the Winter-Kennedy system can be used for continuous flow rate measurement and for determining turbine performance (efficiency) characteristics of for other power plant heads.

3. Winter Kennedy method

Winter-Kennedy method utilizes the phenomena of a static pressure difference between the outside and the inside of the turbine spiral due to the centrifugal force acting on the curved streams of liquid in the spiral case. Contrary to the Gibson method, this is an index (relative) method, which can be used in water machines efficiency tests only after the calibrating by means of the absolute method.

3.1 Theory

The flow measurement performed with the aid of this method makes use of the following relation between the flow rate Q and the difference of the above named pressures $\Delta p = p_1 - p_2$:

$$Q = K \cdot \Delta p_n \tag{8}$$

Where *K* is a constant coefficient and *n* is the power exponent, theoretically equal to 0.5. The values of the constants *K* and *n* are determined experimentally during calibration. The results of flow rate measurement performed, using the Gibson method, were used for calibrating the Winter-Kennedy measuring systems installed in the spiral case of one turbine. The pressure difference between two points established in the spiral case of the examined turbine was measured using a high-precision class pressure difference transducer of the accuracy of 0.08%. The Winter-Kennedy method is only used for water turbines or pump-turbines working in turbine mode. It cannot be used for testing pumps due to excessive turbulent flow in the spiral case in pumping conditions.

3.2 Instrumentation

In installations with steel turbine spiral cases, the pressure reception points are located, as a rule, at the same radial section of the case (Figure 6) The outer hole is located on the outer side of the spiral case, while the inner hole outside of the supporting blades, on the streamline going through the centre of their interblade passage. In case of horizontal spiral case it is recommended to distribute the holes in the upper half, providing better conditions for washing (IEC 41: 1991). The pressure reception points should not be located close to welded joints or areas of rapid change of spiral cross section. For the measurement of pressure with this method, was used differential pressure transducer 3051 type CD, range of 0-120 kPa, cl. 0.06, and 0.1 s time constant (Adamkowski 2006).

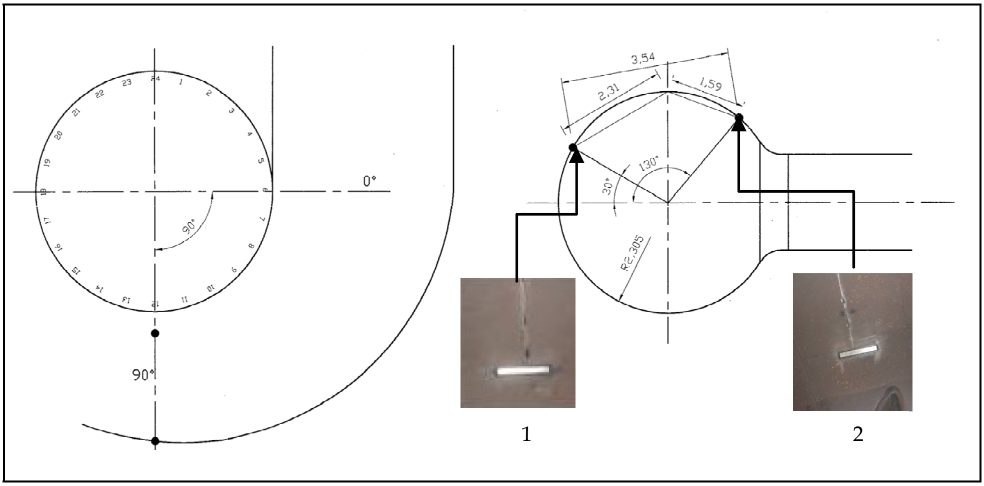

Fig. 6. Localization of the measurement points inside the spiral case (point 1 and 2)

In figure 7 can be observed an example from the location of differential pressure transmitters to measure pressure, outside the spiral case.

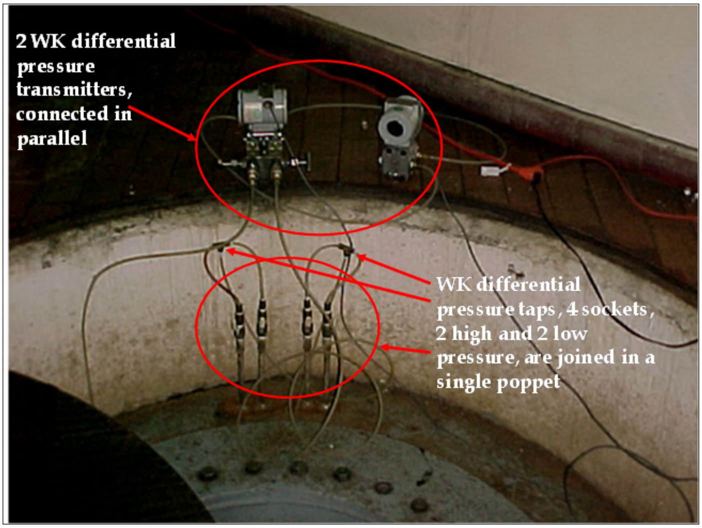

Fig. 7. Position of pressure transmitters outside of the spiral case.

3.3 Examples

From the measurements realized by means of Gibson's method in a turbine in Mexico, was calibrated the Winter-Kennedy system, obtaining the coefficient K, Figure 8 shows the results, a) shows the determination of the coefficient K, which in this case corresponds to a value of 29.42. Also in figure 8 incise b) shows the mean feature of the flow depending on the pressure difference measurements, for pressure taps plate type.

It is remarkable that once calibrated, the Winter-Kennedy system can be used for continuous flow rate measurement and for determining turbine performance (efficiency) characteristics of for other heads.

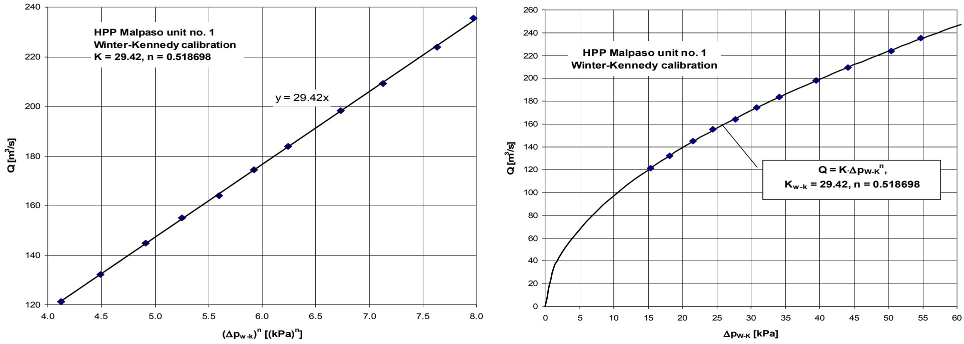

(a) (b)

Fig. 8. System features for Winter-Kennedy measurements: (a) determination of K = 29.42 and (b) flow vs differential pressure.

4. Ultrasonic method

This method has been considered in this work solely for the purpose of comparing, but it is noteworthy that the experience concerning the application of the acoustic methods for flow measurements is still limited.

4.1 Theory

The principle of flow measurement using ultrasonic is that the speed of propagation of an ultrasonic acoustic pulse is affected by flow velocity. Accordingly, an ultrasonic acoustic pulse sent upstream travels at a ground speed less than an acoustic signal sent downstream. By measuring the travel times of the pulses sent in both directions, determine the axial velocity of fluid passing through the path of the pulse. Repeated measurements are an average time to establish and minimize the random error. Sensors must be located as show the next figure:

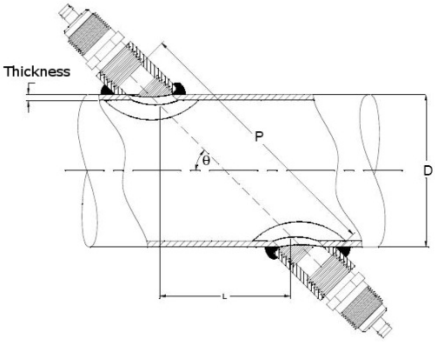

Fig. 9. Location of the sensors in the penstock.

Each sensor sends an ultrasonic signal and the delay time from downstream sensor (*t_2*) at upstream sensor (*t_1*) it's measured electronically. The sound propagation velocity of the moving fluid (*c*) is:

$$c = c_0 + \bar{v}\cos\theta \tag{9}$$

Were:

$\bar{v}$ is water average velocity

Traveling time for propagating ultrasonic signals from downstream sensor to upstream sensor are:

$$t_1 = \frac{P}{c_0 - \bar{v}\cos\theta} \tag{10}$$

$$t_2 = \frac{P}{c_0 + \bar{v}\cos\theta} \tag{11}$$

Were:

P = distance between sensors (as can be seen on figure 9).

Therefore:

$$\frac{1}{t_1} - \frac{1}{t_2} = \frac{2\bar{v}\cos\theta}{P} = \frac{2\bar{v}L}{P} \tag{12}$$

Where:

L = inner signal distance between both sensor, parallel to penstock axe.

From last equation, velocity is obtained then:

$$\bar{v} = \frac{P^2 \Delta t}{2Lt_1 t_2} \tag{13}$$

Where: $\Delta t = t_1 - t_2$

4.2 Instrumentation

For measurements were used two ultrasonic devices G.E. Panametrics, models PT868 and PT878, in different sections of the penstock, both in real time:

The characteristics of sensors are:

- Transducer clamp-on type (for external installation)
- Range: -12.2 to 12.2 m/s
- Accuracy (velocity): 0.5 to 1%
- Manufacturer: G.E. Panametrics
- The specifications assume a stable flow profile

Fig. 10. Electronic devices to perform Ultrasonic measurements.

4.3 Example

Some of the results obtained from ultrasonic measurements are presented in table 2 and figure 11 (Hernández 2010).

Test variables

Power from electric generator [MW]	P_e	27.14	26.01	24.80	23.69	22.05	19.97	18.17	15.26	11.98	8.83
Turbine inlet pressure [kPa]	p_{in}	3271.03	3276.53	3280.28	3284.06	3291.47	3299.50	3307.37	3320.12	3332.99	3342.57
Flow measured by ultrasonic method [m³/s]	Q_u	9.56	9.16	8.82	8.48	7.96	7.32	6.77	5.86	4.84	3.89

Calculated variables

Water inlet velocity [m/s]	V_{in}	10.06	9.64	9.28	8.93	8.37	7.70	7.13	6.17	5.09	4.10
Water outlet velocity [m/s]	V_{out}	1.56	1.50	1.44	1.39	1.30	1.20	1.11	0.96	0.79	0.64
Test net head [m]	H_n	337.61	337.76	337.86	337.81	338.23	338.59	339.19	339.80	340.64	341.29
Generator Efficiency [%]	η_g	**98.45**	**98.44**	**98.43**	**98.41**	**98.40**	**98.35**	**98.26**	**97.97**	**97.50**	**96.85**
Mechanical power [kW]	P_m	27.57	26.42	25.20	24.07	22.41	20.31	18.49	15.58	12.28	9.12
Turbine efficiency [%]	η_t	**87.52**	**87.43**	**86.59**	**86.03**	**85.31**	**83.94**	**82.47**	**80.13**	**76.34**	**70.34**

Table 2. Variables obtained and calculated by ultrasonic method

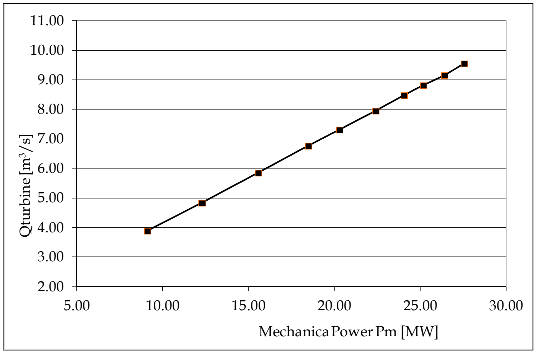

Fig. 11. Graphic of Flow vs Mechanical power, obtained by Ultrasonic method.

5. Comparison between methods

Present section showed a comparison between measurements obtained by ultrasonic and Gibson methods in one hydraulic turbine. The comparison was realized from tests in the same Power Plant with a short period of time between them. These comparisons were realized by Hernández (2010) in his Master Thesis, by measurements performed by Urquiza *et al* (2008).

In figure 12 can be observed a graphic of flow measured vs mechanical power, for both methods, which behavior is very similar.

Flow measured with ultrasonic and Gibson methods is very close and within the uncertainty of measurement at full load, however as measuring low flow, value of flow from ultrasonic method is less than the flow measured by Gibson, because the efficiencies vary strongly as the test powers are lower.

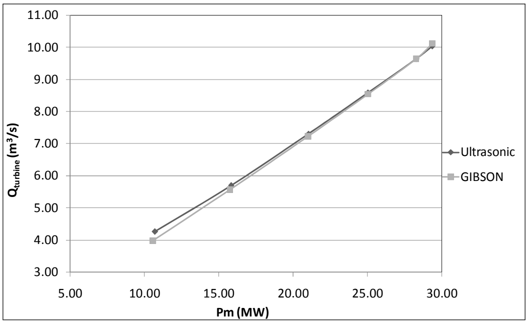

Fig. 12. Flow measured by both method vs Mechanical Power.

In figure 13 the behavior or the Net Head (H_n) are similar, however, are closer the values as they reach the maximum power (there are differences approximately 0.2 m between them) and virtually 0 to full load.

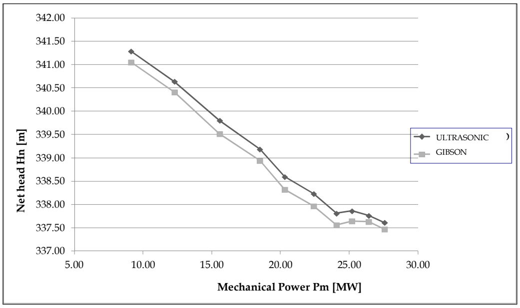

Fig. 13. Net head measured vs Mechanical Power.

The net head values for both methods (ultrasound and Gibson) are very similar and the same trends, but are more as they reach values close to maximum power as have differences of about 0.2 m and minimum loads almost 0 at full load.

Figure 14 shows a final comparison between the turbine efficiency vs. electrical power, here can be appreciated that measured efficiency by Gibson's method is greater than ultrasound method, because the ultrasound method, due to it's an experimental method, is follows that as water flow is lower or velocity is slower inside the penstock, inaccuracy is increasing, under which the results are less than the value obtained by Gibson, which is reliable and is supported by the IEC 41.

6. Other optical techniques for measurement of pressure applied on flow measurement

In CIICAp are developing pressure sensors based on optical methods to assist in measuring the flow through the above methods. The use of the sensors by optical means is an area of support for the electronic sensors, which is gaining strength. The type of arrangement may be from patterns interferometric on holographic tables until the micro actuator fully micro fabricated by surface micromachining on a single silicon wafer.

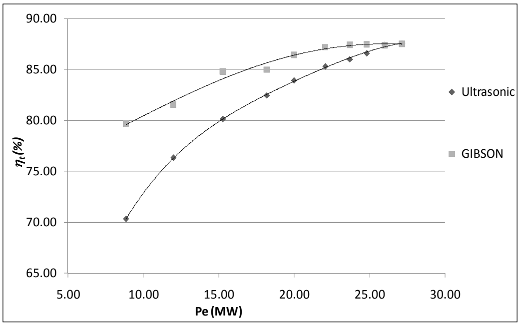

Fig. 14. Efficiency obtained by both methods vs Electric Power.

6.1 Fiber Bragg sensors

The use of Bragg gratings has different applications such as displacement, temperature and pressure sensors among others. A Bragg grating optical fiber can be defined as a periodic modulation (period or modulation of non-uniform) refractive index of the core of an optical fiber, usually single-mode, which can also be seen as a periodic arrangement of plates two films of different refractive indices designed to operate with a specific wavelength, an easier way to understand their function is imagining a beam of light (consisting of different wavelengths) travels within the fiber passing through Bragg grid (designed for a particular wavelength) will have two behaviors, such as a filter, it will only be rejected is that the wavelength at which it was designed, the second is as a mirror, in this case only reflect wavelength for which it was designed, other property that has the Bragg grating is that being in tension or compression, the grid changes its point of operation, this property is very useful for measuring the deformation of materials for pressure. Based on the response to tension or compression, the grid can be placed inside a chamber

Using fibers Bragg grating written in a novel high birefringence fiber by phase-mask method. The temperature and gas pressure characteristics of the fiber Bragg grating were analyzed and demonstrated quantitatively. Two Bragg wavelengths corresponding to the fast-axis mode and slow-axis mode shift linearly with temperature change and gas pressure change. Experimental results showed that this Hi-Bi fiber Bragg grating could be used to measure temperature and gas pressure simultaneously with a deviation of less than 1 °C and 0.5 MPa from the set values respectively (Guanghui *et al,* 2003).

Currently there are two configurations of Bragg grating. The most widely used are called-fiber Bragg gratings (FRB) (Hao-Jan *et al,* 2008 & Zhanxiong *et al,* 2008), which have been used in pressure sensors for low pressure range and high pressures equally. There exists application of hydrostatic pressure in resolutions up to 0.5% (Clarke 1995). Some variants of this type of fiber are long-period optical fibers gratings (Rao & Jackson 1996) and the chirped grating, also used in pressure sensors.

6.2 Multimode Interference

The multimode interference effect occurs when the diffracted light and in certain traveled distance can regroup [m]. The first application of this phenomenon was made in the design of bidirectional couplers on integrated optics (Niemeier & Ulrich, 1986). They have since been developed a variety of optical devices based on this phenomenon in planar waveguides, such as Mach-Zender switches (Jenkins *et al*, 1994), couplers (Soldano *et al* 1991), ring lasers (van Roijen *et al*, 1994) and so on. An example of patterns Interferometric Mach-Zehnder Interferometer is, Can it be made using single-mode optical Fibers for the two arms as Shown in Figure 15.

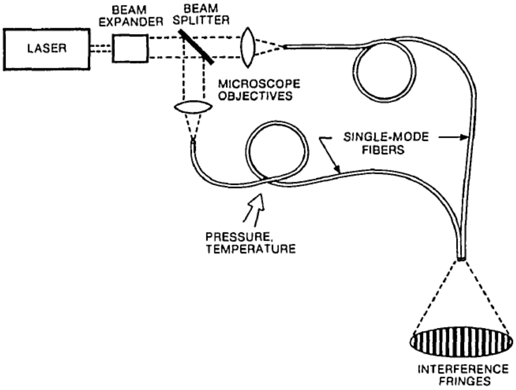

Fig. 15. Setup basic of Mach-Zehnder interferometer.

If the optical pathlengths of the two arms are nearly equal (to within the coherence length of the source), the light from the two fibers interferes to form a series of bright and dark fringes. A change in the relative phase of the light from one fiber with respect to the other is observed as a displacement of the fringe pattern.

Pressure sensitivity measurements were made with a 1.5-m length of one fiber in a cylinder, which could be pressurized to 345 kPA (50 psi) with nitrogen. Pressure measurements were made with a gauge reading to 345 Pa (0.05 psi). The fringe displacement was again recorded on video tape for repeated measurement.

Recently researches have presented studies on the interference between the guided modes in a multimode fiber, excited by a field from a single mode fiber. Under certain conditions, a reconstruction of the input field may be reproduced in amplitude and phase at specific distances within the multimode fiber, known as self-image distances. These conditions are determined by the physical parameters of the fibers used as the light source. If an optical fiber is spliced to the multimode fiber in the distance just self-image, the transmitted field will be sensitive to alterations of the physical parameters involved in the multimode fiber section. This can be used in pressure sensors, because the intensity of the output signal can be attenuated by altering the phase of modes propagated. The phase may be modified by changing the optical path length traveled by the guided modes or modifying the refractive index of the fiber coating.

Another technique consists of two MMI couplers, two arms and a membrane. One arm (arm 1) is located on the center of the membrane and the other arm (arm 2) is located on the edge. An input MMI coupler has been designed (as showed on figure 16) to divide input light into two equal-power lights in the two arms. When no pressure is applied to the membrane, the divided lights meet at the output MMI coupler in the same phase, so that they can be constructively interfered at the output MMI coupler. When the pressure is applied to the membrane, the strain induced in the membrane due to deflection causes the phase changes in the two arms.

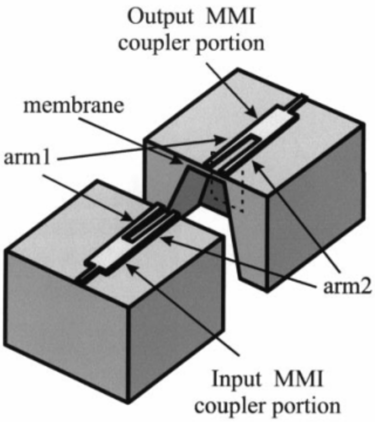

Fig. 16. Membrane whit two couplers 1x2 and 2x1.

When no pressure is applied to the membrane Figure 17 (a), the divided lights meet at the output MMI coupler in the same phase, so that they can be constructively interfered at the output MMI coupler. When the pressure is applied to the membrane as can be observed on Figure 17(b), the strain induced in the membrane due to deflection causes the phase changes in the two arms by the following two mechanisms.

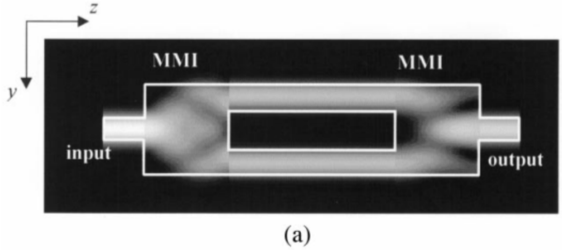

(a)

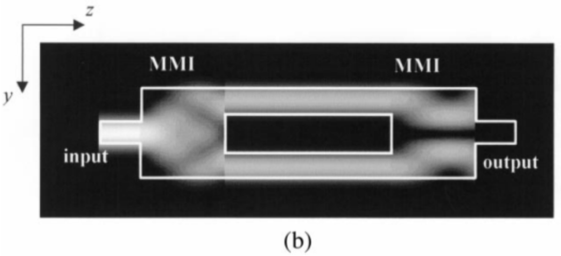

(b)

Fig. 17. Simulated light propagation through the MMI couplers in the proposed sensor when (a). no pressure is applied and (b) pressure is applied (not to scale).

This device has a size of 0.4 mm (width) x 13 mm (length) and the total thickness of the membrane is 7 μm. The device characteristics are measured using a He–Ne laser (λ= 632.8 nm) as a light source. High sensitivity of 8.2 ppm/Pa has been obtained in the range of 100 kPa.

7. Conclusion

Was described the theoretical and practical aspects considered to carry out the measurement of flow by 3 selected methods: Gibson, Winter-Kennedy and Ultrasonic, as well as instrumentation selection and installation on hydroelectric power plants. Gibson's method is used by measuring the static pressure variation in two sections of pipe pressure for different loads of the turbine to determine the flow.

Finally, the results of Gibson's method were used for calibrated flow measuring Winter-Kennedy. This makes it possible to measure flow during normal operation of the turbine continuously.

In the section of the comparison between methods, was observed that for the ultrasonic method, as it decreases the load increases the inaccuracy of the method. Gibson's method applied is still more reliable and thus recommended in IEC standard.

Has been acquired experiences in the methods here described which help to analyze the performance of hydraulic turbines in Mexico and Poland.

In CIICAp are developing sensors based on optics fibber for measuring differential pressure, in addition to the obvious advantage of developing its own technology, can help in a future on flow measurement in hydroelectric power plants.

8. Acknowledgment

Authors would like to thanks at the Mexican Federal Council of Electricity (CFE) for the facilities to perform the tests in their installations. And especially to Eng. José Manuel Fernández Dávila, Hydropower Generator Coordinator and MsC Humberto Hernández Hernández, Regional Mechanical Superintendent.

9. References

Adamkowski A., Janicki W., Kubiak J., Urquiza B.G., Sierra E.F. & Rangel R.(2006) *Water turbine efficiency measurements using the gibson method based on special instrumentation installed inside pipelines* 6th International Conference on Innovation in Hydraulic Efficiency Measurements, July 30 – August1 2006, Portland, Oregon, USA

B.G. Clarke, *Pressuremeters in geotechnical design*, Blackie Academic & Professional, 1995. Pag.111

Castro L, PhD Thesis *Estudio Experimental y Numérico de la Potencia y la Eficiencia en una Turbina Francis: efecto de la Modificación Geométrica del Tubo de Aspiración*, Universidad Autónoma del Estado de Morelos, Centro de Investigación en Ingeniería y Ciencias Aplicadas (CIICAp) 2011

Gibson, N.R.: (1923) *The Gibson method and apparatus for measuring the flow of water in closed conduits*, ASME Power Division, pp. 343-392

Guanghui Ch., Liying L., Hongzhi J., Jimin Y., Lei X. & Wencheng W. (2003) *Simultaneous pressure and temperature measurement using Hi-Bi fiber Bragg gratings* Original Research Article, Optics Communications, Volume 228, Issues 1-3, 1 December 2003, Pages 99-105,

Hernández H.(2010) *Eficiencia de turbinas de la central hidroeléctrica "El Cóbano" mediante los métodos de medición de flujo por Ultrasonido y Gibson* Master Thesis, Universidad Autónoma del Estado de Morelos, Centro de Investigación en Ingeniería y Ciencias Aplicadas (CIICAp), November 2010

Hao-Jan S., Wen-Fung L., Kuei-Ru L., Sheau-Shong B. & Ming-Yue F.(2008), *High-sensitivity temperature-independent differential pressure sensor using fiber Bragg gratings*, 29 September 2008 / Vol. 16, No. 20 / Optics Express.

IEC 41: 1991, *International Standard: Field acceptance tests to determine the hydraulic performance of hydraulic turbines, storage pumps and pump-turbines*

Jenkins R. M., Devereux R. W. J. & Heaton J. M. (1994), *A novel waveguide Mach-Zehnder interferometer based on multimode interference phenomena,* Optics Commun., vol. 109, pp. 410-424, August 1994.

Kubiak J., Urquiza B.G., Adamkowski A., Sierra E.F., Janicki W. & Rangel R.(2005) *Special Instrumentation and Hydraulic Turbine Flow Measurements using a Pressure-Time Method*, Proc.of 2005 ASME Fluids Engineering Division Summer Meeting and Exhibition, June 19-23, Houston, TX, USA. FEDSM2005-77394.

Niemeier Th. & Ulrich R. (1986), *Quadrature outputs from fiber interferometer with 4 × 4 coupler*, Optics Letters, Vol. 11, Issue 10, pp. 677-679 (1986)

Soldano L, B., Veerman F. B., Smit M. K., Verbeek B. H. & Pennings E. C. M.(1991),*Multimode interference couplers*, Proc. Integr. Phot. Research (IPRC), Monterey, CA, Apr. 1991, p. 13

Urquiza B. G., Adamkoswki A, Kubiak J., Sierra F., Janicki W. & Fernández J.M. (2007)*Medición del flujo de una turbina hidráulica de 170 MW utilizando el método Gibson* Ingeniería Hidráulica en México, Vol. 22, No. 3, pp. 125-137 (2007)

Urquiza B. G., Kubiak J., Adamkoswki A. & Janicki W.(2008) *Resultados de medición de flujo y cálculo de eficiencia de la unidad no. 1 en la C. H. El Cóbano* Informe Parcial No. 176P/DM/CIICAp

Urquiza B. G., Kubiak J., Adamkoswki A. & Janicki W.(2008) *Resultados de medición de flujo y cálculo de eficiencia de la unidad no. 1 en la C. H. Santa Rosa* Informe Parcial No. 03P/09/DM/CIICAp

van Roijen R., Pennings E. C. M., van Stralen M. J. N., T. van Dongen, Verbeek B. H. & van der Heijden J. M. M.,(1994) *Compact InP-based ring lasers employing multimode interference couplers and combiners*, Appl. Phys. Lett., vol. 64, no. 14, pp. 1753-1755, 1994.

Rao Y.J. & Jackson D.A. (1996), *Universal fiber-optic point sensor system for quasi-static absolute measurements of multiparameters exploiting low coherence interrogation*, Journal of Lightwave Technology, vol. 14, no. 4, Pp. 592 –600, April 1996.

Zhanxiong W., Dongcao S., Qiming Z. & Hong-Liang C.(2008), *High Pressure Sensor Based on Fiber Bragg Grating and Carbon Fiber Laminated Composite*, IEEE Sensors Journal, Vol. 8, No. 10, October 2008.

8

Microfabricated Implantable Pressure Sensor for Flow Measurement

Sheng Liu, Reginald Farrow and Gordon Thomas
Physics Department, New Jersey Institute of Technology, Newark, NJ
USA

1. Introduction

Gas and liquid pressure and flow are required to be measured and controlled in many applications, such as biomedical system, environmental monitoring and industrial control. Capacitive pressure and flow sensors have been developed and the detailed capacitive pressure sensors have been reviewed and most capacitive sensors use silicon, glass, silicon nitride membrane as sensing plate (Puers, 1993; Baxter, 1997). But in some applications like implanted medical devices, poison gases and high temperature places, the flow is not easy to be recorded. People have developed ways to measure flow and pressure remotely (Akar, 2001; Ong, 2001; Grimes, 2000). The pressure and flow sensors use capacitor as sensing part (Akar, 2001; Oosterbroek, 1999). Combined with the inductor, they are designed as LC resonant circuit. And the LC circuit resonant frequency can be measured by external wireless circuit. From measuring the resonant frequency change, the flow and pressure can be shown. This paper presents a new designed RF wireless capacitive flow and pressure sensor. The design has a parallel capacitor and thin film spiral square inductor as resonant circuit. The capacitor is sensing the pressure change. The inductor is fabricated with the capacitor on wafer using MEMS technique. Because the sensors are used to measure cmH2O pressure, the capacitor has to be very sensitive. One ultra low stress Silicon Nitride was used as the sensing membrane.

2. Sensor design and fabrication

In this section, sensor design and fabrication methods are going to be talked. For flow sensor design, the flow rate and sensor sensitivity have to be concerned first. A RF wireless pressure sensor has been developed. The design has a parallel capacitor and thin film spiral square inductor as resonant circuit. The capacitor is sensing the pressure change. The inductor is fabricated with the capacitor on wafer using MEMS technique.

2.1 Silicon nitride membrane deflection

Flow and pressure sensors use capacitor as sensing part. The capacitor has two parallel plates, one is fixed, one is deflected under pressure. However, the residual stress in the sensing membrane plays an important role. It will be talked first. In all cases, the deflection of membrane under pressure is described by in equation (1) (Vlassak, 1992; Pan, 1990):

$$P = \frac{B_1 t \sigma_0}{a^2}\delta + \frac{B_2 f(v) t E}{a^4 (1-\nu)}\delta^3 \tag{1}$$

where P is the pressure, δ is the deflection of membrane under pressure, t is the thickness of membrane, a is the radius or half length of the membrane, E is Young's Modulus, ν is Poisson Ratio, σ_0 is the initial or residual stress, B_1, B_2 are dimensionless constants, f(v) is function geometry and model depended. These parameters are listed in Table. 1.

Parameter	Value
Pressure range (cmH_2O)	0-45
Thickness of LPCVD SiN_x membrane (nm)	500
Half width of LPCVD SiN_x membrane (mm)	0.686
Young's Modulus of LPCVD SiN_x membrane (Gpa)	90
Poison's ratio of LPCVD SiN_x membrane	0.25
Dimensionless constant B_1	3.23 (Pan, 1990)
Dimensionless constant B_2	1.37 (Pan, 1990)
Geometry and model dependant function 1990)	1.26-0.36v (Pan,
Inductance (nH)	14
Capacitor plates spacing (nm)	500
Resonant frequency as P=0 (GHz)	1.37
Residual Stress (GPa)	139

Table 1. LPCVD SiNx membrane characteristics and used parameters for initial stress computation, summarized characteristics and expected performance parameters of pressure sensor.

For square membranes, the magnitude of the deflection, z, as a function of position on the membrane, x and y, can be described by (Pan, 1990).

$$z = \delta \cos\left(\frac{\pi x}{2a}\right)\cos\left(\frac{\pi y}{2a}\right) \tag{2}$$

For the circular membrane as a hemispherical cap as follows (Pan, 1990):

$$z = \delta - R + \sqrt{R^2 - r^2} \tag{3}$$

where R is radius curvature of the deflected membrane given in Equation (3), r is the distance from the membrane center, and

$$R = \frac{a^2 + \delta^2}{2\delta} \tag{4}$$

The membrane sensitivity, S, is defined by the derivative of displacement with respect to pressure:

$$S = \frac{d\delta}{dP} \tag{5}$$

The full form of S is complicated, but in the region of deflection less than 5 microns shown in Figure 1, the second term of displacement δ in Equation 1 is negligible and S is given just by the first term. Therefore,

$$S = \frac{a^2}{B_1 t \sigma_0} \tag{6}$$

The main result here is that S decreases as the inverse of the residual stress, σ_0. Three values of σ_0 are shown in Figure 1, where the inverse of the linear slopes is the membrane sensitivity.

The other result illustrated in Fig. 1 is that, if the residual stress were to approach zero, the sensitivity would be given by the inverse slope of the second term in Equation 1 that is cubic in δ. In this case the sensitivity would be extremely high at low displacements tending toward infinity as the displacement approaches zero in the approximation of Equation (1).

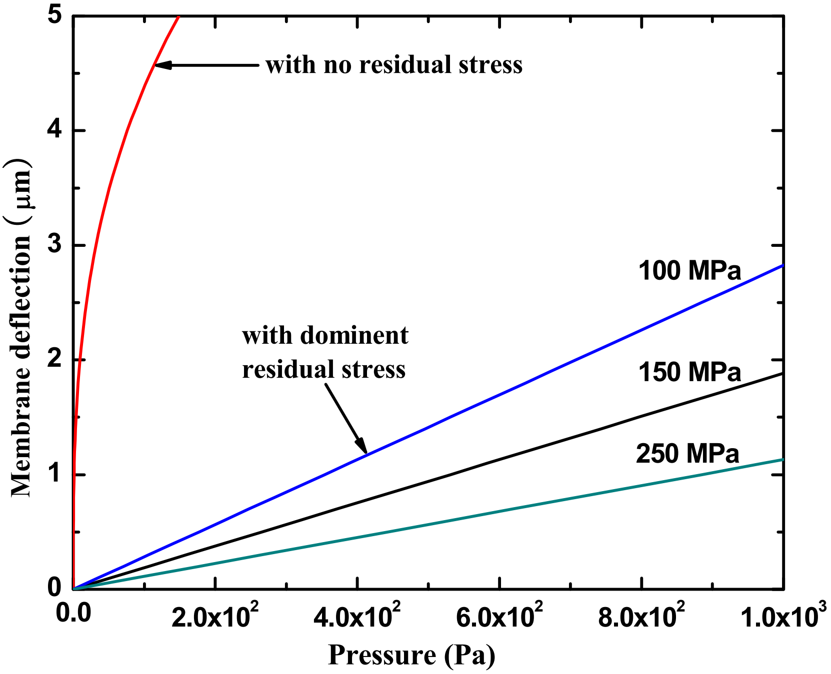

Fig. 1. Computed results for the pressure related to two terms with and without residual stress of Equation 1 as a function of membrane deflection. The lower lines are proportional to the residual stress and are shown for 3 values of it. For higher residual stress, the sensitivity $d\delta / dP$ is smaller, as shown. The membrane sensitivity is proportional to the slope. With achievable value of residual stress, the first term dominates below about 5 microns, where increasing residual stress produces lower sensitivity. If the residual stress were negligible, the sensitivity would be determined by the slope of the second term and would be extremely high.

At small pressures according to Equation 6, the sensitivity is increased as the membrane dimension increases and as the thickness decreases. The computed results were plotted in Figure 2 and Figure 3.

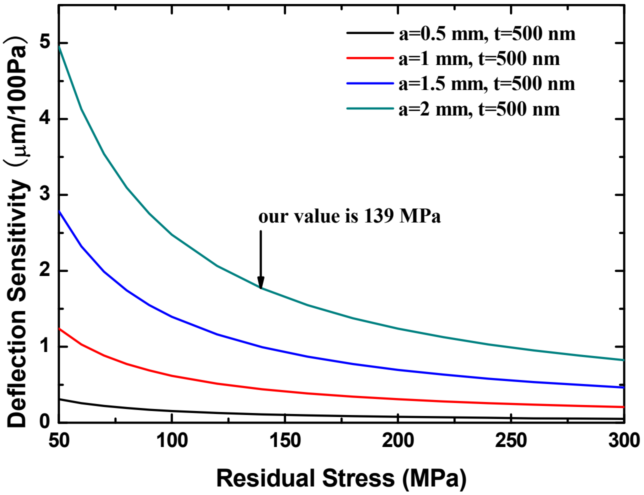

Fig. 2. The computed membrane sensitivity as function of residual stress for different film dimensions .

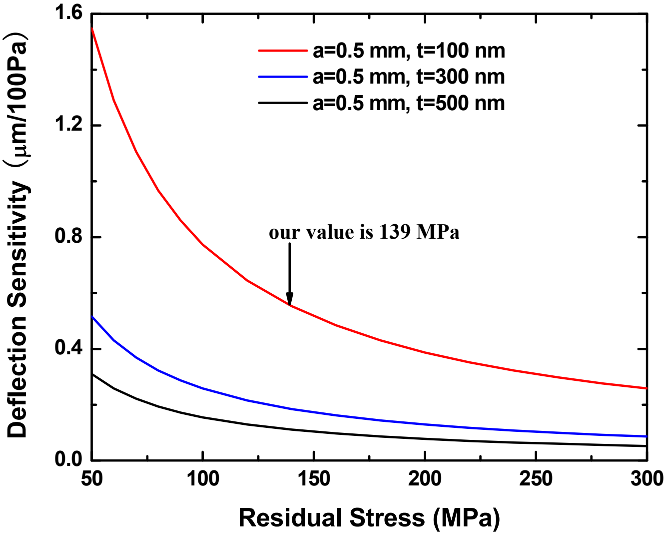

Fig. 3. The computed membrane sensitivity as function of residual stress for different film thickness

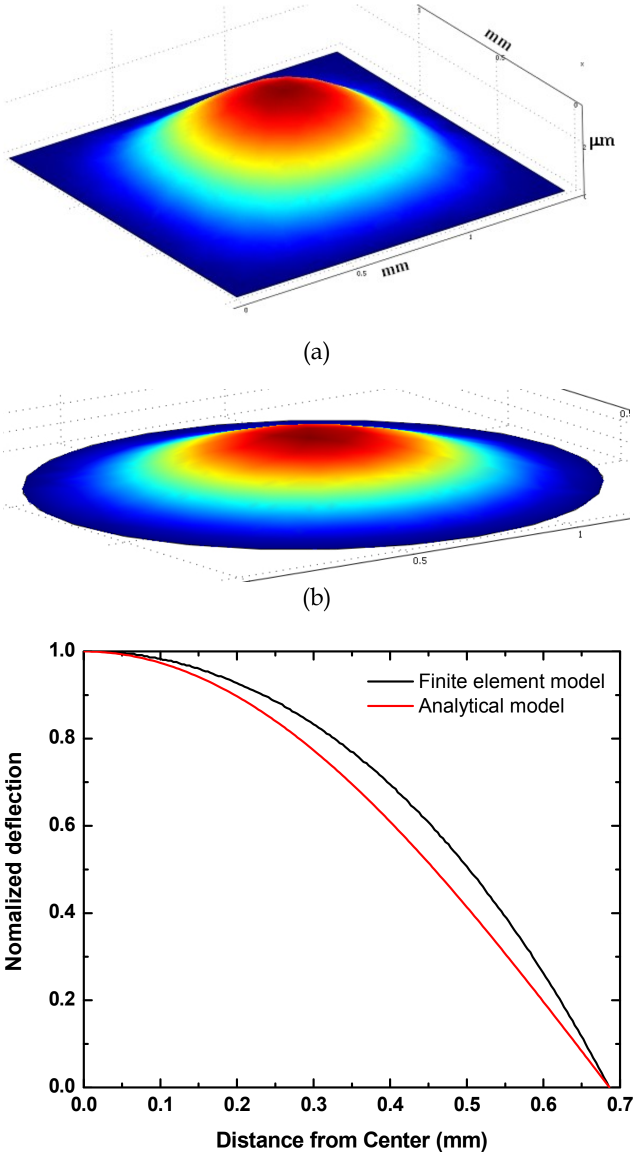

(a)

(b)

(c)

Fig. 4. The simulation of deflection of square membrane (a) and circular membrane (b) as a function of distance under pressure for the parameters listed in Table 1. (c) is the comparison for square membrane.

Because of the importance of the residual stress, a fabrication process has been designed to produce a suitable membrane. Since author plan to make a capacitive sensor at a later stage, the membrane consisted of a metallic layer in addition to the insulating amorphous SiN.

The final membrane was designed as a tri-layer, mostly a 500nm thick a-SiN layer with a thin 10nm layer of Cr to improve adhesion of a thin 40nm layer of Ni. The finite element method (FEM) and theory results are shown in Figure 4. In Fig.4 (a), (b) the deep red color indicates the bigger deflection.

For square membrane, the capacitance can be computed out by integral Equation 7. .

$$\begin{aligned} C &= \int \frac{\varepsilon_0}{d} dS = \varepsilon_0 \int_0^a dx \int_0^a \frac{1}{gap - z} dy \\ &= \varepsilon_0 \int_0^a dx \int_0^a \frac{1}{gap - \delta \cos(\frac{\pi x}{2a}) \cos(\frac{\pi y}{2a})} dy \end{aligned} \tag{7}$$

where ε_0 is the dielectric constant, d is the distance of two plates, a is half width of membrane, gap is the distance between to plates as P=0, x and y are the distance from the membrane center.

2.2 Pressure sensor design

It is shown in Figure 5 that structure of design of wireless pressure sensor. The sensor has two parts, capacitor and inductor coil. The SiNx film is 500nm thick LPCVD low stress film deposited on the silicon wafer substrate. The gap between capacitor plates is 500 nm. The inductor coil and capacitor top plate are covered by plasma enhanced chemical vapor deposition (PECVD) silicon nitride.

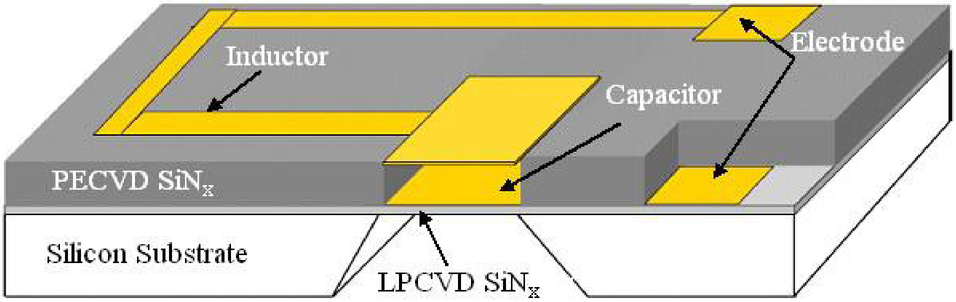

Fig. 5. The 3D structure view inter-electronic part of wireless pressure sensor.

The cross view is shown in Figure 6a. The bottom plate of capacitor can deflect under pressure change. 3D structure view inter-electronic part of wireless pressure sensor

The electrode pads, capacitor plates and inductance coil are 10nm Cr with 40 nm Ni. The electrical equivalent circuit of the sensor is showed in Figure 6b. External inductor or capacitor can connect to the sensor to decrease the resonant frequency. That is the reason two electrodes are opened for connection. The sensor characteristics and expected performance parameters are summarized in Table 1.

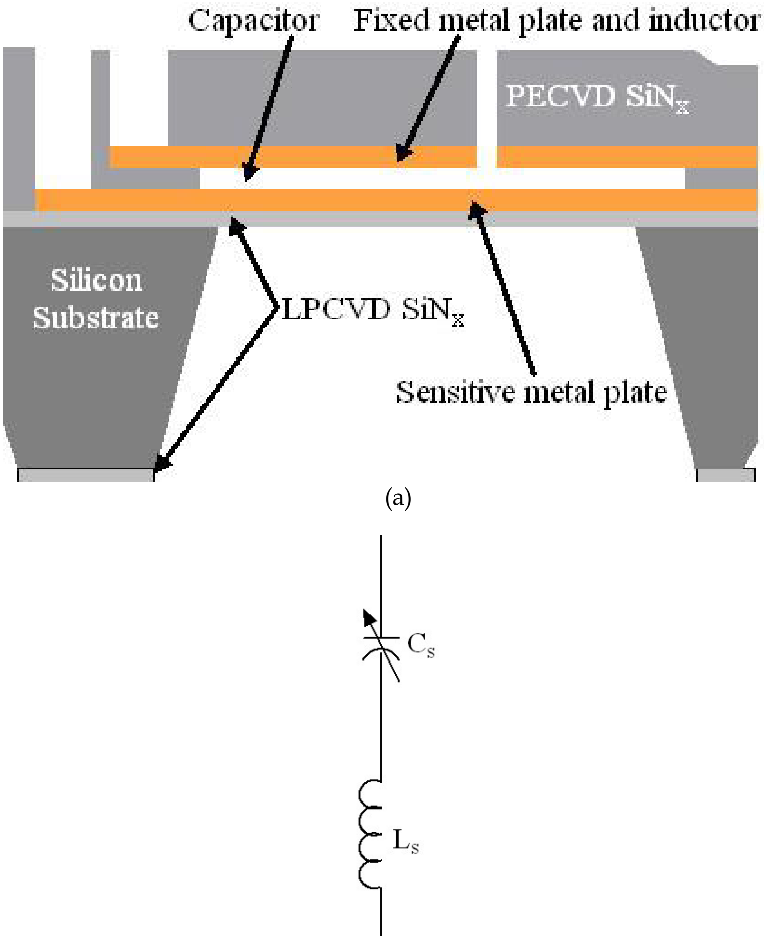

(a)

(b)

Fig. 6. (a) The cross-section of pressure sensor; (b) equivalent electrical circuit.

The self inductance of the inductor can be computed using Equation 8 (Ong, 2001).

$$L_S = 1.39 \times 10^{-6}(OD + ID)N^{5/3}\log_{10}\left(\frac{4OD + ID}{OD - ID}\right) \tag{8}$$

where ID and OD are the inner and outer diameters of the inductor, N is the number of turns.

Therefore, the resonant frequency of the sensor can be calculated out by.

$$f_0 = \frac{1}{2\pi\sqrt{L_s C}} \tag{9}$$

2.3 Fabrication process

The fabrication process of RF wireless pressure sensor is presented in Figure 7. 500nm LPCVD low stress silicon nitride is deposited on both sides of Si wafer (Figure 7a). Cr and 40

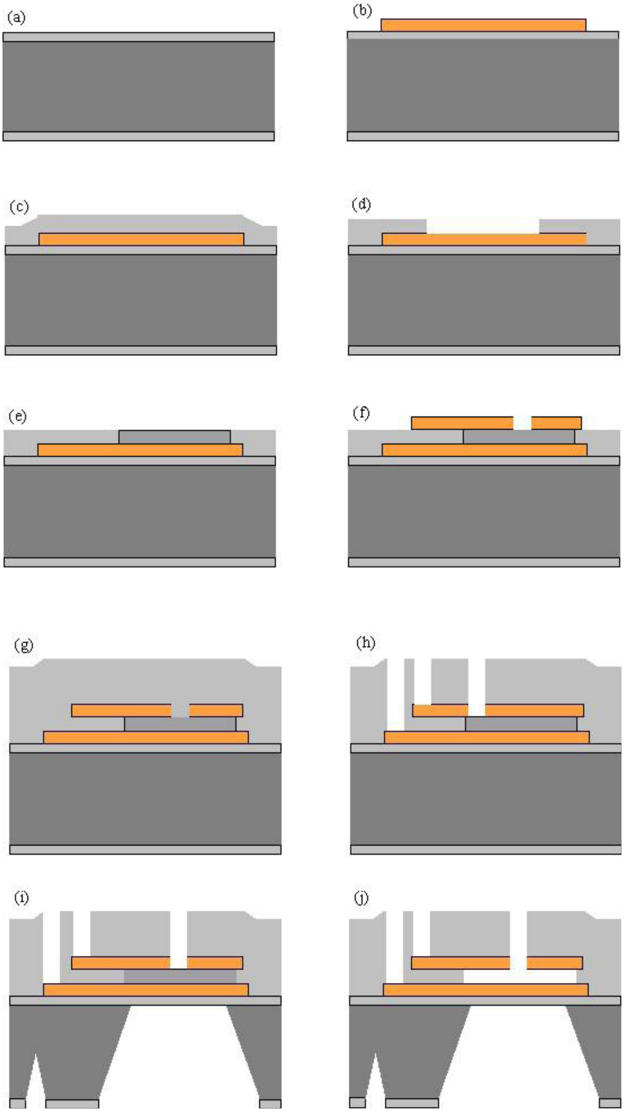

Fig. 7. Fabrication process for the wireless pressure sensor. (a) Silicon with LPCVD silicon nitride; (b) First layer metal deposition; (c) PECVD silicon nitride deposition; (d) RIE PECVD silicon Nitride; (e) silicon dioxide deposition; (f) Second layer metal deposition; (g) PECVD silicon nitride deposition; (h) RIE PECVD silicon Nitride; (i) RIE LPCVD silicon nitride and KOH silicon etching; (j) HF silicon dioxide etching.

nm Ni are deposited on a silicon wafer with 500 nm LPCVD low stress silicon nitride thin film (Figure 7b). PECVD silicon nitride is deposited on the metal for 750 nm as bottom plate of capacitor and electrode (Figure 7c). One window is opened by RIE and 500 nm SiO2 is deposited into the window (Figure 4d and Figure 7e). A thin metal film (50 nm) is then given as top plate of capacitor, inductor and electrode (Figure 7f). A PECVD silicon nitride protection layer (1 um) is then grown on the second metal layer (Figure 7g). Then reactive ion etching (RIE) method is used to etch the PECVD silicon nitride to open window for later etching silicon dioxide (Figure 7h). The back side window of silicon nitride film is etched and the silicon wafer is selectively etched with KOH and the etching stops on top LPCVD silicon nitride layer (Figure 7i). The final step is etching silicon dioxide with HF to open cavity for capacitor (Figure 7j).

3. Experimental results and discussion

The residual stress of LPCVD silicon nitride film has been measured by using Mickleson interferometer. It is σ_0=139MPa. The experiment setup is showed in Figure 8.

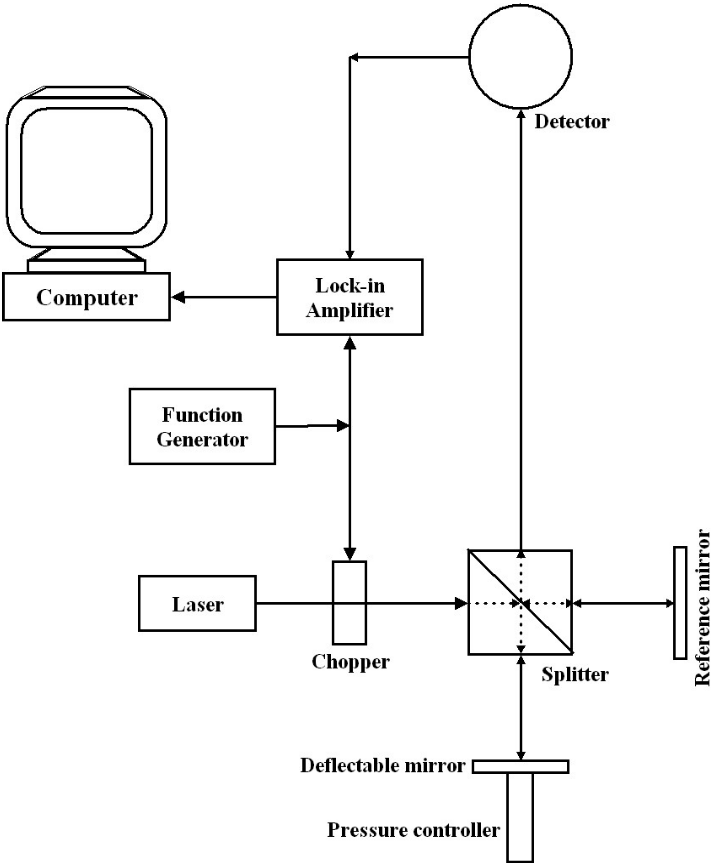

Fig. 8. Schematic of setup of optical measurement for membrane deflection and residual stress.

Based on the design, the RF wireless flow and pressure sensor has been fabricated shown in Figure 9. In Figure 9, it shows top view of the sensor and Figure 9b shows the back side window. Because of HF etching window, the real top metal area is reduced 5%. The resonant frequency as function of pressure is measured by setup shown in Figure 10. In Figure 10, manometer_1 is for pressure reading. Flow rate can be read out by the pressure difference of manometer_1 and manometer_2. The resonant frequency change in response to pressure is shown in Figure 11. The frequency shifted from 1016 MHz to 1002 MHz. The result is replotted in Figure 12.

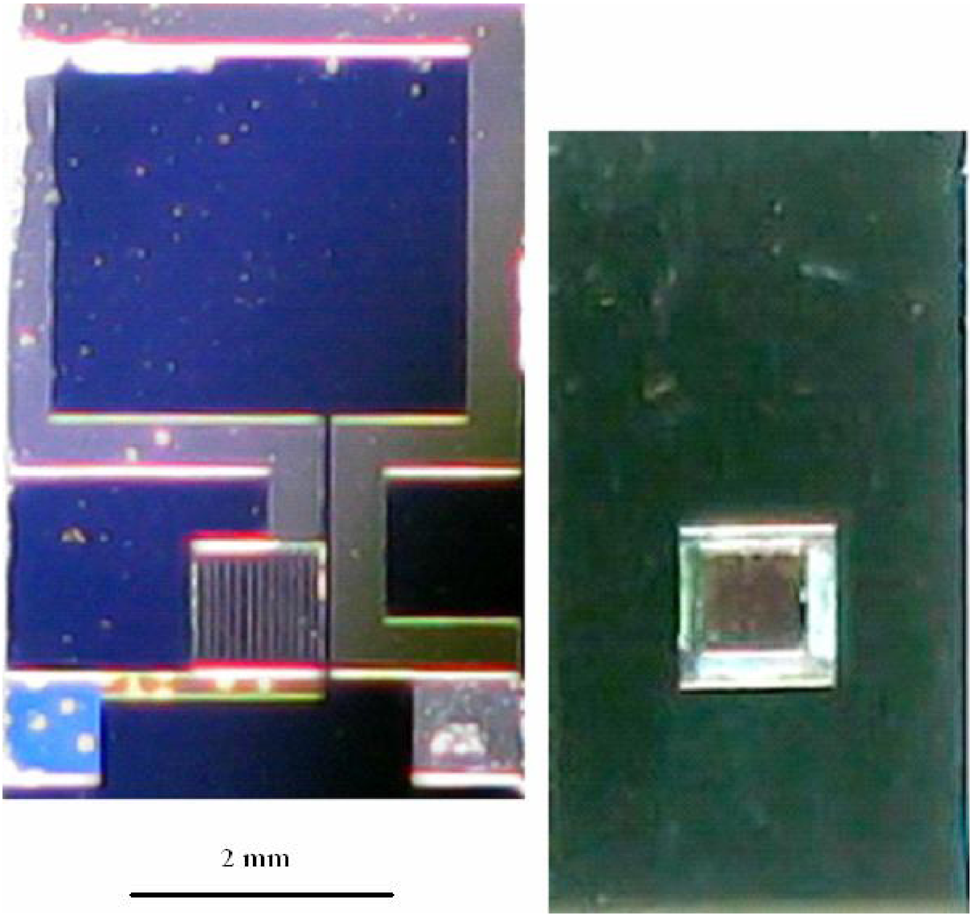

(a) (b)

Fig. 9. The photograph of a fabricated sensor. (a) the top view of the sensor; (b) the back side view of the sensor and window.

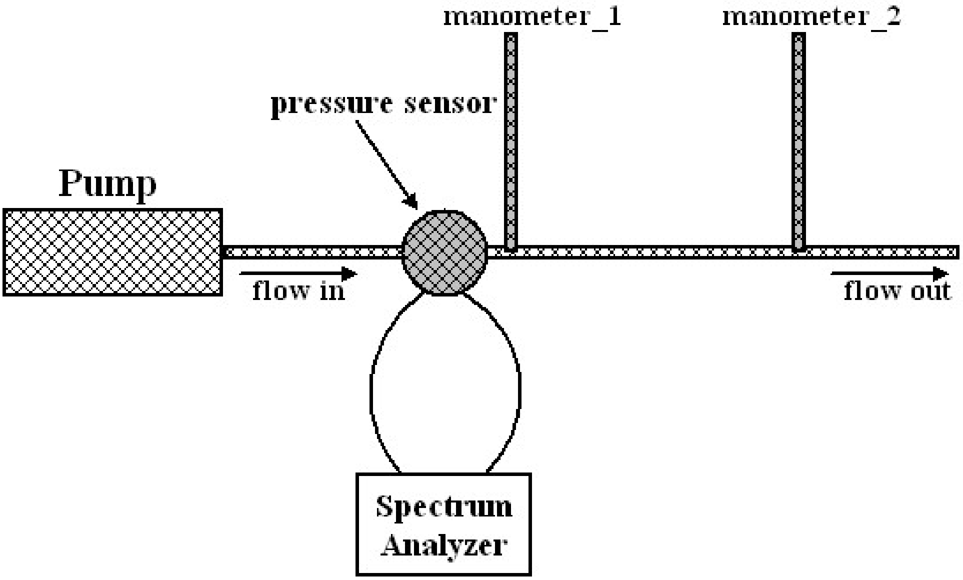

Fig. 10. Schematic of setup of wireless pressure and flow measurement.

There are several parameters can affect the sensor frequency sensitivity. Equation 10 shows the capacitance pressure sensitivity.

$$\begin{aligned}\frac{dC}{dP} &= \varepsilon_0 \int_0^a dx \int_0^a \frac{z}{P \times (gap - z)^2} dy \\ &= \varepsilon_0 \int_0^a dx \int_0^a \frac{\delta \cos(\frac{\pi x}{2a}) \cos(\frac{\pi y}{2a})}{P \times (gap - \delta \cos(\frac{\pi x}{2a}) \cos(\frac{\pi y}{2a}))^2} dy\end{aligned} \tag{10}$$

Equation 11 presents the frequency pressure sensitivity. Substituted the Equation 10 into Equation 11, the frequency pressure sensitivity can be computed out from Equation (12).

$$FreqSens = \frac{df_0}{dP} = \frac{df_0}{dC}\frac{dC}{dP} = \frac{1}{4\pi\sqrt{LC^3}}\frac{dC}{dP} \tag{11}$$

$$
\begin{aligned}
FreqSens &= \frac{1}{4\pi\sqrt{LC^3}}\varepsilon_0\int_0^a dx\int_0^a \frac{z}{P\times(gap-z)^2}dy \\
&= \frac{\varepsilon_0}{4\pi\sqrt{LC^3}}\int_0^a dx\int_0^a \frac{\delta\cos(\frac{\pi x}{2a})\cos(\frac{\pi y}{2a})}{P\times(gap-\delta\cos(\frac{\pi x}{2a})\cos(\frac{\pi y}{2a}))^2}dy
\end{aligned}
\tag{12}
$$

The frequency pressure sensitivity was plotted as function of gap between two metal plates, residual stress, sensing membrane thickness and half width of sensing membrane shown in Figure 13-16. From Figure 13, author found as the gap increasing, the frequency pressure sensitivity decreased. Figure 14, the frequency pressure sensitivity decreased when membrane residual stress increased. In Figure 15, the frequency pressure sensitivity decreased when membrane thickness increased. From Figure 16 when the half width of membrane increased, the frequency pressure sensitivity increased.

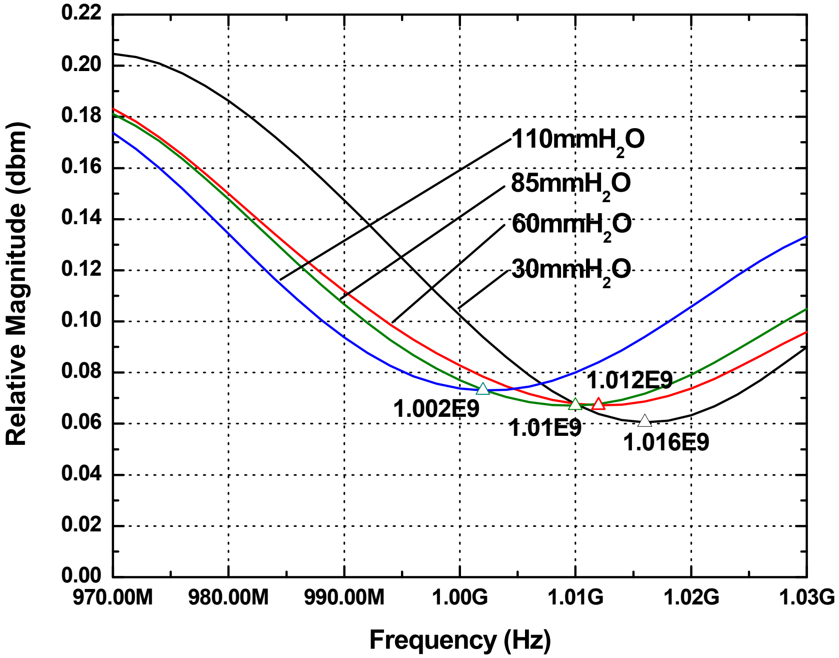

Fig. 11. The absorption response as a function of pressure.

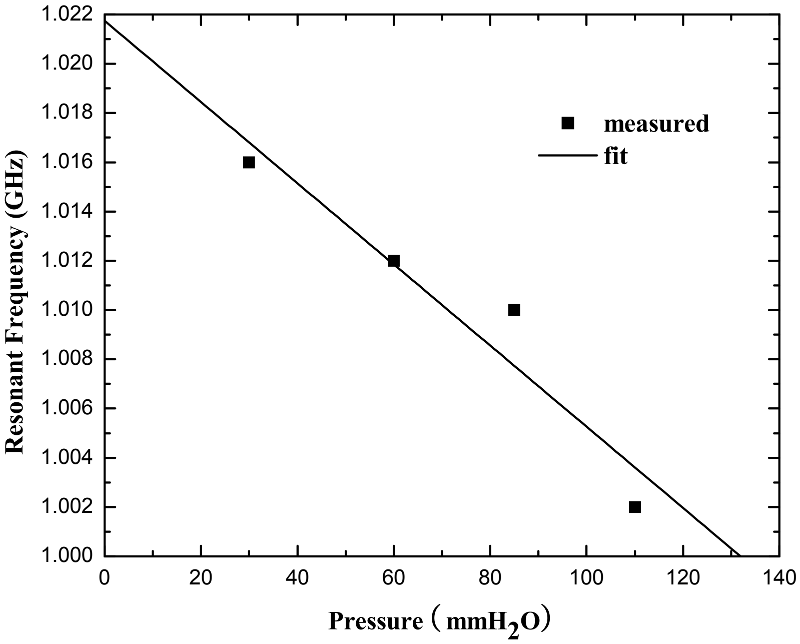

Fig. 12. The measured resonant frequency as a function of applied pressure.

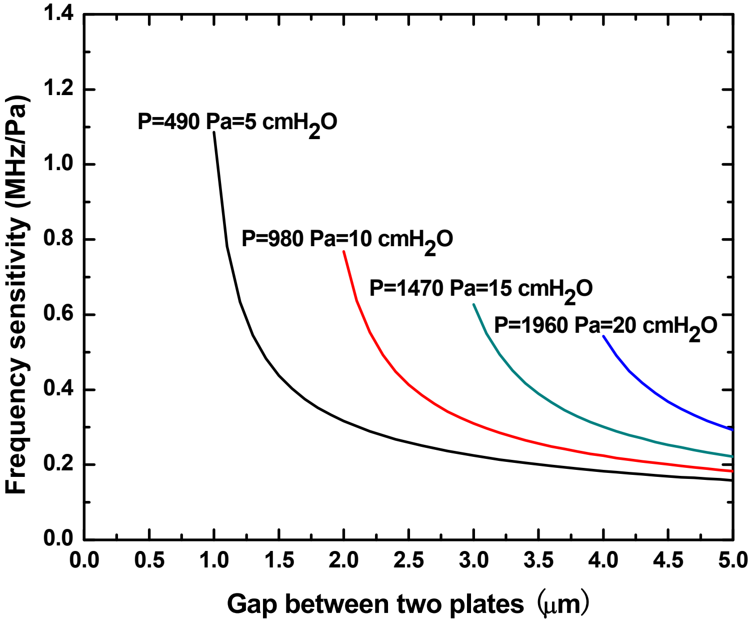

Fig. 13. The frequency pressure sensitivity responses with the gap between two metal plates

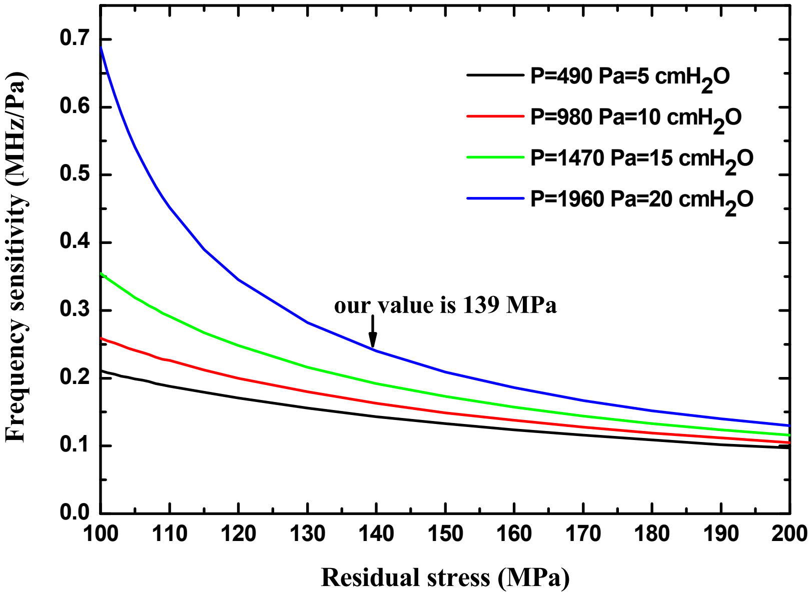

Fig. 14. The frequency pressure sensitivity responses with the residual stress of sensing membrane.

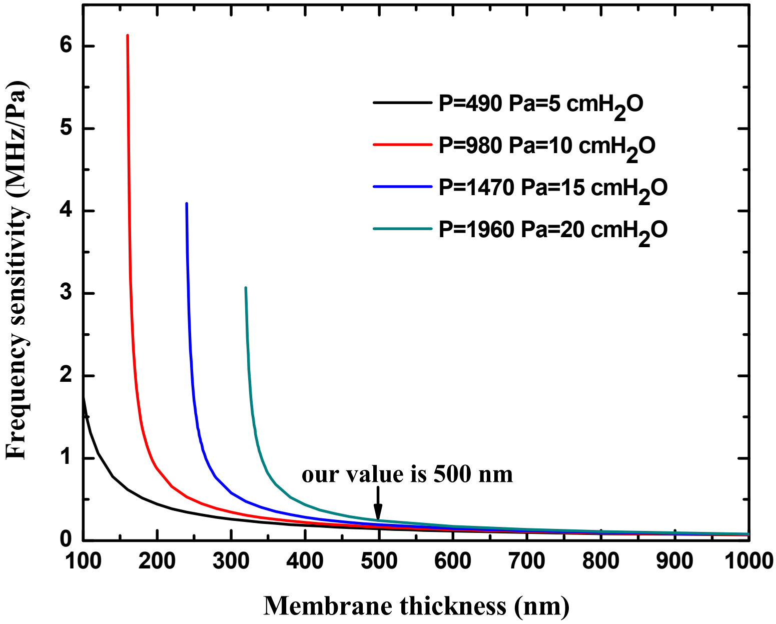

Fig. 15. The frequency pressure sensitivity responses with sensing membrane thickness.

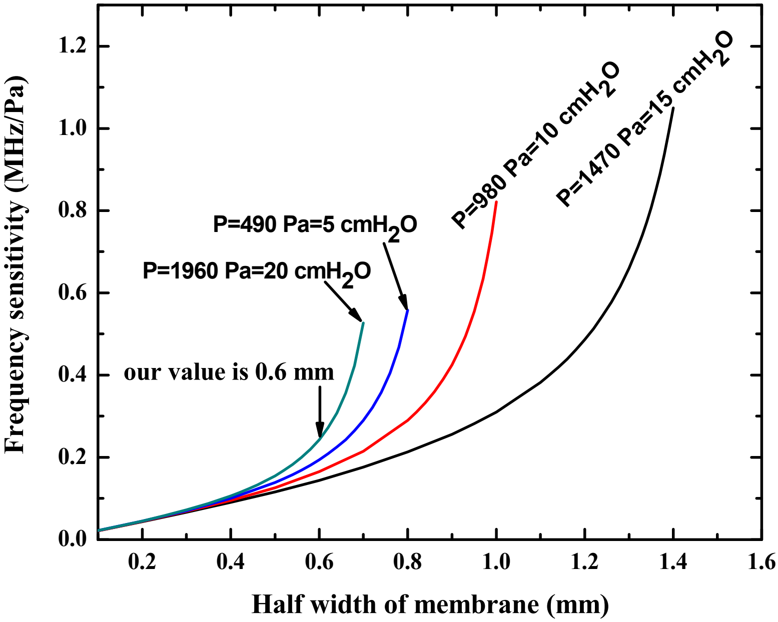

Fig. 16. The frequency pressure sensitivity responses with half width of sensing membrane.

4. Conclusion

A RF wireless flow and pressure sensor has been designed and fabricated. The sensor has a pressure sensitive capacitor and an inductor. The device size is 10 mm × 4 mm ×0.5 um and can measure a pressure range of 0-20 cmH_2O. The resonant frequency of the sensor has been measured and computed and the sensitivity is 1.65 MHz/cmH_2O. The parameters of sensor which can affect the frequency pressure sensitivity have been discussed. The computed results give the very useful information for sensor design. Future work will focus on optimization the distance of between two plates, improvement pressure sensitivity, development of external detection system and design of new inductor coil.

5. Acknowledgment

We appreciate the fabrication support by Cornell Nanofabrication Facility.

6. References

Puers, R; (1993). Capacitive sensors: When and how to use them, Sensors and Actuators A: Physical Vol. 37-38, pp. 93-105.

Baxter, L. K. (1997) Capacitive Sensors: Design and Applications, IEEE Press.

Akar, O.; Akin, T.; Najafi, K. (2001). A wireless batch sealed absolute capacitive pressure sensor, Sensors and Actuators A: Physical Vol. 95, pp. 29-38.

Ong, K. G.; Grimes, C. A.; Robbins , C. L.; Singh, R. S. (2001). Design and application of a wireless, passive, resonant-circuit environmental monitoring sensor, Sensors and Actuators A: Physical Vol.93, pp. 33-43.

Grimes, C. A.; Kouzoudis, D. (2000). Remote query measurement of pressure, fluid-flow velocity, and humidity using magnetoelastic thick-film sensors, Sensors and Actuators A: Physical Vol.84, pp. 205-212.

Oosterbroek, R. E.; Lammerink, T. S. J.; Berenschot, J. W.; Krijnen, G. J. M.; Elwenspoek, M. C.; Berg, A. van den. (1999). A micromachined pressure/flow-sensor, Sensors and Actuators A: Physical Vol.77, pp.167-177.

Vlassak, J.J.; Nix, W.D. (1992). A new bulge test technique for the determination of Young's modulus and Poisson's ratio of thin films, Journal of material research, Vol.7, pp. 3242-3249.

Pan, J. Y.; Lin, P.; Maseeh, F.; Senturia, S. D. (1990). Verification of FEM analysis of load-deflection methods for measuring mechanical properties of thin films, solid-State Sensor and Actuator Workshop, 4th Technical Digest., IEEE, pp. 70-73.